T2R2 東京科学大学 リサーチリポジトリ
Science Tokyo Research Repository

論文 / 著書情報
Article / Book Information

題目(和文)	
Title(English)	Spectroscopic Study on an Arc-heated Magnetically Trapped Expanding Plasma Jet
著者(和文)	赤塚洋
Author(English)	HIROSHI AKATSUKA
出典(和文)	学位:博士(工学), 学位授与機関:東京工業大学, 報告番号:乙第2743号, 授与年月日:1995年3月31日, 学位の種別:論文博士, 審査員:
Citation(English)	Degree:Doctor of Engineering, Conferring organization: , Report number:乙第2743号, Conferred date:1995/3/31, Degree Type:Thesis doctor, Examiner:
学位種別(和文)	博士論文
Type(English)	Doctoral Thesis

Powered by T2R2 (Science Tokyo Research Repository)

Spectroscopic Study on an Arc-heated Magnetically Trapped Expanding Plasma Jet

Hiroshi AKATSUKA

Research Laboratory for Nuclear Reactors

Tokyo Institute of Technology

Contents

The list of dissertations with regard to the present thesis of the present author

1. "Arc-heated magnetically trapped expanding plasma jet generator", H. Akatsuka and M. Suzuki, *Rev. Sci. Instrum.*, **64**, 1734 (1993). (Ref. [59])

2. "Preparations of carbon clusters by arc-heated expanding plasma jet", T. Sone, H. Akatsuka, and M. Suzuki, *Plasma Sources Sci. Technol.*, **2**, 46 (1993). (Ref. [2])

3. "Stationary population inversion of hydrogen in an arc-heated magnetically trapped expanding hydrogen-helium plasma jet", H. Akatsuka and M. Suzuki, *Phys. Rev. E*, **49**, 1534 (1994). (Ref. [62])

4. "Numerical study on population inverion and lasing conditions in an optically thick recombining helium plasma", H. Akatsuka and M. Suzuki, *Contrib. Plasma Phys.*, **34**, 539 (1994). (Ref. [69])

5. "An experimental study of stationary population inversion in a cold recombining expanding helium plasma jet", H. Akatsuka and M. Suzuki, *Plasma Sources Sci. Technol.*, **4**, 125 (1995). (Ref. [68])

6. "Spectroscopic study on a magnetically trapped expanding plasma jet" (in Japanese), H. Akatsuka and M. Suzuki, *J. Plasma Fusion Res.*, (1994), **70**, 1196. (Ref. [70])

The list of presentations at the societies by the author

1. "Population inversion in magnetically trapped expanding plasma jet", H. Akatsuka and M. Suzuki, *Extended Abstracts of the 39th spring meeting, 1992, The Japan Society of Applied Physics and Related Societies*, No. 1, p21, 29p-ZS-10 (1992) (in Japanese).
2. "Population inversion in a magnetically trapped expanding plasma jet (1)", H. Akatsuka and M. Suzuki, *Abstracts of 1992 Fall Meeting of the Atomic Energy Society of Japan*, p236, D56 (1992) (in Japanese).
3. "Population inversion in a magnetically trapped expanding plasma jet (2)", H. Akatsuka and M. Suzuki, *Abstracts of 1993 Annual Meeting of the Atomic Energy Society of Japan*, p109, B49 (1993) (in Japanese).
4. "Population inversion in a magnetically trapped expanding plasma jet (3)", H. Akatsuka and M. Suzuki, *Abstracts of 1993 Fall Meeting of the Atomic Energy Society of Japan*, p590, L2 (1993) (in Japanese).
5. "Population inversion in a magnetically trapped expanding plasma jet (4)", H. Akatsuka and M. Suzuki, *Abstracts of 1994 Anual Meeting of the Atomic Energy Society of Japan*, p255, F11 (1994) (in Japanese).
6. "Population inversion in a magnetically trapped expanding plasma jet (5)", H. Akatsuka and M. Suzuki, *Abstracts of 1994 Fall Meeting of the Atomic Energy Society of Japan*, **1**, 556, H48 (1994) (in Japanese).
7. "Population inversion in magnetically trapped expanding plasma jet, I, Hydrogen and Helium", H. Akatsuka and M. Suzuki, *Abstracts of the Meeting of the Physical Society of Japan, 1993 Sectional Meeting Part 4*, p56, 14a-DB-5 (1993) (in Japanese).

Chapter 1. Introduction

Nowadays expanding plasmas are widely applied to a plasma processing, such as generation of thin films [1] and preparation of various cluster materials [2]. And the methods for the diagnostics about them are examined and developed eagerly from the fundamental viewpoint [3-4]. In order to measure various plasma parameters, such as electron temperature and density, spectroscopic observations are convenient [5-6]. When the plasma is applied to the studies on the recombination lasing [7], it is essential to examine the population densities of the laser upper levels and of the lower levels in the plasmas by means of spectroscopic analysis. We have an excellent monochromator in an ultra-violet and visible wavelength region which is calibrated absolutely in our laboratory [8]. Plasmas are not perturbed by spectroscopic observations, which is most different from a probe analysis and advantageous. Diagnostics of the plasmas by various probes, such as a Langmuir probe [9], are also convenient and suitable to scrutinize the spatial distribution of the plasma parameters because of its spatial resolution [10]. But the measurement by probes is inevitably accompanied by considerable errors, say, factor $2-10$, and the explanation of the data is difficult when a magnetic field is applied [11] or the plasma is in a high speed jet [12]. At that time, spectroscopic observations are preferable to the probe analysis. In general, spectroscopic observations will show more exact data than the probe method.

Apart from plasma processing, another interesting potential of expanding plasmas is an application to a lasing medium [7]. The plasma comes into a recombining phase when it is expanded due to an adiabatic expansion or some other reasons. The electron temperature becomes low, and the population inversion is expected to occur between the excited level pairs of atoms and ions in the plasma [13]. About three decades have passed since one of the earliest proposals was made that a cold recombining plasma would be applied to a lasing medium [14]. Since then, many experiments [15-25] and theoretical calculations have been performed [26-29], and the conditions for generating population inversions have been discussed. Especially, the researches in USSR had been continued eagerly from the

fundamental viewpoint [14, 30-40]. Recently many authors have examined the potential for lasing experimentally by pulsed laser-produced recombining plasmas to create short wavelength lasers [41-43]. Nowadays, the wavelength of recombination pumping lasers covers the VUV (vacuum ultra violet) and XUV (extreme ultra violet) region. In the nuclear engineering, the recombining plasmas are also expected to become a coherent light source in the X-ray wavelength region [44]. Extensive researches and development have been carried out in many institutes in order to create X-ray lasers using recombining plasmas [45-48].

As for the pumping methods of X-ray lasers, two schemes are being developed now. One is a collisionally pumped X-ray laser, in which the orbital electrons are excited through collisions with high energy electrons in a high-temperature plasma. The pumping scheme is illustrated in Fig. 1.1 [49]. Multi-charged ions of a closed electron shell, such as Ne-like ions ($2p^6$) and Ni-like ions ($3d^{10}$), are used as ground states. Population inversion is created between the level pairs with the same principal quantum number in this collisional excitation pumping scheme ($\Delta N = 0$). The other is a recombining plasma X-ray laser, where multi-charged ions of light atoms of high density in a recombining state are used in a cold plasma. A pumping mechanism of a recombining plasma X-ray laser of Li-like Al ion is illustrated in Fig. 1.2 [50]. In this scheme, the multi-charged ions recombine mainly through three-body recombination processes, which makes the recombined ions into high-lying excited states dominantly. In these high-lying levels, electrons depopulate these high-lying levels through the collisional de-excitations with free electrons. On the other hand, in the low-lying excited levels, radiative decay process becomes very dominant. Therefore, the population inversion is created between the levels with the different principal quantum numbers ($\Delta N = 1 - 2$). When we compare these two pumping schemes in the same laser wavelength, the recombination pumping is more efficient than the collisional pumping. Therefore, the recombination pumping is expected to be an X-ray laser of high-efficiency.

In addition to the technological point of view, expanding plasmas are also interesting

from a fundamental aspect. Electrons, heavy charged particles and neutral species will move in a different way, especially in a magnetic field. Each particle will be separated, which results in another electric field. The consequent electromagnetic field will determine the movement of the charged particles. Moreover, it is considered to exist many kinds of atomic elementary processes in the expanding plasmas, such as radiative recombinations, three-body recombinations, excitations and deexcitations by electron collisions. Such atomic processes interact with magnetohydro dynamic properties of the plasma, for example, variations of electron temperature and density [51-53].

In the field of nuclear fusion engineering, examinations of a recombining plasma are significant because they tell us much knowledge on atomic processes in a boundary plasma such as a divertor plasma of a nuclear fusion reactor [54]. There exist recombining plasmas of hydrogen, deuterium, tritium and helium in a boundary area of a fusion reactor [13]. Studies should be made on the effective cooling of these recombining plasmas using atomic processes in the plasma, such as an effective remote radiative cooling, which leads to the decrease of the heat flux onto the first wall of a nuclear fusion reactor [55,56]. The effects of the applied magnetic field, the background pressure and species of a target gas, should be investigated quantitatively, because it gives us suggestive information on the designing of the divertor in the future. Recently a gas target divertor is often discussed as a divertor of ITER (Intermational Thermonuclear Experimental Reactor [57,58]). If the remote radiative cooling is localized in the divertor, the cooling of it is effectively accomplished without contaminating the core plasma. Basically, it is considered that the high collision frequency and the short mean free path will prevent the core plasma from being cooled. Although, at present, it seems difficult to cool the plasma without increasing impurities in the main plasma by a gas divertor, it should be emphasized that we should examine the possibility of the gas contact cooling of the divertor plasma. It is one of the effective methods to decrease the thermal load onto the divertor plate, where the engineering design is one of the most critical problems in ITER [58].

We developed an apparatus that produced an arc-heated magnetically trapped ex-

panding plasma jet, where an arc-heated thermal plasma was continuously spouted from a small nozzle of $\sim$ 1 mm diameter into a large rarefied gas wind tunnel with a parallel magnetic field, for the purpose of applications of a thermal and a recombining plasma [59]. At first, the apparatus was applied to a chemical engineering, such as a cluster preparer, and we generated rare gas plasmas [60,61]. Then, we examined the spectroscopic characteristics of the plasma, and measured the population densities of some excited states of He I. In consequence, population inversions were observed between several excited states [59]. In addition, when a certain amount of hydrogen gas was mixed into a discharging helium gas, it was found that a stable hydrogen expanding plasma was generated [62]. Hence, these plasmas are expected to show us fundamental knowledge on the characteristics of recombining hydrogen and helium plasmas. It is expected that the plasma jet can simulate a boundary plasma of a nuclear fusion reactor. It is also expected that the effective methods are examined in order to cool recombining plasmas rapidly in a divertor region in a nuclear engineering, and in order to create large population inversions with this apparatus in a laser engineering.

A number of papers have been published with regard to the spectroscopic study on the plasma of a divertor simulator, such as TPD-I,II of National Institute for Fusion Science [17, 18, 63-65], NAGDIS-I of Nagoya University [66], MAP of Tokyo University, PISCES-A,B of UCLA [67] and PSI-1 of IPP/Berlin [54]. The plasmas in our apparatus is generated by an arc discharge, hence its electron temperature T_e is about $1-2$ eV and electron density n_e is about 10^{17} cm^{-3} before the expansion, and $T_e \simeq 0.1$ eV and $n_e \simeq 10^{13}$ cm^{-3} in the expansion area [59, 61]. Although the electron temperature in the expansion area is a little lower than that in the various foregoing simulators, the expansion ratio of the neutral particles is much larger ($\sim 10^4 - 10^5$). The conductance of the plasma expansion area is very large, and it has a large pumping speed (10 m^3/s at $10^{-2} - 10$ Pa). In addition, the velocity of the plasma jet is considered to be supersonic [62], which is also one of the features of our plasma generator.

As is explained above, the specifications of our apparatus is rather unique, therefore it

is expected that new ideas will be shown to cool recombining plasmas of hydrogen, deuterium and helium efficiently. The main purpose of this thesis is to clarify the conditions to cool the recombining plasmas effectively and rapidly. From that point of view, we investigate the characteristics of the plasmas in our apparatus "Arc-heated magnetically trapped expanding plasma jet generator", mainly by spectroscopic observations [68]. In chapter 2, we describe the design of this apparatus, and the basic characteristics of the plasma generator [59]. Then, we discuss the strength of the magnetic field which is required for stable generation of the plasmas. Possible applications to the cluster preparer of the apparatus are also shortly discussed.

The second purpose of this thesis is to discuss the potential for the cw lasing by recombining plasmas. As is mentioned so far, a number of spectroscopic observations of expanding plasmas have also been performed in this field. However, when the plasma was expanded in a lower pressure chamber, the magnetic field had seldom been applied. And it was numerically shown that the electron density should not be too low to create large population inversion, although the electron temperature should be as low as possible [28, 29]. In addition, the velocity of the plasma jet should be as large as possible because the neutral particles should be cooled rapidly. In this study, we examine the conditions to keep the electron density appropriate in cooling the electrons. We discuss the effect of the magnetic field and the background pressure on the plasma parameters [68]. This is one of the fundamental physics of developing cw recombination lasers, which will be applied to a short wavelength laser pumped by recombining plasmas in the future.

From that point of view, in and after chapter 3, we discuss the effects of experimental parameters, such as an axial distance from the nozzle, the magnetic field and the pressure in the plasma expansion area, on the various plasma parameters like T_e and n_e. We will discuss helium plasmas in chapters 3 and 4, hydrogen and deuterium plasmas in 5, argon plasmas in 6. For helium plasmas, we take two chapters. Chapter 3 mainly deals with the experimental results and discussions [68], whereas chapter 4 deals with the numerical calculations using a collisional radiative model of He I that we modified slightly [69].

We discuss experimental results of the effect of the magnetic field and the pressure in the plasma expansion area on the electron density, temperature and the populations of excited states of He I in chapter 3. As will be shown later, the generated helium plasmas are optically thick for the transitions to the ground state, and it is very difficult to generate optically thin helium plasmas by this apparatus. This is indirectly confirmed by the experimental examinations of the radial profile of the population densities of some excited states.

In this thesis, the theoretical analysis is performed in terms of atomic processes, and we use a collisional radiative model. The population densities of excited states in the plasma can be calculated with the model as functions of the electron temperature and density. We modified the customary collisional radiative model slightly for an expanding recombining helium plasma in which an optical thickness cannot be neglected, which is explained in detail in chapter 4. We discuss the background pressure required for the laser oscillation quantitatively in chapter 4. The mechanisms of forming population inversions are also discussed in terms of atomic processes. Likewise, the experimental and numerical examinations are described for hydrogen and deuterium plasmas in chapter 5, and for argon plasmas in chapter 6 [70]. Although it seems that an argon plasma is not important in a nuclear fusion engineering, its cooling property is somewhat different from the plasmas of helium and hydrogen. It is worth while to examine the variation of the electron temperature of the argon expanding plasma since it suggests one of the common methods of cooling any plasmas. Finally, summary and conclusions are described in chapter 7.

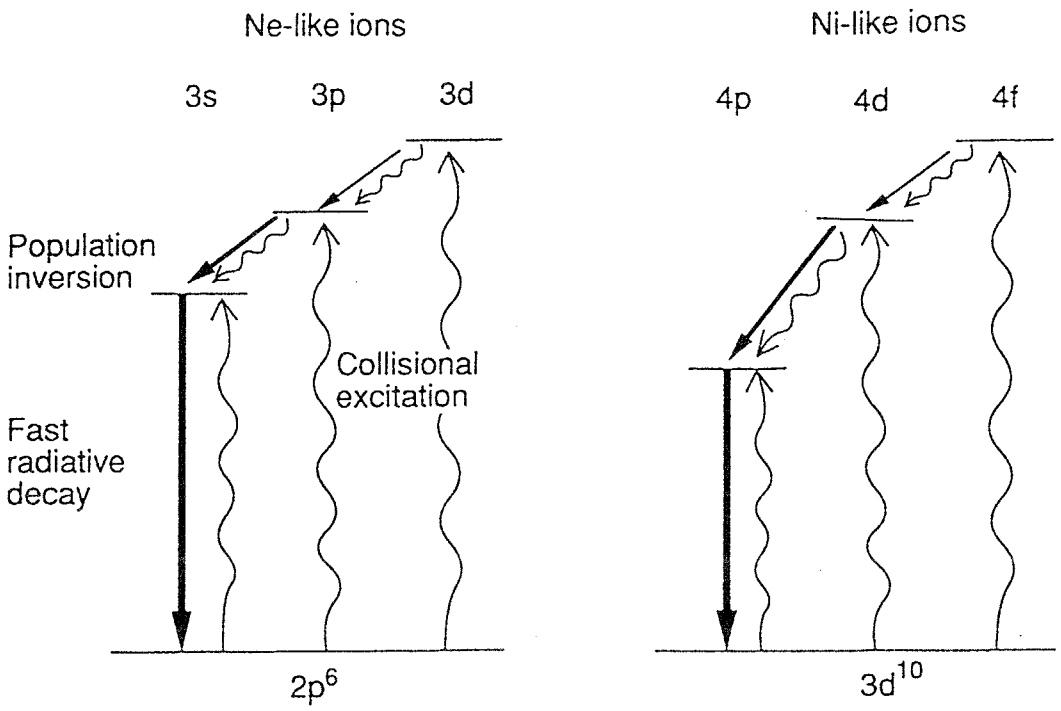

Fig. 1.1. Simplified energy level diagrams of neon-like (left) and nickel-like (right) ions. Wavy lines and straight lines correspond, respectively, to collisional and radiative processes. (Although each process consists of excitation and deexcitation processes, only one of them is shown for simplicity.)

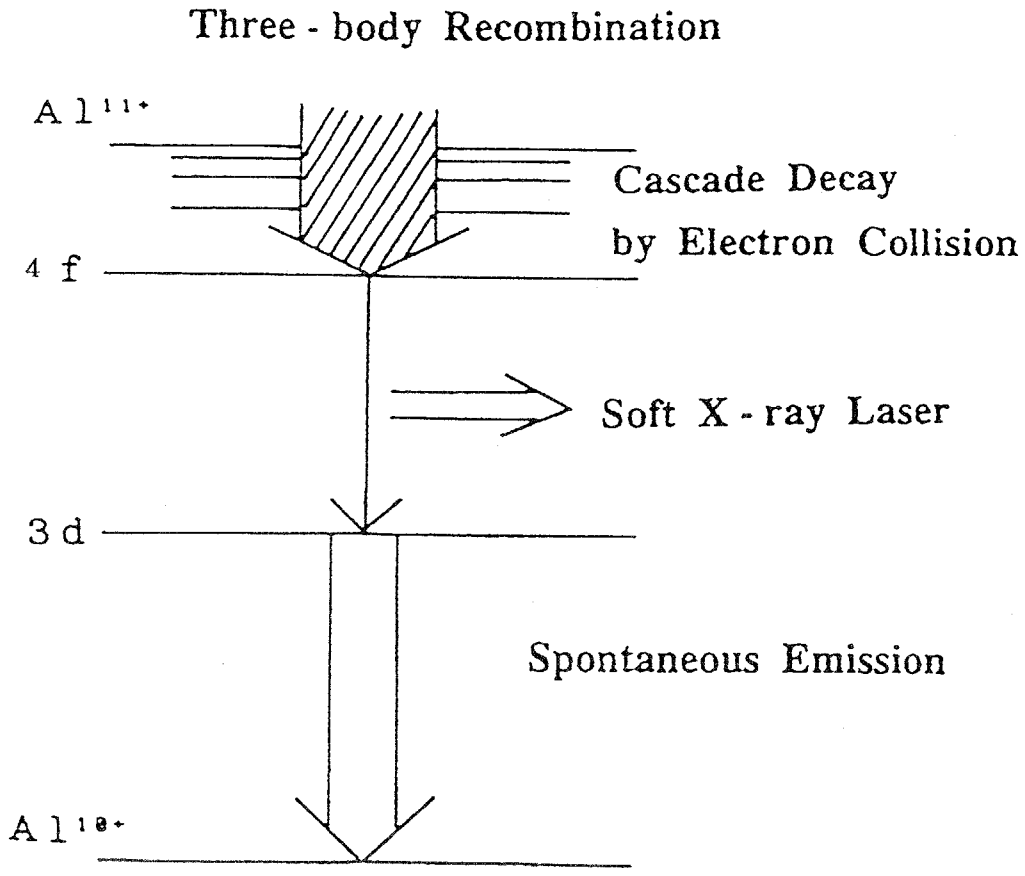

Fig. 1.2. Pumping mechanism of a recombining plasma X-ray laser of Li-like Al ion.

Chapter 2. Experimental Apparatus, an Arc-heated Magnetically Trapped Expanding Plasma Jet Generator

2.1 Introduction

Nowadays a thermal plasma generated by an arc discharge is commonly applied to many fields of engineering, because it is easily and economically produced and its flow has a very high enthalpy [71]. Its applications are, however, limited mainly to a heat source such as a welder up to the present time. Various engineering applications should be developed, taking advantage of its characteristics as a plasma [72]. In thermal plasmas, ions and atoms as well as electrons are efficiently heated into a state of thermodynamic equilibrium where the temperature is more than $1-2$ eV. It is different from non-equilibrium plasmas generated by a glow discharge in a low pressure space, where the ion temperature is much lower than the electron temperature [61]. When a thermal plasma of an atmospheric pressure is spouted into a lower pressure vessel, a stationary recombining plasma should be produced and a control by a magnetic field becomes possible. Because charged particles as well as neutral ones diffuse into various directions by frequent collisions in thermal plasmas of an atmospheric pressure, the magnetic control of the plasma seems to have been considered to be less interesting. They are, in general, stabilized by the flow of the feeding gas [73].

In a nuclear engineering, an examination of a stationary recombining plasma is important because it gives us much information on atomic processes of a divertor plasma of a nuclear fusion reactor, and it is used to investigate interactions between a plasma and the first wall of the reactor [54-58]. Of course, as described in the previous chapter, it will be useful to examine the cooling properties of the plasma under various conditions. In a chemical and material engineering, such a plasma is fundamentally significant as a radical source to prepare extraordinary materials which cannot be synthesized under normal chemical operations. If the thermal plasma is heated enough to vaporize the elec-

trode materials, they may become even monoatomic in the plasma. When the plasma is made to be expanded rapidly, chemical reactions in it can be quenched. A magnetic field will be able to control the way of quenching and decide the final products. Atoms of refractory materials in the expanding jet are made to coalesce one another and finally large clusters should be prepared. Although high power lasers have been often used to prepare clusters [74], they are very expensive, and only pulsed operations are available. Spouting a thermal plasma into a lower pressure space is ideal to prepare clusters, and it has a potential for a continuous operation.

From the viewpoint of a study on a plasma spectroscopy, a stationary recombining plasma is very interesting because a population inversion is created in it [13]. If a thermal plasma is spouted into a lower pressure space and made to be expanded and cooled rapidly, the electron temperature and density will become much lower. Population inversion is expected in the plasmas of a recombining phase, and many authors have attempted to create a plasma dynamic laser through this method [14-40]. A pulsed discharge and a rapid expansion of the plasma made short wavelength lasers as pulsed lasers [42-48]. Up to the present time, however, a continuous plasma discharge and the following expansion have not enabled us to oscillate cw lasers [39]. If we can produce recombining plasmas stationarily, we will be able to scrutinize their spectroscopic characteristics accurately, and recombining processes will be examined more clearly.

This chapter presents the design of the plasma generator "Arc-heated magnetically-trapped expanding plasma jet generator" and the characteristics of the generated plasma. It is a low pressure plasma jet where an arc heated thermal plasma is continuously spouted from a small nozzle into a lower pressure vessel with a parallel magnetic field. First, details of the design of the apparatus will be described. Then, the results of the diagnostics about the plasma will be described. Next, we will confirm that the population densities of excited states are determined by the kinetics of ionization-recombination. Namely, we can examine the properties of the plasmas by the spectroscopic characteristics in the present plasmas. Then, we examine its fluid dynamic characteristics by reviewing a simple

source flow model. In the final section, we will discuss its applications as a potential laser medium and a cluster preparer.

2.2 Design of the Plasma Generator

The experimental apparatus consists of a plasma generator, magnetic coils and traversing mechanisms for driving an optical fiber terminal assembly and a Langmuir probe. The apparatus except a feed control motor which controls the gap length between an anode and a cathode is placed in a rarefied gas wind tunnel of 1.2 m in diameter and 2 m in length. Figure 2.1 shows a schematic view of the rarefied gas wind tunnel. It is evacuated with a 12-in. mechanical booster pump and a 4-in. rotary pump with an ultimate pressure 0.4 Pa, whose pumping speed is about 10 m^3/s. When we need much lower pressure, two 20-in. oil diffusion ejector pumps are available, and the ultimate pressure becomes about 1.3×10^{-2} Pa with them. Even when the ejector pumps are used, the pumping speed is not changed very much. The plasma is expanded in the wind tunnel continuously. The pressure in the tunnel is monitored by a Pirani gauge and an ionization vacuum gauge.

The design of the electrodes of the plasma generator is just the same as that of an ordinary thermal plasma torch except that the nozzle is very small. Figure 2.2 shows the schematic view of the plasma generator. The anode is made of copper, has a convergent throat shape and a small nozzle of $\sim 0.8 - 1.2$ mm in diameter. It is cooled by water not to be damaged by the plasma heat. The cathode is a 3 mm rod of 98% tungsten with 2% thorium. The cathode except the tip is insulated by ceramics to protect from abnormal discharges in a lower pressure. When it is applied to preparing clusters, the cathode is made of a material for the prepared clusters. Carbon cathodes with the same shape are chosen when carbon clusters are prepared. The cathode is also cooled by water to protect from thermal damage in any experiments. Besides, the electrode gap length can be chosen optimumly. Even if the cathode is vaporized, the gap length can be controlled by a motor connected to the cathode.

The plasma is generated by an arc discharge under a relatively high pressure (1.0×10^4 Pa $-$ 1.0×10^5 Pa), which is monitored by a mercury manometer. The plasma is made to be spouted through the anode nozzle into a vacuum space, that is, into the rarefied gas wind tunnel. The electrical power is supplied by a common supplier for an arc welder and the discharge is ignited by RF.

The electric discharge is generated with the help of a magnetic field so that the nozzle may be choked with the viscous arc plasma. The viscosity of the arc plasma enlarges the pressure difference between the arc discharging region and the expanding region. Six coreless coils of 80 mm in i.d. and of 60 mm in thickness are placed with 10 mm gap coaxially with the plasma torch axis. Two of them placed nearer the torch are used to stabilize the discharge and to keep the large pressure difference of the discharging region and the gas wind tunnel, while four other coils generate a uniform magnetic field.

Typical experimental conditions are the following: arc voltage $V_{\rm arc} \simeq 18 - 25$ V, arc current $I_{\rm arc} \simeq 80 - 120$ A, pressure in the discharging region $P_{\rm dc} \simeq 1.0 \times 10^4 - 1.0 \times 10^5$ Pa, magnetic field $B \simeq 0.025 - 0.162$ T, gas flow rate $\sim 1.0 \times 10^{-6} - 4.0 \times 10^{-6}$ kg/s, and pressure in the wind tunnel is $P_{\rm lc} \simeq 3 - 20$ Pa during generating the plasma jet except preparation of clusters. When we prepare clusters, the pressure conditions in the tunnel are slightly different, and the details are specified elsewhere [2].

2.3 Systems for the Diagnostics

The schematic diagram of the spectroscopic measurement system is shown in Fig. 2.3. The emission from the plasma is observed along the direction perpendicular to the jet axis through the gaps of the coils. The light is collected by a concave mirror of 30 mm in diameter into an optical fiber terminal, fed to and analyzed by a monochromator-photomultiplier system [75] (SS-50, systematized by JASCO corporation). A concave mirror is used as a condenser instead of a convex lens, since we should avoid the chromatic aberration in spectroscopic observations in a wide range of the wavelength. The

optical fiber assembly is a bundle of uv-grade fibers (ST-U200-DSY, by Mitsubishi Cable Industries, LTD.), whose length is 5 m, and whose diameter of the core is 200 μm. Its numerical aperture is 0.2. The fiber terminal assembly with the condensing mirror are connected to a three-dimensional traverse mechanisms. It can be moved when the plasma is generated without breaking the vacuum. The light is taken out of the wind tunnel to the monochromator through the fiber. Before the light enters the monochromator, it is chopped at the rate of 270 Hz. The monochromator (fabricated by JASCO corporation, f 5.3) has a Czerny-Turner configuration [76], a focal length of 500 mm, and a linear reciprocal dispersion of 1.5 nm/mm. The widths of the entrance and exit slits are controllable and usually set at 200 μm in the detection of He I, Ar I lines and Balmer series of H I (Otherwise specified). The widths are chosen relatively wide in order to decrease the photon counting error and they can be closed to $\sim 1-2$ μm if necessary. Its nominal resolving power is 0.04 nm. The slit function is trapezoidal and its bandwidth is mainly determined by the entrance slit [77]. The slit height is set at 10 mm. The grooves of the grating of the monochromator are 1200/mm and the blaze wavelength of it is 500 nm. The output of the photomultiplier (R374, by Hamamatsu Photonics Corp. Ltd.) is fed to a preamplifier, whose output is led to a single-phase lock-in amplifier (5600A, by NF Electronic Instruments) and the electric signal is demodulated with the chopping signal. Finally, the output of the lock-in amplifier is converted into a digital signal and recorded by a 16-bit microcomputer (PC9801VM by NEC Corp.). The microcomputer also controls the pulse motor which drives the grating and accomplishes the acqusition of the data, conforming to the programmed sequence through a general-purpose interface-bus interface.

The spectral sensitivity of the detection system was calibrated by a standard halogen lamp (JPD100V500WCS, manufactured by Ushio Elec. Corp. and authorized by JEMIC) as an illuminace standard and a white standard reflectance plate (No. 6091 barium sulfate prepared by Eastman Kodak Co.) as a diffuse reflector, which acted as a luminance standard. The spectroscopic system is sensitive to the wavelength region of 250 – 870

nm. The diffracted lines of higher orders are cut off by optical filters.

In addition, if necessary, a Langmuir probe can be inserted into the plasma parallelly with the magnetic field. The probe can also be moved by the traverse mechanism without breaking vacuum. The probe is made of a tungsten wire of 0.15 mm in diameter. Its tip is exposed to the plasma by 5 mm and other part is covered with a ceramic tube. Since the magnetic field is applied in parallel with the probe surface, the electron density is evaluated by the saturated ion current.

2.4 General Characteristics of the Plasma

2.4.1 Stabilization of discharge by a magnetic field

A typical example of the effect of the magnetic field on the discharge is illustrated in Fig. 2.4. In this chapter, the discharging gas is helium, otherwise specified. The discharge pressure and voltage change drastically when the magnetic field $B \simeq 0.025$ T, while both of them are almost constant under the magnetic field more than that. When the magnetic field is less than that, the discharge is extremely unstable and the plasma comes out of the nozzle only intermittently. When the magnetic field $B \geq 0.025$ T, the arc discharge continues very stably, and the plasma jet illustrated in Fig. 2.2 is observed axially symmetrically in the rarefied gas wind tunnel. It is concluded that the arc spot on the anode would become unstable and would stray into various directions without the magnetic field. With the help of the sufficient magnetic field, the generated plasma chokes the nozzle and it makes the pressure in the discharging chamber high enough due to its strong viscosity. It is also supported by the experimental facts that the pressure in the wind tunnel becomes about ten times larger once the discharging is stopped. This is because the plasma makes the Reynolds number very low at the nozzle. The growth of the boundary layer reduces the effective diameter of the nozzle. When Ar was used instead of He, almost the same results were obtained. Therefore it is concluded that the magnetic field more than 0.025 T effectively helps the stabilization of an arc discharge

where the pressure in the discharging region is about atmospheric.

2.4.2 Fluid dynamic characterisctis at the nozzle

As was written in the previous section, the ratio of the pressure in the discharging chamber $P_{\rm dc}$ to that in the expansion area $P_{\rm lc}$ can be maintained $10^4 - 10^5$ in this apparatus. The reason for it is considered that the effective diameter of the nozzle becomes small owing to the boundary layer on the inner wall of the nozzle due to the viscosity of the plasma. The effective diameter of the nozzle is experimentally investigated in the study of a free jet of general gases [78]. The effective diameter of the nozzle is expressed as a function of the Reynolds number Re in which the characteristic length is the real diameter of the nozzle. When the Reynolds number is less than $\sim$ 1000, the effect of the boundary layer should not be neglected. The effective diameter decreases when the Reynolds number becomes small.

The viscosity of helium gas increases when its temperature $T_{\rm He}$ becomes high when $T_{\rm He} \leq 16000$ K [79]. However, when the temperature becomes higher than that, the viscosity becomes smaller due to the ionization. Meanwhile, the sound velocity, which is considered to be equal to the velocity of flow, is in proportion to $\sqrt{T_{\rm He}}$, and the density is in inverse proportion to $T_{\rm He}$. Therefore, the Reynolds number Re at the nozzle drastically decreases with the increase of the temperature when the diameter of the nozzle is assumed to be constant, which is shown in Fig. 2.5. The Reynolds number becomes very small, even 60 at $T_{\rm He} \simeq 20000$ K. The viscosity of the plasma makes the boundary layer thick enough. Consequently, we can keep the pressure ratio sufficiently high when the arc spot is on the nozzle. On the other hand, when the magnetic field is weak, the arc spot is not on the nozzle, and there exists a helium gas, not a helium plasma. At that time, the Reynolds number is sufficiently large at the nozzle, and the discharging pressure is considered to become small, as was shown in Fig. 2.4.

2.5 Results of the Diagnostics by Probes

Variations of electron temperature T_e and density n_e on the plasma jet axis are illustrated in Fig. 2.6 and in Fig. 2.7, respectively, as functions of the axial distance from the nozzle and the strength of the magnetic field. They were measured by a Langmuir probe in these figures. This apparatus can continuously produce the helium plasma whose electron temperature is about $0.1 - 1$eV and whose electron density is about $1.0 \times 10^{12} - 2.0 \times 10^{13}$cm^{-3}, although they contain considerable errors, especially the electron density is affected by the rapid flow [12]. If we would like to examine the plasma much more precisely, we should measure the plasma by spectroscopic methods, and we will discuss it in and after chapter 3.

However, the relative variation of the parameters is easily understood by the results in the figures. It is concluded that the stronger the magnetic field is, the higher the electron temperature and density are on the center axis on the jet. The plasma becomes cooler and less dense as it comes downstream. The reasons are considered to be (1) the adiabatic expansion of the plasma and (2) the collisions of the plasma with the cold residual gas in the wind tunnel. The electron temperature both in an arc region and in an expanding jet region was calculated [60]. The cathode was supposed to be much thicker in the calculation, and the temperature in an arc region was estimated slightly higher than that measured at 2 cm down from the nozzle. It gives a consistent result. In the expanding region, the calculation was made by a simple source flow model, and this calculation explained only weak field data ($B = 0.027$ T), whereas other strong field data showed a different tendency, which will be discussed in section 2.7. Two reasons are considered as following: (1) a free expansion is suppressed by the magnetic field, and (2) the discharge current is suppressed by the field, a sufficient discharge area is required in the outside area of the torch, and the path of the electric current penetrates into a vacuum area. Since the free expansion of the plasma is suppressed by the magnetic field, it is naturally concluded that the cooling is mainly caused by collisions with cold residual gas molecules.

We can obtain the electron energy distribution function by a probe method [10]. The

Langmuir probe collects electrons selectively, corresponing to the electric field in an ion sheath. If the energy distribution of electrons is the Maxwellian, the electron current of the probe increases exponentially with the probe voltage near the floating potential. In the present experiments, it was found that this was almost always the case. Therefore, it is considered that the electrons in the present plasma has the Maxwell energy distribution.

Generally, it is difficult to measure the ion temperature of a cold plasma only with a passive spectroscopic method. At that time, we should use a Thomson scattering method with an irradiation of an appropriate laser [80-82]. Unfortunately, we do not have a sufficient laser oscillator in our laboratory, and some other methods have to be used. In order to measure its ion temperature under a sufficient strength of a magnetic field, an ion sensitive probe method can be used. It is based on the difference of the Larmour radius of an electron and that of an ion [83,84]. Although measured errors of the ion temperature are considerably large, it is confirmed that its ion temperature is not as low as that in a glow discharge, and it is about $70 - 80\%$ of the electron temperature. The plasma is found to be cooled very rapidly as flowing downstream, and various quenching of reactions can be expected.

2.6 Discussion

Although the plasma is not very bright near the nozzle, it becomes gradually brighter as it comes downstream, and the brightest region is situated at about $7-12$ cm downward from the nozzle. Recombining processes are most dominant in this region.

In general, charged particles go downstream whirling around a magnetic line of force. Electrons can be easily trapped with a weak magnetic field. Although Larmour radius of an ion is much larger than that of an electron, electrons near the axis make a strong electric field and they prevent ions from diffusion. The effect of the magnetic field to the helium plasma is evidently observed. As the magnetic field becomes stronger, the bright plasma column becomes thinner, fully trapped in the coils and set apart from the inner

wall of the coils. The plasma becomes cold in flowing downstream and the degree of the cooling depends partly on the strength of the magnetic field which controls the expansion rate of the plasma. But the pressure in the tunnel is about $3 - 20$ Pa in generating the plasma. It is considered that the plasma becomes cold through collisions with residual gas molecules as well, and we will discuss it more profoundly in the latter chapter of this thesis.

If we examine the plasmas by spectroscopic methods, we should confirm that the spectroscopic properties of the plasmas should be determined by the kinetics of ionization-recombination. Namely, we have to confirm that the population densities of the excited states are determined by the characteristics of the charged particles. If they are influenced by phenomena like a beam-gas interaction, it is difficult to measure the characteristics of the plasmas. The plasma jet in problem now is not accelerated by an electric field, and it is, indeed, rather more difficult for us to observe the phenomena like a beam-gas spectroscopy. However, it is worth while to examine the velocity of the jet. If the time required to flow some characteristic distance is much larger than the relaxation time of electron-electron collisions, the characteristics of the "plasma" are dominant. In addition, if the collision frequency between charged particles is larger than between electrons and neutrals, it is naturally concluded that the population densities of excited atoms are determined by the kinetics of ionization-recombination, not by a beam-gas interactions.

Hence, the typical parameters are briefly discussed here. As described beforehand, the typical electron temperature $T_e \simeq 0.1$ eV, the typical electron density $n_e \simeq 1 \times 10^{13}$ cm^{-3}, the pressure of the surrounding gas $P_{lc} \simeq 10$ Pa, the temperature of the surrounding gas $T_g \simeq 700$ K. Then, the density of the neutral molecules $n_N \simeq 1 \times 10^{15}$ cm^{-3}. The Debye length λ_D is calculated as follows:

$$\lambda_D = \left(\frac{\epsilon_0 k T_e}{n_e e^2} \right)^{1/2} \simeq 1 \ \mu\text{m}, \tag{2.1}$$

where ϵ_0 is the permittivity of vacuum, k the Boltzmann constant, e the elementary electric charge. The plasma frequency ν_p is calculated as follows:

$$\nu_{\rm p} = \frac{1}{2\pi}\left(\frac{e^2 n_{\rm e}}{m_{\rm e}\epsilon_0}\right)^{1/2} \simeq 30 \text{ GHz}, \tag{2.2}$$

where $m_{\rm e}$ is the mass of the electron. The thermal velocity of electrons in the plasma $v_{\rm th}$ is given by the following equation:

$$v_{\rm th} = \lambda_{\rm D}\,(2\pi\nu_{\rm p}) \simeq 1 \times 10^7 \text{ cm/s}. \tag{2.3}$$

Later, we will describe that the velocity of the plasma jet is measured by a Doppler shift of the emitted line, and it tells us that the mean velocity of the jet is about 1×10^6 cm/s for the hydrogen plasma, and 5×10^5 cm/s for the helium plasma. The thermal velocity is larger than that of the jet.

It is essential to evaluate the collisional characteristics of the plasma, especially, collisions of electron-neutrals and of charged particles. The cross section of a neutral hydrogen or helium molecule for an electron of this energy range $\sigma_{\rm eN}$ is 1×10^{-15} cm^2 at most [85, 86]. The mean free path of the electron in hydrogen or helium gas $\lambda_{\rm eN}$ is given as follows:

$$\lambda_{\rm eN} = 1/(\sigma_{\rm eN} n_{\rm N}) \simeq 1 \text{ cm}. \tag{2.4}$$

The frequency of the electron collision with the neutral particles $\nu_{\rm eN}$ is the following:

$$\nu_{\rm eN} = v_{\rm th}/\lambda_{\rm eN} \simeq 10 \text{ MHz}. \tag{2.5}$$

On the other hand, the characteristics of the plasma should be discussed through collisions between charged particles. First, the Coulomb logarithm $\ln\Lambda$ of the plasma is calculated as follows [87]:

$$\ln\Lambda = \ln\left(\frac{12\pi\epsilon_{\rm o} k T_{\rm e} \lambda_{\rm D}}{Z_{\rm N} e^2}\right) \simeq 4.8, \tag{2.6}$$

where $Z_{\rm N}$ is the electric charge of the ion, and equal to 1 in the present plasma. The existence of the doubly charged helium ions can be neglected, which is discused in the next

chapter. As the relaxation time of electron-electron collisions, we calculate the time of equipartition $t_{\rm eq}$, at which the test particles and the field particles both have Maxwellian velocity distributions [88]. It is calculated as follows:

$$t_{\rm eq} = \frac{3\sqrt{m_{\rm e}}(kT_{\rm e})^{3/2}}{4\sqrt{2\pi}\ n_{\rm e}(\ln\Lambda)e^4} \simeq 7 \text{ ns}. \tag{2.7}$$

The relaxation time $t_{\rm eq}$ is much smaller than the time required for the plasma to flow several centimeters.

As a cross section of the collisions between an electron and an ion $\sigma_{\rm ei}$, it is obtained that

$$\sigma_{\rm ei} = 6\pi\bar{b}_0^2 \ln\Lambda \simeq 2.8 \times 10^{-11}\ \text{cm}^2, \tag{2.8}$$

with

$$\bar{b}_0 = \frac{Z_{\rm N}e^2}{12\pi\epsilon_0 kT_{\rm e}}, \tag{2.9}$$

where $\bar{b}_0$ represents the impact parameter for a 90° scattering of an average particle [87]. It should be noted that the cross section of the collisions between charged particles does not depend on the masses of the particles involved in the collision for $Z_{\rm N} = 1$. Namely, the cross section of the electron-electron collisions $\sigma_{\rm ee}$ is equal to $\sigma_{\rm ei}$. And the mean free path of an electron in charged particles $\lambda_{\rm ei}$ is

$$\lambda_{\rm ei} = 1/(n_{\rm i}\ \sigma_{\rm ei}) \simeq 36\ \mu\text{m}, \tag{2.10}$$

where $n_{\rm i}$ is an ion density, which is assumed to be equal to $n_{\rm e}$, if we use the 90° scattering cross section. As a matter of fact, the scattering cross section should be much larger, since the 90° scattering is a rare event. Therefore, the real mean free path $\lambda_{\rm ei}$ is much smaller than that given by Eq. (2.10). The corresponding value for the average electron-ion momentum transfer collision frequency $\overline{\nu}_{\rm ei}$ is

$$\overline{\nu}_{ei} = n_i \frac{4\sqrt{2\pi}}{3} \left(\frac{m_e}{kT_e}\right)^{3/2} \left(\frac{e^2}{4\pi\epsilon_0 m_e}\right)^2 \ln\Lambda \simeq 4.4 \text{ GHz}. \tag{2.11}$$

Consequently, for the plasma in problem now, it is obtained that

$$\nu_p > \overline{\nu}_{ei} \gg \nu_{eN}, \tag{2.12}$$

and

$$\lambda_{ei} \ll \lambda_{eN}. \tag{2.13}$$

Therefore, it is naturally concluded that the characteristics of the charged particles are dominant to those of electron-gas interactions. Consequently, the spectroscopic characteristics of the plasma are determined by the kinetics of ionization-recombination in the plasma. It means that the plasma can be examined by the spectroscopic observations of the plasma.

The results of the spectroscopic observations are discussed in chapters 3 and 4 in detail for the helium plasma, in chapter 5 for the hydrogen plasma, and in chapter 6 for the argon plasma. Of course, the fundamental properties of the plasmas are also discussed there in detail from the viewpoint of plasma spectroscopy. In this chapter, as an application other than a potential active laser, we discuss its application as a cluster preparer briefly.

2.7 Fluid Dynamic Discussion on the Variation of Electron Temperature Using a Simple Source Flow Model

Although fluid dynamic discussion is not the main subject of this thesis, it is useful for us to confirm the fluid dynamic characteristics even in a very roughly approximated manner, and even if we have to use a very rough method to treat the numerical calculation of the fluid dynamics of a weakly ionized plasma flowing in a magnetic field. In this subsection, numerical analysis of the plasma jet based on a source flow model is reviewed

in order to understand the basic hydrodynamic phenomena according to the method described by Suzuki [60].

The semi-empirical formula derived from the results of characteristic solution for a freejet of neutral gas given by Ashkenas and Sherman [78] are particularly useful in determining flow quantities, although this can be obtained as a limit of the ionization degree $\rightarrow 0$ in the source flow calculation as described later. The relationships for the center-line pressure distribution and the radial density distribution are the following:

$$\frac{p_i}{p_0} = \left(\frac{\gamma+1}{\gamma-1}\right)^{\frac{\gamma}{\gamma-1}} \left(\frac{\gamma+1}{2\gamma}\right)^{\frac{1}{\gamma-1}} A_0^{-\frac{2}{\gamma-1}} \left(\frac{z-z_0'}{D}\right)^{-2}, \tag{2.14}$$

$$\frac{\rho(r,z)}{\rho(0,z)} = \cos^2\theta \ \cos^2(1.15\theta) \ , \tag{2.15}$$

where p_0 is the stagnation pressure, and z_0' and A_0 are the constants given as 0.04 and 3.26 for $\gamma = 5/3$, respectively, p_i is the center-line impact pressure, γ the specific-heat ratio and 5/3 for helium, D the diameter of the nozzle, z is the axial distance from the nozzle. Suzuki used these equations to the neutral expanding unaffected by the magnetic field in the partially ionized plasma.

In the magnetically trapped expanding plasma jet, neutral expanding, recombination, magnetic effect, and so on are combined in a complicated way. Ref. [60] adopted the source-flow model without the external magnetic field for the charged particle expanding as well as for the neutral species for simplicity. Even though the density may be sufficiently high for the flow to be collision-dominated near the source, collisions become less frequent and the flow eventually approaches a collisionless regime. Hence, a kinetic approach is necessary to obtain a result which is valid over the entire range of interest. A set of the global equations can be obtained by choosing different functions for each species. The final form as a summation of the global conservation equations for mass, momentum, and energy are the following:

$$\frac{\mathrm{D}\rho}{\mathrm{D}t} + \rho\nabla\cdot\mathbf{u} = 0, \tag{2.16}$$

$$\rho \frac{\mathrm{D}\mathbf{u}}{\mathrm{D}t} + \nabla \cdot \hat{\mathbf{P}} = 0, \tag{2.17}$$

$$\frac{\mathrm{D}(\tilde{n}\tilde{E})}{\mathrm{D}t} + \tilde{n}\tilde{E}(\nabla \cdot \mathbf{u}) + \nabla \cdot \mathbf{q} + \hat{\mathbf{P}} : \nabla \mathbf{u} = -R. \tag{2.18}$$

Here, $\tilde{n}$ and ρ denote the total number and mass densities, $\hat{\mathbf{P}}$ is the stress tensor, $\mathbf{q}$ the heat flux vector, and $\tilde{E}$ the average total energy per particle. The term R represents the energy per unit volume radiated away. Suzuki took the distribution function proposed by Holway [89], which assigned different temperatures to the energy of random motion parallel and perpendicular to the flow direction. Therefore, two more moment equations must be added to the three conservation equations. These accounts were taken from Chou and Talbot [90].

In Fig. 2.8, the ratio of centerline impact pressure p_{i} to the stagnation pressure p_0 is shown for the magnetic field $B = 0.027, 0.08, 0.13$, and 0.16 T [60]. Figure 3.10 also shows the value of p_{i}/p_0 obtained from Eq. (2.14). It was reported that the impact pressure profile of the plasma without magnetic field is quite similar to the free jet of a perfect gass [91]. This figure shows that only the data with $B = 0.027$ T are close to the calculated values, and other data deviate more as the magnetic field increases. It also shows that the Mach disk locates at $z/D = 108$ (about $7 - 8$ cm from the nozzle). Neutral components expands regardless of the magnetic field. Although the existence of the Mach disk is not recognized clearly, the glowing region is observed around the Mach disk location given by Suzuki's calculation [60].

On the other hand, the center-line temperature distribution of the simple source-flow calculations and the electron temperature which Suzuki measured by a Langmuir probe are shown in Fig. 2.9. Although the different temperature to the random motion energy parallel ($T_{\mathrm{j}\,\parallel}$) and perpendicular ($T_{\mathrm{j}\,\perp}$) to the flow direction were obtained, the calculated value in the figure was expressed by the averaged one which was defined by the equation,

$$T_{\mathrm{j}} = (T_{\mathrm{j}\,\parallel} + 2T_{\mathrm{j}\,\perp})/3. \tag{2.19}$$

Only data under a weak magnetic field ($B = 0.027$ T) showed the similar tendency to

the calculated profile, whereas the other data could not be explained by the source-flow model. We can evidently find the effect of the magnetic field on the expansion of charged particles due to the magnetic field. The magnetic field suppressed the free expansion of the plasma, therefore, we cannot expect the cooling due to the adiabatic expansion.

2.8 Application as a Cluster Preparer

In general, there are two methods to prepare clusters. One is breaking down process, namely, solid or liquid bulk is divided into clusters, and unfortunately, this process is very inefficient [74]. The other is building-up process, that is, isolated atoms or molecules in the gas or plasma are made to gather into clusters. It is essential for the building-up process to make the material evaporated or sublimated into gaseous atoms or ions by heating, then cooling them rapidly for coalescence. In order to improve conventional laser ablation methods, the developed "Arc-heated Magnetically-trapped Plasma Jet Generator" is useful. As a test of the apparatus, carbon clusters, especially C_{60} was tried to be prepared.

The experimental apparatus was slightly modified from Fig. 2.2. The expanding velocity of the plasma should be controlled not only by the magnetic field but also by the pressure in the expanding region in this experiment lest the expansion should be too fast. It was confirmed that this apparatus ran continuously without plugging the nozzle. Collected soot should contain various size of carbon cluters. The soot was analyzed through Fourier Transform Infrared Spectroscopy(FT-IR) [92], and it was found that C_{60} was prepared under some appropriate conditions. More detailed discussions are given in Refs. [2,93].

Of course, in addition to the applications described above, various applications are expected, such as propulsion of satellites in space use [94].

2.9 Conclusion

"Arc-heated and magnetically-trapped expanding plasma jet generator" was developed, and this apparatus produced continuous recombining plasma. Two examples of applicaitons were discussed as a cluster preparer and as a potential active laser medium. Conclusions are summarized below:

(1) The magnetic field stabilized arc discharge, namely, the field prevented the arc spot from straying. And when the generated thermal plasma was spouted into a lower pressure space,the plasma whose ion temperature was about $70-80\%$ of the electron temperature, which had been impossible by an ordinary low pressure discharge. Consequently, this apparatus is expected to have various applications in chemical and material engineering areas.

(2) A helium plasma generated by this apparatus was completely trapped by a common magnetic field, and a beamlike plasma jet was produced continuously. It was confirmed that the spectroscopic characteristics of the plasma were determined by the kinetics of ionization-recombination. It meant that the plasma parameters could be examined by the spectroscopic measurements. In and after the next chapter, we will discuss the spectroscopic characteristics of the plasmas in detail.

The results of chapter 2 have already been published in Ref. [59].

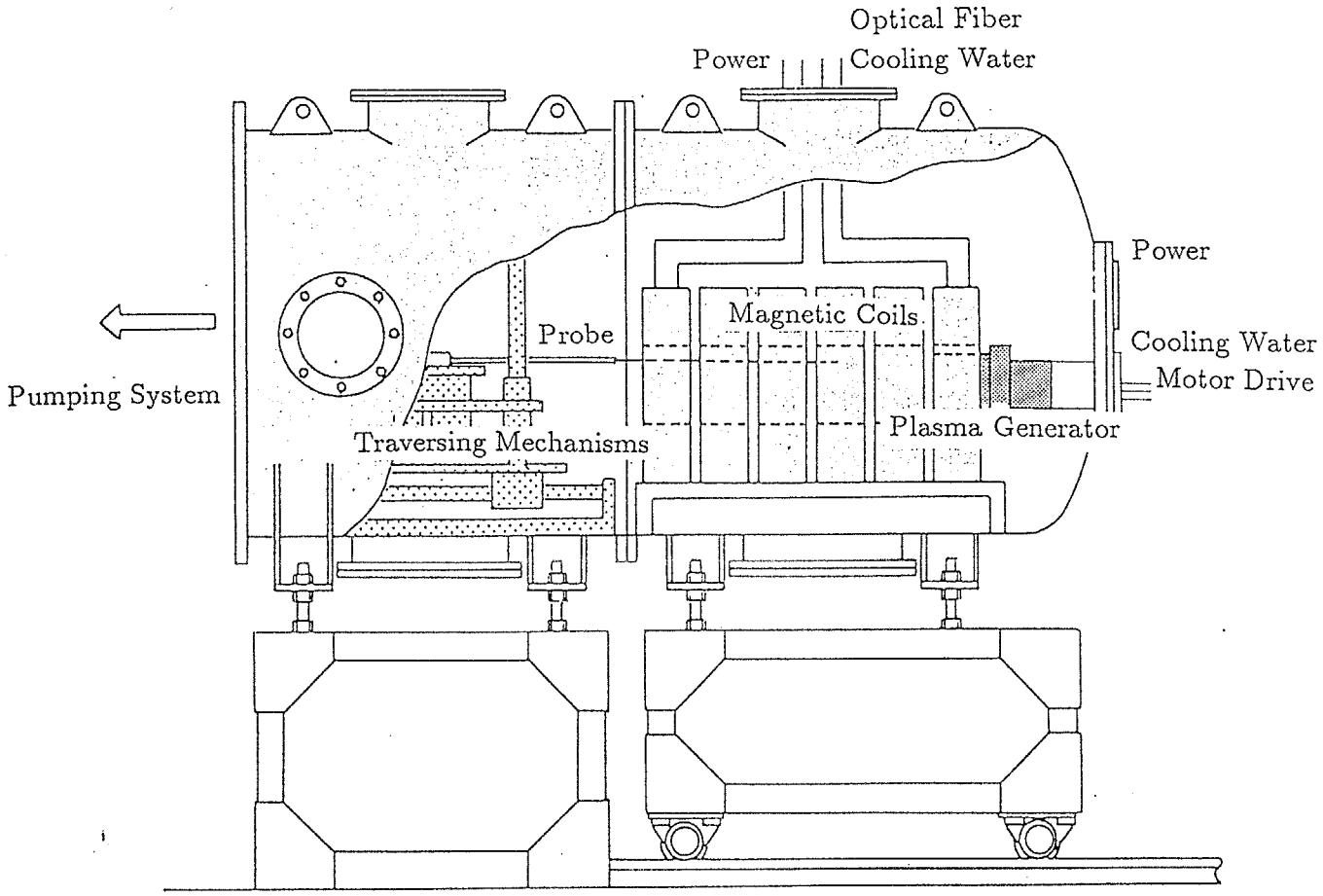

Fig. 2.1. Schematic view of the rarefied gas wind tunnel, diameter 1.2 m, length 2 m, which contains the plasma generator illustrated in Fig. 2.2.

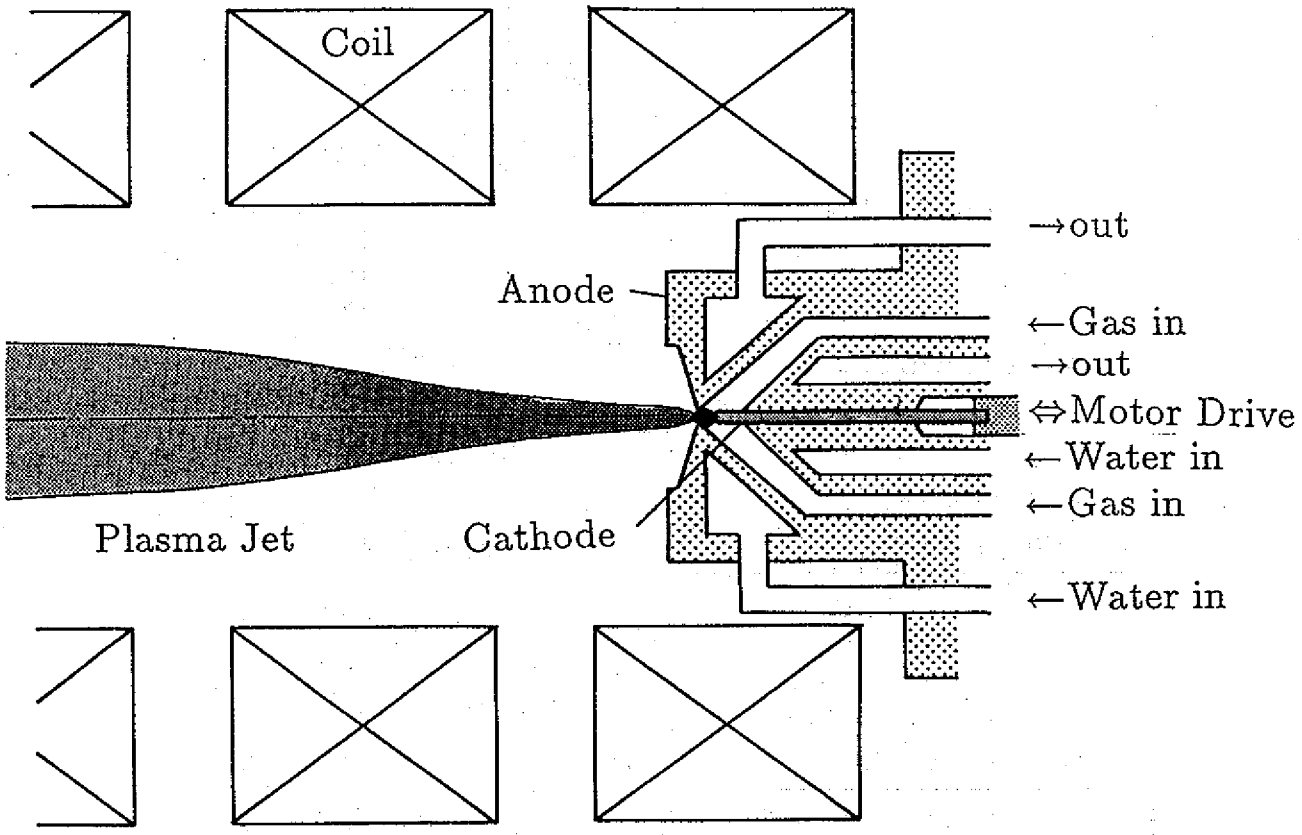

Fig. 2.2. Schematic view of the experimental arrangement of the electrodes and expanding plasma jet.

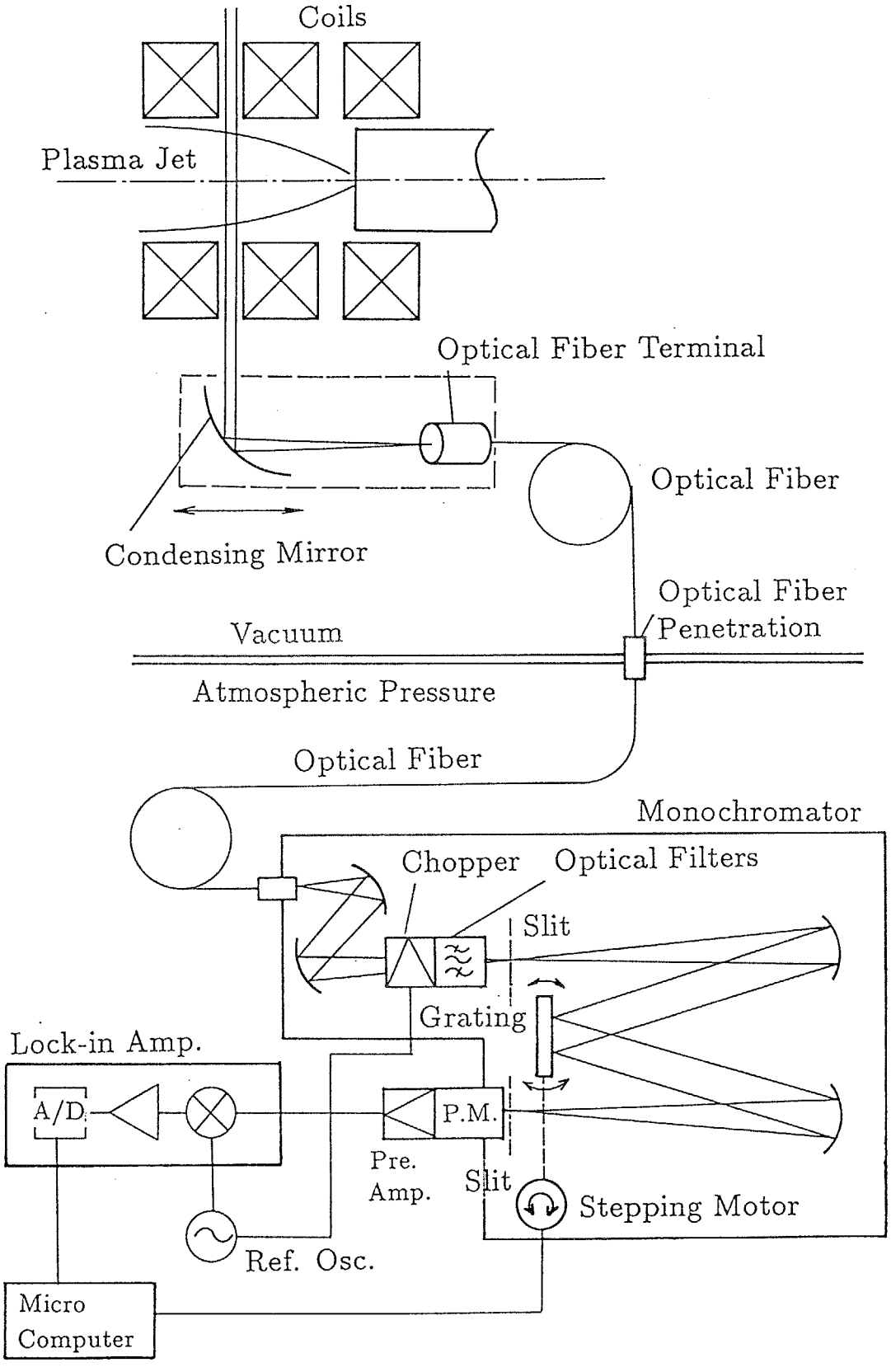

Fig. 2.3. Block diagram of the detection system. Components: condensing mirror, optical fiber, chopper, optical filters, monochromator, photomultiplier (P.M.), preamplifier (Pre. Amp.), reference oscillator (Ref. Osc.), Lock-in amplifier (Lock-in Amp.), analog to digital converter (A/D), and microcomputer.

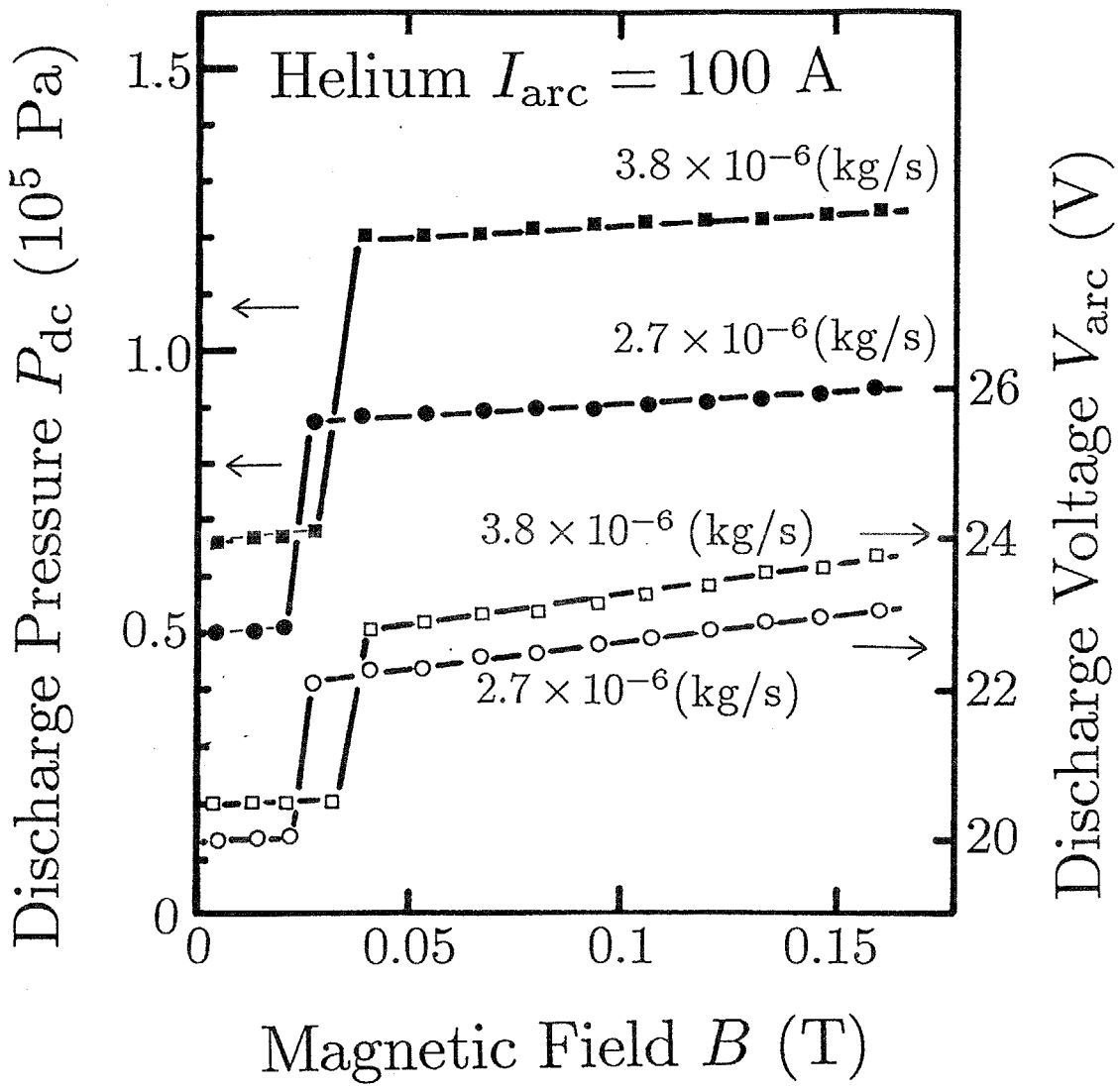

Fig. 2.4. Influence of field strength on discharge characteristics on conditions of constant gas flow and constant discharge current.

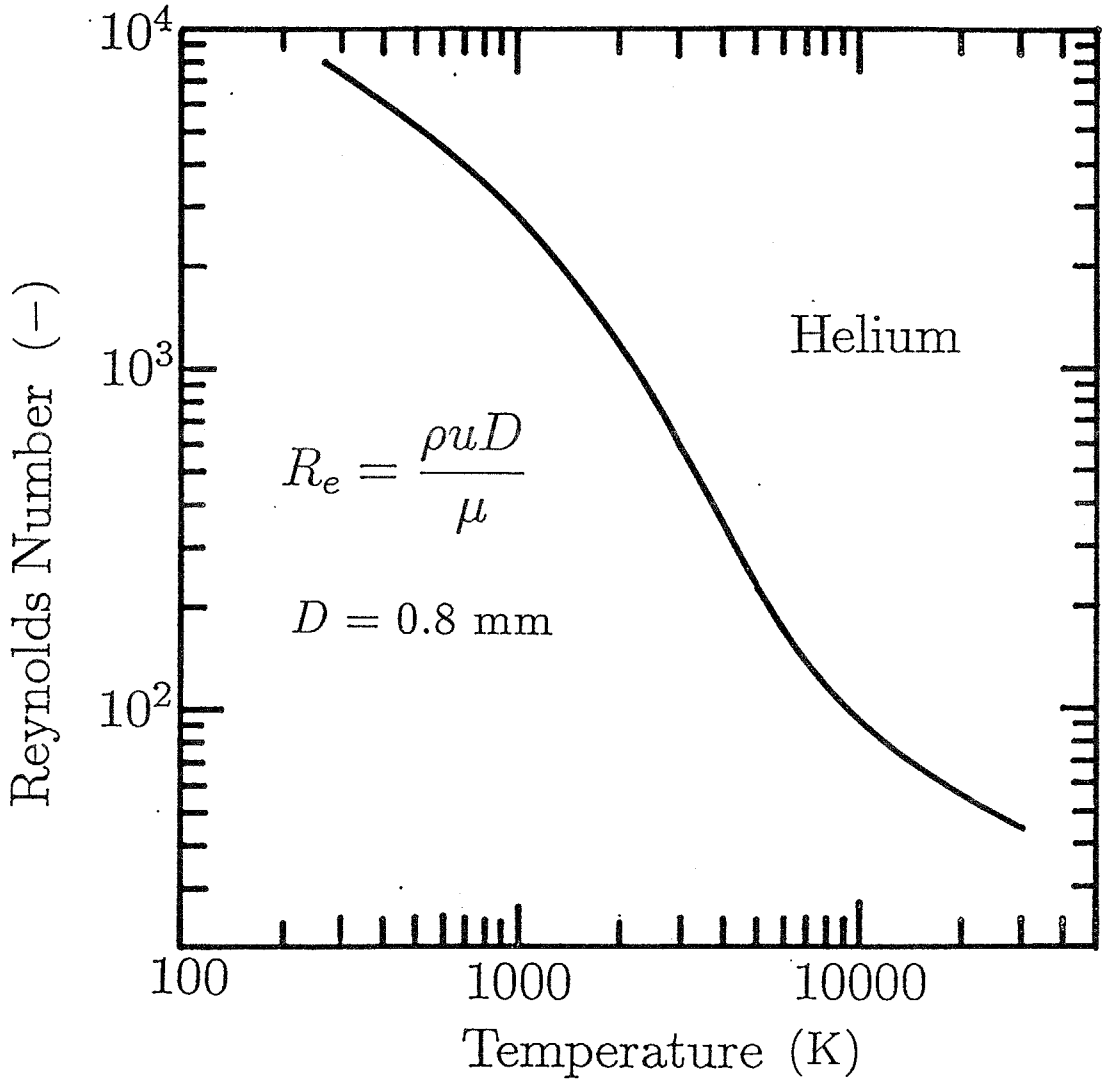

Fig. 2.5. Temperature dependence of Reynolds number based on accoustic velocity.

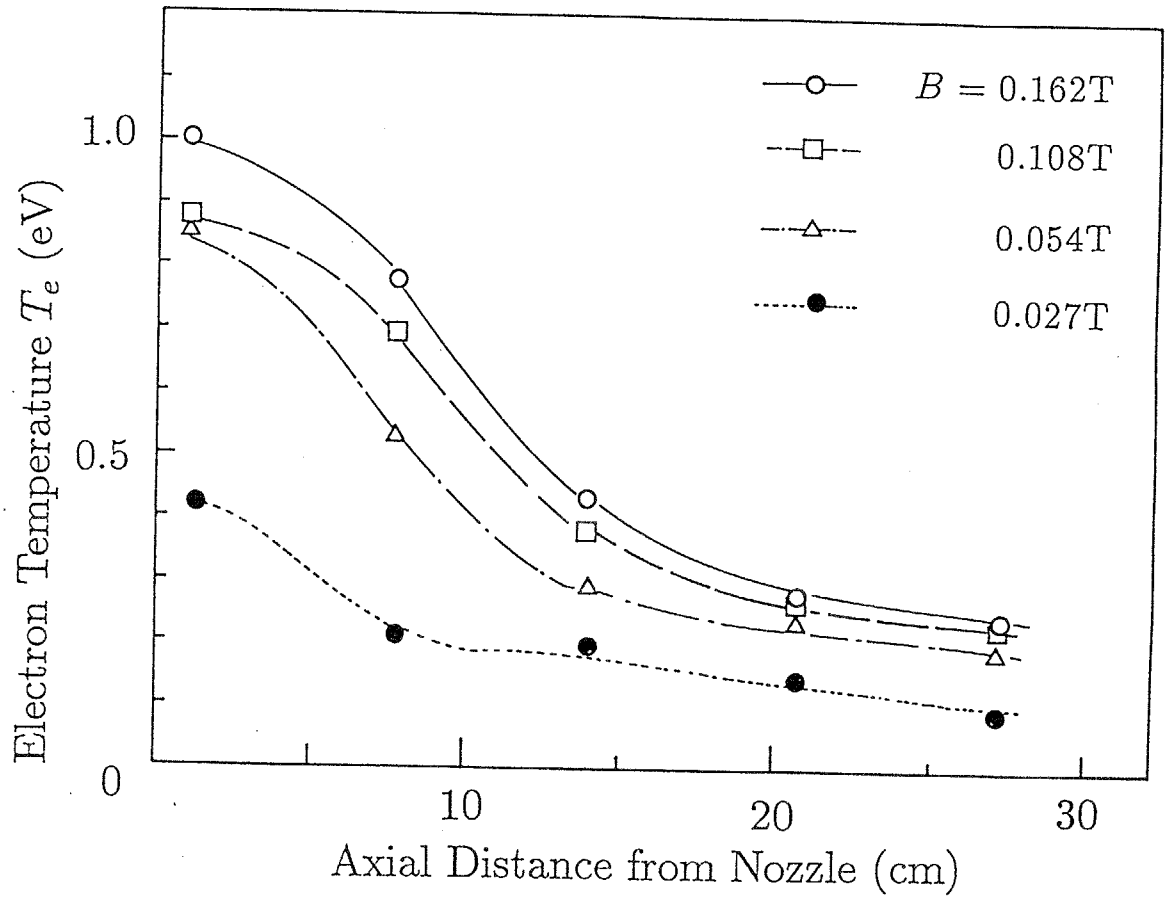

Fig. 2.6. Measured electron temperature T_e by a Langmuir probe.

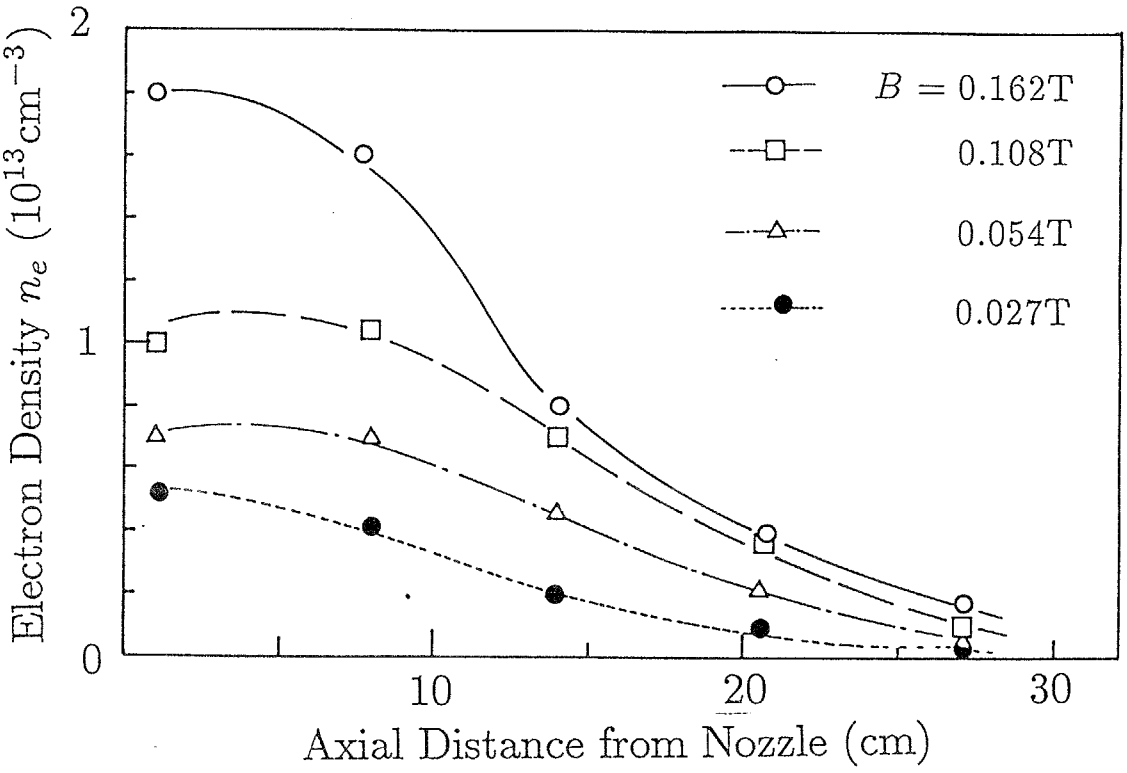

Fig. 2.7. Measured electron density n_e by a Langmuir probe.

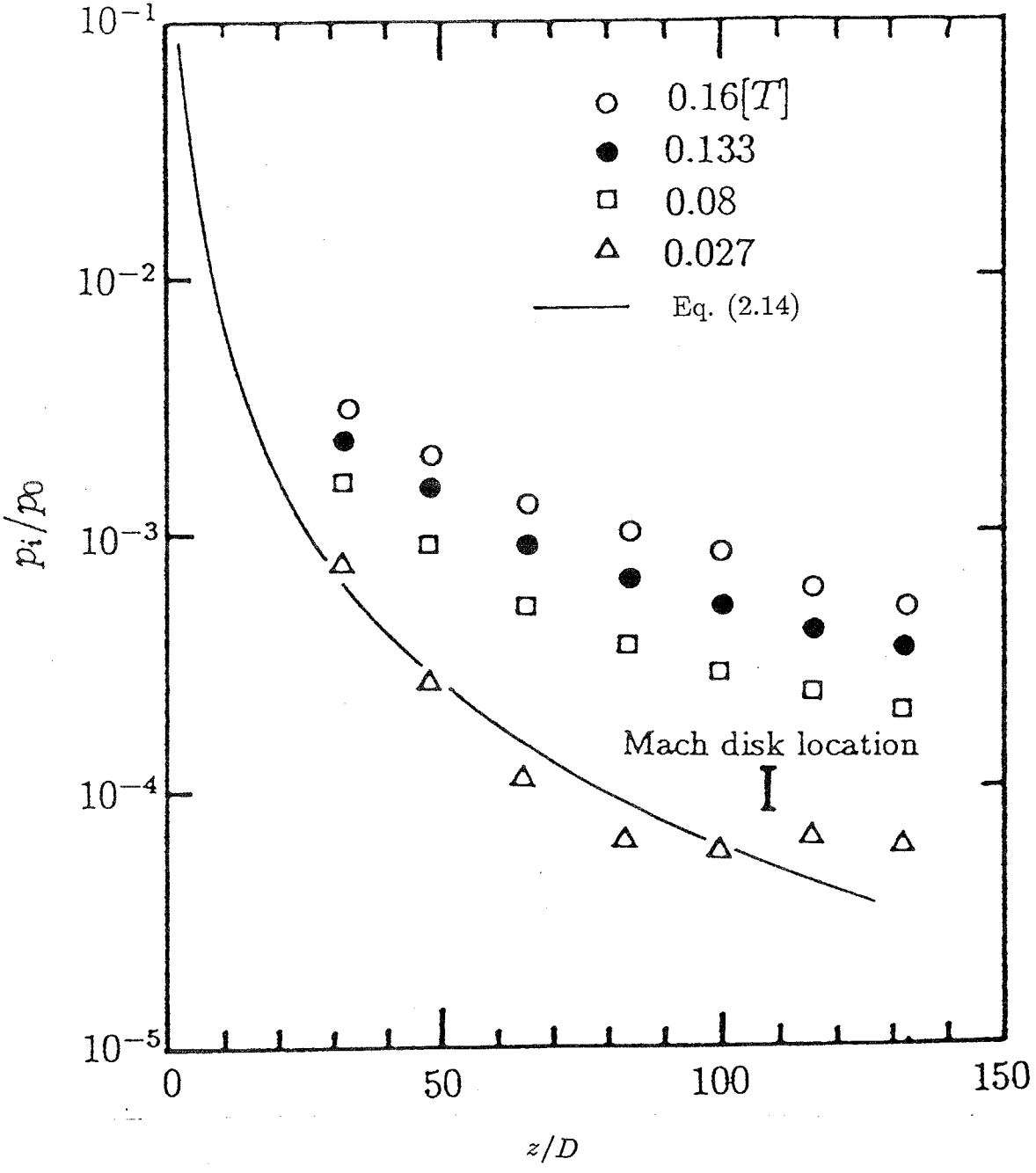

Fig. 2.8. Center-line impact pressure distribution. (Ratio of an impact pressure p_i to a stagnation pressure p_0.)

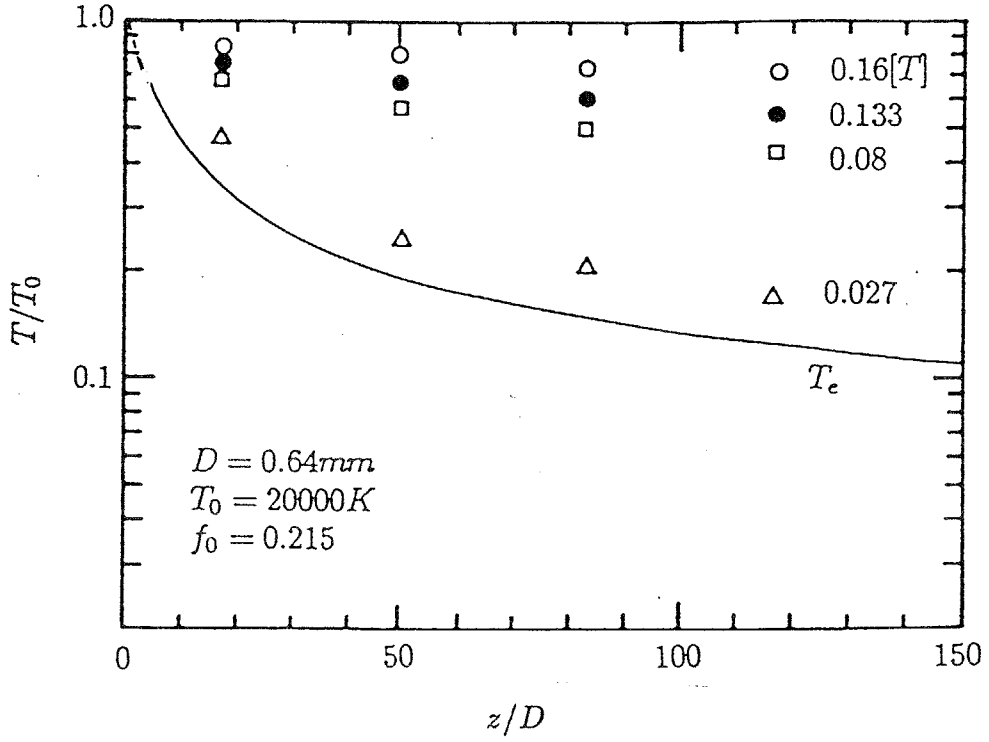

Fig. 2.9. Electron temperature measured by a Langmuir probe at the center-axis and calculated temperature variations in a simple source flow model [Eqs. (2.16)-(2.18)].

Chapter 3. Experimental Study and Spectroscopic Analysis of an Arc-Heated Magnetically Trapped Expanding Helium Plasma

3.1 Introduction

As described in the previous chapter, the examination of the cooling properties of recombining helium plasmas is significant in the field of a nuclear fusion engineering. And at that time, generally, spectroscopic diagnostics are more favorable than the probe analysis, because the former can give us more precise data [10]. Of course, the plasma is also interesting in the field of a laser engineering. If we try to apply the plasma to a lasing medium, it is essential for us to examine the population densities of the laser upper levels and of the lower levels. For that purpose, a spectroscopic measurement is the only way to obtain them experimentally.

About three decades have passed since one of the earliest suggestions that a recombining plasma of low electron temperature could be applied as an active laser medium was made [14]. The stationary population inversion of He I had been observed in a helium plasma jet by Goldfarb, Ilina, Kostygova, and Lukyanov [33], by Zhinzhikov, Luk'yanov, Nazarov, and Pavlova [38]. However, the magnetic field was seldom applied there. Otsuka, Ikee, and Ishii reported that a contact with a neutral gas was effective for the rapid cooling of the electrons in a helium plasma to make inverted populations under a certain magnetic field [63]. However, the plasma in their apparatus named TPD-I was spouted rather slowly through a large nozzle into a lower pressure space where the conductance of the gas was small. The velocity of the plasma jet was considered to be subsonic [65]. And the expansion ratio of the neutral helium is not as large as in our apparatus. The rapid expansion also helps decrease the optical thickness. In general, the optical thickness is an obstacle to making population inversions. Our apparatus is considered to be also advantageous in this sense.

In this chapter, we describe the results of spectroscopic observations of the helium

plasma in the arc-heated magnetically trapped expanding plasma jet. The population densities of He I in the plasma are examined and the variations are investigated when the plasma comes downstream. Then, we examine the effect of the magnetic field and the background pressure of the expanding plasma region on the plasma.

3.2 Experimental Results

The experimental arrangement was already described in the previous chapter. The population densities of the excited helium atoms of principal quantum number $N \geq 3$ were obtained from the intensity integrated over the spectral peaks. For the transition probabilities A of He I, we used the values in Ref. [95]. The electron density of the plasma n_e was estimated at $\sim 10^{13}\mathrm{cm}^{-3}$, and the plasma is considered to be optically thin at least for the transitions to the $N = 2$ levels. As for the optical thickness, we will continue to discuss in the next chapter in terms of semi-empirical formula. As a result, the plasma is optically thin for the transitions in the visible wavelength region. The temperature of the arc before the expansion was considered to be $\sim 1-2$ eV. The excited helium ion line at 468.57 nm was not detected in the expanding plasma region [96]. Hence, the existence of He^{2+} ions may be neglected there.

We measured the population densities of the levels of principal quantum number $3 \leq N \leq 6$ with angular momentum quantum number $0 \leq L \leq 2$ in the present experiments. We should use the population densities of sufficiently high-lying levels in determining the electron temperature and density in recombining plasmas, since it was shown that the population densities of high-lying levels were described by a Saha-Boltzmann equation in recombining plasmas, whereas those of lower-lying levels became much smaller and they gave much higher excitation temperatures than the true electron temperature [13]. Therefore we measured those of the levels 7^3D, 8^3D, and 9^3D.

Some of the observed reduced population densities n/g are shown in Figs. 3.1(a)-3.1(d). ("Reduced" means that the population density n is divided by the statistical

weight g [97].) The reduced population densities given there are the averaged value $\overline{n/g}$ along the line of sight from the condensing mirror directed to the plasma axis perpendicularly, that is,

$$\overline{n/g} = \left[\int_{\text{line of sight}} (n/g)\,\mathrm{d}l\right] \Big/ \left[\int_{\text{line of sight}} \mathrm{d}l\right], \tag{3.1}$$

which is more essential in a laser operation, and Abel inversion [6, 98-100] is not applied in Fig. 3.1. The axial distance from the nozzle z is (a)8 cm, (b)15 cm, (c)22 cm, and (d)29 cm. These distances correspond to the gap positions of the coreless coils. When $z = 1$ cm, the intensity was insufficient for precise analysis. Experimental errors were not more than the size of the keys representing the reduced population densities of Fig. 3.1. The reproducibility of the experimental results lay within $\sim \pm 3\%$. We add there the electron temperature T_e and the electron density n_e, both of which were determined from the spectroscopic measurements and will be discussed in the next section.

To estimate the mean velocity of the plasma jet v_{jet}, the Doppler shift of the He I line of $3^3D \rightarrow 2^3P$ (587.56 nm) was measured. A plane mirror was set downstream where the head-on view of the plasma was observed, and the reflected light was examined in the same way as the side-on view. This showed that the blueshift of the line, $\sim 1 \times 10^{-2}$ nm, was barely resolved. Therefore the mean velocity of the flow where the recombination radiant was dominant was evaluated at $\sim 5 \times 10^3$ m/s. It was difficult for us to measure the effects of the magnetic field B and the pressure of the plasma expanding area P_{lc} on the velocity, since the spectral resolution was not sufficient.

3.3 Discussion

3.3.1 Observed population inversion and effects of the magnetic field and pressure of the plasma expansion area

Figure 3.1 shows that the generated plasma was in a recombining phase; that is,

neither in an ionizing phase nor in an equilibrium phase [13]. First, the Boltzmann plot of the high-lying levels $N \geq 6$ tends to be on a straight line. In consequence, the high-lying levels are considered to be in a state of local thermodynamic equilibrium (LTE). The reduced population densities in LTE are described by the Saha-Boltzmann equation

$$n(p) = n_e n_i Z(p), \tag{3.2}$$

with

$$Z(p) = \frac{g(p)}{2g_i} \left(\frac{h^2}{2\pi m_e k T_e} \right)^{3/2} \exp\left[\frac{\chi(p)}{kT_e} \right] , \tag{3.3}$$

where g_i is a statistical weight of the ion, h is the Planck constant, and $\chi(p)$ is the ionization potential of level p [13]. $Z(p)$ is referred to as the Saha-Boltzmann coefficient [101].

Second, for the lower-lying levels, Eq.(3.2) gives population densities that are too large, which is characteristic of a cold recombining plasma [13]. Therefore, it is confirmed that the generated plasma is in a state of "partial" LTE (PLTE) [102]. Since the plasma was generated by an ordinary arc discharge under atmospheric pressure, it is considered that the plasma was in the state of LTE when it was generated, that is, at $z = 0$, where z is an axial distance from the nozzle. As the plasma comes downstream, the population inversion appears gradually. In Fig.3.1, the population inversion is observed between the level pair $4^3S - 3^3P$ at $z = 15$ cm [Fig.3.1(b)], between $4^1S - 3^1P$, $4^1P - 3^1D$, $4^3S - 3^3P$, and $4^3P - 3^3D$ at $z = 22$ cm [Fig.3.1(c)], and between $4^1S - 3^1P$, $4^1P - 3^1D$, $4^1D - 3^1P$, $5^1S - 3^1P$, $4^3S - 3^3P$, $4^3P - 3^3D$, and $5^3P - 3^3D$ at $z = 29$ cm [Fig.3.1(d)] in optically allowed transitions. The state of the plasma becomes far from equilibrium as it comes downstream. In the $N = 3$ levels, the levels 3^1S, 3^3S, and 3^3P are more populated and the rest are less populated.

The inversions between level pairs $4^1S - 3^1P$ and $4^3P - 3^3D$ were large. We examined the variation in population densities of these levels with the axial distance from the nozzle,

see Fig 3.2. We also examined the effect of the magnetic field B and the pressure in the plasma expanding area $P_{\rm lc}$. When $B = 0.162$ T and $P_{\rm lc} = 6.4$ Pa, inversion is observed at $z \geq 22$ cm for the level pair $4^1S - 3^1P$ and $z \geq 29$ cm for the level pair $4^3P - 3^3D$ [Fig. 3.2(a)]. It is thereby concluded that the rate of decrease of the laser upper levels is faster than that of the lower levels. When the magnetic field is lower [Fig. 3.2(b)] $B = 0.054$ T, population inversion between the levels was observed at any position of $z \geq 8$ cm. The reason is that the electron density becomes low. At this time, since the population density of the laser upper levels also becomes low, it is considered that expansion of the plasma is not always advantageous for creating a large inverted population [29].

When the pressure of the expanding plasma region is lowered using the ejector pumps, the population densities of the excited levels tend to be small, and it becomes difficult to obtain the population inversion [Fig. 3.2(c)]. The reason is that the electron temperature as well as the electron density become high. We will discuss the variation of electron temperature and density in the next subsection.

With regard to the lasing medium, the important parameter is the reduced overpopulation density

$$\Delta[n/g(p_{\text{upper level}}, p_{\text{lower level}})].$$

Namely, in

$$\Delta[n/g(p,q)] = [n(p)/g(p)] - [n(q)/g(q)], \tag{3.4}$$

the subtraction is more essential than the quotient [26-29]. The variations in the reduced overpopulation densities $\Delta(n/g)$ of the level pairs $4^1S - 3^1P$ and $4^3P - 3^3D$ are shown in Fig. 3.3. When the magnetic field becomes strong, the axial distance at which the overpopulation densities become their maximum comes downstream. On the other hand, the maximum value of the overpopulation density is not much affected by the magnetic field in the present experiments [Fig. 3.3(a) for the level pair $4^1S - 3^1P$, Fig. 3.3(c) for

$4^3P - 3^3D$]. In the present experiments, the maximum of the reduced overpopulation density is $\sim 1.6 \times 10^7$ cm^{-3} for the level pair $4^1S - 3^1P$ ($B = 0.162$ T, $P_{\rm lc} = 6.4$ Pa, $z = 29$ cm), and $\sim 2.2 \times 10^7$ cm^{-3} for $4^3P - 3^3D$ ($B = 0.054$ T, $P_{\rm lc} = 6.4$ Pa, $z = 15$ cm).

When the pressure of the plasma expanding area becomes low, the overpopulation density becomes small in the $4^1S - 3^1P$ level pair [Fig. 3.3(b)]. It is considered that the plasma will be expanded more rapidly under low pressure than under high pressure. However, as will be shown in the next subsection, the electron temperature becomes lower in $P_{\rm lc} = 6.4$ Pa than in $P_{\rm lc} = 4.0 \times 10^{-2}$ Pa. As was shown numerically, the plasma in the present experiments is considered to be cooled due to elastic collisions with the residual gas molecules in the expanding plasma area, which is referred to as gas contact cooling [103,104].

On the other hand, the threshold overpopulation density for the laser oscillation $\Delta(n/g)_{\rm th}$ is calculated as follows if the line has a Gaussian profile [29]:

$$[\Delta n/g(p,q)]_{\rm th} = \frac{8\pi^{3/2}}{g(p)A(p,q)\lambda(p,q)^3}\left(\frac{2kT_{\rm He}}{m_{\rm He}}\right)^{1/2}\left(-\frac{\ln\sqrt{R_1R_2}}{l}\right), \qquad (3.5)$$

where $A(p,q)$ is the transition probability $p \rightarrow q$, $\lambda(p,q)$ is the wavelength, $m_{\rm He}$ is the mass of a helium atom, $T_{\rm He}$ is the temperature of the helium atom (in kelvins), R_1 and R_2 are the reflectivities of the cavity mirrors, and l is the separation of the mirrors and assumed to be the same as the length of the plasma region. We supposed the following values for the calculation: $T_{\rm He} = 1000$ K (temperature of the surrounding residual helium), $R_1 = 0.99$, $R_2 = 0.998$, and $l = 5$ cm (the observed bright area). This results in $[\Delta n/g(4^1S, 3^1P)]_{\rm th} = 2.6 \times 10^8$ cm^{-3}, and $[\Delta n/g(4^3P, 3^3D)]_{\rm th} = 2.8 \times 10^8$ cm^{-3}. We are sorry to say that the observed inversion was still insufficient for us to oscillate a cw recombination laser. The overpopulation densities for any other transitions could not surpass the threshold in the present experiment with common laser resonator mirrors. In order to increase the overpopulation density, the plasma should be further cooled without decreasing the electron density.

3.3.2 Macroscopic characterictics of the plasma

The population densities of the sufficiently high-lying levels are described by the Saha-Boltzmann equation, namely, Eqs. (3.2)-(3.3). The electron temperature is determined from the gradient of the Boltzmann plot in Fig. 3.1. We used a least-squares fitting of the reduced population densities of the levels 6^3D, 7^3D, 8^3D, and 9^3D. The obtained electron temperature is shown in Fig. 3.4 for various conditions. The electron temperature becomes gradually lower with increasing axial distance. Although the effect of the magnetic field is not very remarkable, the pressure of the plasma expanding area affects the electron temperature drastically. When the background pressure is low, the cooling by contact with residual gas is not accomplished effectively.

Then, since the detection system was calibrated for absolutely, we determined the electron density from Fig. 3.1. The amount of He^{2+} is negligible as explained above. In the expanding plasma, the amount of the molecular helium ion $He_2{}^+$ is also negligible. In general, most of the molecular ions are lost through rapid dissociative recombinations, which are much faster than the recombination of atomic ions. In section 4.5.3, we will continue to discuss molecular helium ions created via associative ionization. Therefore n_e is calculated from the Boltzmann plot (Fig. 3.1) through Eqs. (3.2)-(3.3) with the assumption of $n_e = n_i$. The electron density obtained is shown in Fig. 3.5. Figures 3.4-3.5 show the avaraged plasma parameters along the line of sight.

When the magnetic field is strong, the electron density becomes large. On the other hand, the pressure of the plasma expansion area P_{lc} does not affect the electron density very much. It means that the electron density can be controlled mainly by the magnetic field, and that the electron temperature can be controlled mainly by the pressure in the plasma expansion area. They can be controlled independently in principle in the present plasma. It is concluded that the gas contact cooling is effective even if the magnetic field is strong and even when the adiabatic expansion cannot be used for the cooling.

Another interpretation of the Figs. 3.4-3.5 is that they show the time history of the

recombining plasma, like an afterglow plasma. The plasma is considered to flow with mean velocity $\sim 5 \times 10^3$ m/s as described beforehand. If the time origin ($t = 0$) is set to when the the plasma passed through the nozzle, Fig. 3.1 shows the population densities of $t \simeq 16$ μs in (a), 30 μs in (b), 44 μs in (c), and 58 μs in (d). The relaxation time $t_{\rm eq}$ is much smaller than the time required for a flow of several centimeters. ($t_{\rm eq} \simeq 7$ ns.) In consequence, when the collisional radiative model is applied, the components of the flowing are much smaller than the collisional-radiative terms. The initial temperature of the plasma is considered to be $\sim 1 - 2$ eV. This means that gas contact cooling is accomplished on a time scale of several microseconds, which agrees with the simulation of gas contact cooling by Furukane, Sato, and Oda [103,104].

The radial profiles of electron temperature and density as well as population densities are also interesting. (Examples of the radial profiles of population densities will be shown in the next subsection.) In order to obtain them, the radial profiles of population densities of high-lying levels should be examined by applying Abel inversion [98-100]. However, the intensities of the lines from the high-lying levels were too weak for us to measure them accurately near the edge of the plasma. Hence, we used a Langmuir probe for detection of the radial profiles of electron temperature and density. The probe analysis inevitably contains considerable errors, and it is complicated to analyze the data to obtain an absolute electron density in such a strong flow as that of the present experiment [12]. However, the spatial resolution is satisfactory, and this method is suitable for measurement of relative values of the electron density. The electron density was measured from the ion saturated current, which was not much affected by the magnetic field [11].

Figures 3.6 and 3.7 show the radial profiles of the electron temperature and density, respectively, when $B = 0.108$ T and $P_{\rm lc} = 6.4$ Pa at various positions of axial distance. As for the electron temperature, the $T_{\rm e}$ value becomes about halved from the centerline out to a radius 2 cm, where reproducible data can be obtained. The profiles of the electron temperature are similar to one another at any place. On the other hand, the electron density has a different tendency. The profile is more peaked around the center-

line upstream than downstream, which is considered to be due to the ambipolar diffusion across the magnetic field and the ion-electron recombination. The observed phenomena in the present experiments agree well with the results reported by Nishiyama, Sato, and Kamiyama [53]. These tendencies were not much changed when the magnetic field and the pressure in the expanding plasma region were changed, except that the plasma was more peaked around the center-line when the magnetic field was stronger and the pressure was lower.

3.3.3 Confirmation by calculations using a collisional radiative model

According to the collisional radiative model of He I, we can calculate the population densities of excited levels of He I [105]. In the next chapter, we described the modified method by which to calculate the population densities of the excited levels of a cold recombining helium plasma in which the optical thickness is not negligible due to the large amount of helium atoms situated in the ground state. In the present analysis, the same method as in Ref. [105] is used. The calculational method will be described in the next chapter in detail. The input parameters are the electron temperature T_e, electron density n_e, background helium pressure P_{lc}, helium gas temperature T_{He}, and the diameter of the plasma column d. When the parameters are set at the same values as in Fig. 3.1 with the assumptions that $T_{He} = 1000$ K and $d = 8$ cm, the results of the calculation are as shown in Fig. 3.8.

In general, the calculations agree well with the experimental results. The tendency in $N = 3$ is well explained by the fact that 3^1S, 3^3S and 3^3P levels are more populated and others are less populated. The absolute values also agree with the experiments approximately. However, since the results in Fig. 3.1 are averaged along the line of sight, some difference is observed. The experimental results of the densities of the levels $N = 4$ and 5 tend to be in a non-equilibrium state, that is, levels with a different angular momentum quantun number are not on a smooth line in the experiments. In particular,

the difference in the levels of $N = 5$ between Fig. 3.1(d) and Fig. 3.8(d) is evident.

It may be said that the experimental data are well explained by the calculation [Figs. 3.1(a) and 3.8(a)]. Strictly speaking, however, when the experimental data are compared with the calculation, the population densities in Fig. 3.1 should be converted into local data by applying an Abel inversion. We are sorry to say that the intensity of the emission was not sufficient for the high-lying levels which were suitable to determine the electron temperature and density at the edge of the plasma. It was difficult to compare the calculated data with the experimental results to which the Abel inversion was applied. The data shown in Fig. 3.1 is affected by the population densities at the edge area of the plasma, where the electron temperature is much lower than at the central area. Hence, the observed high-lying levels tend to be in a state of non-equilibrium than the calculated values.

Figure 3.9 shows the radial profiles of some levels when $B = 0.054$ T, $P_{\rm lc} = 6.4$ Pa, and $z = 15$ cm, where (a) shows those of the singlet system, and (b) the triplet system. In general, the levels of the triplet system have a Gaussian profile [Fig 3.9(b)], whereas the 3^1P level has a different profile [Fig 3.9(a)]. At the edge of the plasma, the population density of 3^1P levels is much larger than those of 4^1S, 3^1D and of the triplet system. This is considered to be due to the opacity effect, namely, the emitted lines of transitions to the ground state 1^1S are absorbed by the background residual helium gas, almost all of which is situated in the ground state. The plasma is considered to be optically thick for transitions to the ground state. On the other hand, numerical calculations showed that transitions to the excited states in the plasma were optically thin, and this detail is explained in the next chapter. If the plasma is made to be optically thin, the rate of the radiative decay may increase. It means that the requirement for the background pressure should and can be investigated quantitatively in which the laser oscillation is expected. These are also discussed in the next chapter.

From the calculation, we can calculate the population rates and the depopulation frequencies of each elementary process. The results of the numerical examinations on

what the dominant process is are also discussed in the next chapter.

3.4 Conclusion

A stationary recombining helium plasma was generated in the arc-heated magnetically trapped expanding plasma jet generator. The plasma was generated very stably and spectroscopic observation was accomplished with sufficient accuracy by a monochromator that was calibrated absolutely. Population densities of He I of principal quantum number 3−6 and of 7^3D, 8^3D, and 9^3D levels were obtained in the downstream part of the plasma jet. Population inversions between the level pairs 4^1S-3^1P, 4^1P-3^1D, 4^1D-3^1P, 5^1S-3^1P, 4^3S-3^3P, 4^3P-3^3D, and 5^3P-3^3D were obtained in the downstream of the plasma jet. However, the inversion was smaller than the threshold value for lasing with common laser resonator mirrors. The electron temperature and density averaged along the line of sight were determined from the population densities of high-lying levels, and the electron temperature was $0.1-0.5$ eV and the density was $8\times10^{12}-1\times10^{14}$ cm^{-3}. The magnetic field was effective in retaining the electron density. When the pressure in the plasma expansion area became low ($\sim 4.0\times10^{-2}$ Pa), the electron temperature became high. The radial profiles of the electron temperature and density were measured. The radial profiles of the population densities of some excited levels were determined by an Abel inversion.

The results of chapter 3 have already been published in "Plasma Sources: Science and Technology" [68].

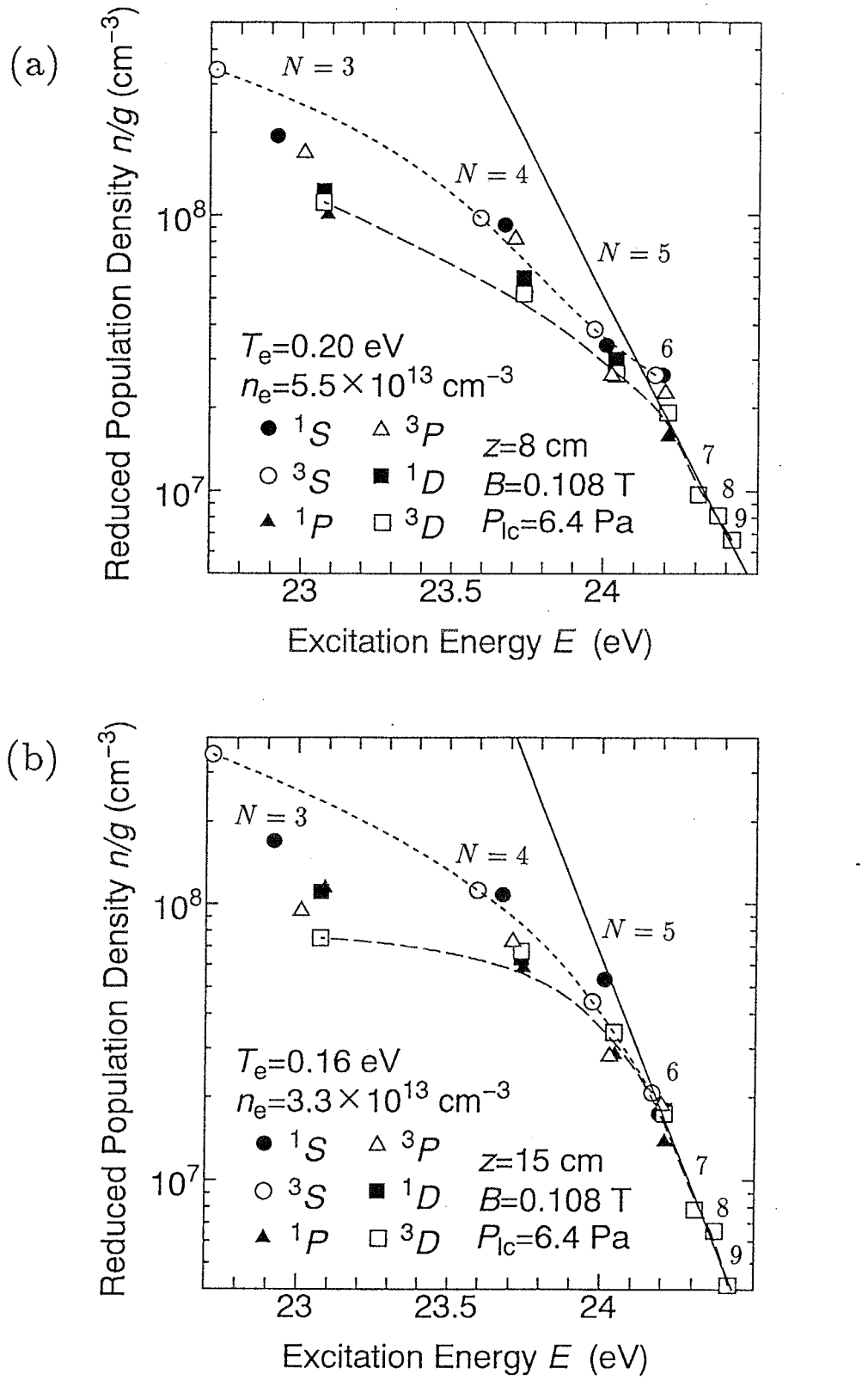

Fig. 3.1. Boltzmann plots of helium atoms in the present experiments. The solid lines show the Saha-Boltzmann populations given by Eqs. (3.2) and (3.3). The pressure in the plasma expanding region $P_{lc} = 6.4$ Pa and the strength of the magnetic field $B = 0.108$

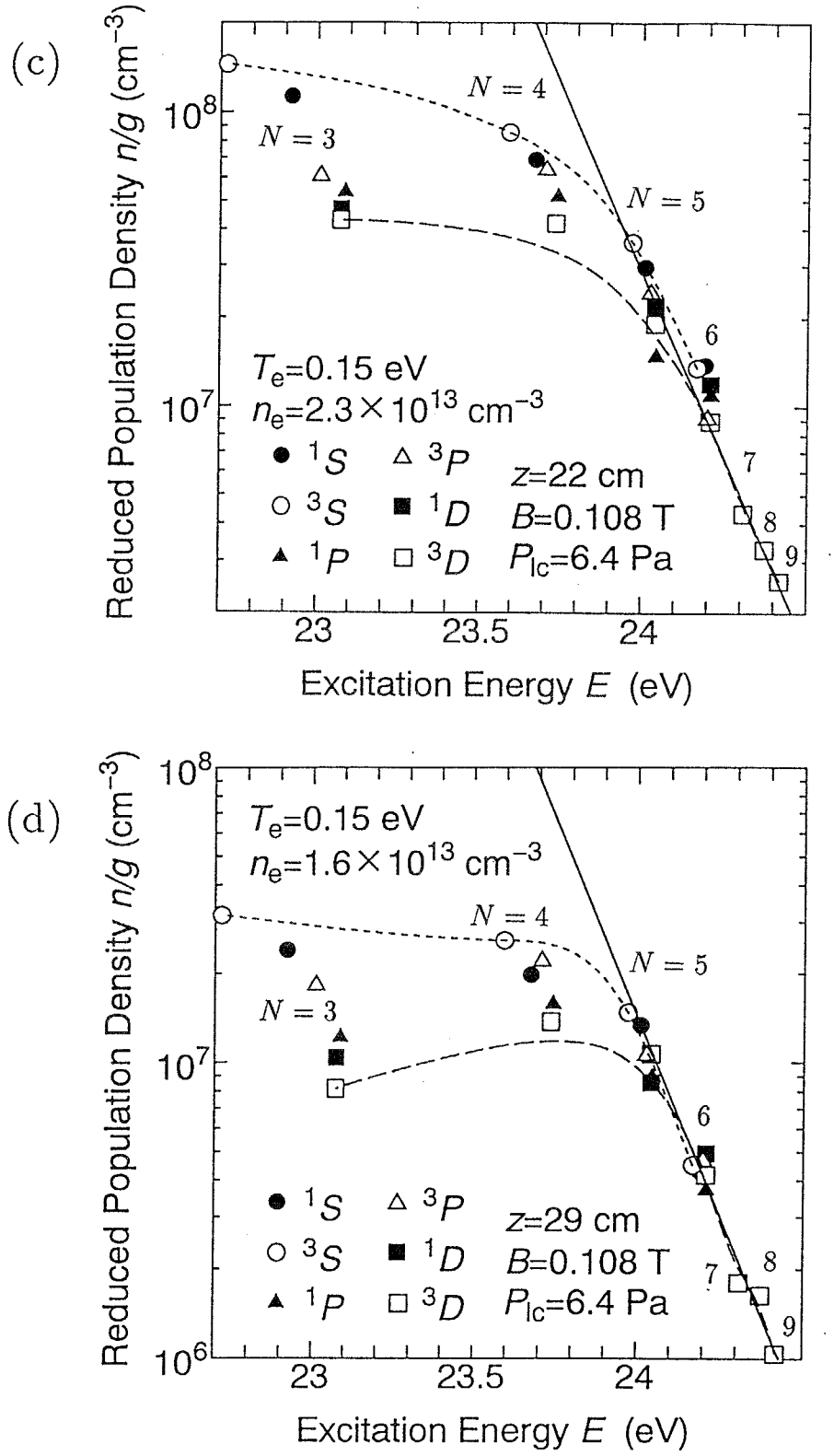

T. The pressure in the discharging region $P_{dc} \simeq 1.0 \times 10^5$ Pa. The axial distance from the nozzle is 8, 15, 22, and 29 cm in (a), (b), (c), and (d), respectively.

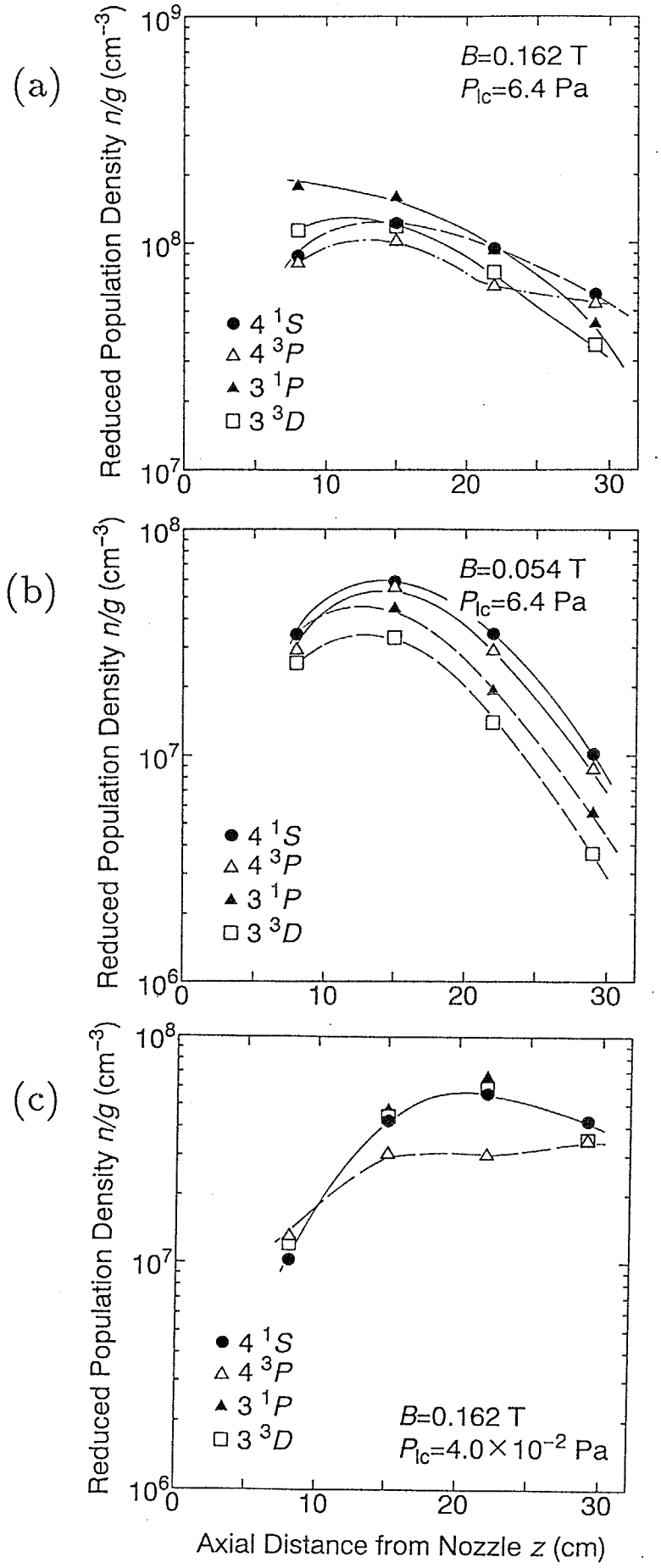

Fig. 3.2. Variation of the reduced population density n/g of levels 4^1S, 4^3P, 3^1P and 3^3D. Experimental conditions: $B = 0.162$ T, $P_{\rm lc} = 6.4$ Pa in (a), $B = 0.054$ T, $P_{\rm lc} = 6.4$ Pa in (b), $B = 0.162$ T, $P_{\rm lc} = 4.0 \times 10^{-2}$ Pa in (c).

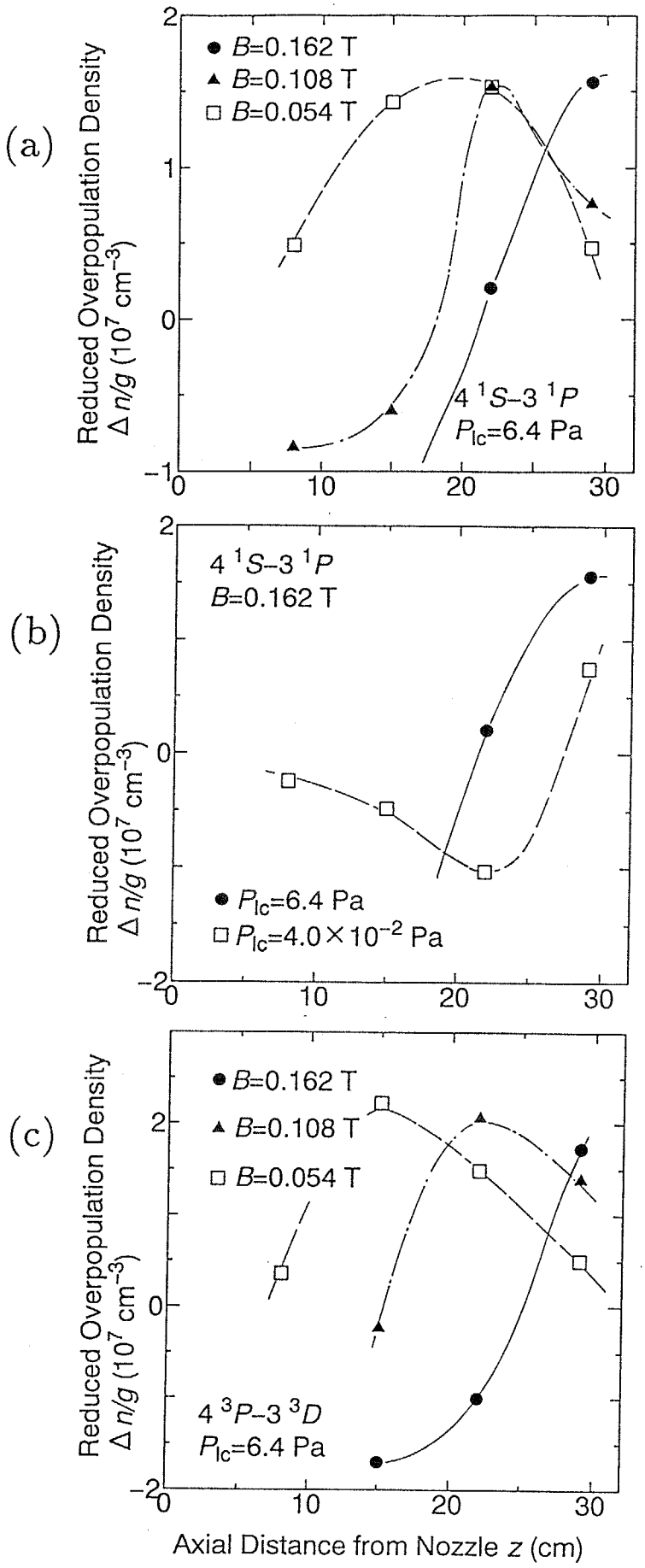

Fig. 3.3. Variation of the reduced overpopulation density $\Delta(n/g)$ between level pairs $4^1S - 3^1P$ and $4^3P - 3^3D$. Experimental conditions: $P_{\rm lc} = 6.4$ Pa in (a) and (c), $B = 0.162$ T in (b).

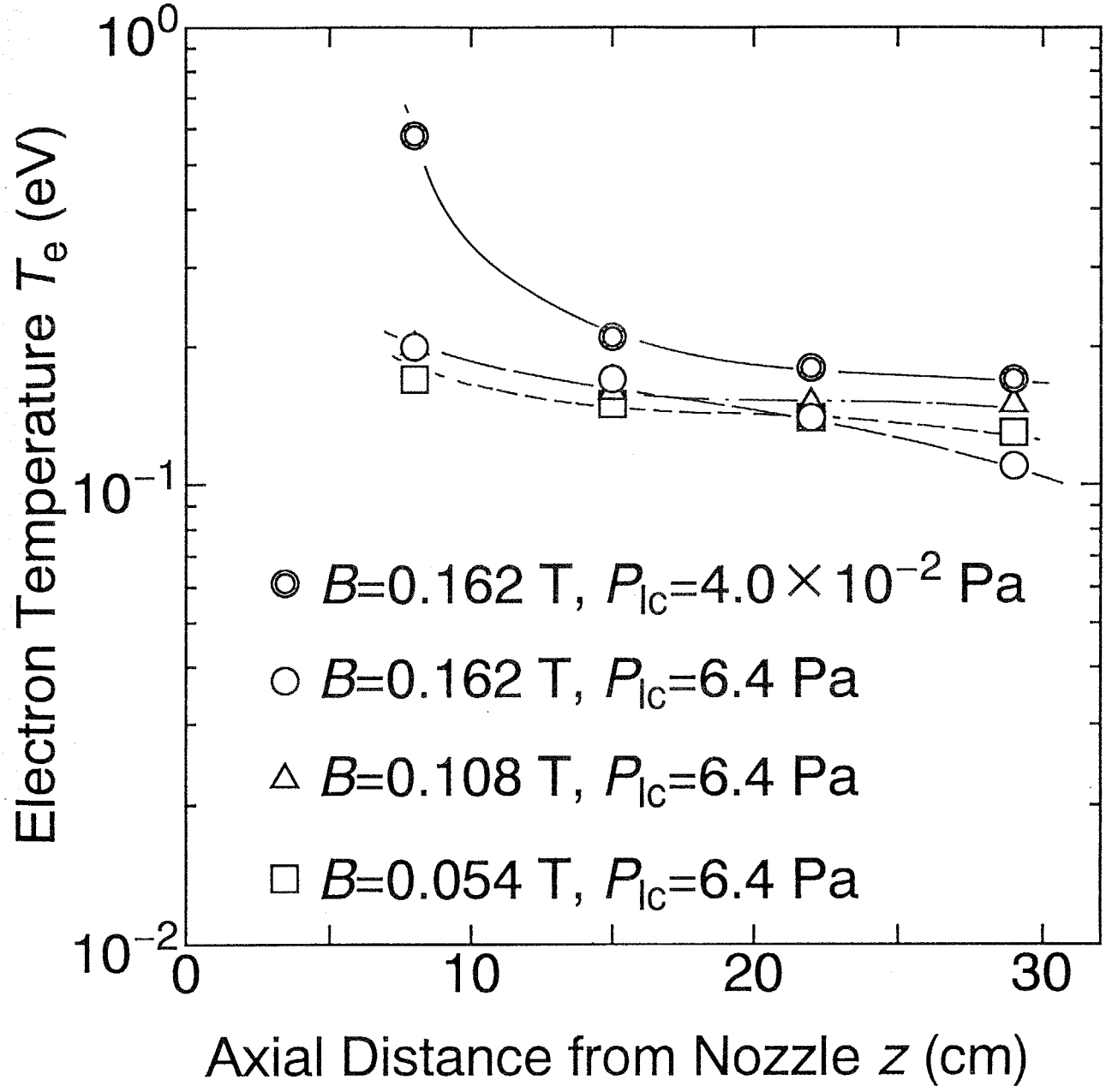

Fig. 3.4. Variation of the electron temperature T_e of the helium plasma measured by the spectroscopic observations.

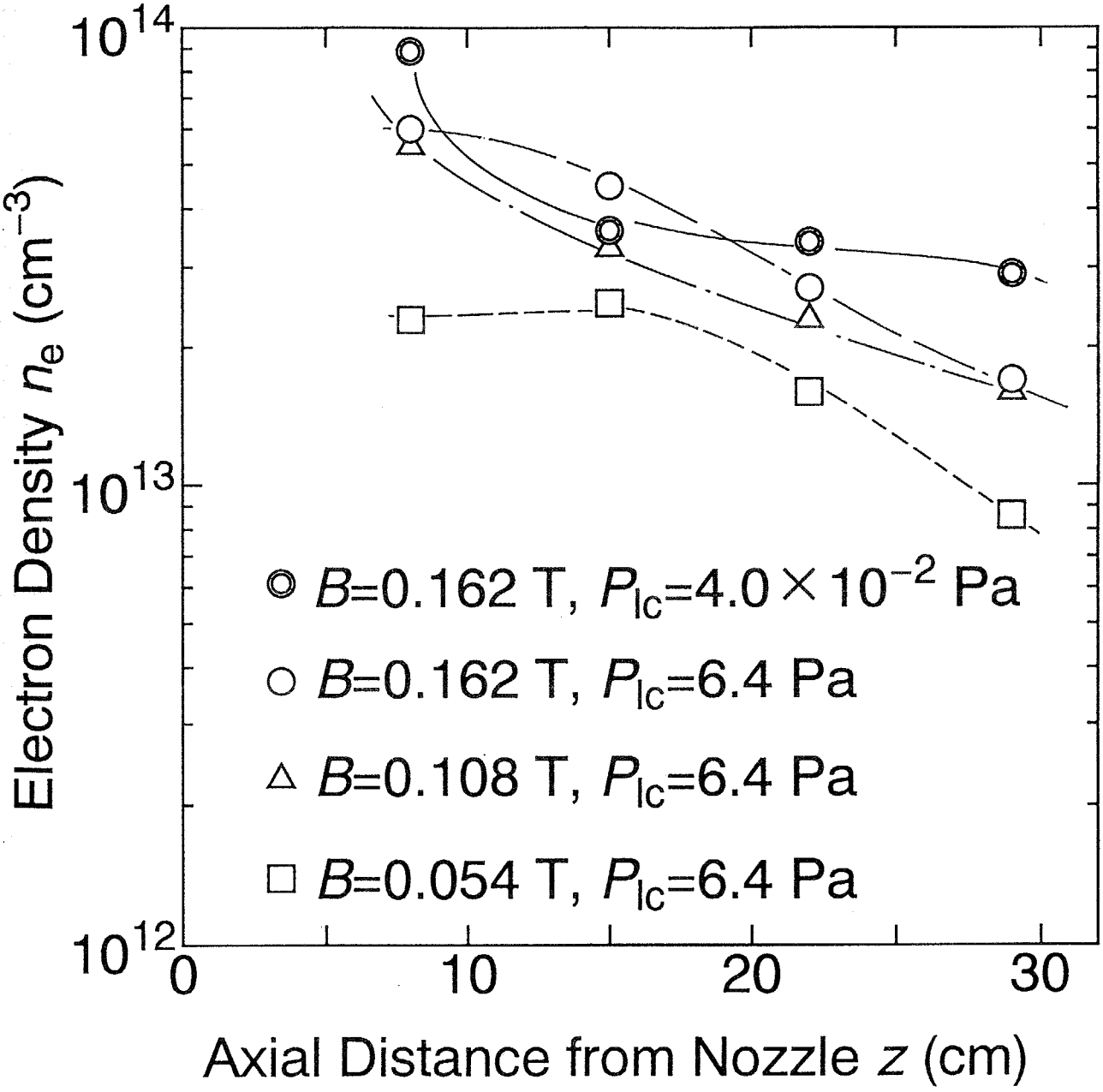

Fig. 3.5. Variation of the electron density n_e of the helium plasma measured by the spectroscopic observations.

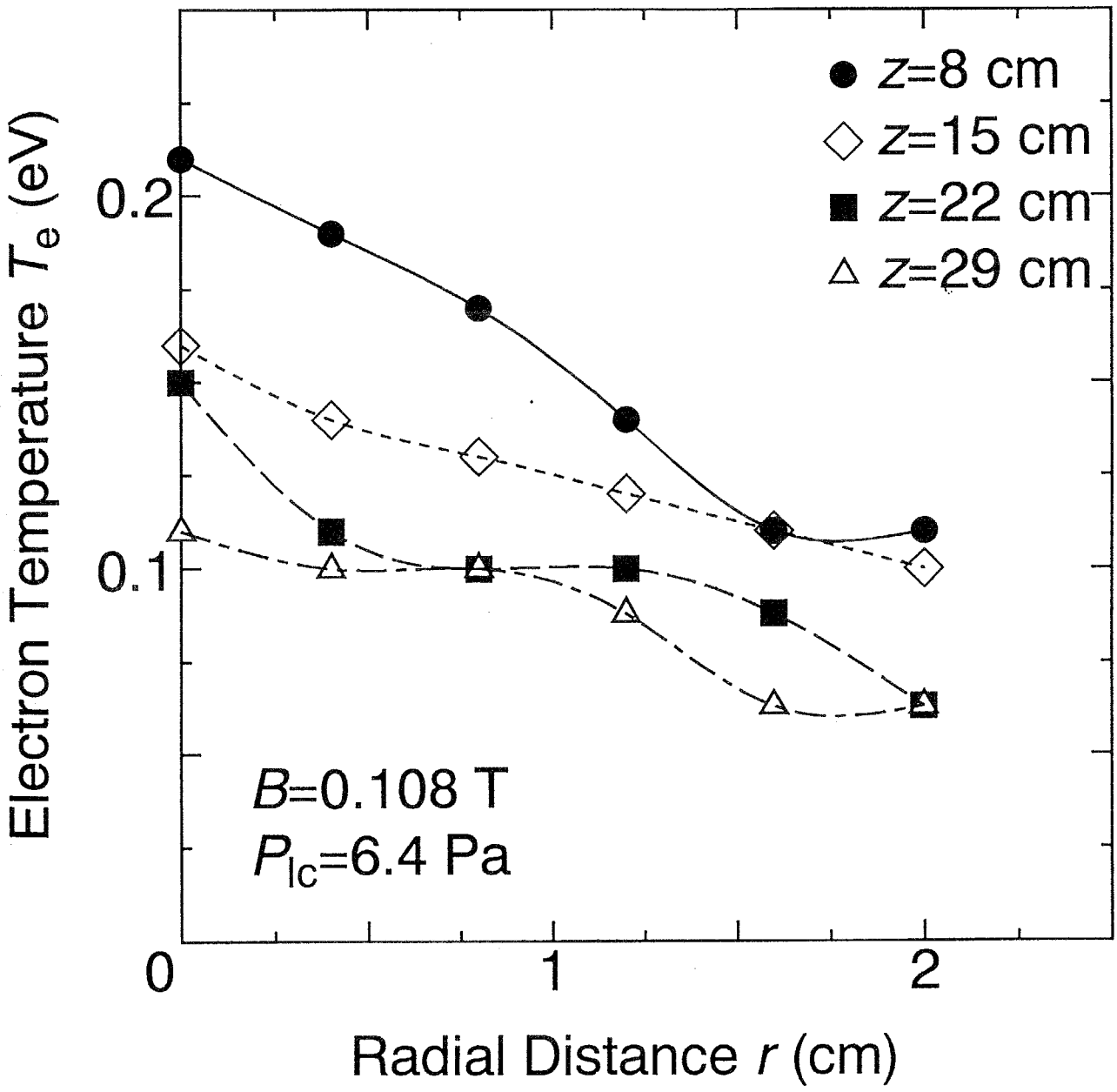

Fig. 3.6. Radial profile of the electron temperature T_e of the helium plasma when $B = 0.108$ T and $P_{lc} = 6.4$ Pa.

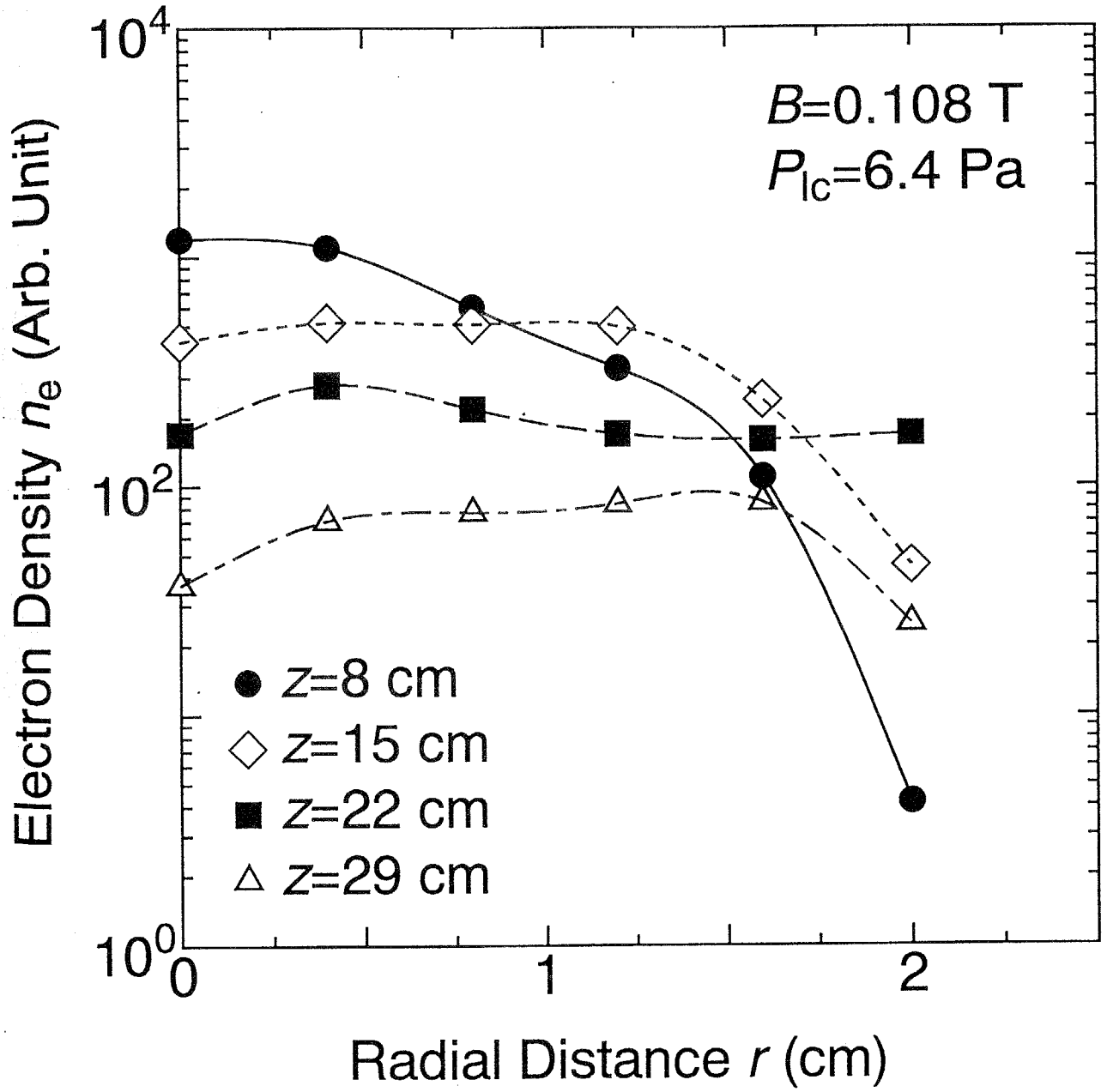

Fig. 3.7. Radial profile of the electron density n_e of the helium plasma when $B = 0.108$ T and $P_{lc} = 6.4$ Pa.

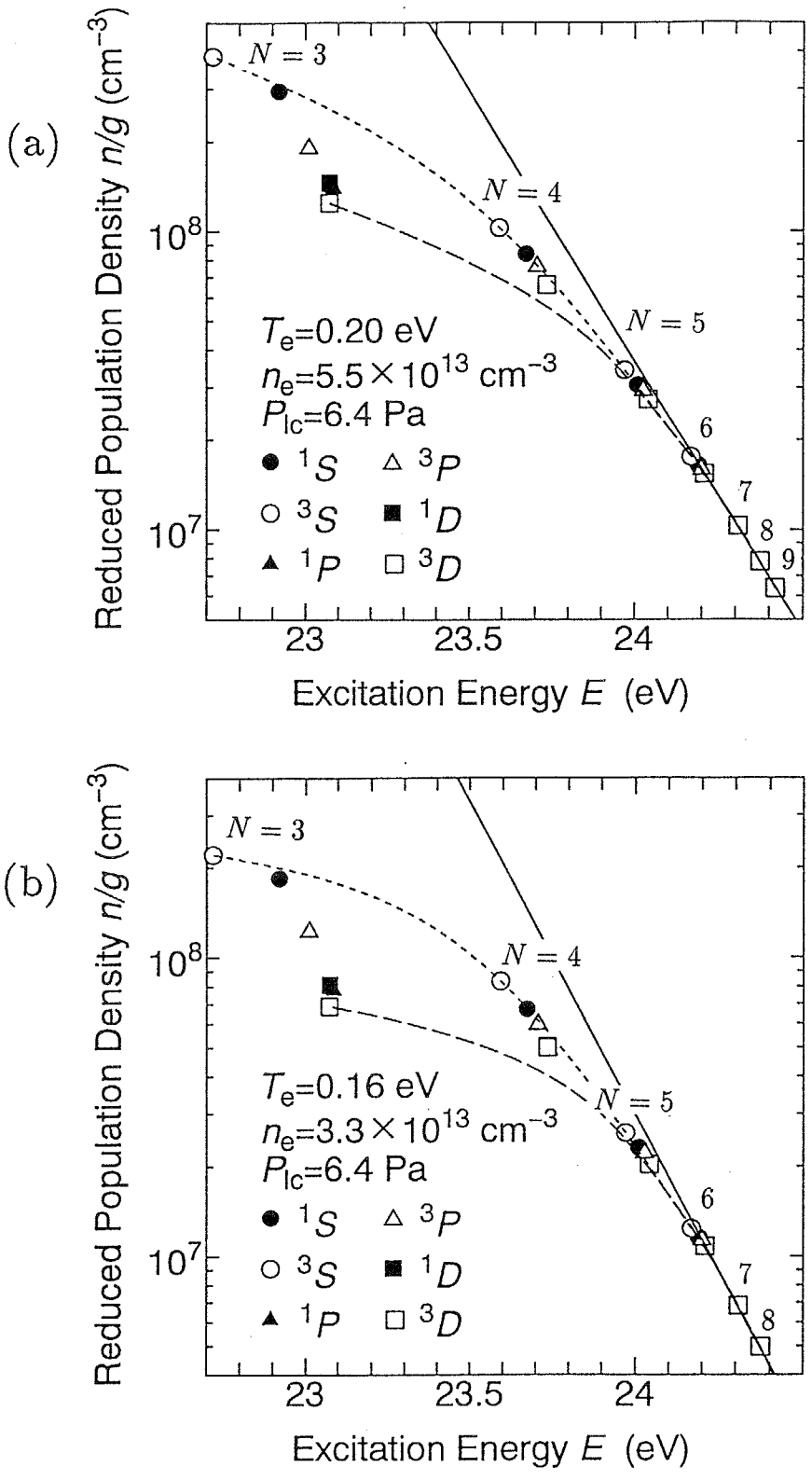

Fig. 3.8. Boltzmann plots of He I calculated by a collisional radiative model under the same conditions as in Fig. 3.1. The population densities are functions of the electron

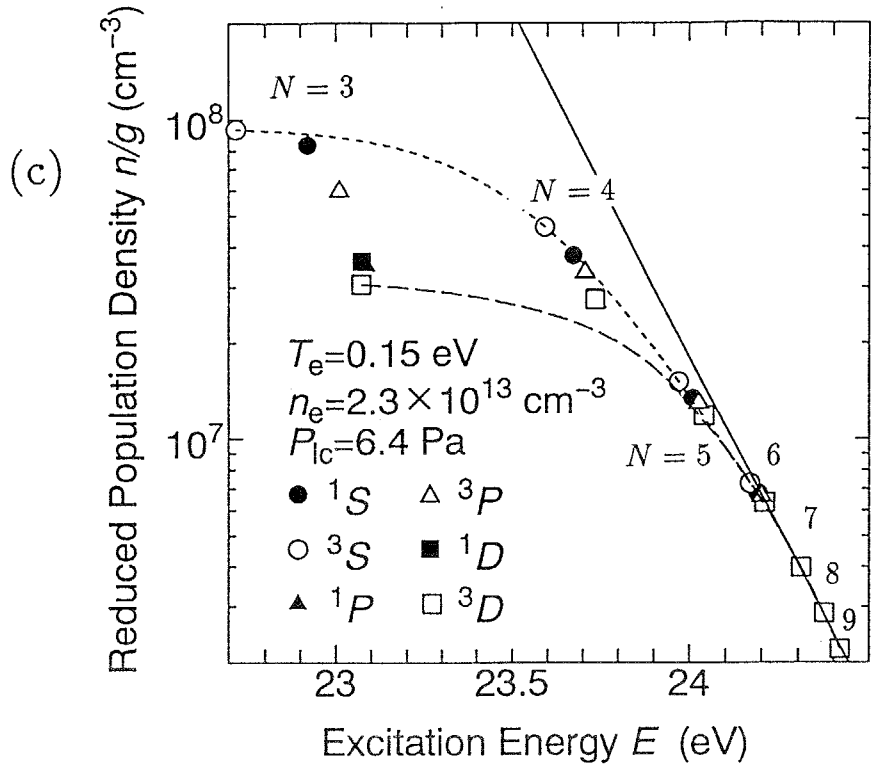

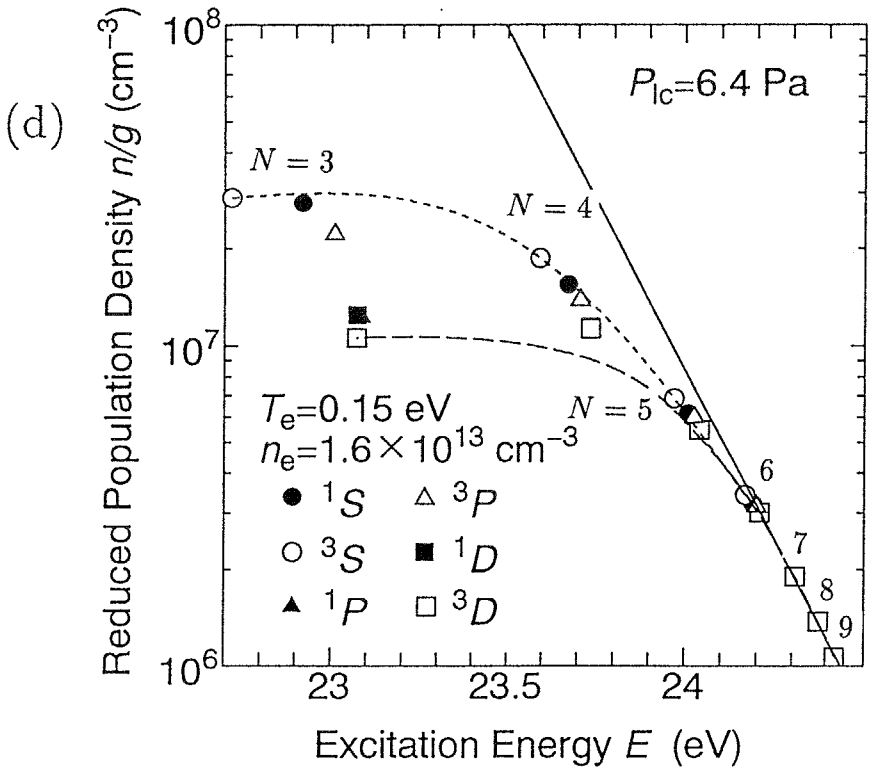

density, the electron temperature and the pressure of the plasma expansion area. The calculational methods will be described in detail in the next chapter. The diameter of the plasma column is assumed to be 8 cm. The gas temperature is assumed to be 1000 K.

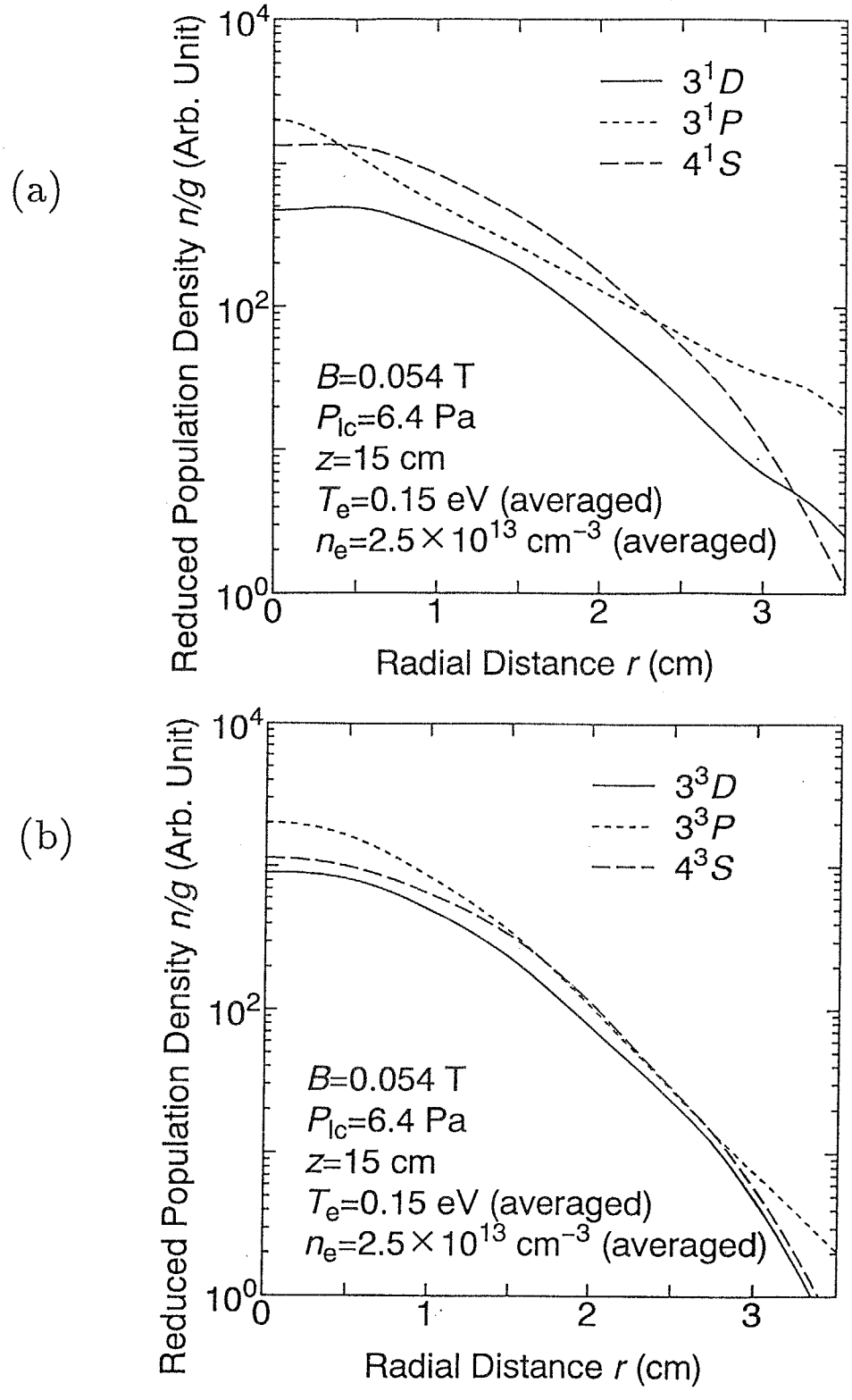

Fig. 3.9. Examples of radial profiles of the population densities of some levels: (a) singlet system, (b) triplet system of He I. $B = 0.054$ T, $P_{lc} = 6.4$ Pa, the axial distance from the nozzle $z = 15$ cm, the averaged electron temperature $T_e = 0.17$ eV, and the averaged electron density $n_e = 2.4 \times 10^{13}$ cm^{-3}.

Chapter 4. Numerical Study on Excited-level Populations of a Recombining Helium Plasma Based on a Collisional Radiative Model

4.1 Introduction

A collisional radiative model is the most essential to calculate population densities in plasmas, since it can tell us the population densities of the various plasmas not only in a recombining phase but also in an ionizing phase as functions of the elctron temperature and density [13]. A collisional radiative model of a helium plasma was reviewed by Slavík recently [106]. Although his model was basically identical with the old model by Fujimoto [105], atomic parameters were revised and the sensitivity of the model was examined. In addition, atomic parameters in a helium plasma were completely reviewed by Janev, Langer, Evans Jr., and Post Jr. [107]. Hence, it is timely for us to reconsider the population inversions and lasing conditions of He I in a recombining helium plasma with these revised atomic parameters.

As for the analysis of the recombining He plasma for the purpose of laser oscillations, Furukane and Oda calculated maximum overpopulation densities between several levels on the suppositions that the plasma was optically thin and various nonlinear processes could be negligible [29]. They also examined how the overpopulation densities change with the electron density n_e at a fixed electron temperature T_e. Their results were limited to the optically thin plasmas, although they had discussed optically thick hydrogen plasmas in their preceding paper [28]. From the experimental viewpoint, however, it was very difficult for us to generate optically thin helium plasmas in a recombining phase, as described in the previous chapter. It was difficult for us to evacuate the residual helium sufficiently and to avoid self absorptions of vacuum ultraviolet lines. Then, if we numerically treat the recombining helium plasmas, we should include the optical thicknesses in the collisional radiative model to simulate practical plasmas more precisely. From the viewpoint of remote radiative cooling of a divertor plasma, it is also interesting to examine the vacuum

condition in which the VUV emission is not absorbed by the plasma itself.

In this chapter, in order to discuss the lasing conditins of He I in an optically thick cold recombining helium plasma, recalculations of a helium collisional radiative model are carried out. Our main purpose in the present chapter is to recalculate the lasing conditions of He I in some optical thicknesses, which has not been treated yet. Then, the mechanisms of forming population inversions are discussed in terms of atomic processes. Next, experimental verifications are described using our apparatus, an arc-heated magnetically trapped expanding plasma jet generator. It is quantitatively shown that population inversions in recombining helium plasmas are strongly affected by the optical thicknesses.

4.2 Calculational Method

Population densities of He I levels can be calculated by a collisional radiative model. The model includes following processes as linear processes:

$$\mathrm{He}(p) + \mathrm{e}^- \rightleftharpoons \mathrm{He}(q) + \mathrm{e}^- \qquad (p < q) \tag{4.1}$$

$$\mathrm{He}(p) + \mathrm{e}^- \rightleftharpoons \mathrm{He}^+ + \mathrm{e}^- + \mathrm{e}^- \tag{4.2}$$

$$\mathrm{He}(p) \rightarrow \mathrm{He}(q) + h\nu \qquad (p > q) \tag{4.3}$$

$$\mathrm{He}^+ + \mathrm{e}^- \rightarrow \mathrm{He}(p) + h\nu. \tag{4.4}$$

Equation (4.1) denotes the excitation by electron collisions from a level p to q when it goes rightward, and the deexcitation from a level q to p leftward, Eq.(4.2) ionization from a level p rightward and three-body recombination to this level leftward, Eq.(4.3) spontaneous transition from a level p to q, and Eq.(4.4) radiative and dielectronic recombination to a level p. If the same notations are used as Fujimoto [13], the time development of the population density of a level p is described as following, including all the reactions above:

$$\frac{\mathrm{d}n(p)}{\mathrm{d}t} = -\left\{\sum_{q>p} C(p,q)n_\mathrm{e} + \sum_{q<p}[G(p,q)A(p,q) + F(p,q)n_\mathrm{e}] + S(p)n_\mathrm{e}\right\} n(p)$$
$$+ \sum_{q>p}\Big\{F(q,p)n_\mathrm{e} + G(q,p)A(q,p)\Big\}n(q) + \sum_{q<p} C(q,p)n_\mathrm{e}n(q)$$
$$+ \big\{\alpha(p)n_\mathrm{e} + \beta(p)\big\}n_\mathrm{i}n_\mathrm{e}, \tag{4.5}$$

where $C(p,q)$ $(p<q)$ is the rate coefficient for Eq.(4.1) rightward, $F(q,p)$ $(p<q)$ is that of its inverse way, $S(p)$ and $\alpha(p)$ are the rate coefficients for Eq.(4.2) when rightward and leftward, respectively, $A(p,q)$ is the spontaneous transition probability of Eq.(4.3), $G(p,q)$ is the optical escape factor for the transition, $\beta(p)$ is the rate coefficient of Eq.(4.4), and n_i is the ion density, and is set equal to n_e in the calculation. In the present calculations, $G(p,q)$ is calculated by the method of Fujimoto [105], when $q = 1^1S, 2^1S$, and 2^3S. Other transitions are assumed to be optically thin. The formulation of the escape factor will be shown in the next section.

The time derivative is assumed to be negligible for excited states except metastables in Eq.(4.5). The flowing term is also allowed to be neglected in Eq.(4.5) except for the ground state and the metastable states, since, as described beforehand, the flowing is rather slow ($v_\mathrm{jet} \simeq 5 \times 10^3$ m/s) and the relaxation time of the excited states is small enough. Practically, the upper limit of the levels whose population density is unknown is set at a sufficiently high-lying level, v. With these assumptions, Eq. (4.5) becomes coupled linear equations, which we solved by an LU decomposition method in this thesis [108]. The population densities of the excited levels p of He I are given as a superposition of contributions made by He^+ (recombining component), ground state He I (1^1S) (ionizing component), and metastable states He I (2^1S) and He I (2^3S) (metastable driven components), that is,

$$\rho(p) = r_0(p) + r_1(p)\rho(1^1S) + r_2(p)\rho(2^1S) + r_3(p)\rho(2^3S),$$

$$\text{for } \ 2^{1,3}P \le p \le v \tag{4.6}$$

where ρ is a Saha decrement, defined

$$\rho(p) = n(p)/n_{\rm E}(p) \tag{4.7}$$

and $n_{\rm E}$ is the population density given by Saha-Boltzmann equilibrium, whereas r_i's ($i = 0, 1, 2, 3$) are global population coefficients derived from Eq.(4.5) and functions of $n_{\rm e}$ and $T_{\rm e}$. The subscripts 0, 1, 2, and 3 stand for the ion, 1^1S, 2^1S, and 2^3S levels, respectively. The population density given by Saha-Boltzmann equilibrium is written as follows:

$$n_{\rm E}(p) = n_{\rm e} n_{\rm i}\ Z(p), \tag{4.8}$$

where $Z(p)$ is a Saha-Boltzmann coefficient and given by Eq.(3.3).

Generally in recombining plasmas, the input parameters for the collisional radiative model are $T_{\rm e}$ and $n_{\rm e}$. However, in order to estimate the effects of radiation trapping by the ground state, we have to know the density of the ground state, which is left unknown. In recombining plasmas, the density of the ground state has not been considered as important, because population densities of the excited states can be calculated only by $T_{\rm e}$ and $n_{\rm e}$, if the plasma is optically thin. In this chapter, the ground state of He I is considered to be originated from the background residual gas in the space where the plasma exists. Since the helium gas in the present calculations has relatively low temperature, it is supposed that most of them should be situated at the ground state. Then, the density of the ground state of He I is approximated by the law of ideal gases,

$$n(1^1S) = P_{\rm He}/(kT_{\rm He}), \tag{4.9}$$

where $T_{\rm He}$ is the gas temperature and $P_{\rm He}$ is the gas pressure. If the plasma is ionized weakly, the plasma pressure is almost equal to the background neutral gas, particularly of the ground state. In the calculation, $P_{\rm He}$ and $T_{\rm He}$ are given as input parameters, even if the degree of ionization becomes large and the pressure of charged particles becomes large.

And P_{He} is assumed to be the background helium pressure, and it is also assumed that all the atoms of the background helium are situated at the ground state. Therefore P_{He} is supposed to be equal to $P_{\mathrm{He}(1^1S)}$. Later, we will compare the calculational population densities with the experiments in section 4.5.2, and there we will confirm that the pressure in the expanding plasma area is about the same as the background pressure.

In addition, we have to set the geometry of the plasma and the emission profile when we calculate the optical escape factors. In the present calculation, we assume that the plasma has the cylindrical geometry and the line has a Doppler profile. With these assumptions, we can use the optical escape factors formulated by Fujimoto without further modifications [105]. Therefore, when the diameter of the plasma column is given, we can calculate the optical thicknesses together with the density of the lower level of the transitions.

Next, the population densities of two metastable states, $n(2^1S)$ and $n(2^3S)$, should be calculated, including various non-linear processes, such as atom-atom collisions, Penning ionization processes, and diffusion to the plasma boundary. It is assumed that the axial distribution of the metastables has Bessel function profiles and that the densities of them become 0 at the plasma boundary in the present calculation. It is also assumed that the population densities of the two metastable levels change more slowly than their relaxation times. Namely, the time derivatives of the metastable levels are set equal to zero. On the other hand, in a cold recombining expanding plasma, the time derivative of the population density of the ground state should never be set equal to zero. Therefore, we consider that the expanding process cancels the increase of the ground state. In the present calculation, however, the expansion of the metastables is neglected for a simple analysis.

Therefore population densities of the metastables are calculated by the following non-linear equations provided that $n(1^1S), n_{\mathrm{e}}, n_{\mathrm{i}}, T_{\mathrm{e}}$ and T_{He} are already known.

$$\frac{\mathrm{d}n(2^1S)}{\mathrm{d}t} = k_{02}n_{\mathrm{i}}n_{\mathrm{e}} + k_{12}n(1^1S)n_{\mathrm{e}} - k_2n(2^1S)n_{\mathrm{e}} + k_{32}n(2^3S)n_{\mathrm{e}}$$

$$- \Big[\Phi_2 + h_2\big\{n(2^1S) + n(2^3S)\big\} + h_{21}n(1^1S)\Big]n(2^1S) = 0, \tag{4.10}$$

$$\frac{\mathrm{d}n(2^3S)}{\mathrm{d}t} = k_{03}n_{\mathrm{i}}n_{\mathrm{e}} + k_{13}n(1^1S)n_{\mathrm{e}} + k_{23}n(2^1S)n_{\mathrm{e}} - k_3n(2^3S)n_{\mathrm{e}}$$
$$- \Big[\Phi_3 + h_3\big\{n(2^1S) + n(2^3S)\big\} + h_{31}n(1^1S)^2\Big]n(2^3S) = 0, \tag{4.11}$$

where k's are the collisional-radiative coupling coefficients, Φ_2 and Φ_3 are diffusion loss rates of 2^1S and 2^3S levels, respectively, h_2 and h_3 are ionization coefficients of 2^1S and 2^3S due to metastable-metastable collisions, respectively, and h_{21} and h_{31} are destruction rate coefficients of metastable atoms due to two-body and three-body collisions, respectively. The parameters Φ_i, h_i, and h_{i1} are the functions of T_{He}. It is assumed that the velocity distribution of the metastables is considered to be the same as that of the ground state. On the other hand, k's are dependent on T_{e} and n_{e}, calculated as follows:

$$k_{02} = \sum_{q>2^1S}^{s}\Big[F(q,2^1S)n_{\mathrm{e}} + G(q,2^1S)A(q,2^1S)\Big]Z(q)r_0(q)$$
$$+ \alpha(2^1S)n_{\mathrm{e}} + \beta(2^1S), \tag{4.12}$$

$$k_{12} = \sum_{q>2^1S}^{s}\Big[F(q,2^1S) + G(q,2^1S)A(q,2^1\mathrm{S})/n_{\mathrm{e}}\Big]Z(q)r_1(q)/Z(1^1S)$$
$$+ C(1^1S,2^1S), \tag{4.13}$$

$$k_2 = \sum_{q>2^1S}^{s}\Big[C(2^1S,q)\big\{1 - r_2(q)\big\}$$
$$- G(q,2^1S)A(q,2^1S)Z(q)r_2(q)/\big\{Z(2^1S)n_{\mathrm{e}}\big\}\Big]$$
$$+ F(2^1S,1^1S) + \big[A(2^1S,1^1S)/n_{\mathrm{e}}\big] + S(2^1S), \tag{4.14}$$

and other k's are calculated similarly. The upper limit of the summation may be cut off at a sufficiently high-lying level s ($s > v$). It is rather troublesome for us to calculate $n(2^1S)$ and $n(2^3S)$, because k's depend on $G(q,2^{1,3}S)$ which also depend on the unknown quantities $n(2^1S)$ and $n(2^3S)$. These equations were solved through Broyden method in this thesis [109].

Though the time derivative of the population density of the ground state is not essential in the present calculation, it is suggestive for us to formulate and confirm it qualitatively in terms of equation. If we consider the flowing of the plasma, the time derivative of the ground state is described as follows:

$$\begin{aligned}\frac{\partial n(1^1S)}{\partial t} =& k_{01}n_{\rm i}n_{\rm e} - k_1 n(1^1S)n_{\rm e} + k_{21}n(2^1S)n_{\rm e} + k_{31}n(2^3S)n_{\rm e} \\ &+ \Gamma n_{\rm i} + \Phi_2 n(2^1S) + \Phi_3 n(2^3S) \\ &+ \left\{n(2^1S) + n(2^3S)\right\}\left\{h_2 n(2^1S) + h_3 n(2^3S)\right\}/2 \\ &+ h_{21}n(2^1S)n(1^1S) + h_{31}n(2^3S)n(1^1S)^2 \\ &- \nabla\cdot\left\{n(1^1S)\mathbf{v}_{\rm jet}\right\}, \end{aligned} \tag{4.15}$$

where Γ is the diffusion loss rate of ions, $\mathbf{v}_{\rm jet}$ the velocity of the expanding plasma jet. In Eq. (4.15), $n_{\rm e}$, $n_{\rm i}$, and $n(p)$ are dependent on the position as well as time. It is explained qualitatively that increasing of the time derivative of the population densities of the ground state is cancelled by the last term of Eq. (4.15), even if Eq. (4.15) is equal to 0.

In this way, when the parameters electron density $n_{\rm e}$, ion density $n_{\rm i}$ (set equal to $n_{\rm e}$), electron temperature $T_{\rm e}$, diameter of the plasma column d, temperature of the neutral helium gas $T_{\rm He}$ and pressure of helium gas $P_{\rm He}$ are given, the population densities n/g of all the levels can be calculated by Eqs. (4.5)-(4.14). The calculation was carried out by a workstation "SUN-3" by SUN Microsystems Inc.

4.3 Atomic Data

First, the included energy levels and their excitation energy should be specified. In the present calculations, the levels listed in Table 4.1 are treated individually. Namely, we consider all of the sublevels to be individual levels for the principal quantum number $N \leq 7$, except that the levels with an orbital angular momentum quantum number $L \geq 3$

are grouped together into a single level F. For the levels $8 \leq N \leq 10$, all of the sublevels with the same spin multiplicity are grouped together. For the levels $11 \leq N \leq 20$, all of the sublevels are grouped together. Namely, the upper limit v in Eq.(4.6) is set 20. The population densities of the more excited levels than v are assumed to be described by Eqs.(4.8)-(4.9), namely, assumed to be in the state of local thermodynamic equilibrium (LTE). The upper limit s is set 26. The values of the energy are adopted from Ref. [96].

Recently, cross sections and reaction rate coefficients of hydrogen and helium atoms were reviewed by Janev, Langer, Evans Jr., and Post Jr. [107]. Almost all the atomic data for excitations, ionizations, and recombinations in our calculations are adopted from their review. Only for the ionization cross section from the ground state and the three-body recombination coefficient to the ground state, the data reviewed by Bell, Gilbody, Hughes, Kingston, and Smith are used [110].

As for the transition probabilities, the data in Ref. [95] are adopted for the optically allowed transitions. When the transition probabilities between high-lying levels are not listed in Ref. [95], the hydrogenic approximation [111] is employed. For the optically forbidden transition probabilities, we adopt Ref. [112] for $2^3P - 1^1S$, Ref. [113] for $2^1S - 1^1S$, and Ref. [114] for $2^3S - 1^1S$. Other forbidden transitions are neglected.

As for the non-linear processes, we adopt Ref. [115] for Φ_2, Φ_3, h_{21} and h_{31}, and Ref. [116] for h_3. The parameter h_2 is assumed to be equal to h_3.

As for the optical escape factors, the formula by Fujimoto [105] is used. For the transition from the state p to q with a Doppler profile and with a cylindrical geometry, the optical escape factor is formulated as follows:

$$G(p,q) = \frac{1.92 - \dfrac{1.3}{1 + \left[\kappa(q,p)d/2\right]^{6/5}}}{\Big[\left(\kappa(q,p)d/2\right) + 0.62\Big]\left\{\pi \ln\Big[1.375 + \left(\kappa(q,p)d/2\right)\Big]\right\}^{1/2}} , \qquad (4.16)$$

where $\kappa(q,p)$ is the absorption coefficient at the line center. It is calculated as follows

[64]:

$$\kappa(q,p) = \frac{h\nu(p,q)}{c} n(q) B(q,p) P(p,q;\Delta\nu = 0), \tag{4.17}$$

where $B(q,p)$ is the Einstein's B coefficient, $\nu(p,q)$ is the frequency of the line, c is the speed of light, and $P(p,q;\Delta\nu)$ is the line profile. The B coefficient can be written as follows:

$$B(q,p) = \frac{g(p)}{g(q)} B(p,q) = \frac{c^3}{8\pi h\nu(p,q)^3} \frac{g(p)}{g(q)} A(p,q). \tag{4.18}$$

And for the Doppler profile,

$$P(p,q;\Delta\nu) = \frac{1}{\sqrt{\pi}\Delta\nu_{\rm D}} \exp\left[-\left(\frac{\Delta\nu}{\Delta\nu_{\rm D}}\right)^2\right], \tag{4.19}$$

with

$$\Delta\nu_{\rm D} = \frac{1}{\lambda(p,q)} \sqrt{\frac{2kT_{\rm He}}{m_{\rm He}}}, \tag{4.20}$$

where $m_{\rm He}$ is the mass of the helium atom, $\lambda(p,q)$ is the wavelength of the line, and $\Delta\nu_{\rm D}$ is the Doppler width. The optical escape factors are calculated with Eqs.(4.16)-(4.20).

It should be confirmed that the Doppler broadening predominates over the total broadening under the plasma conditions assumed in the present calculation. We can calculate the Doppler width of the He I line from Eq. (4.20). If $T_{\rm He} = 1000$ K, then $\Delta\nu_{\rm D}/\nu \simeq 7 \times 10^{-6}$. Of course, the Doppler broadening has the Gaussian profile. On the other hand, for the Lorentzian profile, we have to consider the natural width, the Stark broadening, and the resonance broadening. The natural width $\Delta\lambda_{\rm N}$ is calculated as follows:

$$\Delta\lambda_{\rm N}/\lambda(p,q) = \frac{\lambda(p,q)}{2\pi c} \Delta\omega_{1/2}, \tag{4.21}$$

with

$$\Delta\omega_{1/2} = \sum_k A(p,k) + \sum_j A(j,q), \tag{4.22}$$

for the transition $p \rightarrow q$ [117]. For a transition of $3^1S \rightarrow 2^1P$, Eqs. (4.21)-(4.22) shows $\Delta\lambda_N/\lambda \simeq 7 \times 10^{-7}$, and the natural widths of other lines are of the same order. Next, the Stark broadening of He I lines were calculated in Ref. [118]. In general, the Stark broadening $\Delta\lambda_S$ is strongly dependent on the electron density, and the electron temperature has a much smaller effect on the broadening. For the $3^1S \rightarrow 2^1P$ transition, Ref. [118] shows $\Delta\lambda_S/\lambda \simeq 5 \times 10^{-7}$ when $n_e = 10^{14}$ cm^{-3} and $T_e = 5000$ K. The Stark broadening decreases with decreasing n_e and T_e, therefore, the Stark broadening is considered to be the same order as the natural widths. As for the resonance broadening $\Delta\nu_R$, the following equation was reported [119]:

$$\Delta\nu_R = K_{jj'} \left(\frac{2J+1}{2J'+1}\right)^{1/2} \frac{e^2 f_{JJ'} n}{mc^2 \nu_{JJ'}}, \tag{4.23}$$

where J and J' are total angular momentum quantum numbers of the ground state and the resonance state, $f_{JJ'}$ is the oscillator strength for the transition, and $K_{jj'}$ is a numerical factor of order 1. When the density of the neutral particles n is about 10^{14} cm^{-3}, which corresponds to the pressure of about 1 Pa, $\Delta\nu_R/\nu \simeq 10^{-9}$, which is much smaller than the natural width.

In consequence, the Lorentzian width is at most one-fifth of the Doppler width even when $n_e \simeq 10^{14}$ cm^{-3}. In our experiments, n_e becomes smaller than 10^{14} cm^{-3}, and the Stark broadening is considered to be much smaller. Consequently, the natural width dominates the Lorentzian width, and it is about one-tenth of the Doppler width. Therefore, it is considered that the line profiles of He I in the visible wavelength region are almost Gaussian. It should be noted that it is difficult for us to measure these widths experimentally, since the instrumental widths are much larger in our experimental apparatus.

4.4 Results

The calculations are carried out for the helium plasma at a fixed atomic temperature $T_{\mathrm{He}} = 1000$ K in the temperature range $0.1 \leq T_{\mathrm{e}}$ (eV) ≤ 0.5 and in the density range $10^{11} \leq n_{\mathrm{e}}$ (cm^{-3}) $\leq 10^{17}$. The diameter of the plasma column d is set at 8 cm, which is equal to the inner diameter of the coils of the plasma generator. Figure 4.1 shows the reduced population densities of excited states calculated with this model when the electron temperature T_{e} is 0.1 eV with electron density $n_{\mathrm{e}} = 1.0 \times 10^{13}$ cm^{-3} and the background pressure $P_{\mathrm{He}} = 10$ Pa. Under this condition, the pressure is almost equal to that of the residual helium situated at the ground state. The optical thickness for the transitions to the ground state is found to be essential at this pressure. On the other hand, Fig.4.2 shows the calculated population density with $P_{\mathrm{He}} = 1.0 \times 10^{-3}$ Pa while other parameters are the same as in Fig.4.1. When these figures are compared with each other, the effect of the optical thicknesses on the population densities is evedent, especially for the low-lying levels of the singlet state. It should be noted that the levels of triplet states are not affected very much.

Next, we consider conditions for the laser oscillation. As described in the previous chapter, we rewrite the overpopulation density $\Delta n/g(p,q)$ between level pairs $p-q$ (p is the upper level and q is the lower level) as follows:

$$\Delta[n/g(p,q)] = [n(p)/g(p)] - [n(q)/g(q)]. \tag{3.4}$$

The threshold value of $\Delta n/g(p,q)$ for the laser oscillation $\Delta[n/g(p,q)]_{\mathrm{th}}$ at the center of the spectral line with a Gaussian profile should also be rewritten below:

$$\Delta[n/g(p,q)]_{\mathrm{th}} = \frac{8\pi^{3/2}}{g(p)A(p,q)\lambda(p,q)^3}\left(\frac{2kT_{\mathrm{He}}}{m_{\mathrm{He}}}\right)^{1/2}\left(-\frac{\ln\sqrt{R_1R_2}}{l}\right), \tag{3.5}$$

In the present calculation, l is assumed to be the same as the diameter of the plasma column d.

Now we consider the possibility of lasing in the plasma at the maximum value of the overpopulation density like Ref. [29]. As reported there, $\Delta[n/g(p,q)]$ has its maximum

$\Delta[n/g(p,q)]_{\rm m}$ at $n_{\rm e} = n_{\rm e,\ op}$. Of course, $\Delta[n/g(p,q)]_{\rm m}$ decreses as $T_{\rm e}$ increases. If the relation

$$\Delta[n/g(p,q)]_{\rm m} \geq \Delta[n/g(p,q)]_{\rm th} \tag{4.24}$$

is satisfied, the laser oscillation between the level pair p and q can be produced. Table 4.2 shows $\Delta[n/g(p,q)]_{\rm m}$ at $n_{\rm e,\ op}$ when the electron temperature $T_{\rm e} = 0.1$ eV and $P_{\rm He} = 10^{-3}$ Pa and 10 Pa. It also tabulates the threshold value $\Delta[n/g(p,q)]_{\rm th}$ at $R_1 = 0.99, R_2 = 0.998$ and $l = d = 8$ cm. As the background pressure increases, the maximum overpopulation densities become smaller and the laser oscillation becomes difficult in the singlet system. One of the examples of this effect on the population inversion between a level pair $4^1S - 3^1P$ is shown in Fig.4.3. As the pressure becomes larger, $n_{\rm e,\ op}$ becomes smaller, and consequently, $\Delta[n/g]_{\rm m}$ becomes smaller. The effect of the optical thickness is the most significant for the level pairs whose lower level is 2^1P. When $P_{\rm He} = 10$ Pa, no population inversion is obtained for those level pairs. On the other hand, the overpopulation densities in the triplet system are not affected very much. The difference between these systems is discussed in the next section in terms of atomic processes. If we would like to oscillate the lines which are strongly affected by the optical thickness, we must evacuate the background residual helium and remove the atoms situated at the ground state in the plasma. These are also quantitatively discussed in the next section.

4.5 Discussion

4.5.1 The effect of optical thickness and mechanisms of forming population inversion

As was shown in the previous section, the density of the ground state strongly affects the population densities of the singlet state, whereas it does not affect those of the triplet system. When the density of the atoms of the ground state becomes large, the optical

escape factors for the transitions to the ground state become small. Some of the optical escape factors for the transitions to the ground state are shown in Fig.4.4 as functions of the residual helium pressure when $T_{\rm He} = 10^3$ K and the diameter of the plasma column $d = 8$ cm. The changing of these factors affects the population densities of the singlet system. On the other hand, the transitions to the ground state from any states of the triplet system are forbidden, therefore the pressure of residual helium has little effect on the depopulation of the states of the triplet system.

We calculate each component of the population rate and of the depopulation frequency in Table 4.3 for the level pair $4^1S - 3^1P$, when $P_{\rm He} = 10^{-3}$ Pa (optically thin for any transitions) and $P_{\rm He} = 10$ Pa (optically thick for the transition to the ground state) at $T_{\rm e} = 0.1$ eV, and $n_{\rm e} = 2 \times 10^{13}$ cm^{-3}. We treat five processes for population rates separately, that is, radiative decay $P_{\rm ra}$, collisional deexcitation $P_{\rm cd}$, collisional excitaiton $P_{\rm ce}$, three-body recombination $P_{\rm 3r}$, and radiative recombination $P_{\rm rr}$, each of which is defined as follows:

$$P_{\rm ra}(p) = \sum_{q>p} G(q,p)A(q,p)n(q), \tag{4.25}$$

$$P_{\rm cd}(p) = n_{\rm e} \sum_{q>p} F(q,p)n(q), \tag{4.26}$$

$$P_{\rm ce}(p) = n_{\rm e} \sum_{q<p} C(q,p)n(q), \tag{4.27}$$

$$P_{\rm 3r}(p) = n_{\rm e}^2 n_{\rm i} \alpha(p), \tag{4.28}$$

$$P_{\rm rr}(p) = n_{\rm e} n_{\rm i} \beta(p). \tag{4.29}$$

Likewise, four processes are treated in calculating depopulation frequencies, namely, radiative decay $D_{\rm ra}$, collisional deexcitation $D_{\rm cd}$, collisional excitation $D_{\rm ce}$, and ionization $D_{\rm io}$, where

$$D_{\rm ra}(p) = \sum_{q<p} G(p,q)A(p,q), \tag{4.30}$$

$$D_{\rm cd}(p) = n_{\rm e} \sum_{q<p} F(p,q), \tag{4.31}$$

$$D_{\rm ce}(p) = n_{\rm e} \sum_{q>p} C(p,q), \tag{4.32}$$

$$D_{\rm io}(p) = n_{\rm e} \ \ S(p). \tag{4.33}$$

And we define the total population rate $P_{\rm t}$ and the total depopulation frequency $D_{\rm t}$ as follows:

$$P_{\rm t} = P_{\rm ra} + P_{\rm cd} + P_{\rm ce} + P_{\rm 3r} + P_{\rm rr}, \tag{4.34}$$

$$D_{\rm t} = D_{\rm ra} + D_{\rm cd} + D_{\rm ce} + D_{\rm io}. \tag{4.35}$$

The population inversion is created for the level pair 4^1S-3^1P not only in $P_{\rm He} = 10^{-3}$ Pa but also in $P_{\rm He} = 10$ Pa. However, the mechanism of forming the population inversion is a little different from each other. When the plasma is optically thin (Table 4.3(a)), the mechanism for inversion is the same as Furukane and Oda pointed out [29]. Namely, a large value of $D_{\rm t}(3^1P)$ is mainly due to a radiative decay, $D_{\rm ra}(3^1P)$. And $P_{\rm t}(4^1S)$ becomes large because collisional cascade processes occur from high-lying levels, which are populated by three-body recombination. $P_{\rm cd}(4^1S)$ is almost equal to $P_{\rm t}(4^1S)$. On the other hand, when the plasma becomes optically thick, important contributions to $D_{\rm t}(3^1P)$ are made by collisional deexcitation processes rather than by radiative decay processes.

This tendency is more remarkable for the level pair 3^1S-2^1P. Each component of the population rate and of the depopulation frequency for the level pair is shown in Table 4.4 when $P_{\rm He} = 10^{-3}$ Pa (Table 4.4(a)) and $P_{\rm He} = 10$ Pa (Table 4.4(b)) at $T_{\rm e} = 0.1$ eV and $n_{\rm e} = 1.0 \times 10^{15}$ cm^{-3}. The transitions to the metastable states are optically thick in this electron density irrespective of the background pressure. When the background pressure becomes 10 Pa, the plasma becomes optically thick for the transition to the ground state. Therefore, the depopulation frequency by radiative decay $D_{\rm ra}(2^1P)$ becomes much smaller, and consequently $D_{\rm t}$ becomes smaller, and finally the population inversion is

destroyed. When the plasma is optically thick, the depopulation of the laser lower levels is mainly due to collisional deexcitations. It is concluded that population inversions are accomplished through collisional processes even in the siglet system in an optically thick plasma.

Some of the optical escape factors for the transitions to the metastables are shown in Fig.4.5(a)-(b), when $T_e = 0.1$ eV, $T_{He} = 1000$ K, and $d = 8$ cm. They are functions of the densities of the metastables, therefore they depend on the electron density. However, the optical thicknesses in the transitions to the metastable states do not affect the total population rate and the total depopulation frequency of $N^{1,3}P$ levels very much. Figures 4.6 (a)-(b) show the variation of depopulation frequencies of levels 2^1P and 3^1P, respectively, with electron density. It is found that the depopulation frequency by radiative decay in $P = 10$ Pa decreases when the electron density becomes more than $10^{13} - 10^{14}$ cm^{-3}. This is because the transition to the metastable states becomes optically thick. When the plasma is optically thin for the transitions to the ground state, the depopulation of the N^1P levels is mainly due to the radiative decay to the ground state. If the electron density becomes very large, the depopulation frequency is determined mainly by collisional deexcitations, and the optical thicknesses for the visible transitions have little effect on the total depopulation frequencies. The transitions to the ground state is the most essential in the optical thickness, when the population and depopulation processes are considered.

The calculated maximum values $\Delta[n/g(p,q)]_m$ are larger than those calculated by Furukane and Oda [29]. This is mainly because our calculation includes non-linear depopulation processes of metastables. Non-linear depopulation of metastables helps depopulate the laser lower levels, particularly N^1P levels.

It was reported that only collisional processes could produce the population inversion in the triplet system [29]. But we find that the theory is not always true. Table 4.5 shows values for each component of the population rate and of the depopulation frequency of a level pair $4^3P - 3^3D$, when $T_e = 0.1$ eV, $n_e = 2.0 \times 10^{13}$ cm^{-3}, $T_{He} = 1000$ K, and

$d = 8$ cm. The important contribution of the depopulation of the lower levels is due to the radiative decay not only for the level 3^3D but also the levels 3^3S, 4^3S, and 4^3D. As expected, the mechanisms of forming population inversions are hardly affected by the background pressure in the triplet system.

4.5.2 Comparison of the calculation with the experiments

In chapter 3, we tried to explain the experimental results by the calculation described in this chapter. And it was shown that the Abel inversion should be applied to the experimental data when they were compared with the calculation based on a collisional radiative model. We tried to apply the Abel inversion to the population density of the levels whose principal quantum number $3 \leq N \leq 6$. It was difficult to apply it to the higher levles since the photon yield was insufficient. After the inversion, T_e and n_e were determined by the levels of $N = 5$ and 6, with the assumption that these levels were in the state of LTE.

Two examples to which the Abel inversion was applied are shown in Figs. 4.7-4.8. Figure 4.7(a) shows the experimentally observed population densities of some excited levels where the axial distance from the nozzle is 15 cm on the jet axis ($r = 0$) with the applied magnetic field $B = 0.162$ T. The parameters in Fig. 4.7(a) are the following: $T_e = 0.16$ eV, $n_e = 2.1 \times 10^{13}$ cm^{-3}, $d = 8$ cm, and $P_{He} = 10$ Pa. Unfortunately, in the experiment of Figs. 4.7-4.8, the diameter of the nozzle of the plasma generator were smaller than those in chapter 3, therefore the electron temperature and density were not equal to those in Fig. 3.1. On the other hand, Fig. 4.7(b) shows the calculated population densities with the same parameters with the assumption that T_{He} is 1000 K. The plasma was found to be optically thin for the transitions to the levels of $N = 2$ through the calculation. The experimental results agree with the present calculation very well, although the population densities of levels $N = 5, 6$ contain substantial error. The levels with $N \geq 4$ tend to stay in the state of LTE, whereas the levels of $N = 3$ are far

from LTE. Moreover, in levels $N = 3$, the levels of 3^3S, 3^1S, and 3^3P are more populated and the rest are less populated.

The same tendency is observed in Fig. 4.8(a) which shows the experimental results where the axial distance from the nozzle is 15 cm on the jet axis and the applied magnetic field $B = 0.108$ T. The plasma parameters are the following: $T_e = 0.086$ eV, $n_e = 6.0 \times 10^{12}$ cm^{-3}, $d = 8$ cm, and $P_{He} \simeq 10$ Pa. The experimental results agrees with the present calculation shown in Fig. 4.8(b), where the same parameters are used as Fig. 4.8(a) with the assumption that the gas temperature $T_{He} = 1000$ K. The population density of the level 3^3P is largest in the levels with $N = 3$. And the agreement of the experimental results with the present calculations is very good. The agreement of the data was improved by the Abel inversion, although T_e and n_e might have considerable errors.

In section 4.2, we assumed that the density of the helium ground state could be calculated by Eq. (4.9). Namely, we assumed that $n(1^1S)$ in the expanding plasma area was the same as that of the background level. We should confirm this assumption. Then, we measured the radial profile of the helium signal by a quadrupole mass spectrometer (Q.M.S.) with a skimmer. We cannot distinguish the quantum state of the helium detected by the Q.M.S. However, as described beforehand, almost all the helium atoms are situated at the ground state in the expanding plasma area. Hence, it is allowed for us to consider this signal as proportional to $n(1^1S)$. Figure 4.9 shows the radial profiles of the helium signal when $B = 0.027$ T and 0.16 T with $P_{lc} \simeq 7$ Pa, together with radial profiles of an ion saturation current. We can thereby conclude that the density of the ground state of helium is about 1.5 times of that of the background level. It is considered that the density $n(1^1S)$ in the expanding plasma area is approximated with the background helium pressure.

It was very difficult for us to generate optically thin helium plasmas with our apparatus with low electron temperature, since the ultimate pressure of plasma expanding region in our apparatus was not low enough without the ejector pumps. When we used the ejector

pumps, the electron temperature was not low enough. In the section 4.5.4, we will discuss the requirement for the vacuum condition in which the plasma becomes optically thin.

4.5.3 Effects of the collisions between the metastables on their population and depopulation

In Eqs. (4.10)-(4.11), we considered some elementary processes in which electrons did not participate when the population densities of two metastable states were calculated. Namely, we considered the diffusion loss, the ionizations of 2^1S and 2^3S states due to metastable-metastable collisions, and the destructions due to two-body and three-body collisions. Particularly, the metastable-metastable collisions are generally considered to be very important processes in an afterglow plasma of low electron temperature [120]. The following processes should be considered for the metastable states:

$$\mathrm{He}(q) + \mathrm{He}(q) \rightarrow \mathrm{He}^+ + \mathrm{He}(1^1S) + \mathrm{e}^-, \tag{4.36}$$

$$\rightarrow \mathrm{He}_2^+ + \mathrm{e}^-, \tag{4.37}$$

where $q = 2^1S$ and 2^3S. The total reaction coefficients of Eqs. (4.36) and (4.37) were defined as h_2 and h_3 for 2^1S and 2^3S levels, respectively. For 2^3S level, the branching ratio for Eq. (4.36) was reported to be about 0.30 ± 0.05 [121]. Namely, Eq. (4.37), the associative ionization process is dominant.

In order to evaluate the contributions of these processes to the populations and depopulations, we define following depopulation frequencies other than Eqs. (4.30)-(4.33):

$$D_{\mathrm{dif}}(q) = \Phi_i, \tag{4.38}$$

$$D_{\mathrm{col}}(q) = h_{i1} n(1^1S)^{i-1}, \tag{4.39}$$

$$D_{\mathrm{met}}(q) = h_i[n(2^1S) + n(2^3S)], \tag{4.40}$$

where $q = 2^1S$ and 2^3S, and $i = 2$ for $q = 2^1S$ and $i = 3$ for $q = 2^3S$. As Eq. (4.40) shows, $D_{\rm met}$ contains the contributions of Eqs. (4.36)-(4.37). Of course, the total depopulation frequency of the metastables should include the above processes, namely,

$$D_{\rm t}(q) = D_{\rm ra} + D_{\rm cd} + D_{\rm ce} + D_{\rm io} + D_{\rm dif} + D_{\rm col} + D_{\rm met}. \tag{4.41}$$

As an example, Table 4.6 shows the population rates and depopulation frequencies of the metastables, together with their population densities, when $T_{\rm e} = 0.16$ eV, $n_{\rm e} = 2.1 \times 10^{13}$ cm^{-3}, $T_{\rm He} = 1000$ K, $P_{\rm He} = 10$ Pa, and $d = 8$ cm (the same conditions as in Fig. 4.7). Table 4.6 shows that the depopulations of the metastable states are mainly due to the electron collisional deexcitation. Although the depopulation frequency of the electron collisional ionization $D_{\rm io}$ is by far smaller than that of the metastable-metastable collisional ionization $D_{\rm met}$, the depopulation by the associative ionization process is found to be less dominant than the collisional deexcitation process in the generated helium plasma in determining the population densities of the metastable states. Namely, in our plasma,

$$D_{\rm io}({\rm metastables}) \ll D_{\rm met}({\rm metastables}) \ll D_{\rm cd}({\rm metastables}). \tag{4.42}$$

This is because the electron density of our plasma is sufficiently large and the electron collisional deexcitation process is much more dominant than the atomic or ionic collisional processes. It is concluded that the population and depopulation processes in the plasma generated in our apparatus are mainly determined through the electron collisional processes. That's why the collisional radiative model can explain the poplation densities of the excited states very well.

Still, when we consider the electron and ion densities (not the population densities of the excited states) in terms of various elementary processes, we should consider the ionization due to the metastable-metastable collisions, especially, the associative ionization [Eq. (4.37)], even in a recombining plasma. When we consider only the electron collisional

radiative terms in calculating the time derivatives of the density of the ground state, the quasi-steady-state solution for the ground state can be obtained as the following [105]:

$$\begin{aligned}\frac{\mathrm{d}n(1^1S)}{\mathrm{d}t} = &-\left[\sum_{q\geq 2^{1,3}S} C(1^1S,q) + S(1^1S)\right] n_\mathrm{e} n(1^1S) \\ &+ \sum_{q\geq 2^{1,3}S} \left[F(q,1^1S)n_\mathrm{e} + G(q,1^1S)A(q,1^1S)\right] \\ &\times \left[Z(q)r_0(q)n_\mathrm{i}n_\mathrm{e} + \frac{Z(q)}{Z(1^1S)}r_1(q)n(1^1S)\right] \\ &+ [\alpha(1^1S)n_\mathrm{e} + \beta(1^1S)]n_\mathrm{i}n_\mathrm{e}. \end{aligned} \tag{4.43}$$

This equation can be rewitten simply as follows:

$$\frac{\mathrm{d}n(1^1S)}{\mathrm{d}t} = -S_\mathrm{CR} n(1^1S)n_\mathrm{e} + \alpha_\mathrm{CR} n_\mathrm{i} n_\mathrm{e}, \tag{4.44}$$

where

$$\begin{aligned} S_\mathrm{CR} = &\sum_{q\geq 2^{1,3}S} C(1^1S,q) + S(1^1S) \\ &- \frac{1}{Z(1^1S)n_\mathrm{e}} \sum_{q\geq 2^{1,3}S} Z(q)r_1(q)[F(q,1^1S)n_\mathrm{e} + G(q,1^1S)A(q,1^1S)], \end{aligned} \tag{4.45}$$

$$\begin{aligned} \alpha_\mathrm{CR} = &\alpha(1^1S)n_\mathrm{e} + \beta(1^1S) \\ &+ \sum_{q\geq 2^{1,3}S} Z(q)r_0(q)[F(q,1^1S)n_\mathrm{e} + G(q,1^1S)A(q,1^1S)]. \end{aligned} \tag{4.46}$$

S_CR and α_CR are referred as the collisional-radiative ionization rate coefficient and the collisional-radiative recombination rate coefficient, respectively [13,105]. In Eq. (4.46), we assume

$$\frac{\mathrm{d}n_\mathrm{i}}{\mathrm{d}t} + \frac{\mathrm{d}n(1^1S)}{\mathrm{d}t} = 0. \tag{4.47}$$

For the conditions in Table 4.6, we have $S_\mathrm{CR} = 3.8 \times 10^{-70}$ cm^{3}s^{-1} and $\alpha_\mathrm{CR} = 1.3 \times 10^{-10}$ cm^{3}s^{-1}. Of course, since our plasma is a recombining plasma, we can find $\alpha_\mathrm{CR} \gg$

S_{CR}, if we consider only the electron collisional processes. And we can obtain the collisional-radiative recombination rate $\alpha_{CR} n_i n_e = 5.7 \times 10^{16}$ cm^{-3}s^{-1}. On the other hand, if we consider the ionization processes of Eqs. (4.37) and (4.38), the metastable-metastable ionization rate coefficient including the associative ionization is calculated as follows:

$$\left(\frac{dn_e}{dt}\right)_{met} = [D_{met}(2^1S)n(2^1S) + D_{met}(2^3S)n(2^3S)]/2, \tag{4.48}$$

and the metastable-metastable collisional ionization rate becomes $(dn_e/dt)_{met} = 8.6 \times 10^{14}$ cm^{-3}s^{-1}, which is much larger than the collisional radiative ionization rate S_{CR} $\times n(1^1S)n_e \simeq 8 \times 10^{-42}$ cm^{-3}s^{-1}, and about $1-2$ % of the collisional recombination rate $\alpha_{CR} n_i n_e$. When we severely consider the electron ionization-recombination processes in the recombining helium plasma, namely, when we calculate the variation of the electron density, the metastable collisional processes should be considered. Yet, if the population densities of the excited states are calculated as functions of a given electron density, the effect of the associative ionization is considered to be small, as was shown in Table 4.6.

4.5.4 Requirement for the background pressure for the lasing

It was shown in section 4.5.1 that the background helium gas was an obstacle to forming large population inversions in the siglet system of He I . It is also shown in Table 4.2(a) that the lasing between some level pairs in the siglet system is possible when the background pressure is 10^{-3} Pa, while no lasing in the singlet system is expected when the pressure is 10 Pa. It means that there exists a threshold value for the background pressure at which the lasing condition Eq.(4.24) is satisfied. Helium atoms at the ground state must be evacuated below this threshold value.

We examined the dependence of the maximum of overpopulation densities $\Delta[n/g(p,q)]_m$ on the background pressure P_{He}. One of the results is shown in Fig. 4.10. When the background helium pressure increases, the maximum of reduced overpopula-

tion density decreases, and the population inversion is finally destroyed. The threshold pressure $P_{\mathrm{He,th}}$ for the lasing is defined as the pressure at which the following equation

$$\Delta[n/g(p,q)]_{\mathrm{m}} = \Delta[n/g(p,q)]_{\mathrm{th}} \tag{4.49}$$

is satisfied. The threshold background pressure is tabulated in Table 4.7 for the singlet level pairs between which the lasing is expected.

The obtained pressure is rather difficult for us to generate experimentally, if the recombining plasma is spouted into an ordinary wind tunnel. In our experimental apparatus, the background pressure is about $3 - 20$ Pa when the plasma is generated without the ejector pumps. In the meanwhile, when the ejector pumps were used and the pressure of the expansion area became much lower, the electron temperature was not low enough. (See Fig. 3.4.)

If we would like to obtain the laser oscillation by the recombining helium plasma, the plasma should be expanded very rapidly into a vacuum chamber with a large pumping speed and a low ultimate pressure. We have to remove the helium situated at the ground state in the plasma by rapid expansion. However, we have to keep the electron density optimum. Hence, the magnetic confinement of the plasma jet is effective to the lasing. On the other hand, experimental results show that the cooling of recombining plasmas is effectively accomplished by a gas contact method. Since the optical thickness of the plasma should not be increased by the contact gas, we should cool the plasma with another kind of gas other than the plasma itself.

4.6 Conclusion

Lasing conditions for He I in a cold recombining plasma were numerically discussed including optical thicknesses. A collisional radiative model was used to calculate population densities of excited states of He I levels. Optical escape factors were taken into the calculations for the transitions to the ground state and the metastable states. In an

optically thin helium plasmas, laser oscillations between level pairs 3^1S-2^1P, 3^1D-2^1P, 4^1S-2^1P, 4^1D-2^1P, 4^1F-3^1D, 4^1S-3^1P, 4^1D-3^1P, and 4^3F-3^3D were expected when the electron density n_e was optimum at $T_e = 0.1$eV. The laser lower level depopulated mainly by radiative decay. When the background helium pressure increased, the optical escape factor decreased, and the population inversion became small in the singlet system and finally destroyed. This was because the depopulation of the laser lower levels became less frequent owing to the optical thickness. In optically thick plasmas, the depopulation of the laser lower level in the singlet system was mainly due to the deexcitation by electron collisions. When the plasma becomes optically thick due to the increase of the background pressure, no laser oscillation was expected in the singlet system. On the other hand, the population inversion in the triplet system was hardly affected by the background helium pressure. The calculated population densities including the optical thickness agreed well with our experiments. The requirement for the background helium pressure was examined quantitatively for each level above described.

The results of this chapter have already been published in Ref. [69].

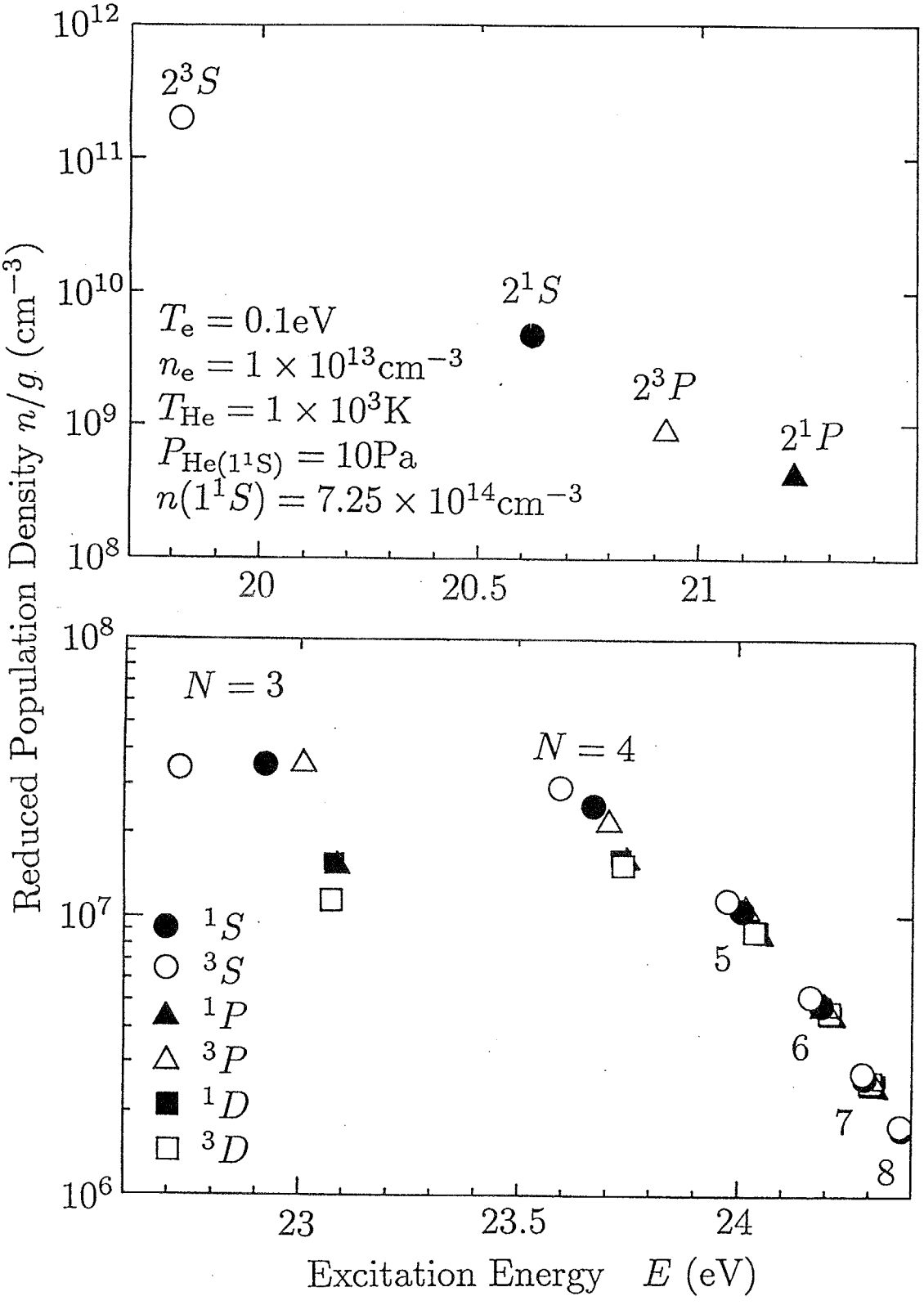

Fig. 4.1. Reduced population densities of He I excited states calculated through Eqs. (4.5) – (4.20) at $T_e = 0.1$ eV, $n_e = 1.0 \times 10^{13}$ cm^{-3}, $T_{He} = 1.0 \times 10^3$ K, $P_{He(1^1S)} = 10$ Pa, and $d = 8$ cm.

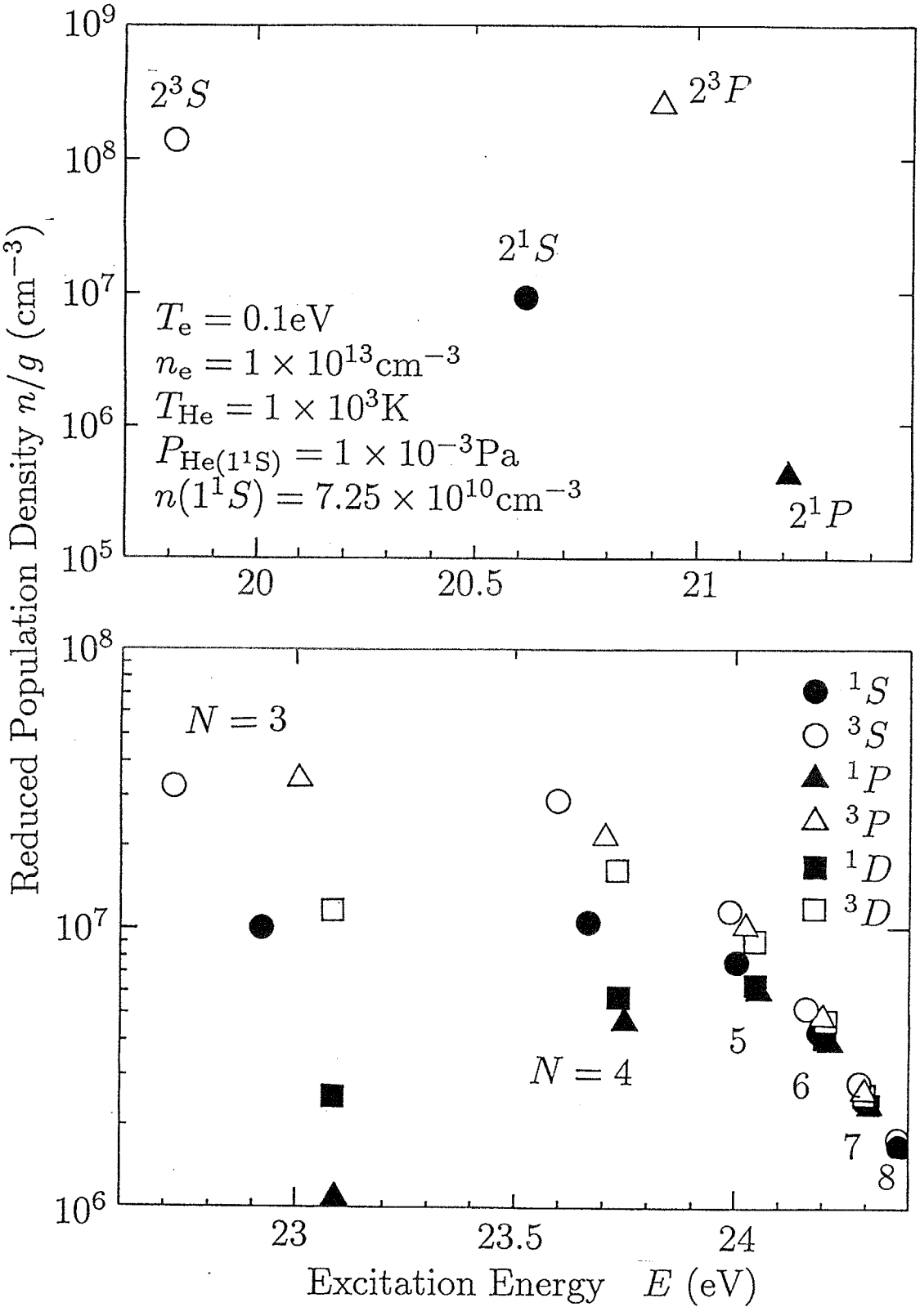

Fig. 4.2. Reduced population densities of He I excited states calculated through Eqs. (4.5) – (4.20) at $T_e = 0.1$ eV, $n_e = 1.0 \times 10^{13}$ cm^{-3}, $T_{He} = 1.0 \times 10^3$ K, $P_{He(1^1S)} = 10^{-3}$ Pa, and $d = 8$ cm.

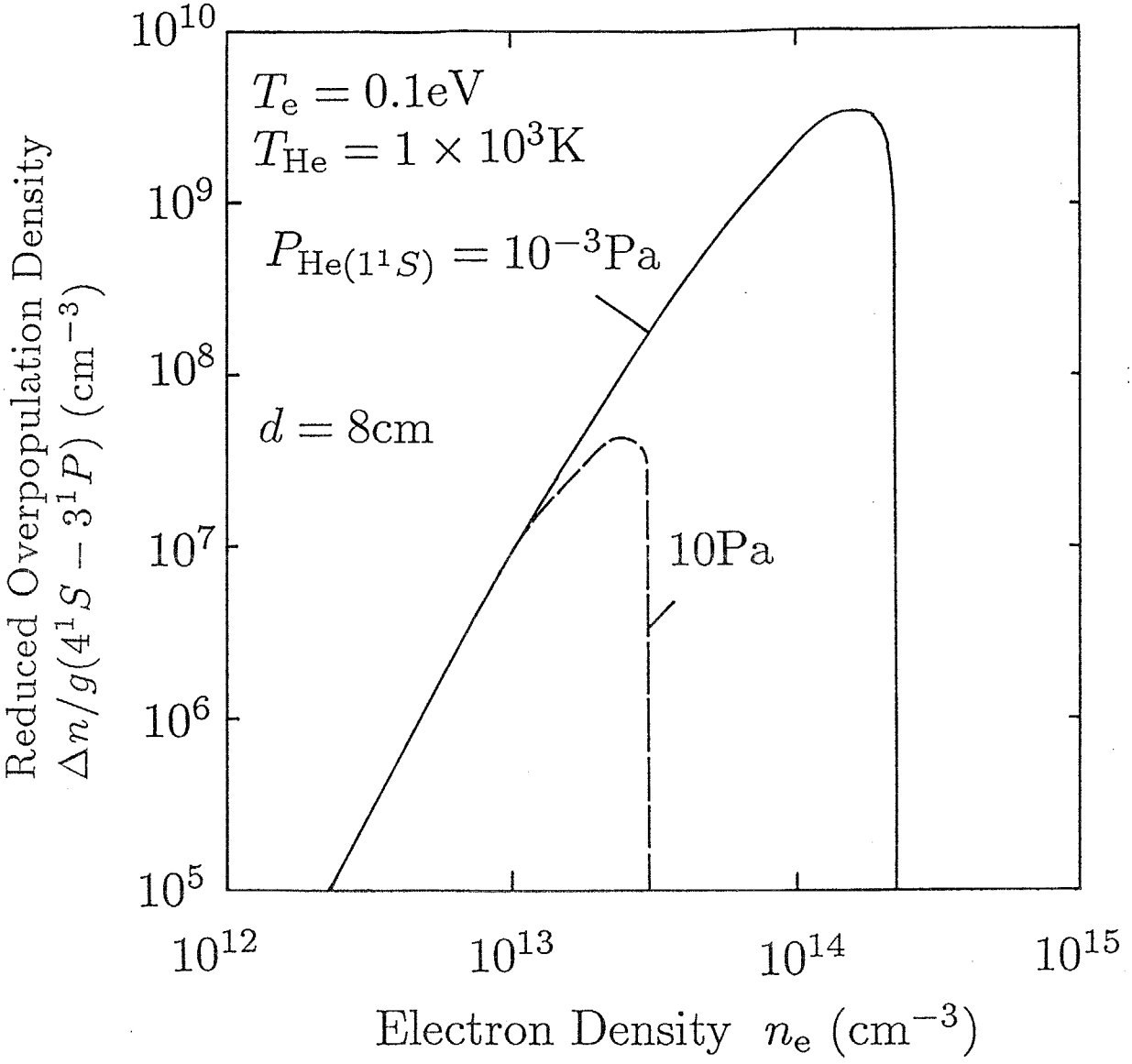

Fig. 4.3. Calculated reduced overpopulation densities between the level pair $4^1S - 3^1P$ at $T_e = 0.1$ eV, $T_{He} = 1.0 \times 10^3$ K, $d = 8$ cm as functions of n_e for $P_{He(1^1S)} = 10^{-3}$ Pa (solid line) and $P_{He(1^1S)} = 10$ Pa (dashed line).

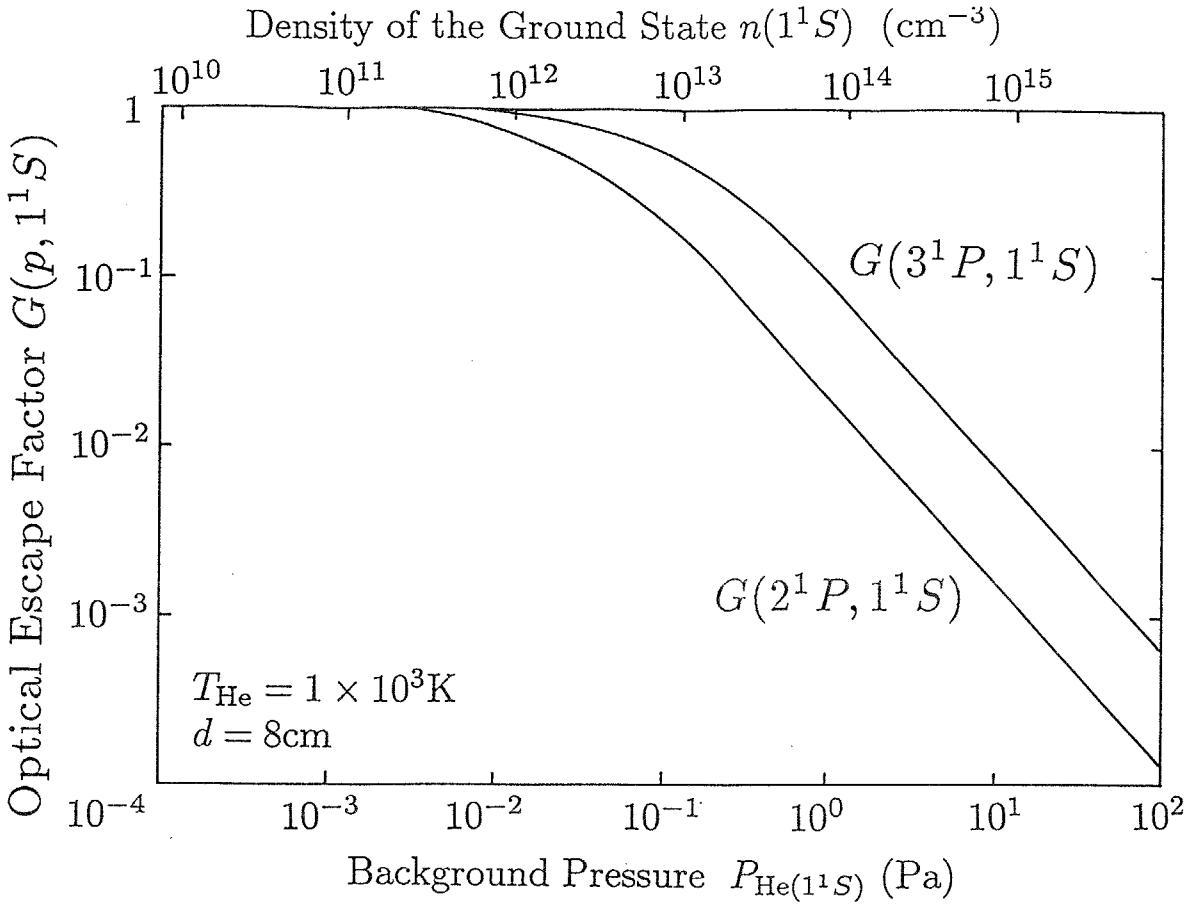

Fig. 4.4. Calculated optical escape factors $G(2^1P, 1^1S)$ and $G(3^1P, 1^1S)$ at $T_{\mathrm{He}} = 1.0 \times 10^3$ K and $d = 8$ cm. In this model, these optical escape factors are independent of n_e and T_e.

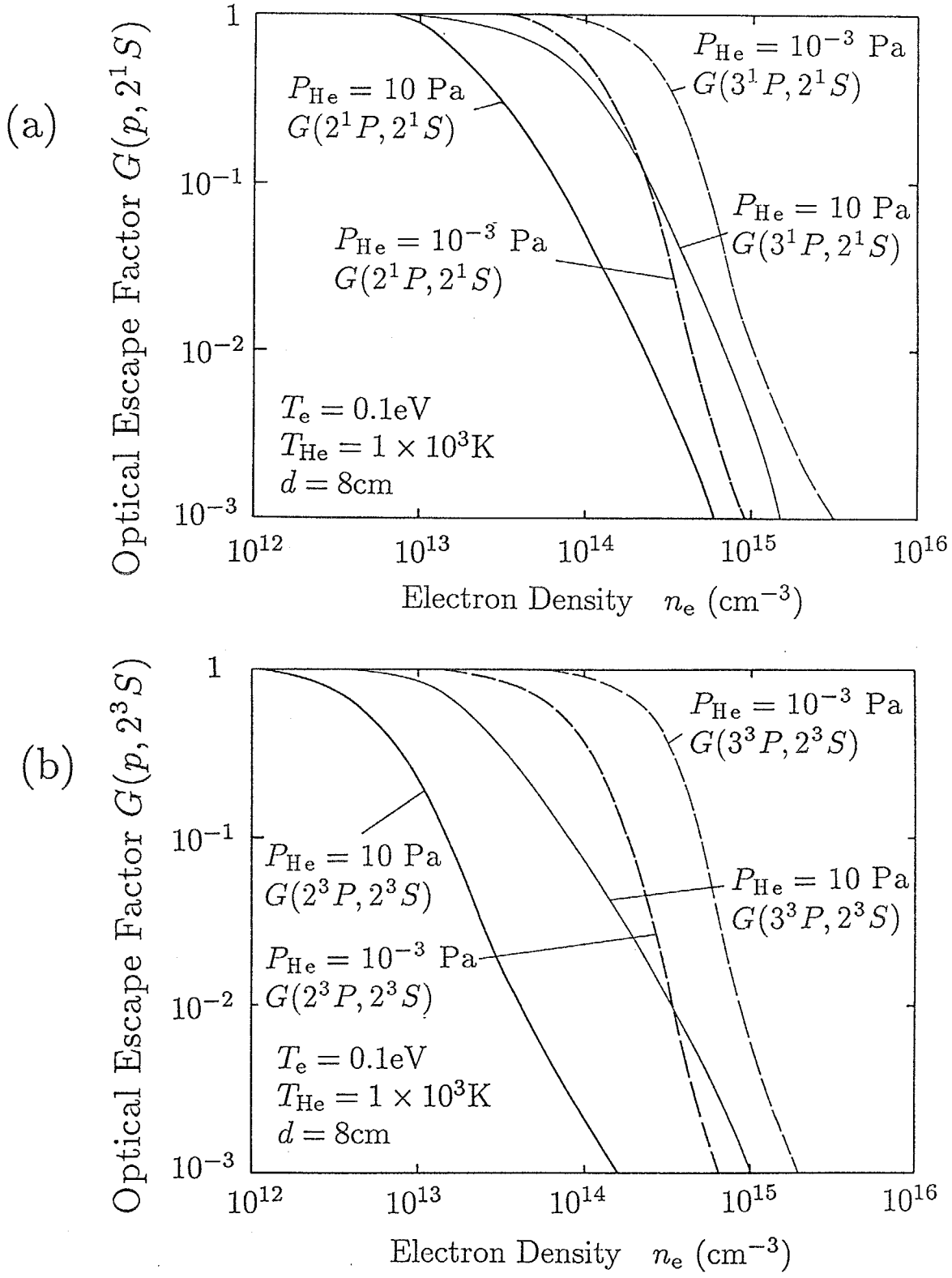

Fig. 4.5. Calculated optical escape factors (a) $G(2^1P, 2^1S), G(3^1P, 2^1S)$ and (b) $G(2^3P, 2^3S), G(3^3P, 2^3S)$ at $T_e = 0.1$ eV, $T_{He} = 1.0 \times 10^3$ K, and $d = 8$ cm, as functions of n_e for $P_{He(1^1S)} = 10$ Pa (solid lines) and $P_{He(1^1S)} = 10^{-3}$ Pa (dashed lines).

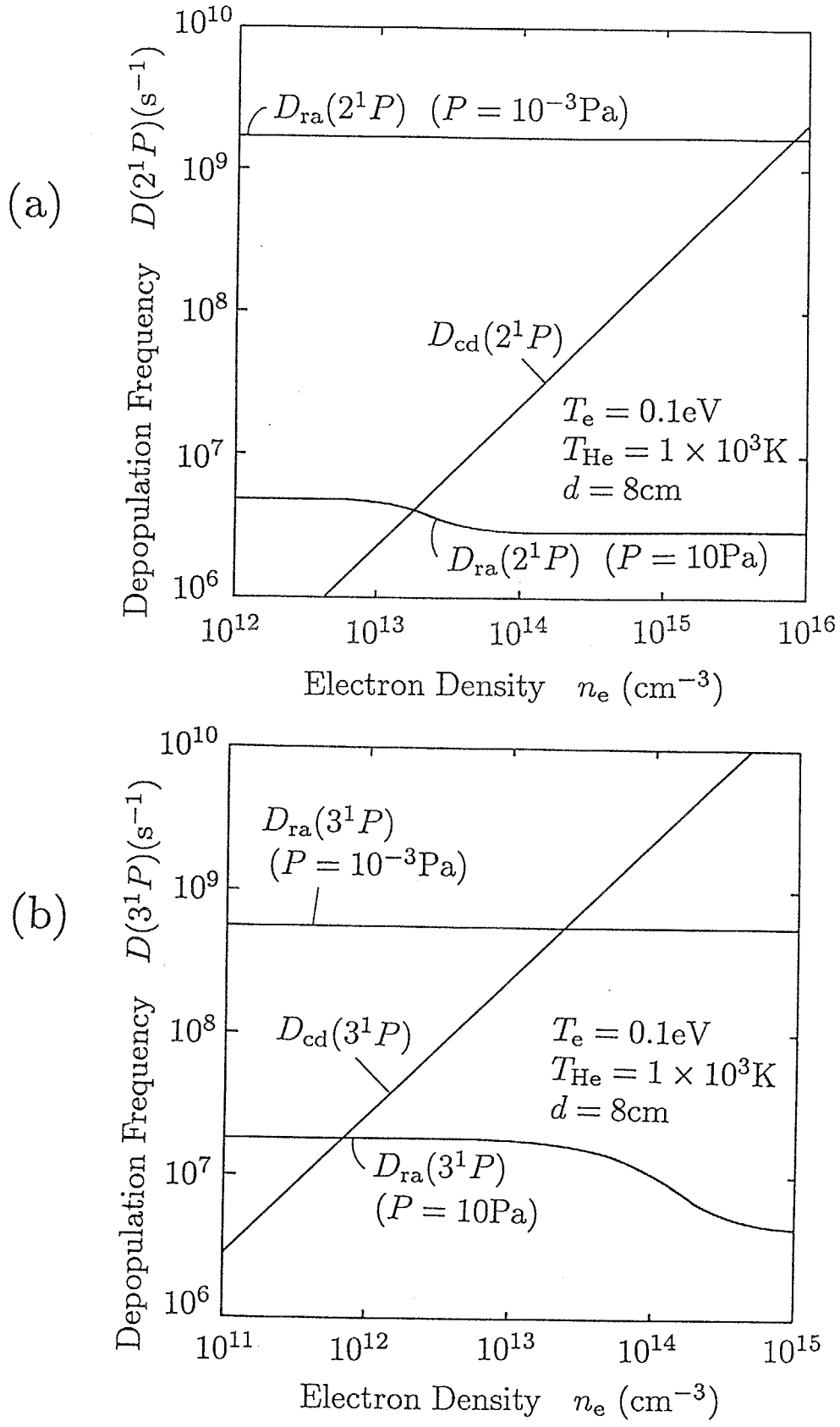

Fig 4.6. Calculated depopulation frequencies of (a) 2^1P level and (b) 3^1P level at $T_e = 0.1$ eV, $T_{He} = 1.0 \times 10^3$ K, and $d = 8$ cm as functions of n_e for $P_{He(1^1S)} = 10$ Pa and $P_{He(1^1S)} = 10^{-3}$ Pa. D_{ce} and D_{io} are too small to be drawn in these figures. D_{cd} is not affected by the background pressure P_{He}.

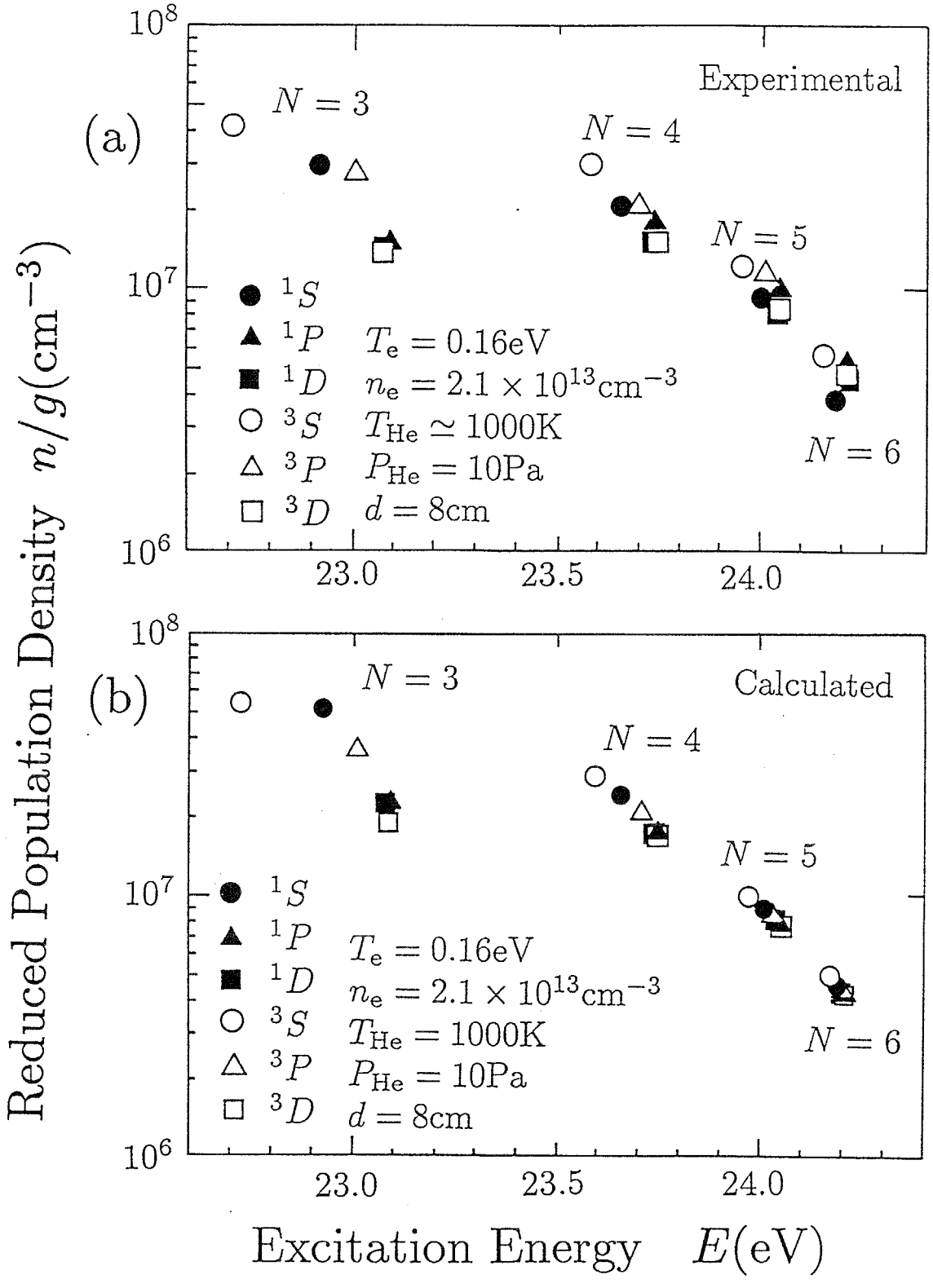

Fig. 4.7. Comparison of the calculated population densities with those observed experimentally at $T_e = 0.16$ eV, $n_e = 2.1 \times 10^{13}$ cm^{-3}, $T_{He} \simeq 1.0 \times 10^3$ K, $P_{He(1^1S)} = 10$ Pa, and $d = 8$ cm. The Abel inversion is applied to the experimental data.

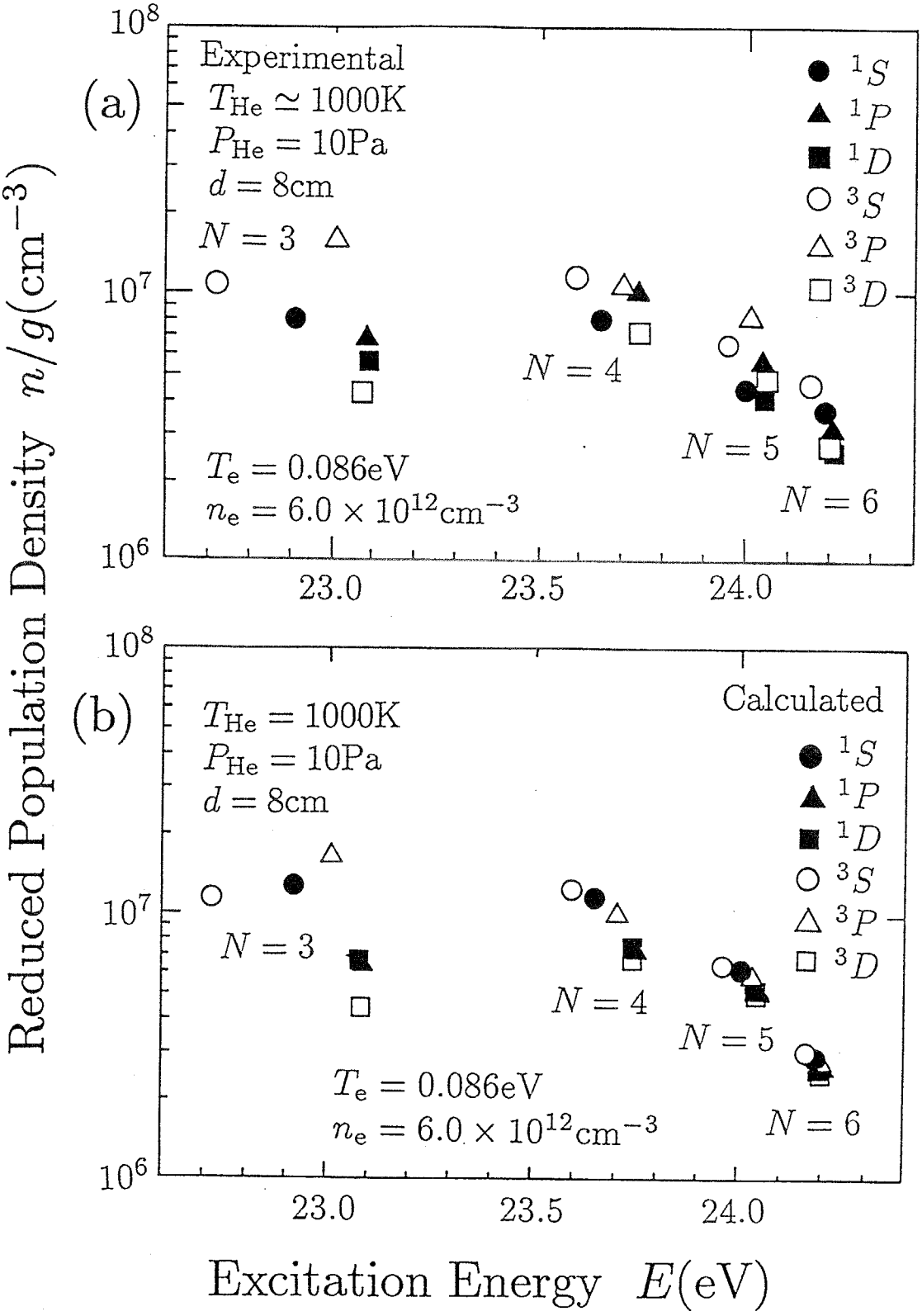

Fig. 4.8. Comparison of the calculated population densities with those observed experimentally at $T_{\mathrm{e}} = 0.086$ eV, $n_{\mathrm{e}} = 6.0 \times 10^{12}$ cm^{-3}, $T_{\mathrm{He}} \simeq 1.0 \times 10^3$ K, $P_{\mathrm{He}(1^1S)} = 10$ Pa, and $d = 8$ cm. The Abel inversion is applied to the experimental data.

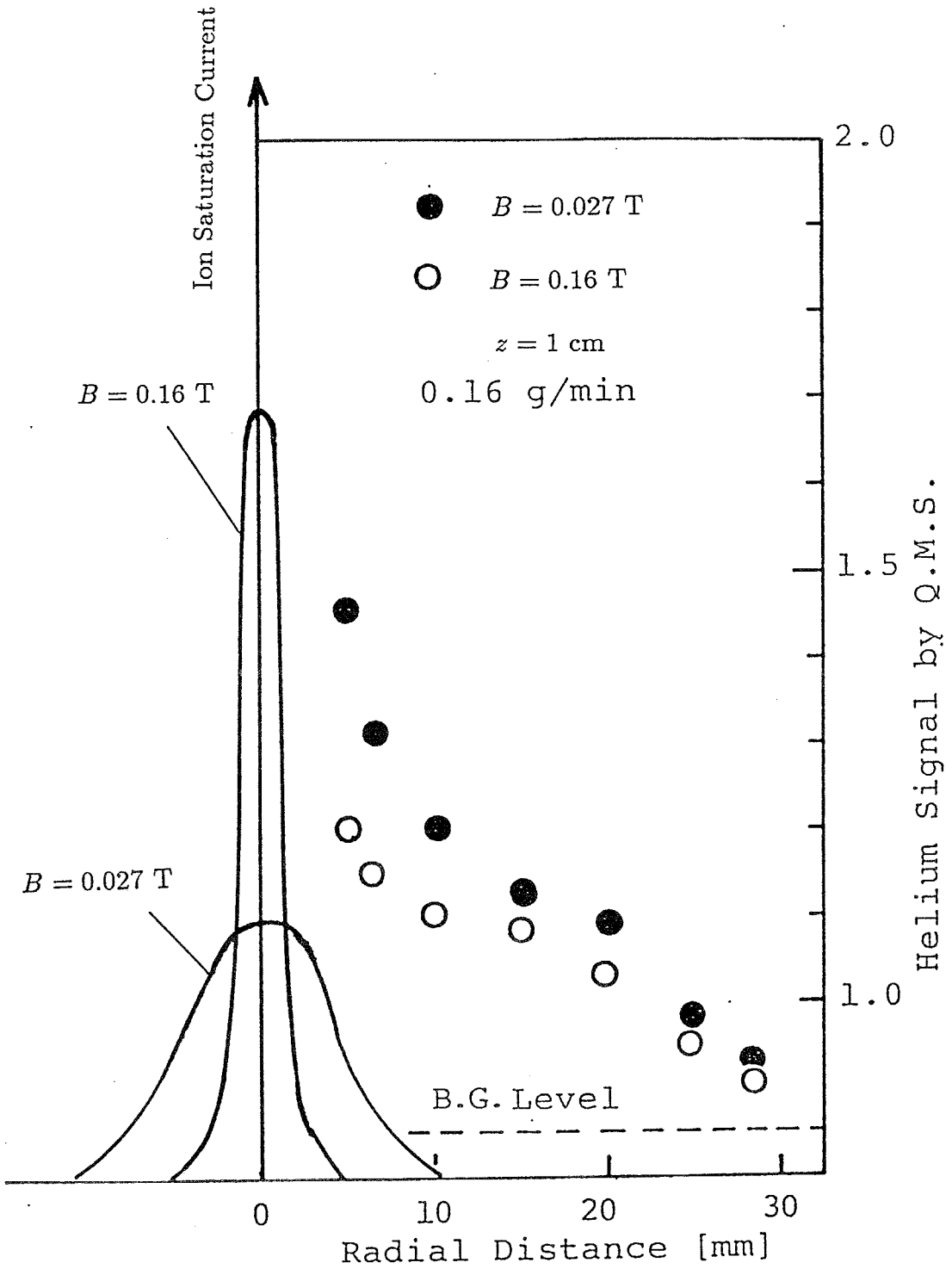

Fig. 4.9. Radial profiles of the helium signals experimentally detected by a quadrupole mass spectrometer with a skimmer, when $B = 0.027$ T and $B = 0.16$ T with $P_{lc} \simeq 7$ Pa (the background pressure), together with profiles of ion saturation current. The axial distance from the nozzle $z = 1$ cm.

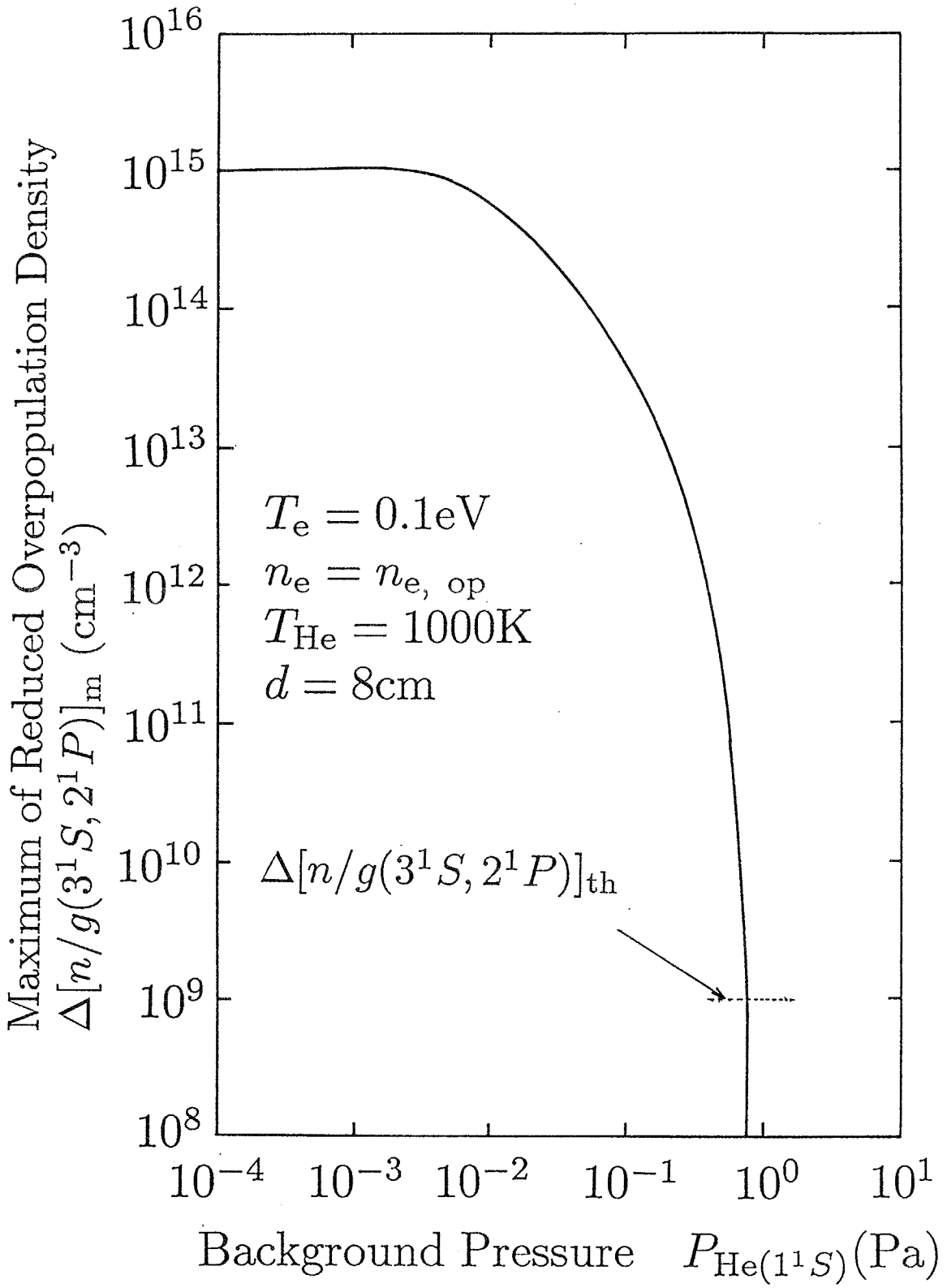

Fig. 4.10. Maximum of the reduced overpopulation density between $3^1S - 2^1P$ levels as a function of the background helium pressure $P_{\mathrm{He}(1^1S)}$, at $T_{\mathrm{He}} = 0.1$ eV, $T_{\mathrm{He}} = 1.0 \times 10^3$ K, $n_{\mathrm{e}} = n_{\mathrm{e,\ op}}$, and $d = 8$ cm. $\Delta[n/g(3^1S, 2^1P)]_{\mathrm{th}}$ is the threshold value for the lasing.

Table 4.1. Included energy levels in the present calculations

State	Energy (eV)	Statistical weight	State	Energy (eV)	Statistical weight
1^1S	00.0000	1	6^3D	24.2087	15
2^3S	19.8191	3	6^1D	24.2087	5
2^1S	20.6152	1	6^1F	24.2089	27
2^3P	20.9636	9	6^3F	24.2090	81
2^1P	21.2175	3	6^1P	24.2105	3
3^3S	22.7179	3	7^3S	24.2841	3
3^1S	22.9198	1	7^1S	24.2978	1
3^3P	23.0066	9	7^3P	24.3038	9
3^3D	23.0730	15	7^3D	24.3090	15
3^1D	23.0735	5	7^1D	24.3091	5
3^1P	23.0865	3	7^1F	24.3092	40
4^3S	23.5934	3	7^3F	24.3092	120
4^1S	23.6731	1	7^1P	24.3102	3
4^3P	23.7074	9	8^1	24.3743	64
4^3D	23.7356	15	8^3	24.3743	192
4^1D	23.7358	5	9^1	24.4189	81
4^3F	23.7365	21	9^3	24.4189	243
4^1F	23.7366	7	10^1	24.4508	100
4^1P	23.7415	3	10^3	24.4509	300
5^3S	23.9715	3	11	24.4752	484
5^1S	24.0107	1	12	24.4932	576
5^3P	24.0277	9	13	24.5071	676
5^3D	24.0422	15	14	24.5182	784
5^1D	24.0423	5	15	24.5272	900
5^1F	24.0425	14	16	24.5345	1024
5^3F	24.0427	42	17	24.5406	1156
5^1P	24.0453	3	18	24.5456	1296
6^3S	24.1685	3	19	24.5499	1444
6^1S	24.1907	1	20	24.5536	1600
6^3P	24.2003	9	continuum	24.5876	–

Table 4.2. The threshold values for the laser oscillation $\Delta[n/g(p,q)]_{\rm th}$ and the maximum values of $\Delta[n/g(p,q)]$ at $n_{\rm e,\ op}$ when $T_{\rm e} = 0.1$ eV, $l = d = 8$ cm, $T_{\rm He} = 1000$ K, $R_1 = 0.99$, $R_2 = 0.998$, and $P_{\rm He(1^1S)} = 10^{-3}$ Pa and 10 Pa. Read 2.0E9 = 2.0×10^9, etc. For other level pairs which are not listed, the population inversion is too small for lasing. For entry "–", the inversion is not obtained for any $n_{\rm e}$.

(1) Singlet system

Level Pair		$P_{\rm He(1^1S)}$	$= 10^{-3}$ Pa	$P_{\rm He(1^1S)}$	$= 10$ Pa
$p-q$ (upper–lower)	$\Delta[n/g(p,q)]_{\rm th}$ ($\rm cm^{-3}$)	$n_{\rm e,\ op}$ ($\rm cm^{-3}$)	$\Delta[n/g(p,q)]_{\rm m}$ ($\rm cm^{-3}$)	$n_{\rm e,\ op}$ ($\rm cm^{-3}$)	$\Delta[n/g(p,q)]_{\rm m}$ ($\rm cm^{-3}$)
3^1S-2^1P	9.8E8	3.2E16	1.0E15		–
3^1D-2^1P	7.3E7	1.9E15	1.6E12		–
4^1S-2^1P	8.1E9	5.1E14	6.1E10		–
4^1D-2^1P	5.6E8	3.5E14	1.9E10		–
5^1S-2^1P	2.5E10	1.5E14	8.9E8		–
5^1D-2^1P	1.8E9	1.0E14	5.5E8		–
6^1S-2^1P	5.4E10	6.0E13	7.4E7		–
6^1D-2^1P	3.9E9	6.0E13	6.4E7		–
5^1P-3^1S	1.8E9	4.0E12	4.0E4	1.5E12	6.4E3
4^1F-3^1D	1.1E7	3.9E13	1.2E8	1.0E13	1.5E6
4^1P-3^1D	1.3E9	7.1E13	1.7E8	8.9E12	1.0E6
5^1P-3^1D	8.6E9	2.5E13	1.3E7	3.3E12	1.1E5
6^1P-3^1D	1.9E10	1.2E13	1.6E6	1.7E12	1.9E4
4^1S-3^1P	1.6E8	1.6E14	3.6E9	2.4E13	4.2E7
5^1S-3^1P	1.4E9	4.1E13	6.1E7	4.3E12	1.6E5
6^1S-3^1P	4.4E9	2.0E13	7.2E6	1.1E12	2.5E3
4^1D-3^1P	2.8E7	9.8E13	6.0E8	1.1E13	1.6E6
5^1D-3^1P	1.9E8	3.5E13	3.8E7	3.0E12	9.1E4
6^1D-3^1P	5.6E8	1.9E13	6.3E6	9.8E11	2.3E3
6^1P-4^1S	7.4E8	2.1E12	2.2E4	8.3E11	4.4E3
4^1F-4^1D	7.5E6	1.9E13	2.1E5	1.0E12	6.1E2
5^1P-4^1D	2.1E8	7.9E12	5.3E5	1.9E12	1.9E4
6^1P-4^1D	1.6E9	4.5E12	1.7E5	1.1E12	7.1E3
5^1D-4^1F	4.0E8	8.3E12	6.9E5	2.0E12	2.4E5
6^1D-4^1F	3.0E9	4.5E12	1.7E5	1.2E12	7.3E3
5^1S-4^1P	4.6E7	1.4E13	3.6E6	2.9E12	8.1E4
6^1S-4^1P	4.5E8	6.1E12	4.6E5	1.2E12	9.2E3
5^1D-4^1P	1.3E7	1.1E13	1.7E6	2.2E12	3.1E4
6^1D-4^1P	8.5E7	6.0E12	4.0E5	1.2E12	8.8E3

(*Contd.*)

Table 4.2. (*Contd.*)

(2) Triplet system

Level Pair		$P_{\mathrm{He}(1^1S)}$	$= 10^{-3}$ Pa	$P_{\mathrm{He}(1^1S)}$	$= 10$ Pa
$p - q$ (upper–lower)	$\Delta n(p,q)_{\mathrm{th}}$ (cm^{-3})	$n_{\mathrm{e,\ op}}$ (cm^{-3})	$\Delta n(p,q)_{\mathrm{m}}$ (cm^{-3})	$n_{\mathrm{e,\ op}}$ (cm^{-3})	$\Delta n(p,q)_{\mathrm{m}}$ (cm^{-3})
$4^3P - 3^3S$	6.4E8	4.0E12	2.6E5	3.9E12	2.5E5
$5^3P - 3^3S$	1.5E9	2.5E12	6.2E4	2.3E12	6.3E4
$6^3P - 3^3S$	6.4E9	1.3E12	1.2E4	1.3E12	1.2E4
$4^3S - 3^3P$	3.8E7		–		–
$4^3P - 3^3D$	1.8E8	2.4E13	3.7E7	2.1E13	3.0E7
$4^3F - 3^3D$	3.6E6	1.5E13	6.1E6	1.3E13	5.3E6
$5^3P - 3^3D$	1.3E9	5.9E12	7.3E5	5.8E12	7.1E5
$6^3P - 3^3D$	1.0E10	2.6E12	6.9E4	2.6E12	6.8E4
$4^3P - 4^3S$	2.6E6	2.3E12	4.9E4	2.3E12	4.9E4
$5^3P - 4^3S$	2.6E8	1.6E12	2.9E4	1.6E12	2.9E4
$6^3P - 4^3S$	6.1E8	1.1E12	1.1E4	1.1E12	1.1E4
$5^3S - 4^3P$	1.1E7		–		–
$4^3F - 4^3D$	1.9E6	2.0E12	1.4E3	2.0E12	1.4E3
$5^3P - 4^3D$	3.0E7	2.9E12	8.8E4	2.9E12	8.7E4
$6^3P - 4^3D$	2.5E8	1.3E12	1.3E4	1.3E12	1.3E4
$5^3D - 4^3F$	1.3E8	2.2E12	3.3E4	2.2E12	3.3E4
$6^3D - 4^3F$	9.9E8	1.2E12	9.4E3	1.2E12	9.4E3

Table 4.3. Values for each component of the population rate and of the depopulation frequency of levels 4^1S and 3^1P when $T_e = 0.1$ eV, $T_{He} = 1000$ K, $d = 8$ cm, and $n_e = 2 \times 10^{13}$ cm^{-3}. Read 1.2E10=1.2×10^{10}, etc.

(a) at $P_{He} = 1.0 \times 10^{-3}$ Pa (The plasma is almost optically thin for any transitions. $G(2^1P, 1^1S) = 0.95$, $G(2^1P, 2^1S) = 0.996$, $G(2^3P, 2^3S) = 0.97$)

The population rate

Level	P_t/g (cm^{-3}s^{-1})	P_{ra}/g (cm^{-3}s^{-1})	P_{cd}/g (cm^{-3}s^{-1})	P_{ce}/g (cm^{-3}s^{-1})	P_{3r}/g (cm^{-3}s^{-1})	P_{rr}/g (cm^{-3}s^{-1})	n/g (cm^{-3})
3^1P	1.2E16	9.8E14	2.7E15	8.7E15	2.5E12	2.1E12	1.2E7
4^1S	9.9E15	5.8E13	9.8E15	3.3E13	7.5E12	9.6E11	7.5E7

The depopulation frequency

Level	D_t (s^{-1})	D_{ra} (s^{-1})	D_{cd} (s^{-1})	D_{ce} (s^{-1})	D_{io} (s^{-1})
3^1P	1.1E9	5.7E8	5.1E8	7.5E4	7.3E−1
4^1S	1.3E8	1.2E7	3.4E7	8.6E7	7.7E2

(b) at $P_{He} = 10$ Pa (The plasma is optically thick. $G(2^1P, 1^1S) = 1.6 \times 10^{-3}$, $G(3^1P, 1^1S) = 7.6 \times 10^{-3}$, $G(2^1P, 2^1S) = 4.7 \times 10^{-1}$, $G(2^3P, 2^3S) = 6.5 \times 10^{-2}$)

The population rate

Level	P_t/g (cm^{-3}s^{-1})	P_{ra}/g (cm^{-3}s^{-1})	P_{cd}/g (cm^{-3}s^{-1})	P_{ce}/g (cm^{-3}s^{-1})	P_{3r}/g (cm^{-3}s^{-1})	P_{rr}/g (cm^{-3}s^{-1})	n/g (cm^{-3})
3^1P	6.1E16	1.9E15	5.5E15	5.4E16	2.5E12	2.1E12	1.2E8
4^1S	2.0E16	7.7E13	2.0E16	4.2E13	7.5E12	9.6E11	1.5E8

The depopulation frequency

Level	D_t (s^{-1})	D_{ra} (s^{-1})	D_{cd} (s^{-1})	D_{ce} (s^{-1})	D_{io} (s^{-1})
3^1P	5.2E8	1.6E7	5.1E8	7.5E4	7.3E−1
4^1S	1.3E8	1.2E7	3.4E7	8.6E7	7.7E2

Table 4.4. Values for each component of the population rate and of the depopulation frequency of levels 3^1S and 2^1P when $T_e = 0.1$ eV, $T_{He} = 1000$ K, $d = 8$ cm, and $n_e = 1.0 \times 10^{15}$ cm^{-3}. Read 1.2E10=1.2×10^{10}, etc.

(a) at $P_{He} = 1.0 \times 10^{-3}$ Pa (The plasma is optically thin for the transitions to the ground state, while optically thick for those to the metastable states. $G(2^1P, 1^1S) = 0.95$, $G(2^1P, 2^1S) = 9.5 \times 10^{-4}$, $G(2^3P, 2^3S) = 2.8 \times 10^{-4}$)

The population rate

Level	P_t/g (cm^{-3}s^{-1})	P_{ra}/g (cm^{-3}s^{-1})	P_{cd}/g (cm^{-3}s^{-1})	P_{ce}/g (cm^{-3}s^{-1})	P_{3r}/g (cm^{-3}s^{-1})	P_{rr}/g (cm^{-3}s^{-1})	n/g (cm^{-3})
2^1P	1.8E21	2.5E20	1.5E21	1.3E20	5.6E16	4.3E16	9.4E11
3^1S	4.9E21	3.6E18	4.9E21	9.0E18	2.5E17	6.2E15	6.0E12

The depopulation frequency

Level	D_t (s^{-1})	D_{ra} (s^{-1})	D_{cd} (s^{-1})	D_{ce} (s^{-1})	D_{io} (s^{-1})
2^1P	2.0E9	1.7E9	2.3E8	7.2E0	4.9E−8
3^1S	8.2E8	1.8E7	3.3E8	4.7E8	5.5E0

(b) at $P_{He} = 10$ Pa (The plasma is optically thick. There is no population inversion in the level pair $3^1S - 2^1P$. $G(2^1P, 1^1S) = 1.6 \times 10^{-3}$, $G(2^1P, 2^1S) = 3.1 \times 10^{-4}$, $G(2^3P, 2^3S) = 4.4 \times 10^{-5}$)

The population rate

Level	P_t/g (cm^{-3}s^{-1})	P_{ra}/g (cm^{-3}s^{-1})	P_{cd}/g (cm^{-3}s^{-1})	P_{ce}/g (cm^{-3}s^{-1})	P_{3r}/g (cm^{-3}s^{-1})	P_{rr}/g (cm^{-3}s^{-1})	n/g (cm^{-3})
2^1P	2.7E21	3.7E20	2.1E21	1.8E20	5.6E16	4.3E16	1.2E13
3^1S	7.2E21	4.4E18	7.2E21	9.0E18	2.5E17	6.2E15	8.8E12

The depopulation frequency

Level	D_t (s^{-1})	D_{ra} (s^{-1})	D_{cd} (s^{-1})	D_{ce} (s^{-1})	D_{io} (s^{-1})
2^1P	2.4E8	2.9E6	2.3E8	7.2E0	4.9E−8
3^1S	8.2E8	1.8E7	3.3E8	4.7E8	5.5E0

Table 4.5. Values for each component of the population rate and of the depopulation frequency of levels 4^3P and 3^3D when $T_e = 0.1$ eV, $T_{He} = 1000$ K, $d = 8$ cm, $P_{He} = 1.0 \times 10^{-3}$ Pa, and $n_e = 2.0 \times 10^{13}$ cm^{-3}. Read 1.2E10=1.2×10^{10}, etc. (The plasma is almost optically thin.)

The population rate

Level	P_t/g (cm^{-3}s^{-1})	P_{ra}/g (cm^{-3}s^{-1})	P_{cd}/g (cm^{-3}s^{-1})	P_{ce}/g (cm^{-3}s^{-1})	P_{3r}/g (cm^{-3}s^{-1})	P_{rr}/g (cm^{-3}s^{-1})	n/g (cm^{-3})
3^3D	1.2E16	2.2E15	3.5E15	6.0E15	2.5E12	2.1E12	9.2E7
4^3P	4.0E16	2.1E14	3.8E16	1.9E15	8.2E12	9.0E11	1.3E8

The depopulation frequency

Level	D_t (s^{-1})	D_{ra} (s^{-1})	D_{cd} (s^{-1})	D_{ce} (s^{-1})	D_{io} (s^{-1})
3^3D	1.3E8	7.2E7	5.5E7	8.8E4	6.3E−1
4^3P	3.2E8	7.3E6	4.8E7	2.7E8	1.2E3

Table 4.6. Values for each component of the population rate and of the depopulation frequency of levels 2^1S and 2^3S when $T_e = 0.16$ eV, $T_{He} = 1000$ K, $d = 8$ cm, $P_{He} = 10$ Pa, and $n_e = 2.1 \times 10^{13}$ cm^{-3}. The conditions are the same as in Fig. 4.7. Read 1.2E10=1.2×10^{10}, etc.

The population rate

Level	P_t/g ($cm^{-3}s^{-1}$)	P_{ra}/g ($cm^{-3}s^{-1}$)	P_{cd}/g ($cm^{-3}s^{-1}$)	P_{ce}/g ($cm^{-3}s^{-1}$)	P_{3r}/g ($cm^{-3}s^{-1}$)	P_{rr}/g ($cm^{-3}s^{-1}$)	n/g (cm^{-3})
2^1S	1.2E16	2.8E15	5.7E15	3.1E 15	2.4E11	1.4E13	3.0E9
2^3S	1.8E16	8.6E15	9.2E15	3.8E-35	7.1E11	7.3E12	1.5E11

The depopulation frequency

Level	D_t (s^{-1})	D_{ra} (s^{-1})	D_{cd} (s^{-1})	D_{ce} (s^{-1})	D_{io} (s^{-1})	D_{dif} (s^{-1})	D_{col} (s^{-1})	D_{met} (s^{-1})
2^1S	3.8E6	5.0E 2	3.2E6	6.1E5	7.0E-6	1.8E4	1.7E 0	3.9E3
2^3S	1.2E5	2.4E-2	8.6E4	1.3E4	1.4E-7	1.9E4	2.1E-5	3.9E3

Table 4.7. The required background pressure for the lasing between each level pair whose overpopulation density exceeds the threshold value tabulated in Table 4.2, when $T_e = 0.1$ eV, $l = d = 8$ cm, $T_{He} = 1000$ K, $R_1 = 0.99$, $R_2 = 0.998$, and $n_e = n_{e,\ op}$. Read 2.0E9 = 2.0×10^9, etc. For other level pairs which are not listed, the population inversion is too small for lasing.

Level Pair $p - q$	$\Delta n(p,q)_{th}$ (cm^{-3})	$P_{He,th}$ (Pa)	$n_{e,\ op}$ (cm^{-3})
$3^1S - 2^1P$	9.8E8	7.2E−1	9.0E13
$3^1D - 2^1P$	7.3E7	1.7E−1	9.0E13
$4^1S - 2^1P$	8.1E9	5.1E−2	1.9E14
$4^1D - 2^1P$	5.6E8	9.2E−2	8.8E13
$4^1F - 3^1D$	1.1E7	5.2E−1	2.1E13
$4^1S - 3^1P$	1.6E8	7.8E−1	4.1E13
$4^1D - 3^1P$	2.8E7	4.8E−1	2.7E13

Chapter 5. Experimental and Numerical Study on an Arc-heated Magnetically Trapped Expanding Hydrogen Plasma

5.1 Introduction

As was already shown so far, it was found that our plasma generator produced a recombining helium plasma like an afterglow with a low electron temperature continuously [59]. Spectroscopic observations showed that the inverted populations between several level pairs in He I, such as $4^1S - 3^1P$ and $4^3P - 3^3D$, were created stationarily. There were two important parameters for making inverted populations in the plasma generator. One was the magnetic field, and the other was the pressure in the plasma expanding region. It was shown that the magnetic confinement of the cold plasma was efficient to keep the electron density optimum and to create larger inversions. On the other hand, the degree of the population inversion became large when the pressure in the expanding region was about $3 - 20$ Pa. When the pressure was made much lower, the observed inversion became smaller. Therefore it was concluded that the cooling of electrons was accomplished mainly by the collisions with the residual gases in the wind tunnel, not by the adiabatic expansion [68]. However, we are sorry to say that the observed inversion was still insufficient for us to oscillate a cw recombining laser, because the electron density was small and the existence of the residual helium atoms in the wind tunnel made the plasma optically thick for the transitions to the ground state [69].

Although we examined only the helium plasma in the preceding chapters, the plasma generator can produce recombining plasmas of various species, provided that the ordinary arc discharge is accomplished stably and continuously, which will result in another interesting potential for the cw lasing. And we consider that the first and best alternative is the hydrogen plasma. The oscillator strengths of hydrogen atoms were calculated accurately [95]. The numerical analysis of the population density of each level is also available in the hydrogen plasma [122]. Another experimental merit of the hydrogen plasma is that

the hydrogen atoms in the residual gas will make diatomic molecules. It means that the optical thickness of the hydrogen plasma, an obstacle to make the inversion, is expected to be smaller than that of the helium plasma.

The temperature of the plasma in the arc region in our apparatus was about $1-2$ eV, and lower than that in TPD-I [17,18,63]. Therefore the hydrogen plasma was generated not by the contact of hydrogen gas with the helium plasma jet in the downstream, but by mixing the hydrogen gas into the discharging helium gas. Namely, the helium gas took a role as a buffer gas in the discharging region. The pure hydrogen plasma was difficult for us to generate stably. The stationary population inversion of H I had been observed as a minor impurity in the discharge of some kinds of rare gas [15,31]. However, the magnetic field was seldom applied there. In addition, the expansion ratio of the plasma and the pumping speed in the plasma expanding chamber are very large in our apparatus.

As for a pure hydrogen recombining plasma, Hara et al developed a quasi-cw laser by a recombining hydrogen plasma, whose pulse length was about several hundred micro second [24,25]. But in their experiment, the rapid cooling of electrons was accomplished mainly by an adiabatic expansion, and the duration of the laser oscillation was limited by the capacity of the electric power supplier. In addition, they did not use the magnetic field. It is considered that the magnetic confinement of the recombining hydrogen plasma as well as a helium plasma is efficient for the lasing.

In the present experiments, the hydrogen helium mixed plasma is cooled rapidly into a state of nonequilibrium by collisions with residual hydrogen and helium molecules. Therefore, it has an aspect of a fundamental study on the atomic processes in a boundary plasma such as a divertor plasma of a nuclear fusion reactor. From the viewpoint of a nuclear engineering, the cooling phenomena are also interesting [54,58].

In this chapter, we describe the results of the spectroscopic observations of the hydrogen helium mixed plasma generated by the arc-heated magnetically trapped expanding plasma jet generator. The population densities of H I in the plasma are examined and the variations of them are also investigated when the plasma comes downstream. Then, the

potential for cw lasing by the plasma is discussed. The experimental results are compared with the calculation based on the collisional radiative model, and the characteristics of the plasma are discussed in terms of atomic processes.

5.2 Experimental Results

When the hydrogen was mixed with the discharging helium gas, the strong magnetic field was required to stabilize the discharge. The applied magnetic field B was set at 0.162 T, which was the maximum field strength in the apparatus. Typical experimental conditions were the following: arc voltage 20–25 V (a little higher than for the pure helium plasma), arc current 120 A, pressure in the discharging region $P_{\rm dc} = 1.0 \times 10^4 - 1.0 \times 10^5$ Pa, magnetic field $B = 0.162$ T, gas flow rate $1.0 \times 10^{-6} - 4.0 \times 10^{-6}$ kg/s, the feeding ratio of the hydrogen molecule to the helium about $20 - 25$ %. During generating the plasma jet, the pressure in the wind tunnel $P_{\rm lc}$ was $3 - 20$ Pa.

The population densities of the excited hydrogen atoms with the principal quantum number $N \geq 3$ are obtained from the intensity integrated over the spectral peaks. The intensity of the Balmer lines was strong enough to neglect the background lines except for the transition $8 \rightarrow 2$, where the line of the transition $3^3P \rightarrow 2^3S$ of He I coincided with substantial intensity. It was difficult for us to measure the line intensity of the excited hydrogen atoms of $N = 8$. As mentioned later, the electron density of the plasma $n_{\rm e}$ is estimated at $\sim 10^{13}$ cm^{-3}, and the plasma is considered to be optically thin at least for the transitions to the level of $N = 2$. The temperature of the arc is considered as $\sim$ 1eV and the existence of He^{2+} ions can be neglected. The line from the excited helium ion at 468.57 nm was not detected. Therefore H_α line was observed precisely without the mixing of 656.0 nm line of He II.

An example of the spectrum near the Balmer series limit is shown in Fig. 5.1. The lines from the large principal quantum number, particularly from $N \geq 13$, tend to merge with their neighboring lines and a continuumlike spectrum is obtained. Lines from the

excited states of $N \geq 16$ cannot be separated if we intend to measure accurately without increasing the photon counting error, and what is worse, the line of $7^3D \rightarrow 2^3P$ transition in He I coincides at the wavelength from the excited hydrogen of $N = 16$. For the simple analysis of the experimental data, the population densities of the excited hydrogen atoms of $N \leq 12$ were determined experimentally. Figure 5.1 shows a strong continuum spectrum of free-bound transitions, and it means that the plasma is in a recombining phase, neither in an ionizing phase nor in an equilibrium phase [13,123].

The reduced population densities n/g measured at some different positions are shown in Fig. 5.2(a)-(d). Like chapter 3, the reduced population densities given there are averaged value $\overline{n/g}$ along the line of sight from the condensing mirror directed to the plasma axis perpendicularly, which is more essential in a laser operation, and the Abel inversion is not applied to. The axial distance from the nozzle is (a)1 cm, (b)8 cm, (c)15 cm, and (d)22 cm. They correspond to the gap position of the coreless coils. Experimental errors are almost the same with the size of keys representing the reduced population densities in Fig. 5.2. The reproducibility of the experimental results lies within $\sim \pm 3$ %. We add there the electron temperature T_e, electron density n_e, both of which were determined from the spectroscopic measurements, and will be discussed later. The reduced population densities which are calculated as functions of the electron temperature and density, based on a collisional radiative model of hydrogen, are also added there. They will be also discussed in the latter part of this chapter. One of the examples of the examined population densities of He I in the generated plasma is shown in Fig. 5.3, which was measured under the same conditions as in Fig. 5.2(b). Later we will show that the ion density of helium is about 1/100 times that of hydrogen from Fig. 5.2(b) and Fig. 5.3.

To estimate the mean velocity of the plasma jet v_{jet}, the Doppler shift of the H_α line (656.280 nm) was measured [51]. A plane mirror was set downstream where the head-on view of the plasma was observed, and the reflected light was examined in the same way as the side-on view. The obtained spectral lines of H_α are shown in Fig. 5.4, where (a)

is a side-on view and (b) is a head-on view. In the experiment, the slits were closed to 4 μm to improve the spectral resolution. And it tells us that the blue shift of the line, about ~ 0.02 nm, was resolved. For the Doppler shift $\Delta\lambda$, we have

$$|\Delta\lambda|/\lambda = v_{\rm jet}/c, \tag{5.1}$$

where c is the speed of light. Therefore the mean velocity of the flow where the recombination radiation is dominant is evaluated at $\sim 9 \times 10^3 - 1 \times 10^4$ m/s [62].

Now we should confirm the linewidth of H_α like section 4.3. For the Gaussian profile, the Doppler profile is essential. The Doppler broadening is calculated by Eq. (4.20), provided that the gas temperature and the mass are rewritten into those of a hydrogen atom. If we assume that $T_{\rm H} = 700$ K (the reason of the assumption will be described later), the Doppler broadening is $\Delta\lambda_{\rm D}/\lambda \simeq 1.1 \times 10^{-5}$. On the other hand, for the Lorentzian profile, the Stark broadening is considered to be the most essential, since the natural broadening and the resonance broadening are much smaller [117]. In order to treat the Stark broadening, two approximations have been developed. One is a quasi-static approximation, in which the motion of the atoms or ions is neglected. The other is an impact approximation, in which the emitting system is unperturbed most of the time and the broadening is described in terms of impacts which are well separated in time [6]. Now, we treat the hydrogen plasma, and it was shown that the effect of ions on the broadening was essential for the hydrogen-like ions or hydrogen atom, owing to the degeneracy of the energy levels with regard to the azimuthal quantum numbers. In this approximation, the effect corresponds to the linear Stark effect, and this leads to no Stark shift. According to the quasi-static approximation, the Stark broadening for a hydrogen atom is given as follows [5]:

$$\Delta\lambda_{\rm S}/\lambda = \frac{12h}{(2\pi)^2 mc}\lambda(N^2_{\rm upper} - N^2_{\rm lower})n_{\rm i}^{2/3}, \tag{5.2}$$

then, if we assume $n_{\rm e} = n_{\rm i} = 10^{13}$ cm^{-3}, the Stark width of the H_α line becomes

$\Delta\lambda_S/\lambda \simeq 1.1 \times 10^{-5}$. This broadening is comparable to the Doppler width, therefore, the H_α line should have a typical Voigt profile, although we could not detect the profile with our apparatus.

In the present experiment, the observed profiles of the H_α line were almost the same as was shown in Fig. 5.4. It is considered that the instrumental width of the monochromator was about 0.06 nm. The linewidth of a He-Ne laser of 633 nm was also about 0.06 nm. Therefore it was very difficult for us to measure the Voigt profile of H_α line. And unfortunately, when the slit was closed to less than 10 μm, the photon counting error became very large, and the precise measurement could not be performed. However, the reproducibility of the Doppler blue shift shown in Fig. 5.4 was sufficient, and we can conclude the mean velocity of the jet was about 10^4 m/s. It was difficult to measure the step-like profile due to a dissociative recombination measured by Frommhold and Biondi [124]. It is considered that the dissociative recombination is more rapid than the electron three-body recombination. And most of the molecular ions are considered to be lost downstream through the dissociative recombination.

5.3 Discussion

5.3.1 Observed population inversion and potential for laser oscillation

Figure 5.2 shows that the generated plasma was in a recombining phase. First, the high lying levels of $N \geq 9$ tend to stay in LTE. The Boltzmann plot there is on a straight line, and the population densities of these high lying levels are described by the Saha-Boltzmann equation,

$$n(N) = n_e n_i(H^+)\ Z(N), \tag{5.3}$$

like the helium plasma in chapter 3. Again, $Z(N)$ is the Saha-Boltzmann coefficient given by Eq. (3.3) [101].

Second, for the lower lying levels, Eq.(5.2) gives too large population densities, which is the characteristic of the cold recombining plasma. And when the electron temperature T_e becomes low with an appropriate electron density n_e, the population inversion is obtained [13]. In the most upstream of the plasma jet, however, the population inversion was not obtained (Fig. 5.2(a)). One of the reasons is that the electron temperature was not low enough there. Other reasons will be discussed later. Since the plasma is generated by an ordinary arc discharge under an atmospheric pressure, it is considered that the plasma was in an equilibrium phase when it was generated, that is, at $z = 0$. As the plasma comes downstream, the population inversion appears gradually. The population inversion is observed between the level pair $4-3$ at the position of the axial distance from the nozzle $z = 8$ cm (Fig. 5.2(b)), between $4-3$, $5-3$ at $z = 15$ cm (Fig. 5.2(c)), and between $4-3$, $5-3$, $6-3$, $7-3$, $5-4$ at $z = 22$ cm (Fig. 5.2(d)). The variation of the population densities of these low lying levels with the axial distance from the nozzle is shown in Fig. 5.5. It shows that the state of the plasma becomes far from the thermal equilibrium as it comes downstream.

Like the helium plasma, another interpretation of Fig. 5.5 is that the figure shows the time history of the recombining plasma like an afterglow plasma. The plasma moves with the mean velocity $v_{\rm jet} \simeq 10^4$ m/s as described in the previous section. If the plasma is assumed to move uniformly with the velocity, it takes 10 μsec to move 10 cm. If the time origin ($t = 0$) is set when the plasma passed through the nozzle, Fig. 5.2 shows the population densities of $t \simeq 1$ μsec in (a), $t \simeq 8$ μsec in (b), $t \simeq 15$ μsec in (c), and $t \simeq 22$ μsec in (d). The initial temperature of the plasma is considered to be ~ 1 eV from the probe analysis. It means that the gas contact cooling is accomplished with the time scale of several micro second, which agrees with the simulation of gas contact cooling by Furukane, Sato, and Oda [103, 104].

As was described in chapter 2, when it is applied to the lasing medium, the important parameter is the reduced overpopulation density $\Delta[n/g(N_{\rm upper\ level}, N_{\rm lower\ level})]$ shown in Eq. (3.4). The variations of the reduced overpopulation densities $\Delta(n/g)$ of the level

pairs $4-3$, $5-3$, and $5-4$ are shown in Fig. 5.6. In the present experiments, the maximum of the reduced overpopulation density is $\sim 3\times10^7$ cm^{-3} for the level pair $4-3$, $\sim 2\times10^7$ cm^{-3} for $5-3$, and 7×10^6 cm^{-3} for $5-4$.

On the other hand, the threshold reduced overpopulation density for the laser oscillation $\Delta(n/g)_{\rm th}$ is calculated by Eq. (3.5) with a slight modification, since the atom is now a hydrogen atom. Namely,

$$\Delta[n/g(p,q))]_{\rm th} = \frac{8\pi^{3/2}}{g(p)A(p,q)\lambda(p,q)^3}\left(\frac{2kT_{\rm H}}{m_{\rm H}}\right)^{1/2}\left(-\frac{\ln\sqrt{R_1R_2}}{l}\right), \qquad (5.4)$$

where $m_{\rm H}$ is the mass and $T_{\rm H}$ is the temperature of the hydrogen atom (in K) [26-28]. We supposed the following values for the calculation, $T_{\rm H}=700$ K (temperature of surrounding residual atom), $R_1=0.99$, $R_2=0.998$, and $l=5$ cm (the observed bright area), which is smaller than for the helium plasma. The threshold overpopulation densities calculated for the level pairs $4-3$ and $5-4$ are added in Fig. 5.6. It shows that the experimentally observed overpopulation densities of these level pairs were larger than the threshold values, whereas the observed values for any other level pairs, such as $5-3$, did not surpass the threshold [62]. If an appropriate resonator mirrors are added to the apparatus, the laser oscillation of these lines is expected, which was not expected in a pure helium plasma.

The obtained overpopulation densities of H I in our apparatus are larger than those reported in Refs.[15] and [31], where the magnetic confinement was not applied. It is concluded that the magnetic field is effective to enlarge the inversion. The electric power required for the discharge is about 3 kW in our apparatus, which is lower than those experiments. In the experiments of TPD-I, the hydrogen gas was not fed to the discharging region but to the plasma jet region [65]. Although the inversion between the level pair $4-3$ was larger in TPD-I than that in our apparatus, the efficiency to produce the hydrogen plasma in TPD-I was low because it was generated by contact with the helium plasma and the power about 13 kW was required. The advantages of our apparatus are summarized as follows: (1) It contains magnets to keep the electron density appropriate.

(2) The expanding ratio of the jet is very large. The pressure of the discharging area is about 10^5 Pa and that of the expanding area is about $\sim$ 7 Pa. Therefore the neutral particles are expanded and cooled very rapidly. (3) The velocity of the jet is very large and considered to be supersonic due to the small diameter of the nozzle, which is considered to be choked with the viscous arc plasma. These are important to develop cw plasma jet lasers.

5.3.2 Macroscopic characteristics of the plasma

For the recombining plasma, the population densities of the sufficient high lying levels are described by Saha-Boltzmann equation, namely, Eq. (5.3) [13]. The electron temperature is determined from the gradient of the high lying levels in Fig. 5.2 like the helium plasma. We used those with $N \geq 10$, and the reason will be discussed later. Then, since the detection system had been calibrated for absolutely, we determined the electron density from Fig. 5.2, provided that almost all the ions in the plasma are atomic hydrogen ions. Later it will be shown that the existence of the helium ions can be neglected.

In the present discussion, the existence of hydrogen molecular ions is also neglected. Since the plasma is in a recombining phase in the expanding region, the diatomic hydrogen molecules which are ionized there can be neglected. The formation of the molecular hydrogen ions through the reactions $H^+ + H^+ + e^- \rightarrow H_2^+$ or $H^+ + H \rightarrow H_2^+$ may be neglected because of their large relaxation times [104]. Even if there may be molecular hydrogen ions, they are originated from the arc discharging region. Most of them are considered to be lost through the rapid dissociative recombination. The recombination coefficient of the molecular hydrogen ion was estimated at $\sim 1 \times 10^{-7}$ cm^3/s in the temperature range $0.1 \leq T_e \leq 10$ eV [107]. On the other hand, the recombination rate coefficient of the atomic hydrogen ion is much smaller than that of the molecular ion, and estimated at about $1 \times 10^{-11} - 1 \times 10^{-10}$ cm^3/s [122]. When the plasma comes from the arc region to the expanding region, it is considered that the molecular ions recombine

much faster (about $300-3000$ times faster) than the atomic ions through the dissociative recombination. When a micro second has passed since the plasma passed the nozzle, the existence of the molecular ions is almost negligible.

The extraporated value of n/g to the ionization limit (13.6 eV for H I) $n/g(\infty)$(in cm^{-3}) is derived from Eq.(5.3) as follows [33]:

$$n_e n_i(\mathrm{H}^+) = 4.9 \times 10^{15} \times [n/g(\infty)]\ T_e^{3/2}, \tag{5.5}$$

where T_e is in K, n_e and n_i are in cm^{-3}. From the condition of the neutrality,

$$n_e = n_i(\mathrm{H}^+) + n_i(\mathrm{He}^+). \tag{5.6}$$

Since the second term of the right hand side of Eq.(5.6) is negligible as described later, n_e is obtained through Eqs. (5.5)-(5.6). The existence of He^{2+} ions is negligible as described beforehand. The obtained values of T_e and n_e are added in Fig. 5.2. And the variation of the electron temperature and density is shown in Fig. 5.7. It shows the averaged value along the line of sight from the detector. Like Figs. 5.5 and 5.6, it shows the time histories of the electron temperature and density. The electron temperature becomes gradually lower as the plasma comes downstream. The important feature is that the cooling by the gas contact method requires several micro second. This is also consistent with the simulation by Furukane, Sato, and Oda [103,104].

The density $n_i(\mathrm{He}^+)$ is calculated from the results shown in Fig. 5.3 by extraporating the value of n/g to the ionization limit of helium atom (24.5876 eV). The statistical weight of the helium ion is twice as large as the hydrogen ion, and Eqs. (3.2)-(3.3) is applied to the helium plasma. And we find that the density of the helium ion is 5.1×10^{10} cm^{-3} in Fig. 5.3. It is about 1/100 times of the density of the hydrogen ion. Therefore it can be said that the density of the helium ions are much smaller than that of hydrogen ions in the plasma.

To confirm the assumption that the levels used in the calculation ($N \geq 10$) was in LTE,

the validity criteria for LTE should be examined for the plasma in problem. Fujimoto and McWhirter showed that two criteria shoud be met for the justification of the LTE assumption, that is,

$$N \geq 118/T_{\rm e}^{0.43} + 279/n_{\rm e}^{0.15} \tag{5.7}$$

and

$$N \geq 282/T_{\rm e}^{0.5} \tag{5.8}$$

for hydrogen plasmas in a recombining phase, where $T_{\rm e}$ is in K and $n_{\rm e}$ is in $\rm cm^{-3}$ [101]. These equations show that N should be equal to or larger than 7 in Fig. 5.2(a), 8 in Fig. 5.2(b), 10 in Fig. 5.2(c)-(d). Therefore our assumption met with the criteria. For lower lying levels than those determined by Eqs. (5.7)-(5.8), the experimental results show much smaller population densities than in the state of LTE. The appropriateness of the criteria Eqs. (5.7)-(5.8) are confirmed in the present experiments.

It was difficult for us to determine the gas temperature from the experiment. The applied magnetic field was rather weak, and the plasma was assumed not to be magnetized. In one dimensional case, the plasma boundary moves with the velocity

$$v_{\rm m} = 2v_0/(\gamma - 1), \tag{5.9}$$

where v_0 is the sound velocity in atomic hydrogen, and γ is the specific-heat ratio, if the plasma is assumed to be pure hydrogen atoms [32]. In the present experiment, the plasma is confined magnetically to the direction perpendicular to the flowing, and approximated as one dimensional. Since $v_{\rm m}$ was estimated at about 9×10^3 m/s, Eq.(5.9) tells that $v_0 \simeq 3 \times 10^3$ m/s. When the temperature of the atomic hydrogen $T_{\rm H}$ is given, v_0 can be calculated as follows:

$$v_0 = \sqrt{\gamma k T_{\rm H}/m_{\rm H}}. \tag{5.10}$$

Then, it is considered that the temperature of the hydrogen atom is about 700 K. This gives a reasonable value. According to the simulation by Furukane, Sato, and Oda [103,104], the electron temperature cooled by the gas contact method becomes that of the contact gas after several microsecond has passed due to the collisional relaxation. In our experiments, the electron temperature becomes 0.066 eV = 770 K at $z = 22$ cm, where the duration of the contact is estimated at 22 μsec. Therefore it is concluded that our experimental results agree with their simulation very well.

When we use deuterium gas instead of hydrogen, we can generate a deuterium-helium mixed plasma, where almost all the ions are deuterium ions. The spectroscopic observations were carried out to the deuterium plasma like to the hydrogen plasma. Figures 5.8 and 5.9 show the variation of the electron temperature and density of the deuterium plasma like Fig. 5.7, respectively. The same method is used to determine them. In the experiments of the deuterium plasma, the diameter of the nozzle was a little larger than in the experiments described in Fig. 5.7, and the direct comparison of Figs. 5.8 and 5.9 with Fig. 5.7 may be meaningless. Therefore we showed the variation of the parameters of a hydrogen plasma with the same nozzle as in the experiments of a deuterium plasma. The results are added in Figs. 5.8-5.9. There is no large difference in the variation of the electron temperature and density between the hydrogen plasmas and the deuterium plasmas.

5.3.3 Comparison of the experimental results with the calculation based on the collisional radiative model

The electron temperature and density were obtained in Fig. 5.7. From these values, the population densities of the excited states of hydrogen atoms can be calculated by the collisional radiative model with the assumption that the plasma is optically thin. In the present calculation, the method in Ref. [122] was used. For the rate coefficients of the excitation and the de-excitation by electronic collisions, the formula for electrons with

the low temperature were used [125,126]. Unlike chapter 4, we do not use the data in Ref. [107], since the electron tempereture is very low in the present analysis. Later we will show how poor the Born approximation is to calculate population densities in the generated plasma.

In this chapter, we grouped all the sublevels with the same principal quantum number into one group. In a hydrogen atom, they have the same energy levels, which is different from a helium atom. The de-excitation rate coefficient $F(N_1, N_2)$ (in $\mathrm{cm^3 s^{-1}}$) for low electron temperature is formulated below [13]:

$$F(N_1, N_2) = 1.8 \times 10^{-6} T_e^{-0.17} N_2^{6.66} N_1^{-5}, \tag{5.11}$$

where T_e is in K. We use Eq.(5.11) for all the transitions. The excitation rate coefficient $C(N_1, N_2)$ is calculated from Eq.(5.11) using the detailed balance equation,

$$C(N_1, N_2) = F(N_2, N_1)\ Z(N_2)/Z(N_1). \tag{5.12}$$

As for the ionization rate coefficient from the ground state $S(1)$, the data by Bell et al. was used [110]. The classical scaling was employed for the ionization rate coefficients from the excited states [127]. That is,

$$S(N) = S(1) \left[\frac{R}{\chi(N)}\right]^2, \tag{5.13}$$

where R is the Rydberg energy and equal to $\chi(1)$, and S is described as a function of $U = kT_e/\chi(N)$. From $S(N)$, the three-body recombination coefficient $\alpha(N)$ is calculated using the detailed balance equation. Namely,

$$\alpha(N) = S(N)\ Z(N). \tag{5.14}$$

The radiative recombination coefficient $\beta(N)$ is calculated as follows [13]:

$$\beta(N) = \frac{2^4}{3\sqrt{3}} \frac{e^4}{m_e^2 c^3 \epsilon_0^2} \frac{1}{N^3} \left(\frac{R}{\pi k T_e}\right)^{3/2} \exp\left[\frac{\chi(N)}{kT_e}\right] \left[-\mathrm{Ei}\left(-\frac{\chi(N)}{kT_e}\right)\right], \tag{5.15}$$

where Ei is the exponential integral function, defined

$$-\mathrm{Ei}(-x) \equiv \int_x^\infty \frac{\exp(-t)}{t}\mathrm{d}t. \tag{5.16}$$

The atomic transition probabilities $A(N_1, N_2)$ listed in Ref. [95] are used. If the values for high lying levels are not listed, $A(N_1, N_2)$ can be calculated by the well-known approximation of oscillator strength f_{N_2,N_1} for the excited states as follows [128]:

$$A(N_1, N_2) = \frac{2\pi e^2 \nu^2}{mc^3 \epsilon_0} \frac{g(N_2)}{g(N_1)} f_{N_2,N_1} \ , \tag{5.17}$$

and

$$f_{N_2,N_1} = \frac{2^6}{3\sqrt{3}\,\pi} \frac{1}{g(N_2)} \frac{1}{{N_1}^3 {N_2}^3} \frac{1}{({N_2}^{-2} - {N_1}^{-2})^3} \ . \tag{5.18}$$

In the present calculation, the optical thicknesses are neglected.

With these coefficients, the rate of variation of the population density $n(N_1)$ of level N_1 is described by the following equation like Eq. (4.5) [122]:

$$\begin{aligned}\frac{\mathrm{d}n(N_1)}{\mathrm{d}t} = & \sum_{N=1}^{N_1-1} C(N, N_1) n(N) n_\mathrm{e} \\ & + \left[\sum_{N=N_1+1}^{\infty} \Big\{ F(N, N_1) n_\mathrm{e} + A(N, N_1) \Big\} n(N) \right] + \Big[\alpha(N_1) n_\mathrm{e} + \beta(N_1) \Big] n_\mathrm{e} n_\mathrm{i} \\ & - \left[\left\{ \sum_{N=1}^{N_1-1} F(N_1, N) + \sum_{N=N_1+1}^{\infty} C(N_1, N) + S(N_1) \right\} n_\mathrm{e} \right. \\ & \left. + \sum_{N=1}^{N_1-1} A(N_1, N) \right] n(N_1). \end{aligned} \tag{5.19}$$

Generally, the time derivative of the population densities of all the excited states ($N \geq 2$) may be set equal to 0 [13]. And in the present calculation, the population densities for all the levels above $N = 35$ are supposed to be described by Eq.(5.3). From the practical viewpoint, the summations to infinity may be cut off at a sufficiently high-lying level N_∞, which is set at 40. Consequently, when the electron temperature and density are given, Eq.(5.19) is solved in the form

$$n(N) = Z(N)r_0(N)n_i n_e + [Z(N)/Z(1)]\, r_1(N)n(1), \tag{5.20}$$

where r_0 and r_1 are the global population coefficients and functions of n_e and T_e, derived from Eq. (5.19) like Eq. (4.6) [122].

In an ionizing plasma like a positive column plasma, the second term of Eq.(5.20) is dominant [13]. On the other hand in a recombining plasma like an afterglow plasma, the first term is dominant. There exists no metastable driven components in the present model. Since the generated plasma in our experiments is evidently categorized into a recombining plasma and the electron temperature is sufficiently low, the second term of Eq.(5.20) can be neglected and the population densities of all the excited states are obtained even if the density of the ground state is left unknown. The results are added in Fig. 5.2.

Figure 5.2 shows that the results of the calculations agree well with the experimental results, particularly in the downstream ((b)-(d)). For the deuterium plasmas, the same consequence as the hydrogen plasmas was obtained. Since the electron temperature of the plasma is very low, the rate coefficients are considered to contain considerable errors such as factor $2-3$ [13]. And the Abel inversion is not applied to the experimental data, which is different from the helium plasma. But the agreement is very good, particularly in Figs. 5.2(b) and 5.2(d). Even in Fig. 5.2(c), the tendency of the variation of population densities with the principal quantum number is explained well by the calculation, and the deviation of the calculation from the experiments lies within a factor ~ 2. The experimental data are described satisfactorily by the collisional radiative model in which the plasma is optically thin in the downstream area, where the residual hydrogen atoms are considered to make diatomic molecules. Consequently, the absorption of the lines of the Lyman series becomes less frequent and the plasma becomes optically thin, which is different from the helium plasma. It resembles the phenomenon observed in an absolute calibration of a VUV monochromator by branching ratio method using hydrogen and helium lines. Kasai et al reported that the hydrogen recombining plasma tended to be

optically thin for the transitions to the ground state, whereas the helium recombining plasmas had a tenency of being optically thick [129]. If we assume that the plasma is optically thick for the transitions to the ground state, the calculation does not agree with the experiments, especially for the population denties of the low-lying levels.

Figure 5.10 shows one of the examples of the radial distribution of the population densities of some low-lying levels. We could not measure the levels which had the different angular quantum numbers of the hydrogen plasma. However, the radial distributions of the levels were almost Gaussian, and the population densities became smaller at the edge of the plasma. Hence, it is considered that the resonance absorption of the Lyman series by the residual hydrogen atom must be neglected. This characteristic is different from the helium plasma very much. This is considered to be one of the reasons why the calculational results agree well with the experimental results to which the Abel inversion is not applied.

From Eqs. (5.11)-(5.18), we can calculate the population rates and the depopulation frequencies of each elementary process. The results for the conditions in Figs. 5.2(b) and 5.2(d) are shown in Table 5.1. These conditions were chosen because the agreement of the calculations with the experiments was very good and each of them represented the medium temperature condition (Fig. 5.2(b), $T_e = 0.15$ eV) and the very low temperature condition (Fig. 5.2(d), $T_e = 0.066$ eV). In Table 5.1, five population processes are treated separately like Eqs. (4.25)-(4.29). We rewrite them following:

$$P_{\mathrm{ra}}(N_1) = \sum_{N=N_1+1}^{N_\infty} A(N, N_1) n(N), \tag{5.21}$$

$$P_{\mathrm{cd}}(N_1) = n_e \sum_{N=N_1+1}^{N_\infty} F(N, N_1) n(N), \tag{5.22}$$

$$P_{\mathrm{ce}}(N_1) = n_e \sum_{N=1}^{N_1-1} C(N, N_1) n(N), \tag{5.23}$$

$$P_{3\mathrm{r}}(N_1) = {n_e}^2 \; n_i \; \alpha(N_1), \tag{5.24}$$

$$P_{\mathrm{rr}}(N_1) = n_e \;\; n_i \; \beta(N_1). \tag{5.25}$$

Likewise, four processes are treated separately in calculating depopulation frequencies like Eqs. (4.30)-(4.33). They should also be rewritten:

$$D_{\rm ra}(N_1) = \sum_{N=1}^{N_1-1} A(N_1, N), \tag{5.26}$$

$$D_{\rm cd}(N_1) = n_{\rm e} \sum_{N=1}^{N_1-1} F(N_1, N), \tag{5.27}$$

$$D_{\rm ce}(N_1) = n_{\rm e} \sum_{N=N_1+1}^{N_\infty} C(N_1, N), \tag{5.28}$$

$$D_{\rm io}(N_1) = n_{\rm e}\ S(N_1). \tag{5.29}$$

We define total population rate $P_{\rm t}$ and total depopulation frequency $D_{\rm t}$ by Eqs. (4.34)-(4.35), respectively. They are rewritten as follows:

$$P_{\rm t}(N) = P_{\rm ra}(N) + P_{\rm cd}(N) + P_{\rm ce}(N) + P_{\rm 3r}(N) + P_{\rm rr}(N), \tag{4.34}$$

$$D_{\rm t}(N) = D_{\rm ra}(N) + D_{\rm cd}(N) + D_{\rm ce}(N) + D_{\rm io}(N). \tag{4.35}$$

From Table 5.1, it is found that the laser upper level populates mainly by the de-excitation processes from the highly-excited states, which are populated dominantly through three-body recombinations. On the other hand, the laser lower levels depopulate more rapidly than the upper levels, mainly by radiative decay. (See level pairs $4-3$ in Table 5.1(a) and $5-4$ and $4-3$ in (b).) In the population processes, the collisional de-excitation process is the most dominant for the laser upper levels ($N = 4$ in Table 5.1(a) and $N = 4,\ 5$ in (b)), while the radiative decay is the most dominant population process for the laser lower level ($N = 3$ in (a) and (b)). If the electron temperature is a little high, the collisional excitation process for high lying levels becomes gradually significant ($N = 5$ in (a)) and it is disadvantageous to form population inversion. As for the depopulation frequency, the total depopulation frequency for $N = 5$ is about twice as large as that for $N = 4$, and population inversion is not expected for the level pair in

Table 5.1(a). For level pairs 4−3 in (a) and any pairs in (b), the depopulation frequencies of the lower levels are larger than those of the upper levels.

It is seen that the tendency of the calculated population density is slightly different from the experiments in the most upstream area (Fig. 5.2(a)). The calculation shows the population inversion is expected between the level pair 4−3, but no inversion was observed in the experiments. It is supposed that the optical thickness to the ground state should be considered at least in the most upstream region, where hydrogen atoms with high density may exist without forming diatomic molecules. The expansion of hydrogen atoms is also insufficient in that region. Neutral hydrogen will expand very rapidly and form diatomic molecule downstream. In consequence, the optical thickness in the downstream can be neglected.

As for the rate coefficients, the electron temperature is very low in the present condition, therefore sufficient attention should be paid in calculating rate coefficients. Particularly, the rate coefficients of excitations and de-excitations by electron collisions (Eqs. (5.11)-(5.12)) are most critical in the present calculation. If we use the following excitation rate coefficients by the Born approximation instead of Eq.(5.11), it makes the population densities of the low lying levels too large to explain the experimental results.

$$C(N_1, N_2) = G \ \frac{R}{\chi(N_1) - \chi(N_2)} \ f_{N_1,N_2} \ \exp\left[-\frac{\chi(N_1) - \chi(N_2)}{kT_e}\right], \tag{5.30}$$

with

$$G = 4\pi {a_0}^2 R \left(\frac{1}{2\pi m k T_e}\right)^{1/2}, \tag{5.31}$$

where a_0 is the Bohr radius [13]. Of course, Eq. (5.30) is derived from the integration of the excitation cross section, which is caculatd asymptotically using a generalized oscillator strength by applying the Bethe limit for the optically allowed (dipole) transition in the high energy limit.

An example of the results is shown in Fig. 5.11 when the electron temperature is 0.1

eV. The calculation yields different results if we use Eq. (5.30) instead of Eq. (5.11). Equation (5.11) gives good results which agree with the experiments, while Eq. (5.30) gives poor results, especially for the population densities of the low-lying levels. It shows that the Born approximation is not valid in such low electron temperature as in our experiments. Equation (5.11) approximates the de-excitation rate coefficients with sufficient accuracy in the temperature range of the present experiments.

On the other hand, for the ionization cross sections from the excited states, Eq. (5.13) gives sufficient results. Janev et al. reported the following equation for the ionization rate coefficient from the excited states [107]:

$$S(N) = \frac{9.56 \times 10^{-6} T_e^{-1.5} \exp(-\chi(N)/T_e)}{(\chi(N)/T_e)^{2.33} + 4.38(\chi(N)/T_e)^{1.72} + 1.32(\chi(N)T_e)}. \tag{5.32}$$

This equation gives almost the same results as Eq. (5.13) in the present experimental conditions.

5.3.4 A brief review of the gas contact cooling

Furukane et al proposed the gas contact cooling [103,104], in which they took into account the collisional energy loss of electrons in a recombining helium plasma with the cold surrounding hydrogen gas molecules, including both elastic and inelastic collisions in addition to the radiative cooling [the term $-R$ in Eq. (2.18)]. It is worth while to review their paper in order to discuss and confirm the processes when the plasma flows from the arc region to the recombining region.

A brief outline of their calculation is the following [104]. They considered a stationary helium plasma drifting in a low temperature, high density gas of hydrogen molecule. The plasma was confined by a magnetic field. They worked in a coordinate system moving with the drift, i.e., $\mathrm{D}/\mathrm{D}t = \partial/\partial t + v_0 \partial/\partial z$. The time origin ($t = 0$) was set at the time when the plasma began to contact the hydrogen molecule. They neglected the expansion of the neutral species. They also neglected the fluid dynamical properties of the plasma.

They considered the following six reactions between electron and hydrogen molecule or molecular ion:

$$e^- + H_2 \rightarrow H + H + e^- \quad (E_1 = 8.8 \text{ eV}), \tag{5.33}$$

$$e^- + H_2 \rightarrow H + H^+ + 2e^- \quad (E_2 = 28.0 \text{ eV}), \tag{5.34}$$

$$e^- + H_2 \rightarrow H_2^+ + 2e^- \quad (E_3 = 15.42 \text{ eV}), \tag{5.35}$$

$$e^- + H_2^+ \rightarrow H + H^+ + e^- \quad (E_4 = 7.5 \text{ eV}), \tag{5.36}$$

$$e^- + H_2^+ \rightarrow H^+ + H^+ + 2e^- \quad (E_5 = 18.4 \text{ eV}), \tag{5.37}$$

$$e^- + H_2^+ \rightarrow H + H \quad (E_6 = 0.33 \text{ eV}), \tag{5.38}$$

where E_i $(i = 1, ..., 6)$ expressed the threshold energies of Eqs. (5.33)-(5.38), respectively. They neglected the inverse processes of these equations because of the large relaxation time. Since the density of the molecular hydrogen $n(H_2)$ was assumed to be constant, the following rate equation for the hydrogen molecule was valid:

$$\frac{Dn(H_2)}{Dt} = -n_e(S_1 + S_2 + S_3)n(H_2) + \psi_0 = 0, \tag{5.39}$$

where S_i $(i = 1, ..., 6)$ denoted the reaction rates of Eqs. (5.33)-(5.38), respectively, and ψ_0 was the influx rate of the hydrogen molecular particle density balanced with the total reactions (5.33)-(5.35). For the hydrogen molecular ion, the excited states of the hydrogen atom and the hydrogen ion, the corresponding equations were given by :

$$\frac{Dn(H_2^+)}{Dt} = n_e S_3 n(H_2) - n_e(S_4 + S_5 + S_6)n(H_2^+), \tag{5.40}$$

$$\frac{Dn[H(i)]}{Dt} = \sum_{j=1}^{20} a(i,j)(H)n[H(i)] + \delta(i)(H), \ (i = 2, ..., 20) \tag{5.41}$$

$$\begin{aligned}\frac{Dn(H^+)}{Dt} = &-\sum_{i=1}^{20}\left[\sum_{j=1}^{20} a(i,j)(H)n[H(j)] + \delta(i)(H)\right] \\ &+ n_e\left[S_2 n(H_2) + (S_4 + 2S_5)n(H_2^+)\right],\end{aligned} \tag{5.42}$$

where the coefficients $a(i,j)(\mathrm{H})$ and $\delta(i)(\mathrm{H})$ were given by the radiative transition probability $A(i,j)$ and the optical escape factor $G(i,j)$, and by the rate coefficients for the electron-impact ionization $S(i)$ and three-body recombination $\alpha(i)$, electron-impact excitation $C(i,j)$ $(i<j)$, and deexcitation $F(j,i)$ $(i<j)$, and radiative recombination $\beta(i)$. The corresponding equations for the helium atom and He^+ ion were given in a similar way. For the ground state density of H, they used the already estimated density $n[\mathrm{H}(1)]$, which was given by the following:

$$n[\mathrm{H}(1)] \simeq 0.38 \times 10^{-10}(\tau/P(\mathrm{H}))n_{\mathrm{e}}n(\mathrm{H}_2), \tag{5.43}$$

where τ was the cooling relaxation time by the Eq. (5.33), and $P(\mathrm{H})$ was the absorption ratio to the wall. Since the sum of the helium ions and atomic density was constant n_0 and the charge neutrality was assumed:

$$n_0 = n(\mathrm{He}^{2+}) + n(\mathrm{He}^+) + n(\mathrm{He}), \tag{5.44}$$

$$n_{\mathrm{e}} = 2n(\mathrm{He}^{2+}) + n(\mathrm{He}^+) + n(\mathrm{H}^+) + n(\mathrm{H}_2^+), \tag{5.45}$$

the time evolution for the helium ion He^{2+} and electron densities were derived like following:

$$\frac{\mathrm{D}n(\mathrm{He}^{2+})}{\mathrm{D}t} = -\frac{\mathrm{D}n(\mathrm{He}^+)}{\mathrm{D}t} - \frac{\mathrm{D}n(\mathrm{He}^+)}{\mathrm{D}t}, \tag{5.46}$$

$$\frac{\mathrm{D}n_{\mathrm{e}}}{\mathrm{D}t} = 2\frac{\mathrm{D}n(\mathrm{He}^{2+})}{\mathrm{D}t} + \frac{\mathrm{D}n(\mathrm{He}^+)}{\mathrm{D}t} + \frac{\mathrm{D}n(\mathrm{H}^+)}{\mathrm{D}t} + \frac{\mathrm{D}n(\mathrm{H}_2^+)}{\mathrm{D}t}. \tag{5.47}$$

The originality of their idea was the treatment of the energy balance of the electrons. The energy balance equation was expressed as

$$\frac{\mathrm{D}T_{\mathrm{e}}}{\mathrm{D}t} = \frac{2}{3}\sum_h \frac{1}{\tau_{eh}}(T_h - T_{\mathrm{e}})$$

$$
\begin{aligned}
&- \frac{2}{3}\sum_{k}\sum_{i=2}^{l}\sum_{j=1}^{i-1}(\chi(j)-\chi(i))[C(j,i)n(j)-F(i,j)n(i)] \\
&- \frac{2}{3}\sum_{k}\sum_{j=1}^{l}(\chi(j)+\frac{3}{2}T_{\mathrm{e}})S(j)n(j) \\
&+ \frac{2}{3}n_{\mathrm{e}}n_{\mathrm{ion}}\sum_{k}\sum_{j=1}^{l}(\chi(j)+\frac{3}{2}T_{\mathrm{e}})\alpha(j) \\
&- \frac{2}{3}\sum_{i=1}^{3}S_iE_in(\mathrm{H}_2) - \frac{2}{3}\sum_{i=4}^{6}S_iE_in(\mathrm{H}_2^+) \\
&- T_{\mathrm{e}}\left[\sum_{i=2}^{3}S_in(\mathrm{H}_2)+\sum_{i=5}^{6}(-1)^{i-1}S_in(\mathrm{H}_2^+)\right], \qquad (5.48)
\end{aligned}
$$

where $h = 1-7$ corresponded to the hydrogen ion H^+, the helium ions He^{2+} and He^+, the hydrogen and helium atoms H and He, the hydrogen molecule H_2 and the hydrogen molecular ion H_2^+, $l = 20, 20, 49$ and $k = 1, 2$ and 3 corresponded to the helium ion He^+, hydrogen atom and helium atom, respectively; τ_{eh} represented the collision time for the electron-h species particle encounters. The fifth and sixth terms showed the dissociation of the molecule into the atoms or ions, and the last term was attributed to the electron creation and loss by the molecular processes. They neglected the kinetic energy increase of the atoms and ions acquired in the molecular dissociation. They also neglected the collisional excitation processes of vibration and rotation for hydrogen molecules.

The electron temperature T_{e} and total energy transfer rate $-\dot{T}_{\mathrm{e}} = -\mathrm{D}T_{\mathrm{e}}/\mathrm{D}t$ which they calculated from Eqs. (5.39)-(5.48) are shown in Figs. 5.12-5.13, respectively, with an initial electron density $n_{\mathrm{e0}} = 3.53 \times 10^{14}$ cm^{-3}, an initial electron temperature $T_{\mathrm{e0}} = 30$ eV, and hydrogen gas density $n(\mathrm{H}_2) = 3.53 \times 10^{15}$ cm^{-3}. Temperatures of neutral hydrogen molecule, hydrogen molecular ion and hydrogen atom were assumed to be constant, 0.2 eV, which resulted in the constant electron temperature after $t = 2 \times 10^{-7}$ s.

Figure 5.13 also shows each contribution by which process the electron energy is lost, the electron energy transfer by all elastic collisions, "Elastic", sum of the electron energy transfer rate by ionization and recombination for H atom "I+R" and the electron energy transfer rate by excitation and deexcitation for H atom "E+D", sum of the electron

energy transfer rate by molecular dissociation processes "Mol". These figures showed that hydrogen gas could cool the electrons in the plasma effectively. It was also shown that the electron inelastic scattering dominated the cooling process when $T_e \geq 1$ eV, and that the elastic collisions dominated the cooling processes when $T_e \leq 1$ eV.

When these data are compared to our experiments, it is found that the initial temperature of their simulation was a little higher than in our experiments. However, the assumed pressure of the hydrogen gas and the electron density were similar to our experiments. And it is considered to be appropriate that these calculations can be approximately applied to our experimental results when the time origin is moved to the time at which $T_e \simeq 2$ eV. On the other hand, the surrounding molecules in our experiments had a lower temperature than their assumptions. If these are considered, it is naturally concluded that the electron in our hydrogen plasma is cooled at least by the collisions with surrounding hydrogen molecules.

It is confirmed from their simulation that the electron temperature in our plasma are also relaxed in several hundred nano-second from the beginning of the contact with cold surrounding gas. In our temperature range, the molecular dissociation processes did not play an important role. However, it should be noted that their simulation did not include the excitation of molecular vibration or rotation. Therefore, even in our temperature range, the inelastic energy loss of electrons is considered to have an essential role in the cooling of the electrons. This is considered to be one of the reasons why the electron temperature in our hydrogen plasma becomes much colder than that in our helium plasma. Hayashi compiled some of the electron excitation cross sections of a hydrogen molecule [85], and the results are as shown in Fig. 5.14. The energy levels are tabulated in Table 5.2. Figure 5.14(a) shows that the excitation cross section of the rotations of hydrogen molecules is fairly large in the energy range $T_e \leq 0.1$ eV. On the other hand, these inelastic processes cannot be expected in our helium plasma where the residual gas consists mainly of helium atoms. If we would like to cool the electron in a helium plasma, we should contact the helium plasma with multi-atomic molecules in

order to use the inelastic collisions.

5.4. Conclusion

A stationary recombining hydrogen plasma was generated in the arc-heated magnetically trapped expanding plasma jet generator by mixing hydrogen gas into the discharging helium gas. The mixing ratio of hydrogen molecule to helium was about 20 %. The plasma was generated very stably and the spectroscopic observation was accomplished with sufficient accuracy by a monochromator calibrated absolutely. Population densities of hydrogen atoms whose principal quantum number was $3 - 12$ were observed. The plasma contained inverted populations in the plasma expanding region. Population inversions between level pairs $4 - 3$, $5 - 3$, $6 - 3$, $7 - 3$, and $5 - 4$ were obtained in the downstream of the plasma jet. The inversion between level pairs $4 - 3$ and $5 - 4$ was so large that the cw laser oscillation would be expected with some appropriate resonator mirrors. The electric power required for the discharge was considerably low ($\sim$ 3 kW) which was enabled by the magnetic confinement, by the supersonic plasma flow, and by the effective cooling of the plasma due to the collisions with residual gas in the plasma expanding region. The electron temperature and density were determined from the population densities of high-lying levels, and the electron temperature was $0.06 - 0.2$ eV and the density was $5 \times 10^{12} - 3 \times 10^{13}$ cm^{-3}, both of which became gradually low when it came downstream. The mean velocity of the plasma jet was estimated from the Doppler shift of the jet, and it was about $\sim 10^4$ m/s. The macroscopic characteristics were consistent with other authors' simulations of the gas contact cooling. The mixture ratio of the helium ion in the hydrogen ion was estimated at about 1/100. The population densities of the excited states of hydrogen were calculated with a collisional radiative model as the functions of the observed electron temperature and density. In the calculation, the hydrogen plasma was assumed to be optically thin. The calculational results agreed very well with the experiments in the downstream.

The results of chapter 5 have already been published in Ref. [62].

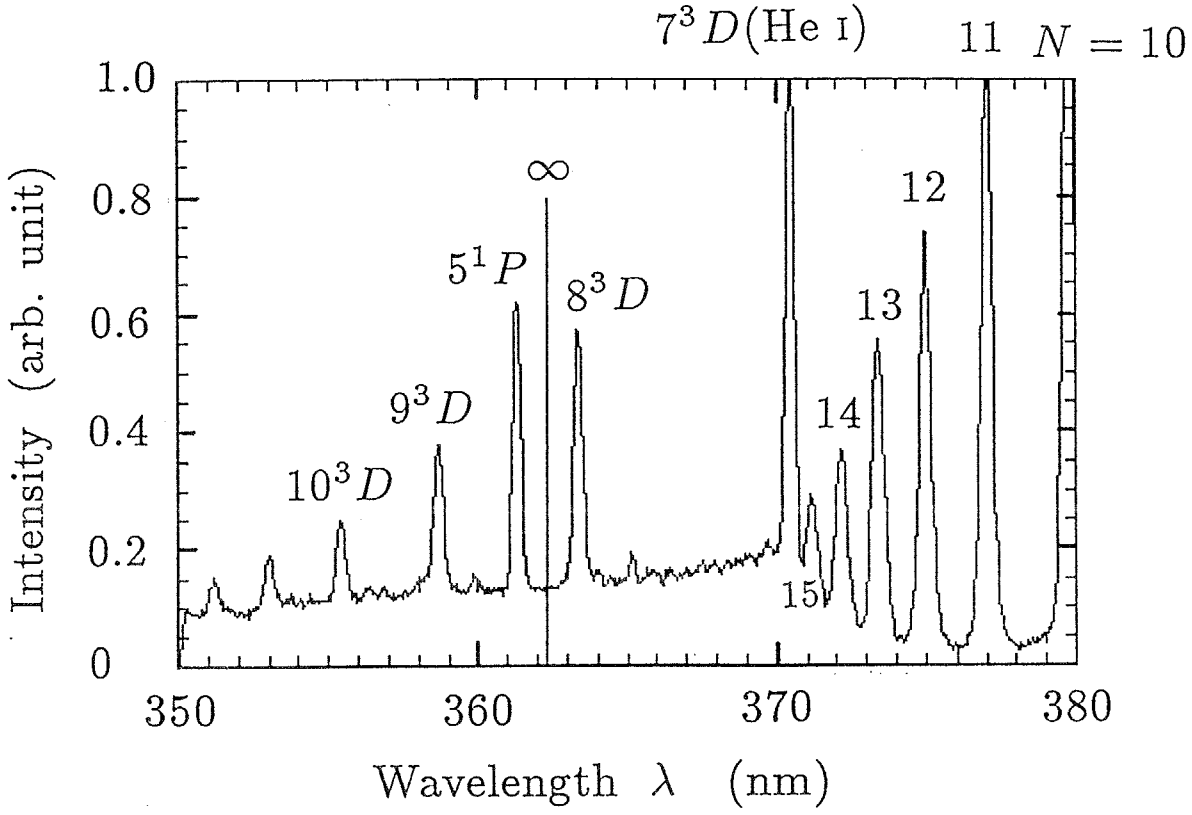

Fig. 5.1. Spectrum near the Balmer series limit. Those marked with the angular momentum quantum number are the lines of He I. The spectrum sensitivity of the detection system is not calibrated for.

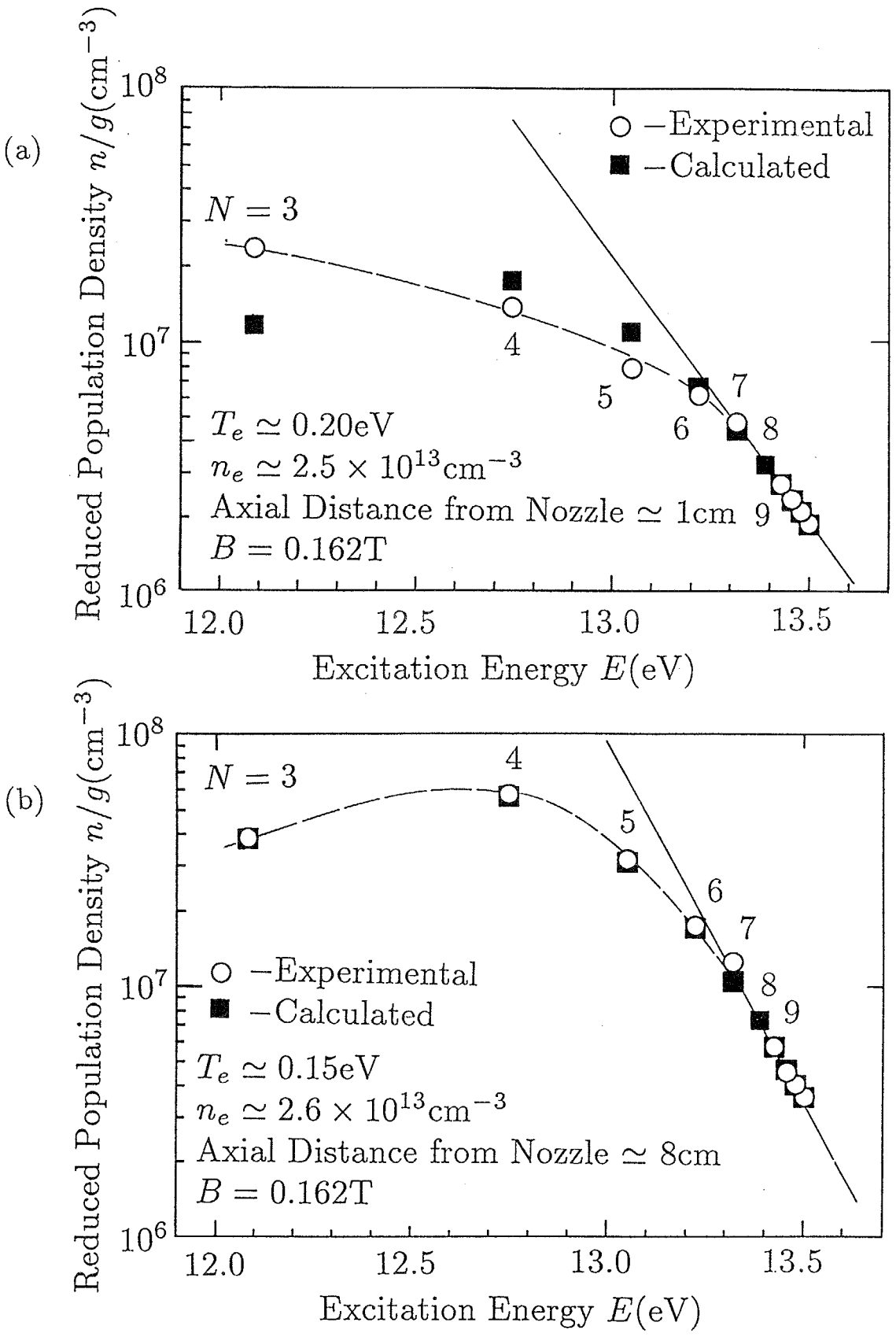

Fig. 5.2. Boltzmann plots of the populations of hydrogen atoms. The solid lines show the Saha-Boltzmann populations given by Eq. (5.3). The pressure in the plasma expanding region $P_{\mathrm{lc}} = 7.2$ Pa and the strength of the magnetic field $B = 0.162$ T. The pressure in the discharging region $P_{\mathrm{dc}} = 1.0 \times 10^5$ Pa and the ratio of the hydrogen in it is about 0.2.

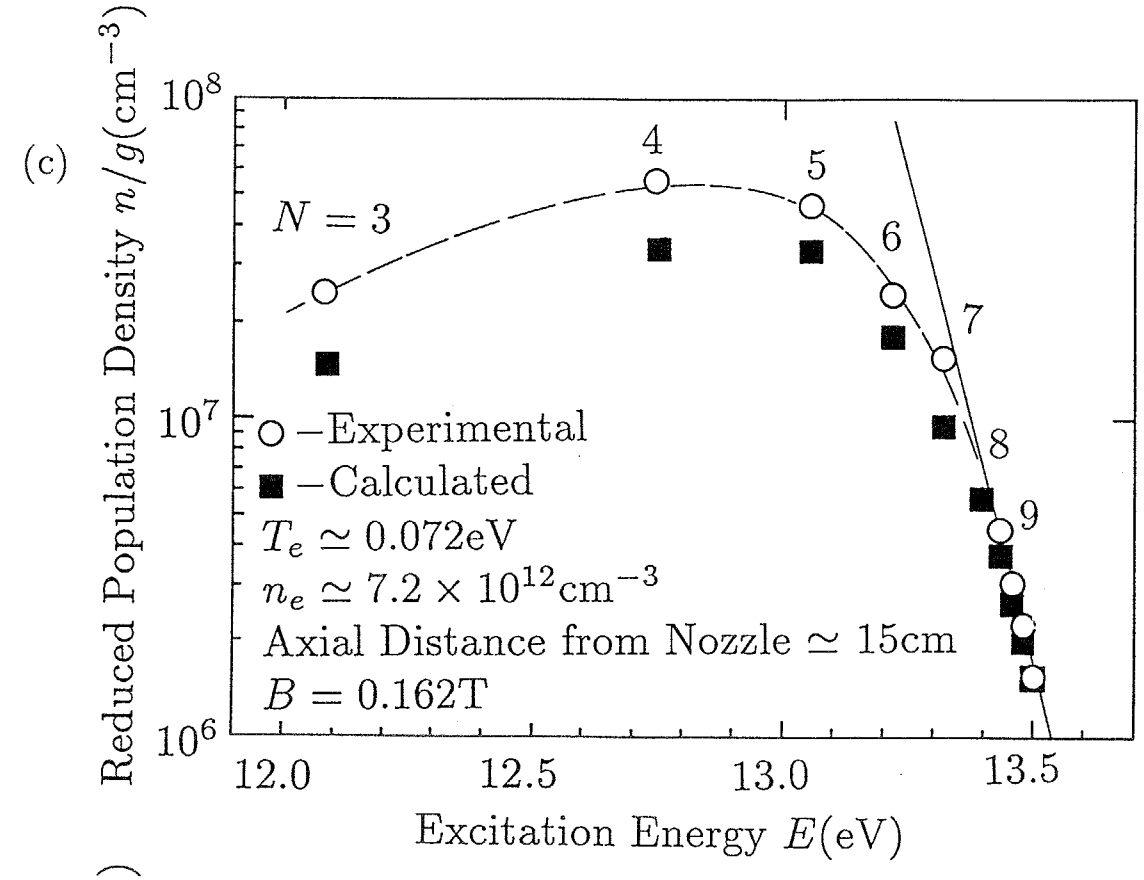

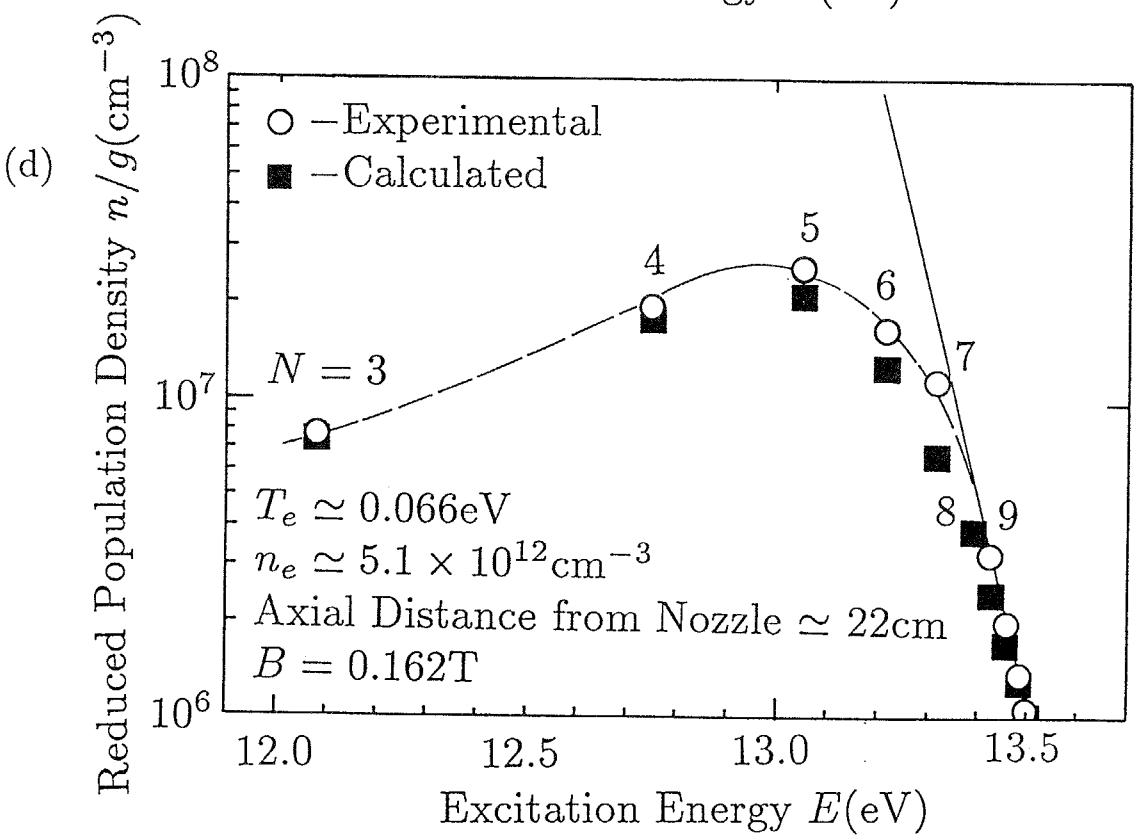

The axial distance from the nozzle is 1 cm, 8 cm, 15 cm, and 22 cm in (a), (b), (c), and (d), respectively. Calculated values are obtained through Eqs. (5.11)-(5.20) as functions of the observed electron temperature and density.

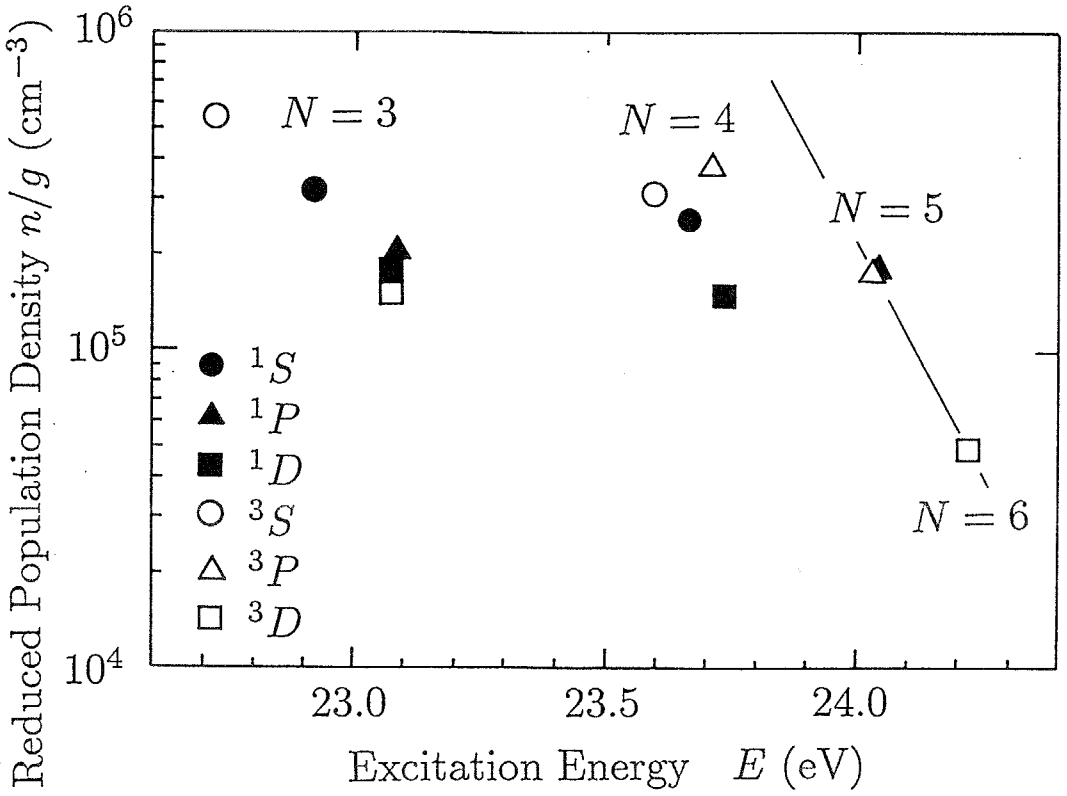

Fig. 5.3. Boltzmann plot of the populations of helium atoms. The solid line shows the Saha-Boltzmann populations given by Eq. (4.8). Experimental conditions are the same as in Fig. 5.2(b).

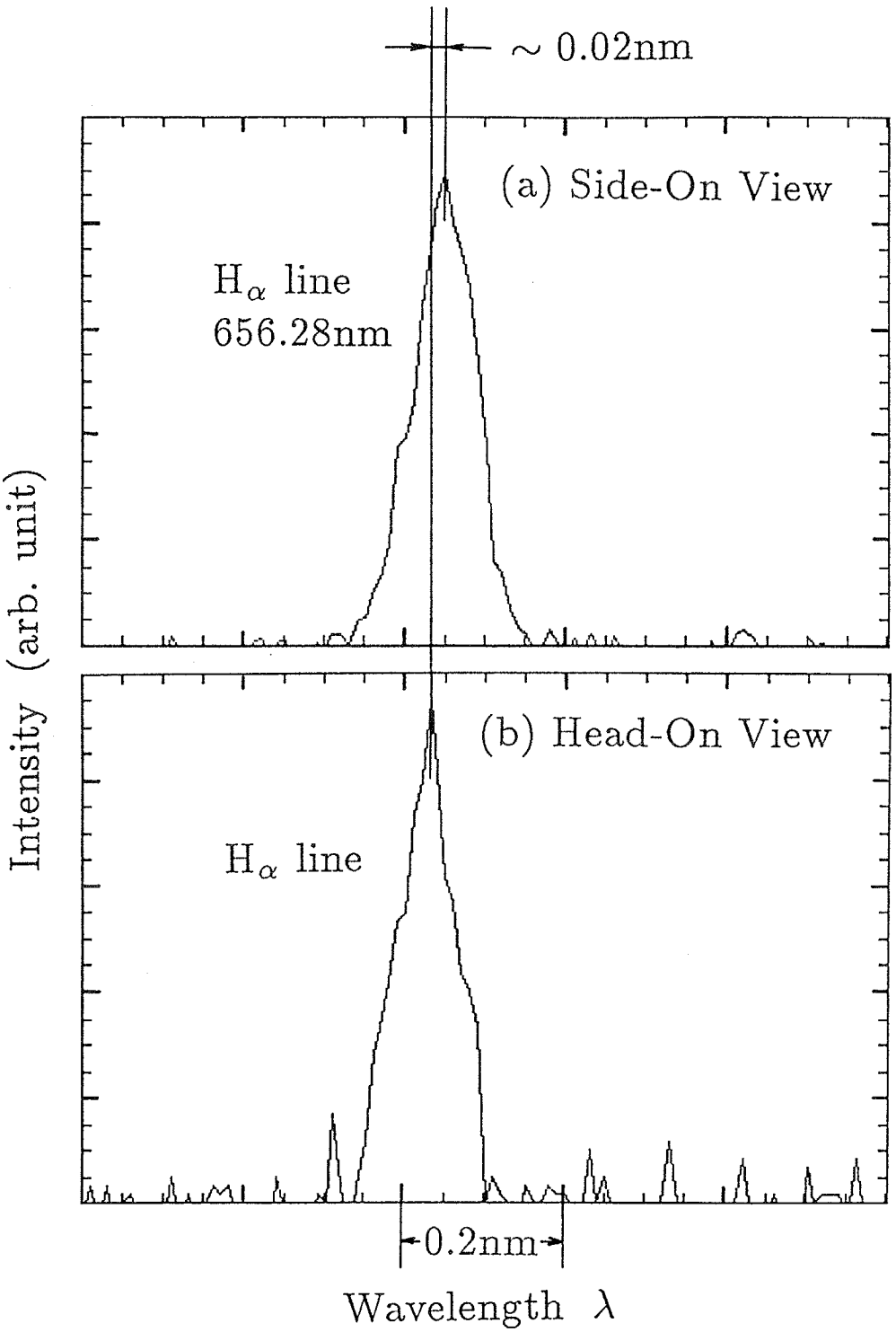

Fig. 5.4. The observed Doppler shift of H_α line. A side-on view gives the line (a), which does not shift, while a head-on view gives the line (b). The experimental conditions are the same as in Fig. 5.2. The slits of the monochromator are closed to 4μm to improve the spectral resolution.

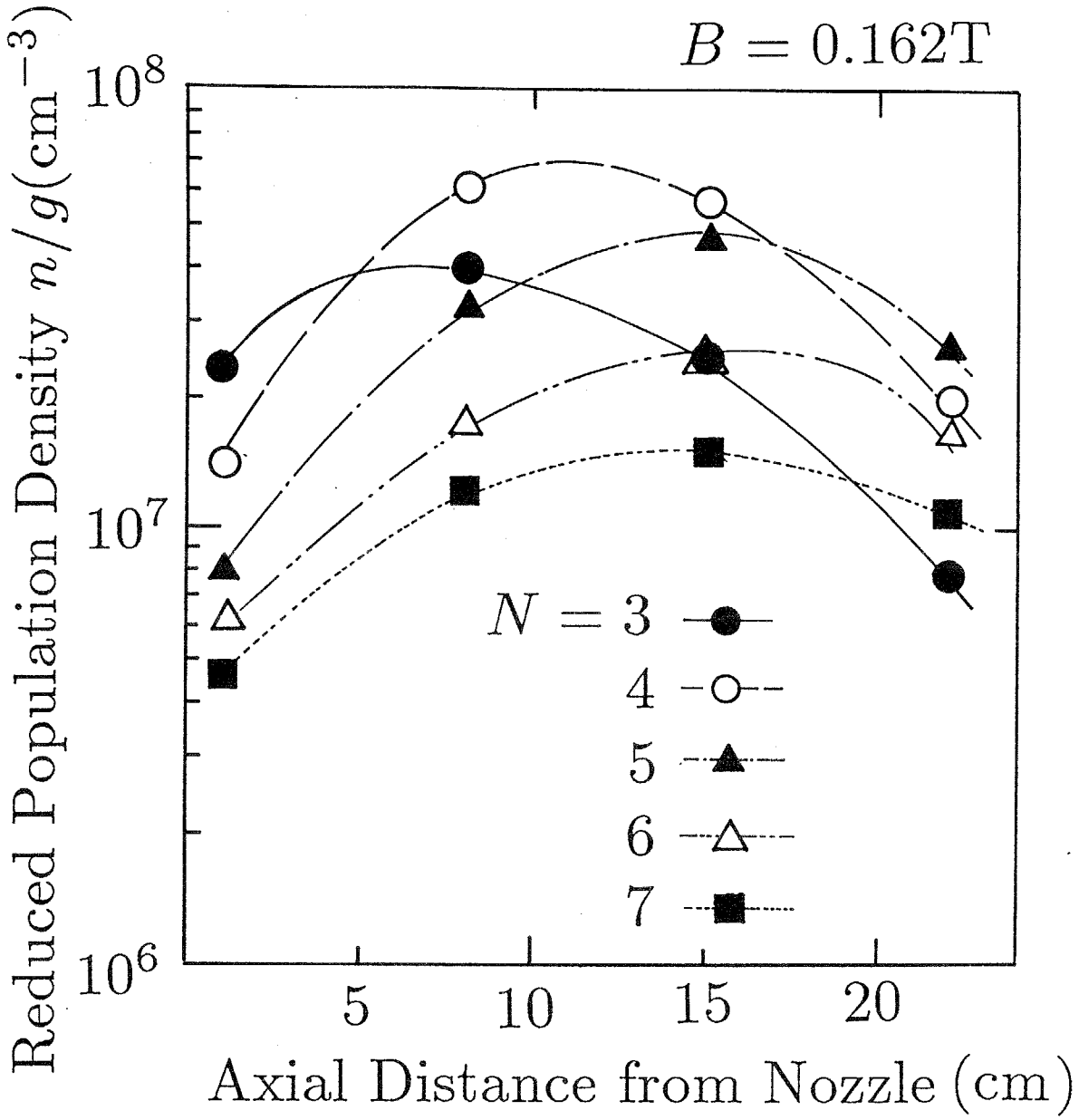

Fig. 5.5. Variation of the reduced population density n/g of levels $N = 3 - 7$. Experimental conditions are the same as in Fig. 5.2.

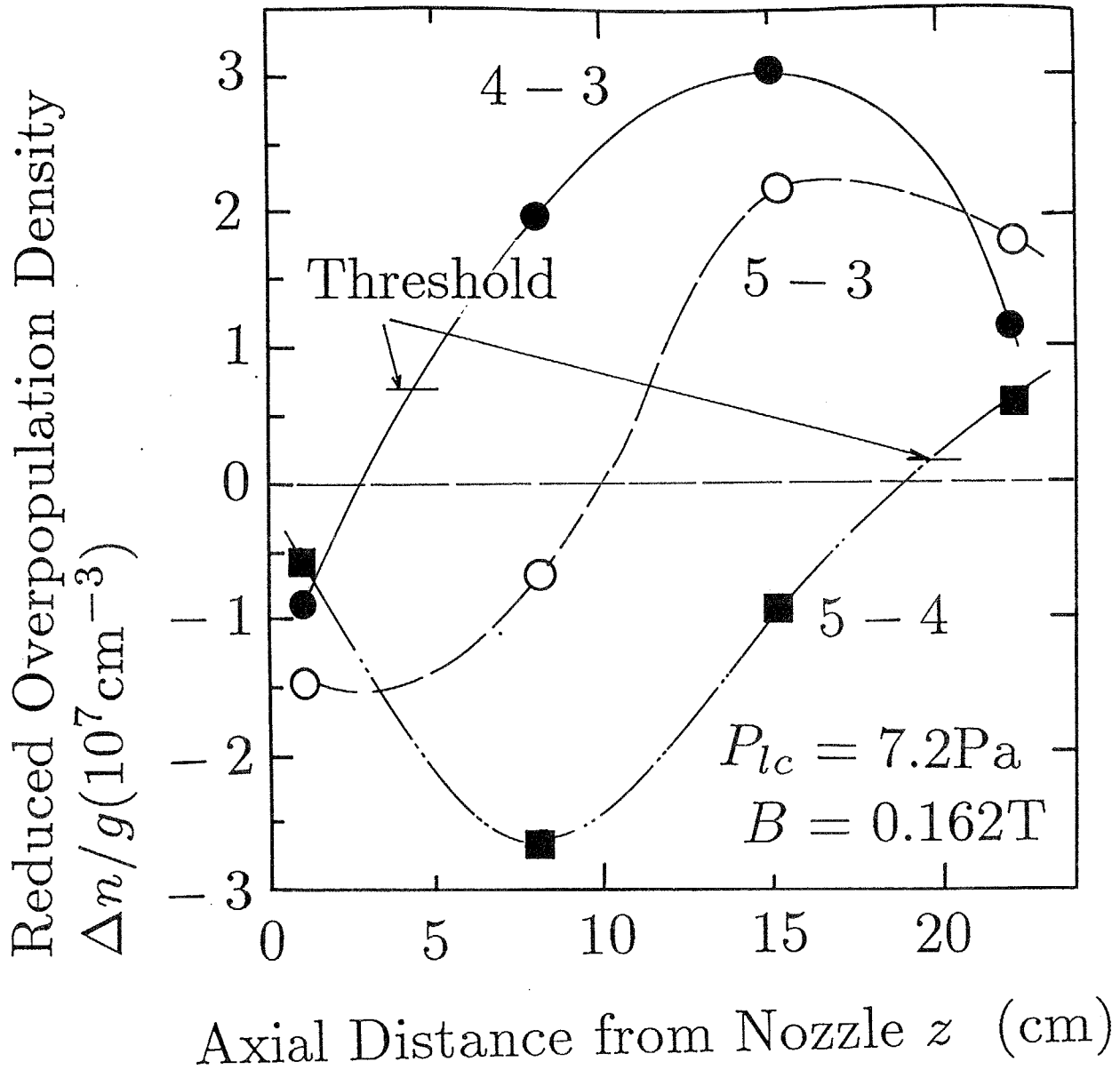

Fig. 5.6. Variation of the reduced overpopulation density $\Delta(n/g)$ between level pairs $4-3$, $5-4$, and $5-3$. Experimental conditions are the same as in Fig. 5.2. The threshold value is calculated using Eq. (5.4).

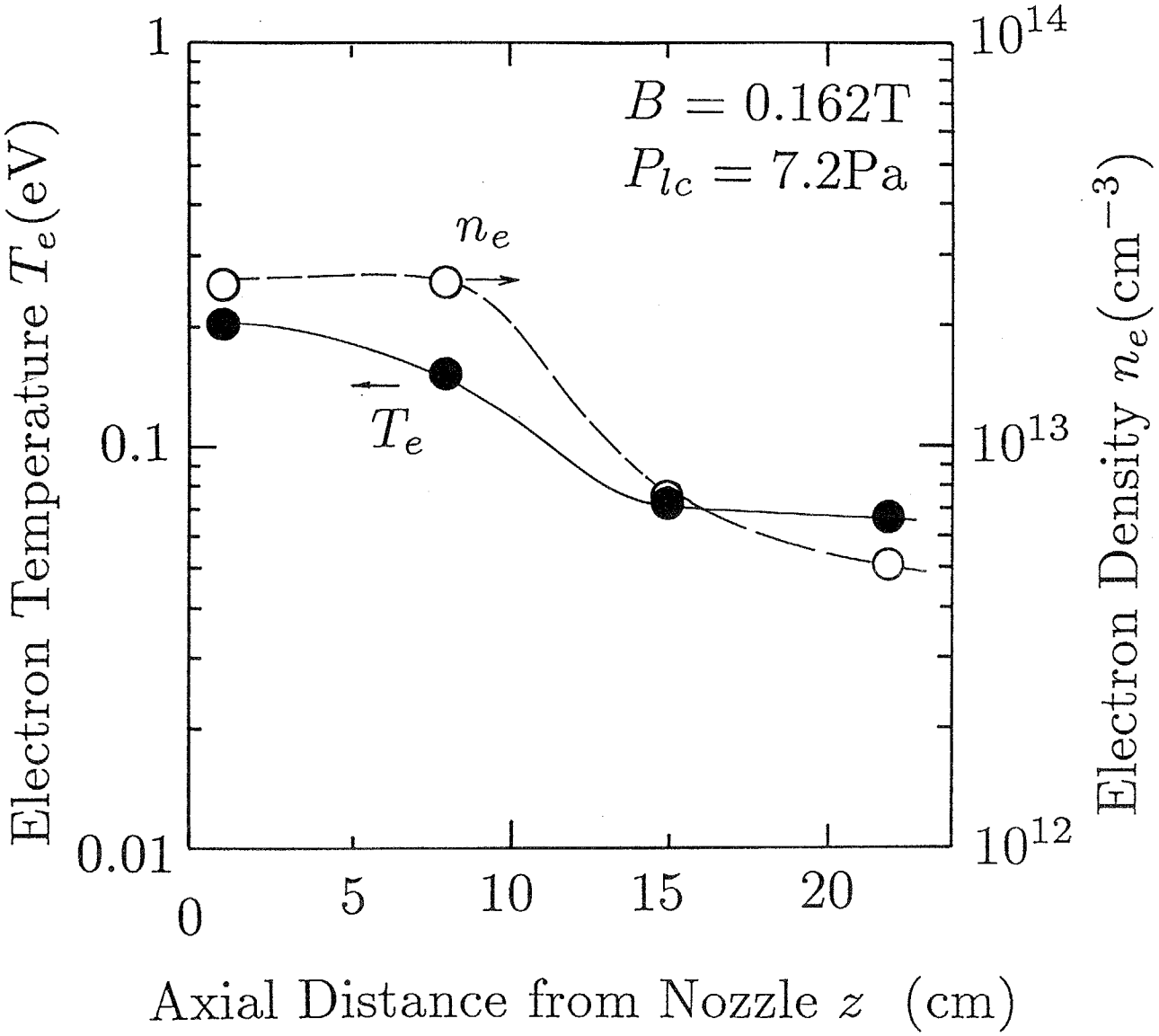

Fig. 5.7. Variations of the electron temperature T_e and n_e of the hydrogen plasma. Experimental conditions are the same as in Fig. 5.2.

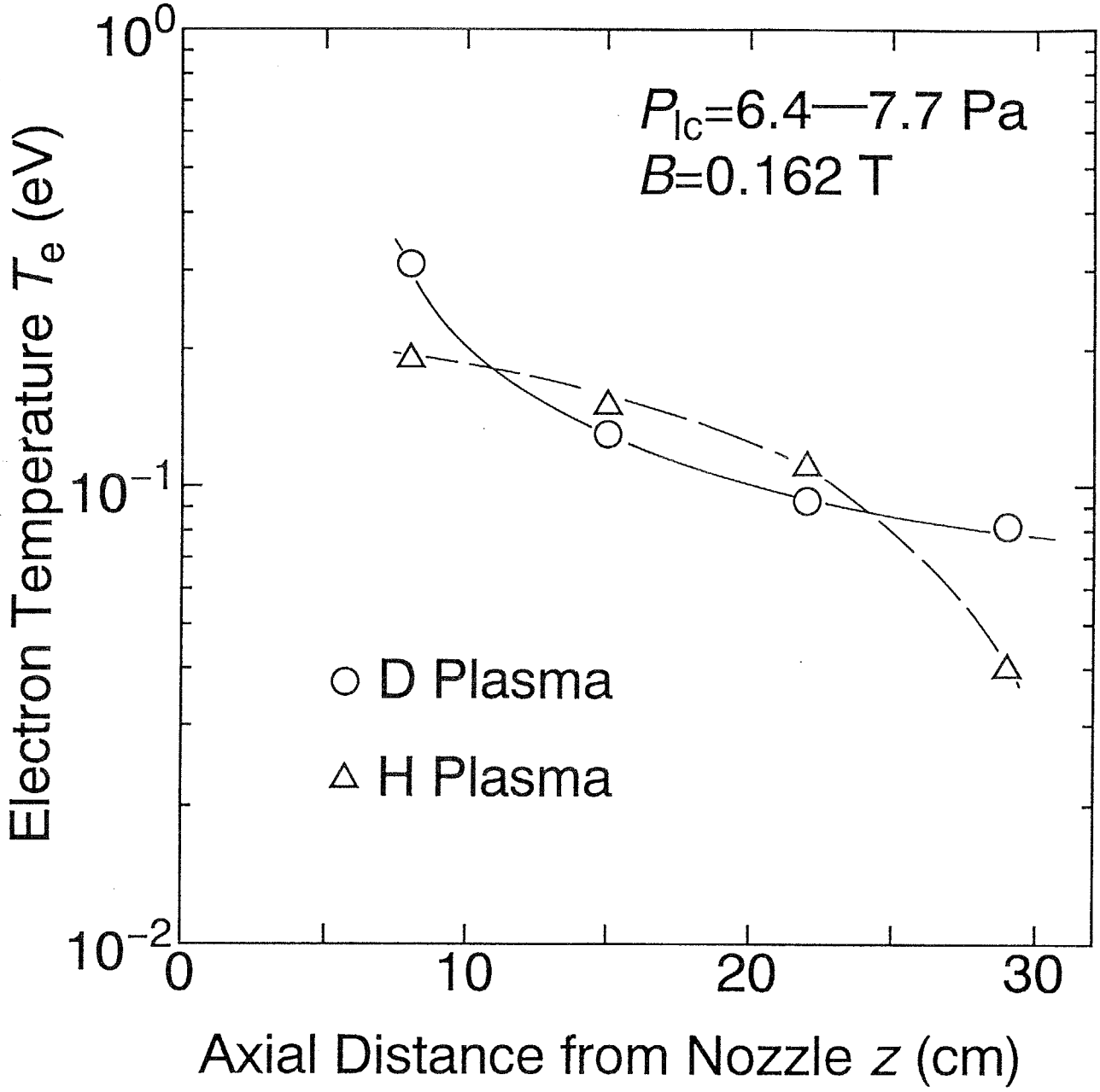

Fig. 5.8. Variation of the electron temperature T_e of a hydrogen plasma and a deuterium plasma.

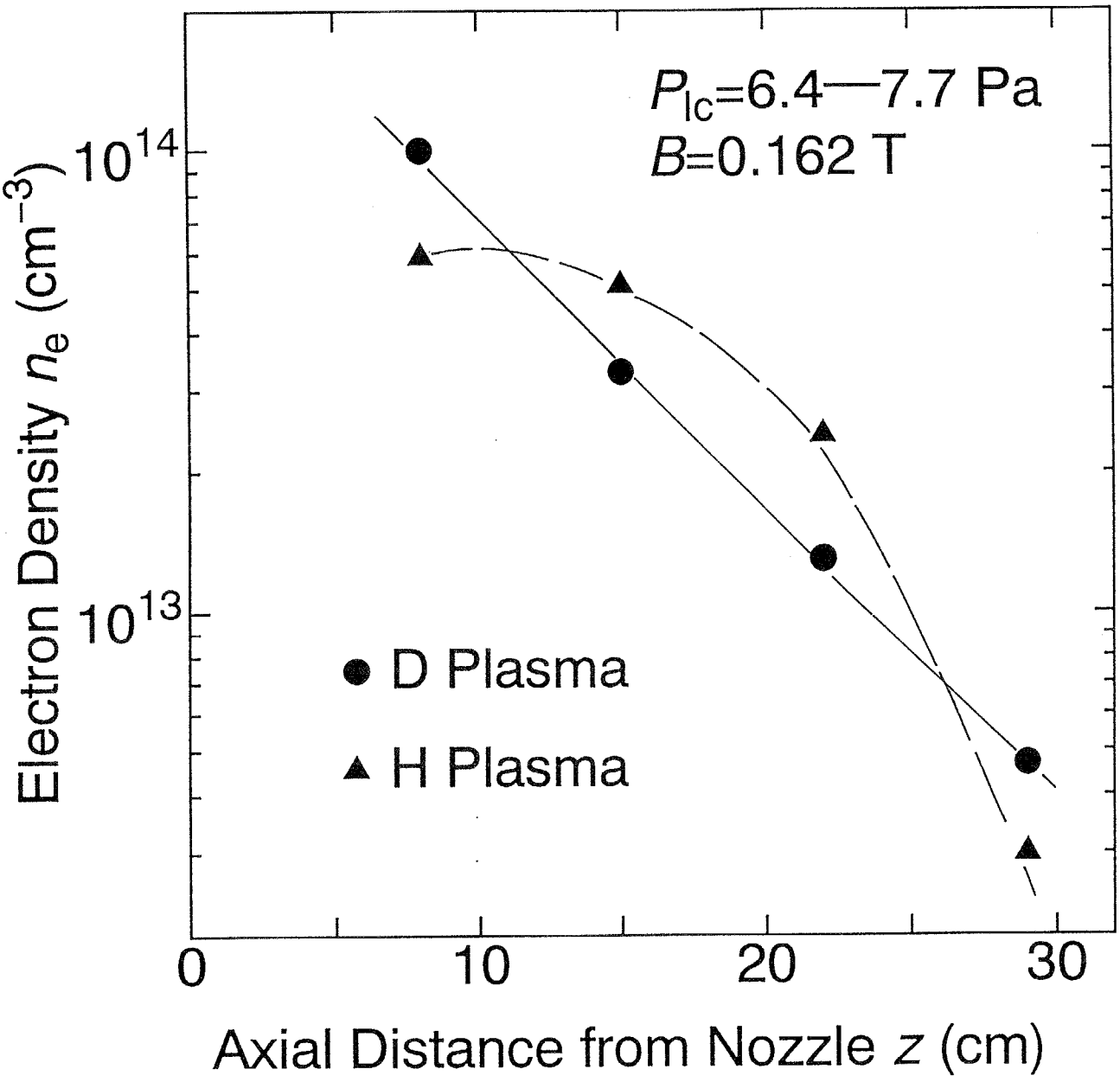

Fig. 5.9. Variation of the electron density n_e of a hydrogen plasma and a deuterium plasma.

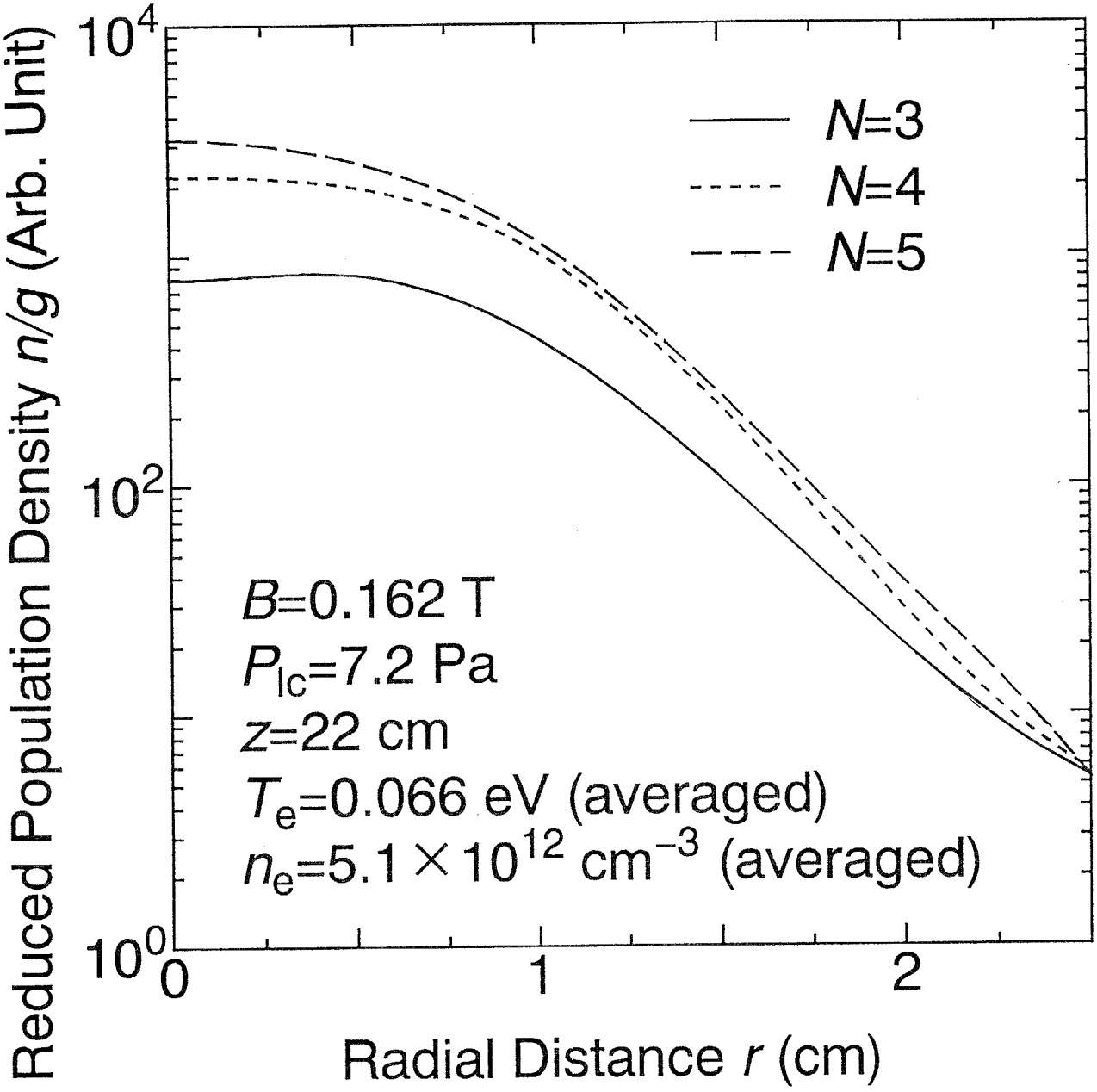

Fig. 5.10. Examples of radial profiles of the population densities of some levels of H I.

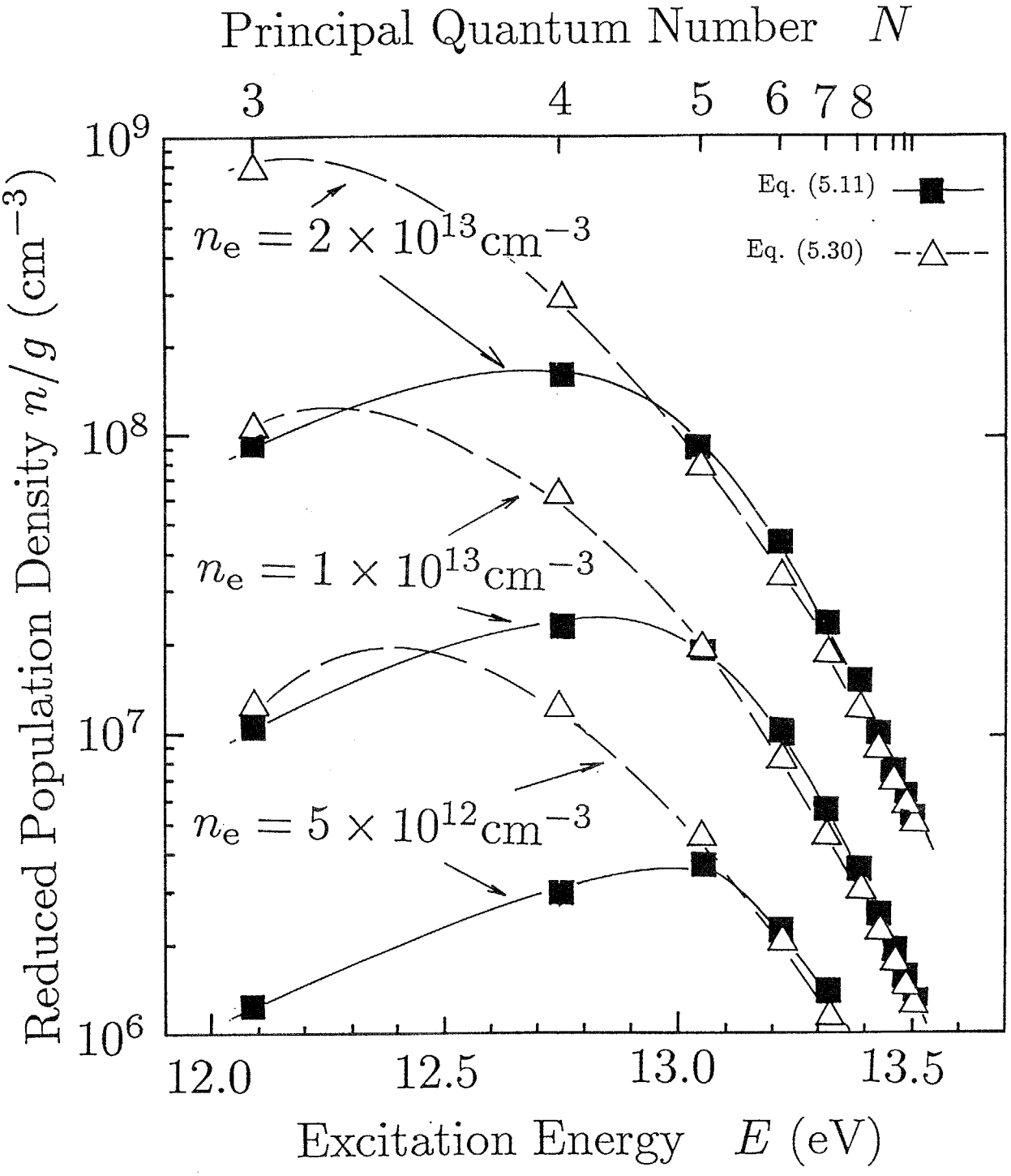

Fig. 5.11. Calculated reduced population densities n/g when the electron temperature T_e is 0.1 eV. The solid lines show them when Eqs. (5.11)-(5.12) are used for the excitation and de-excitation rate coefficients, which agree with the experiments very well. The broken lines show them when Eq.(5.30) is used instead of Eq.(5.11).

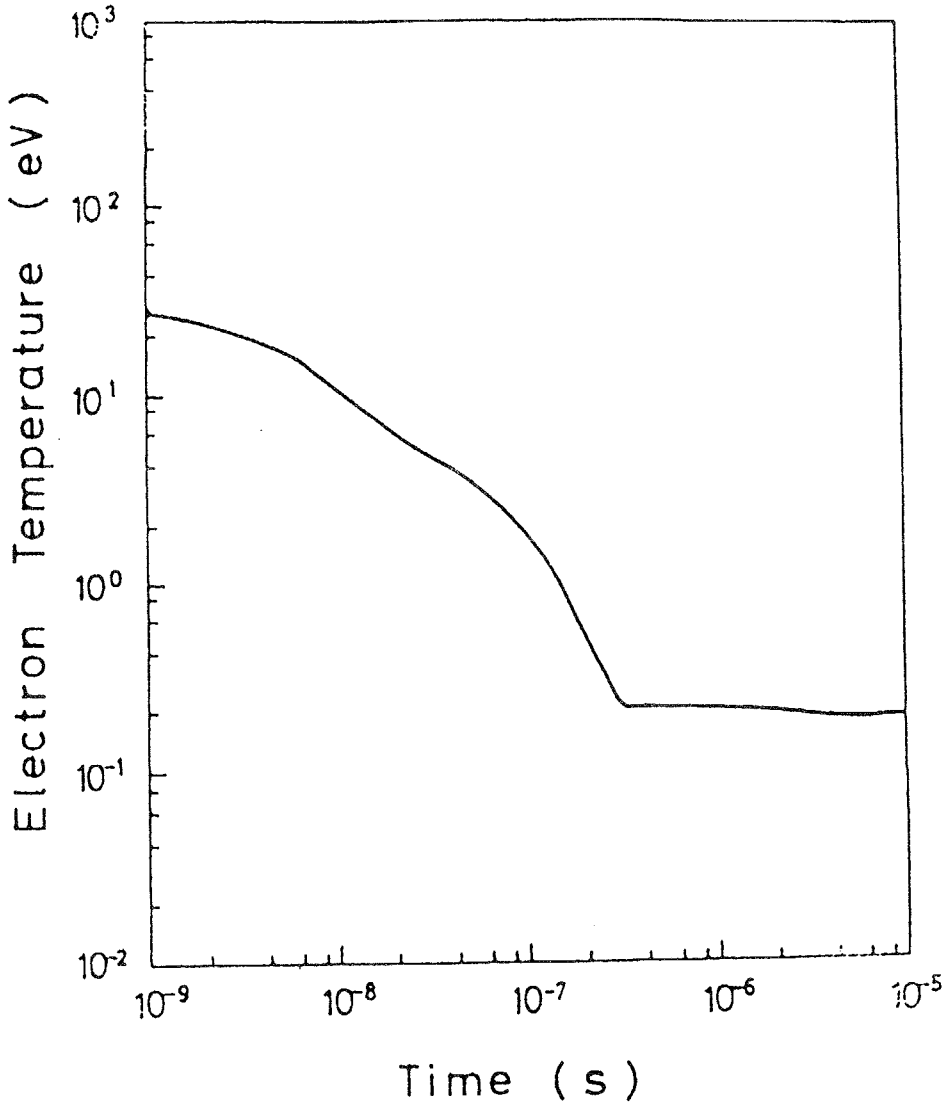

Fig. 5.12. Time history of the electron temperature calculated by Eqs. (5.39)-(5.48) with the initial conditions $n_{e0} = 3.53 \times 10^{14}$ cm^{-3}, $T_{e0} = 30$ eV, and $n(H_2) = 3.53 \times 10^{15}$ cm^{-3}. Temperatures of neutral hydrogen molecule, hydrogen molecular ion and hydrogen atom were assumed to be constant, 0.2 eV.

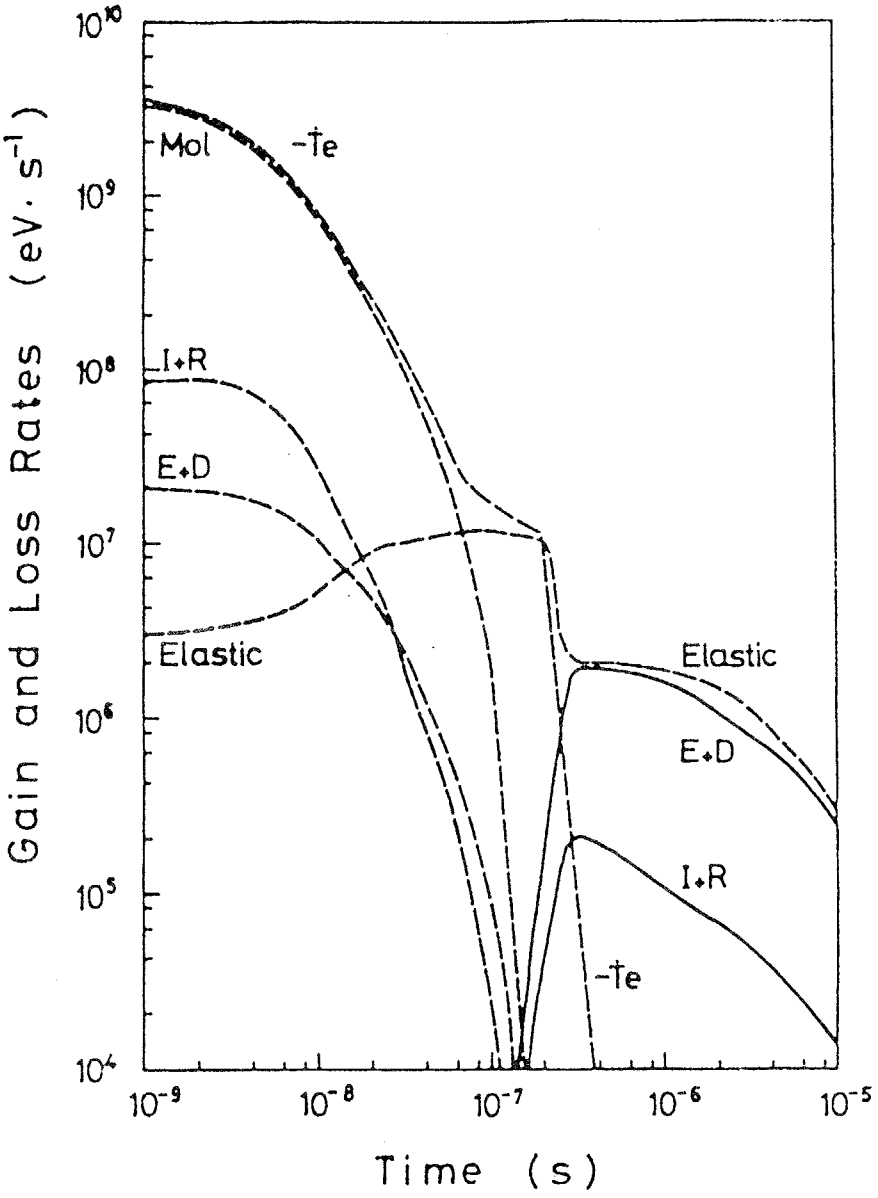

Fig. 5.13. Time history of the total energy transfer rate '$-\dot{T}_e$', the electron energy transfer rate by all the elastic collisions 'Elastic', sum of the electron energy transfer rate by ionization and recombination for H atom 'I+R' and the electron energy transfer rate by excitation and deexcitation for H atom 'E+D', sum of the electron energy transfer rate by molecular dissociation processes 'Mol'. Equations used and the initial conditions are the same as in Fig. 5.12. Full curve, energy gain > energy loss; broken curve, energy gain < energy loss.

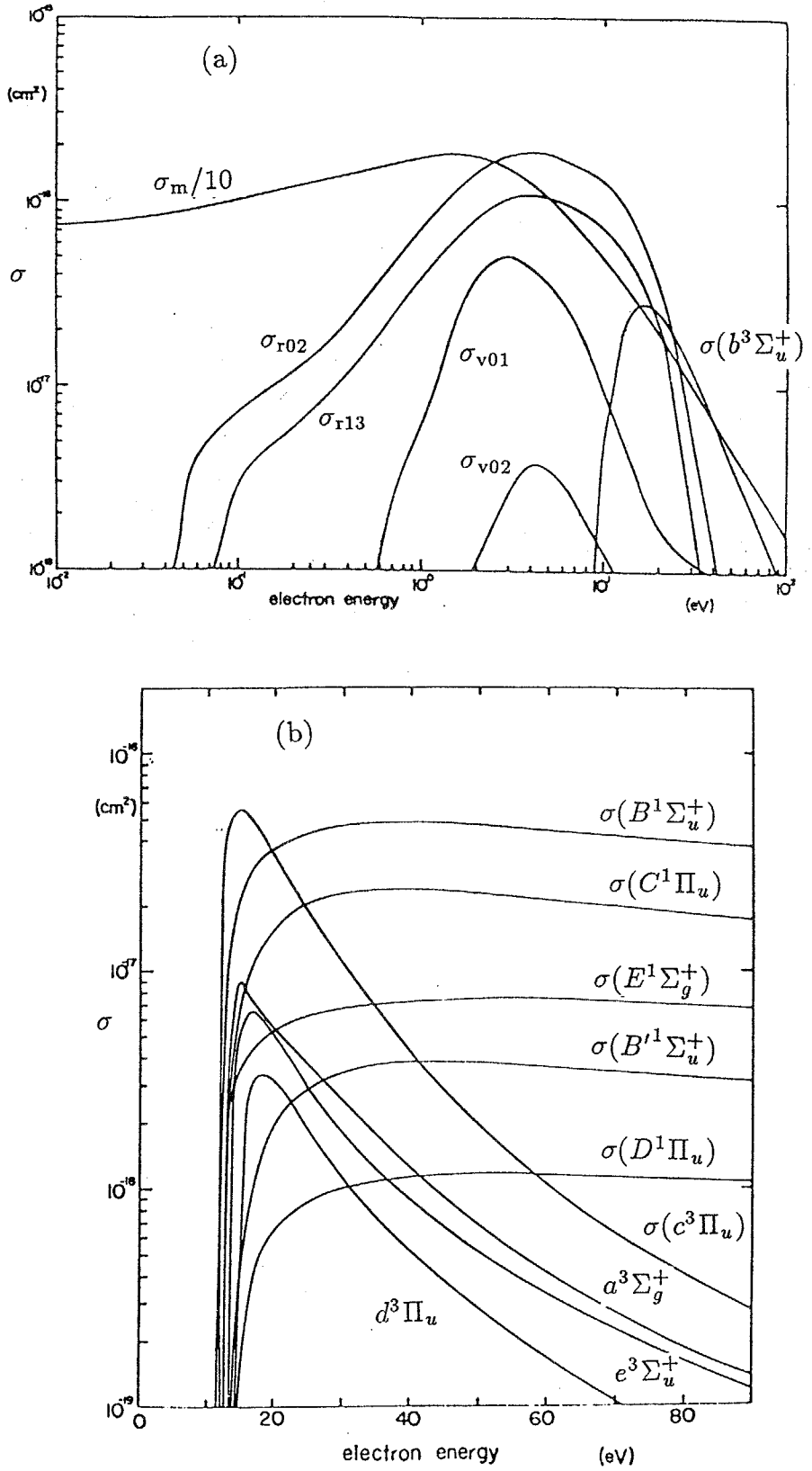

Fig. 5.14. Various cross sections of electrons in hydrogen molecule. σ_{m} denotes the momentum transfer elastic collision cross section, σ_{i} the ionization cross section, and

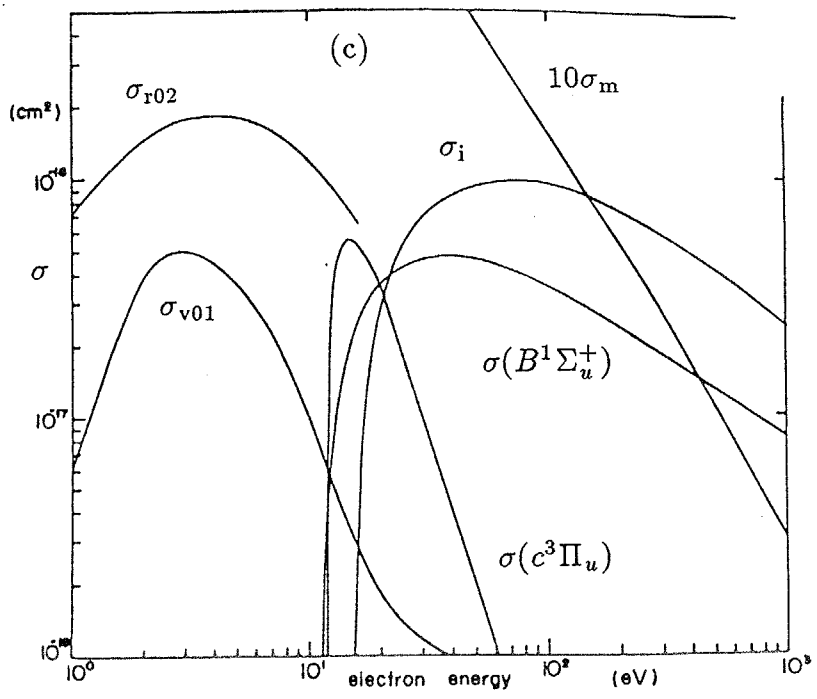

others correspond to the excitation cross sections whose arguments or subscripts show their levels. The energy levels are specified in Table 5.2.

Table 5.1 Values for each component of the population rate and of the depopulation frequency under the conditions in Figs. 5.2(b) and 5.2(d). (a) shows them at middle T_e [correspondent to Fig. 5.2(b)] and (b) at very low T_e [Fig. 5.2(d)]. 1.2E9 = 1.2×10^9, etc.

(a) at $T_e = 0.15$eV and $n_e = 2.6 \times 10^{13}\text{cm}^{-3}$ (Fig.2(b), at middle T_e)

The population rate

N	P/g ($\text{cm}^{-3}\text{s}^{-1}$)	P_{ra}/g ($\text{cm}^{-3}\text{s}^{-1}$)	P_{cd}/g ($\text{cm}^{-3}\text{s}^{-1}$)	P_{ce}/g ($\text{cm}^{-3}\text{s}^{-1}$)	P_{3r}/g ($\text{cm}^{-3}\text{s}^{-1}$)	P_{rr}/g ($\text{cm}^{-3}\text{s}^{-1}$)	n/g (cm^{-3})
3	4.2E15	1.3E15	3.0E15	3.1E8	9.6E12	2.3E13	4.0E7
4	3.7E15	1.9E14	3.5E15	9.4E12	3.1E13	9.1E12	5.9E7
5	4.1E15	3.9E13	3.6E15	3.3E14	7.7E13	4.3E12	3.3E7

The depopulation frequency

N	D (s^{-1})	D_{ra} (s^{-1})	D_{cd} (s^{-1})	D_{ce} (s^{-1})	D_{io} (s^{-1})
3	1.1E8	1.0E8	5.5E6	4.6E5	2.1E2
4	6.3E7	3.0E7	2.1E7	1.2E7	5.5E4
5	1.2E8	1.2E7	5.0E7	6.2E7	1.1E6

(b) at $T_e = 0.066$eV and $n_e = 5.1 \times 10^{12}\text{cm}^{-3}$ (Fig.2(d), at very low T_e)

The population rate

N	P/g ($\text{cm}^{-3}\text{s}^{-1}$)	P_{ra}/g ($\text{cm}^{-3}\text{s}^{-1}$)	P_{cd}/g ($\text{cm}^{-3}\text{s}^{-1}$)	P_{ce}/g ($\text{cm}^{-3}\text{s}^{-1}$)	P_{3r}/g ($\text{cm}^{-3}\text{s}^{-1}$)	P_{rr}/g ($\text{cm}^{-3}\text{s}^{-1}$)	n/g (cm^{-3})
3	7.3E14	4.6E14	2.6E14	1.8E0	1.6E11	1.4E12	7.2E6
4	6.1E14	1.2E14	4.9E14	1.4E9	5.2E11	5.7E11	1.7E7
5	5.2E14	2.5E13	4.9E14	1.6E12	1.3E12	2.8E11	2.1E7

The depopulation frequency

N	D (s^{-1})	D_{ra} (s^{-1})	D_{cd} (s^{-1})	D_{ce} (s^{-1})	D_{io} (s^{-1})
3	1.0E8	1.0E8	1.3E6	3.5E2	7.3E−5
4	3.5E7	3.0E7	4.7E6	1.6E5	5.2E0
5	2.5E7	1.2E7	1.1E7	2.4E6	1.3E3

Table 5.2 Energy levels of hydrogen molecule whose excitation cross sections from the ground state were compiled by Hayashi [85].

Level	Threshold (eV)	Peak Energy (eV)	Cross Section at the Peak (10^{-16} cm^2)
$b\ ^3\Sigma_u^+$	8.8	16	0.28
$B\ ^1\Sigma_u^+$	11.37	40	0.48
$c\ ^3\Pi_u$	11.87	15	0.56
$a\ ^3\Sigma_g^+$	11.89	15	0.09
$C\ ^1\Pi_u$	12.40	35	0.24
$E\ ^1\Sigma_g^+$	12.40	50	0.076
$e\ ^3\Sigma_u^+$	13.36	16.5	0.068
$B'\ ^1\Sigma_u^+$	13.70	40	0.038
$d\ ^3\Pi_u$	13.97	18.5	0.034
$D\ ^1\Pi_u$	14.12	50	0.012
Ion	15.425	70	0.972
r02	0.0439	4	1.84
r13	0.0727	4	1.07
v01	0.516	3	0.50
v02	1.003	4.3	0.040

Chapter 6. Experimental Study on an Arc-heated Magnetically Trapped Expanding Argon Plasma

6.1 Introduction

As was already shown, the recombining plasmas of helium and hydrogen were examined mainly by spectroscopic methods. The cooling properties were investigated. The decrease of the electron temperature was found to be mainly due to the collisions with the residual gas molecules. In addition, the population inversion was obtained in the plasmas, and the inversion in the hydrogen plasma was found to be sufficient to oscillate a cw laser between some level pairs.

Now it is expected that the plasma generated in our apparatus can be various kinds of a cw laser source, provided that the cold recombining plasmas can be generated stationarily. Apart from the nuclear fusion engineering, the spectroscopic observations of various kinds of plasmas other than hydrogen or helium, are very interesting in this sense. If the plasma is easily generated and the transition probabilities A's are already known, the population densities of the excited states can be obtained. The methods are already established in the preceding chapters. As for the populations of Ar I levels in a recombining argon plasma, the experimental examinations have been scarce. Goldfarb et al. reported the inversions of the lowest levels of $5p$ group to the $4p$ group levels [33]. However, the magnetic field was not applied there, and the transition between these levels is forbidden. It is worth while to make much more spectroscopic observations of argon plasmas of recombining phase.

In this chapter, we describe the results of the spectroscopic observations of an argon expanding plasmas, as an example of recombining plasmas. The pure argon plasmas are easily generated. And the transition probabilities of the excited states of Ar I levels were calculated in Refs. [130] and [131]. In addition, the collisional radiative model of Ar I was already reported [132,133], and in the future, it may be possible for us to evaluate

the experimental data with the calculation. Finally, we discuss the cooling property of argon plasmas, which is a little different from the plasmas of hydrogen and helium. We conclude what the essential parameter is in lowering the electron temperature of the expanding plasmas in a magnetic field.

6.2 Experimental Results

When the argon plasma was generated, the effect of the magnetic field was not observed evidently in the field strength $B \geq 0.025$ T [61]. The reason is considered that the argon ions are much heavier than those of hydrogen and helium. In the experiments in this chapter, the magnetic field was set at $B = 0.162$ T, which was again the maximum field strength in the apparatus. Other experimental conditions are almost the same with the experiments of helium plasmas.

The population densities of the excited levels of Ar I were obtained like those of He I or H I described so far. The reduced population densities averaged along the line of sight $\overline{n/g}$ are shown in Fig. 6.1(a)-(d). The Abel inversion was not applied. The axial distance from the nozzle is (a) 8 cm, (b) 15 cm, (c) 22 cm, and (d) 29 cm. Experimental errors are larger than in the experiments of He I and H I . This is mainly because the emitted photons were not sufficient. The other reason is considered to be the inaccuracy of the transition probabilities A of argon atoms. However, the Boltzmann plot has the tendency of being on a straight line for the high-lying levels. The levels are considered to be in the state of LTE [13]. Like preceding chapters, they show the electron temperature and density of the argon plasma. Since the lines of Ar II were too weak for us to detect, almost all the ions in the plasma are considered to be singly charged argon ions. Then, the same method with the helium plasma [Eq. (3.2)] and the hydrogen plasma [Eq. (5.2)] can be applied to the argon plasma when the electron temperature and the density are determined. We added the electron temperature and the density in Fig. 6.1.

6.3 Discussion

The population inversion of the optically allowed transitions was not observed even in the lowest part of the jet. It is quite different from the plasmas of hydrogen and helium. The population densities of $4p$ and $4p'$ levels are smaller than those given by Eq. (3.2). Of course, this is one of the features of the recombining plasmas and the levels are not in the state of LTE. The present results resemble the observations by Goldfarb et al. [33], and we could detect the inversions of the lowest levels of $5p$ group to the $4p$ group levels. It is concluded to be difficult for us to create a large population inversion of the levels of Ar I in a recombining argon plasma. It is suspected that this is the reason why the studies on the populations of recombining argon plasmas have hardly been reported.

Figure 6.2 shows the variations of the electron temperature and density of the argon plasma when it flows downstream. They may have considerable errors. But the important feature of the argon plasma is evident. The electron temperature is not sufficiently low to create large population inversions. It is about $T_e \simeq 0.5$ eV even at the axial distance $z = 29$ cm. It is much higher than that of the hydrogen plasma and of the helium plasma. We cannot expect population inversions at such a high electron temperature.

As was already discussed in section 3.3.1, the electron temperature of the plasma generated in our apparatus decreases maily due to the collisions with the residual gas molecules, not by an adiabatic expansion. Furukane, Sato, and Oda also reported that the elastic collisions of the electrons with them were essential to cool the elecron gas [103,104]. If this is the case, the cross section of elastic collisions between an electron and an argon atom should be examined.

Figure 6.3 shows some of the collision cross sections of electrons in the noble gases [86]. The cross section of an Ar atom (Fig. 6.3(c)) has a minimum value when $T_e \simeq 0.2$ eV. This is due to the Ramsauer effect [134]. Consequently, the collisions of the electrons in the argon plasma with the residual argon atoms are much less frequent than in the helium and hydrogen plasmas. On the other hand, Fig. 6.3 (a) shows the cross sections of electrons in He [86]. There exists no Ramsuer effect for helium. Figure 5.14(a) showed that the Ramsauer effect did not appear in hydrogen molecule, either. A momentum

transfer cross section of a helium atom is more than 10 times larger than that of an argon atom. A hydrogen molecule has a much larger cross section. The observed phenomena confirm the preceding conclusions, that is, the electrons in our plasma are cooled by the collisions with the residual molecules in the expanding plasma area.

6.4 Conclusion

A stationary recombining argon plasma was generated in the arc-heated magnetically trapped expanding plasma jet generator. The spectroscopic observations were carried out like a helium and a hydrogen plasma. Different from helium and hydrogen plasmas, the population inversions in the optically allowed transitions were not observed, although the the population densities of $4p$ levels tend to be smaller than those supposed to be in the state of LTE. The electron temperature was not low enough even in the most downstream of the jet. It was about $T_e \simeq 0.5$ eV, which was much higer than that of the hydrogen and the helium plasma. In the preceding chapters, we had discussed that the electrons in the present experiments became cold mainly by the collisions with the residual gas molecules. The elastic collision cross section of electrons in an argon gas has a minimum value when the energy of the electrons is 0.2 eV due to the Ramsauer effect. Therefore, the electrons in the argon plasma do not collide with the residual argon atoms in the plasma expansion area, and it is dificult to decrease the electron temperature. The results in this chapter reconfirm the discussion in the previous section. Namely, the collisions of the electrons with the residual gas decrease the electron temperature of the recombining plasma in a magnetic field.

The results of chapter 6 have been partly published in Ref. [70].

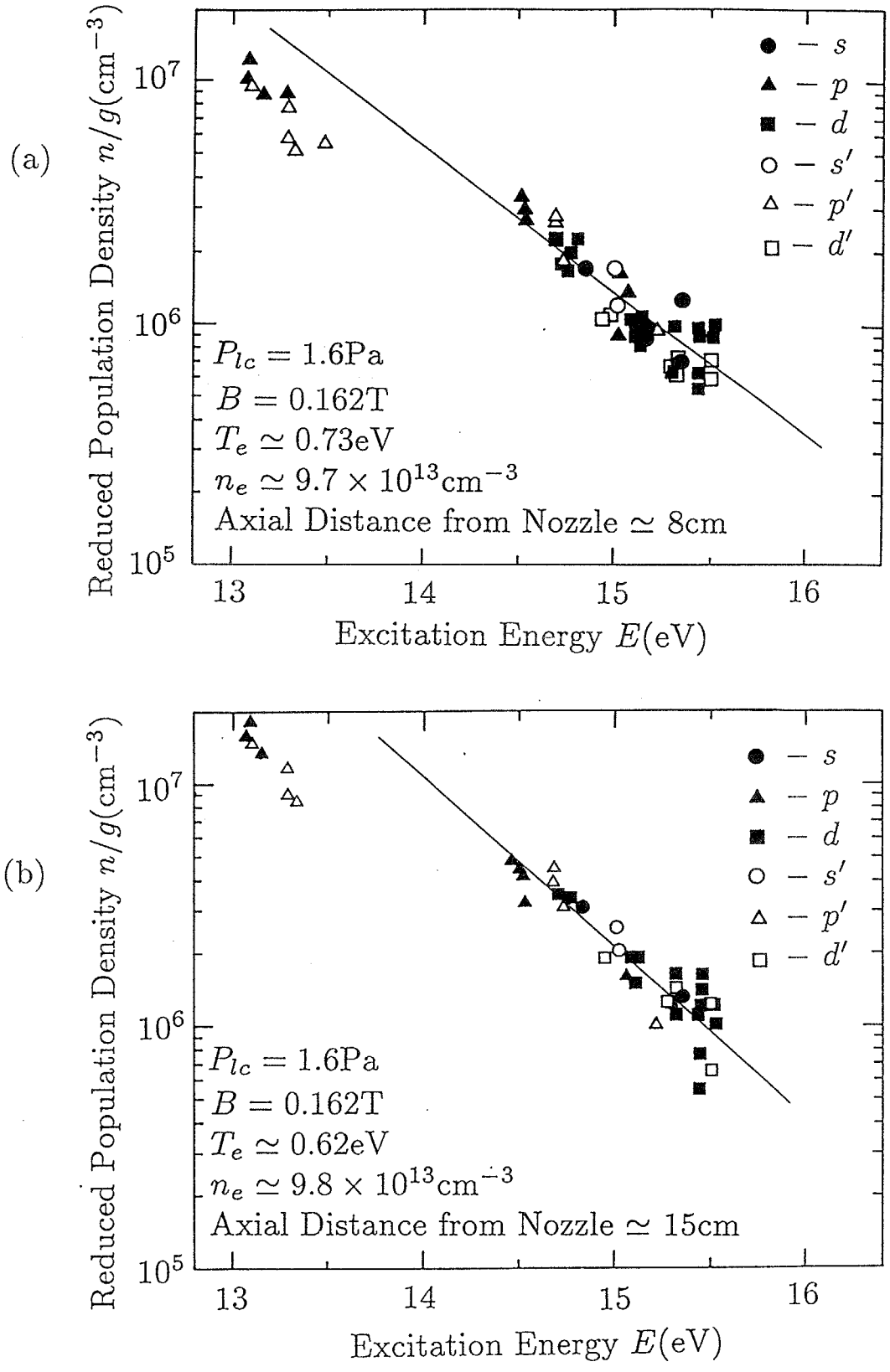

Fig. 6.1. Boltzmann plots of the populations of argon atoms. The solid lines show the Saha-Boltzmann populations given by Eq. (3.2). The pressure in the plasma expanding region $P_{\mathrm{lc}} = 1.6$ Pa and the strength of the magnetic field $B = 0.162$ T. The pressure in

(c)

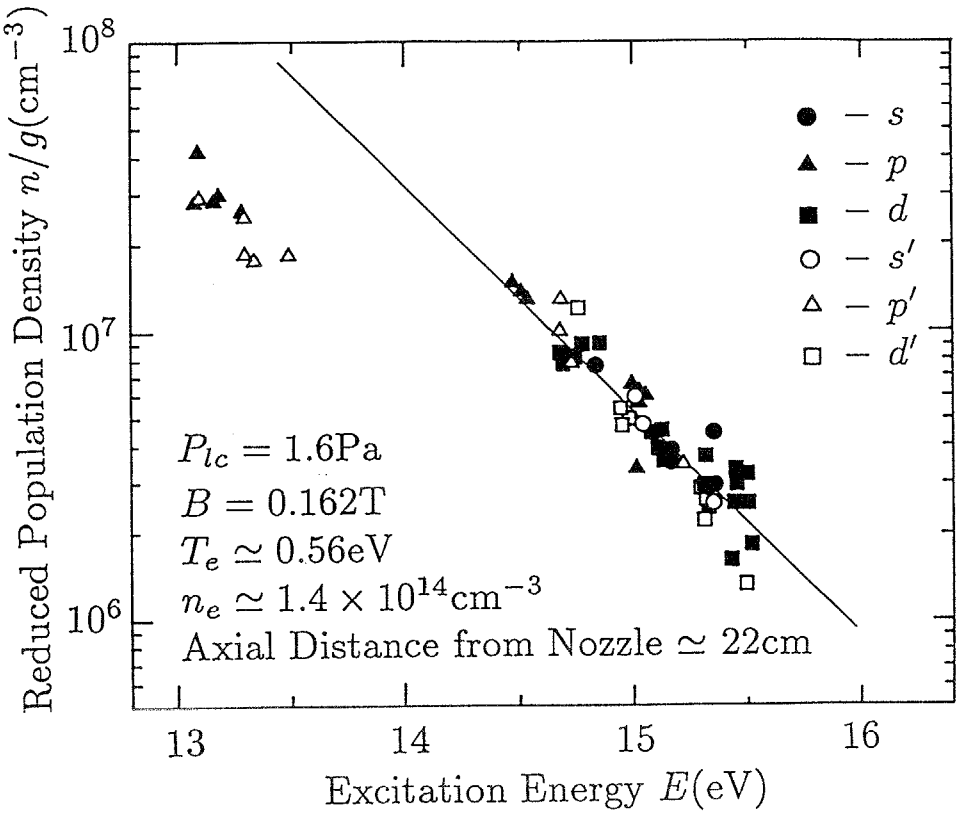

(d)

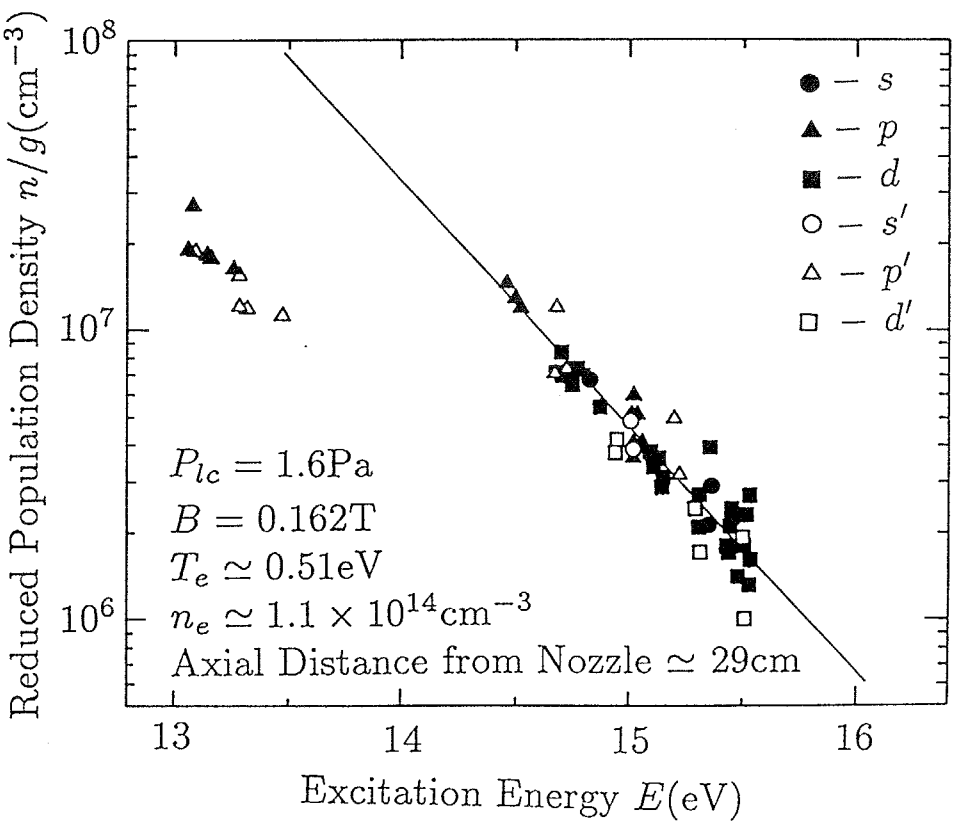

the discharging region $P_{\mathrm{dc}} = 1.0 \times 10^5$ Pa. The axial distance from the nozzle is 8 cm, 15 cm, 22 cm, and 29 cm in (a), (b), (c), and (d), respectively.

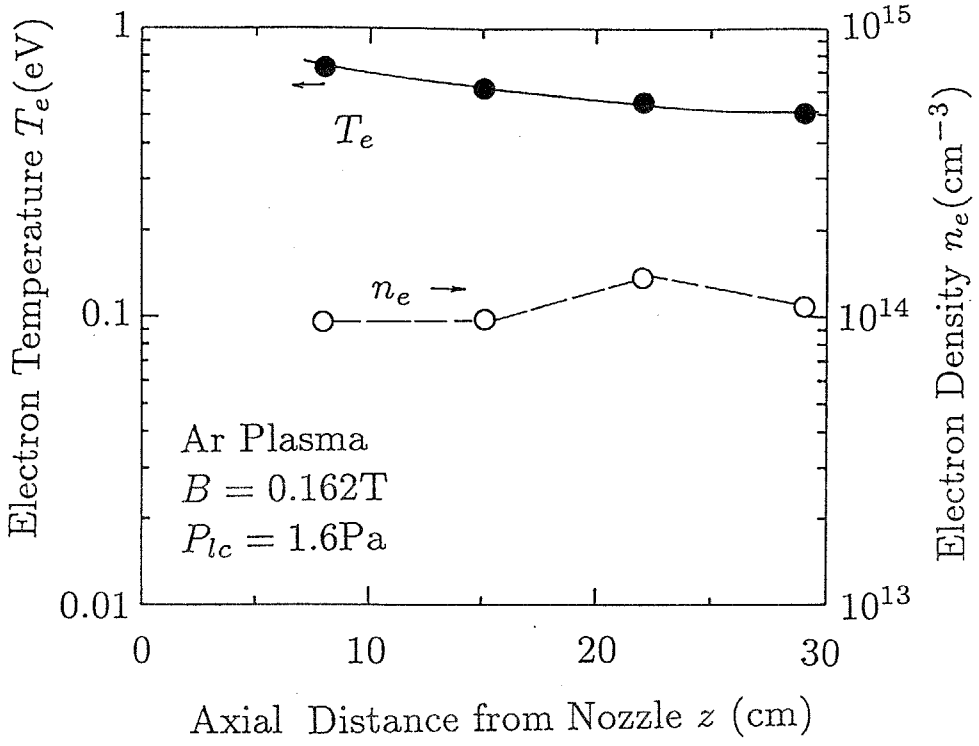

Fig. 6.2. Variations of the electron temperature T_e and n_e of the argon plasma. Experimental conditions are the same as in Fig. 6.1.

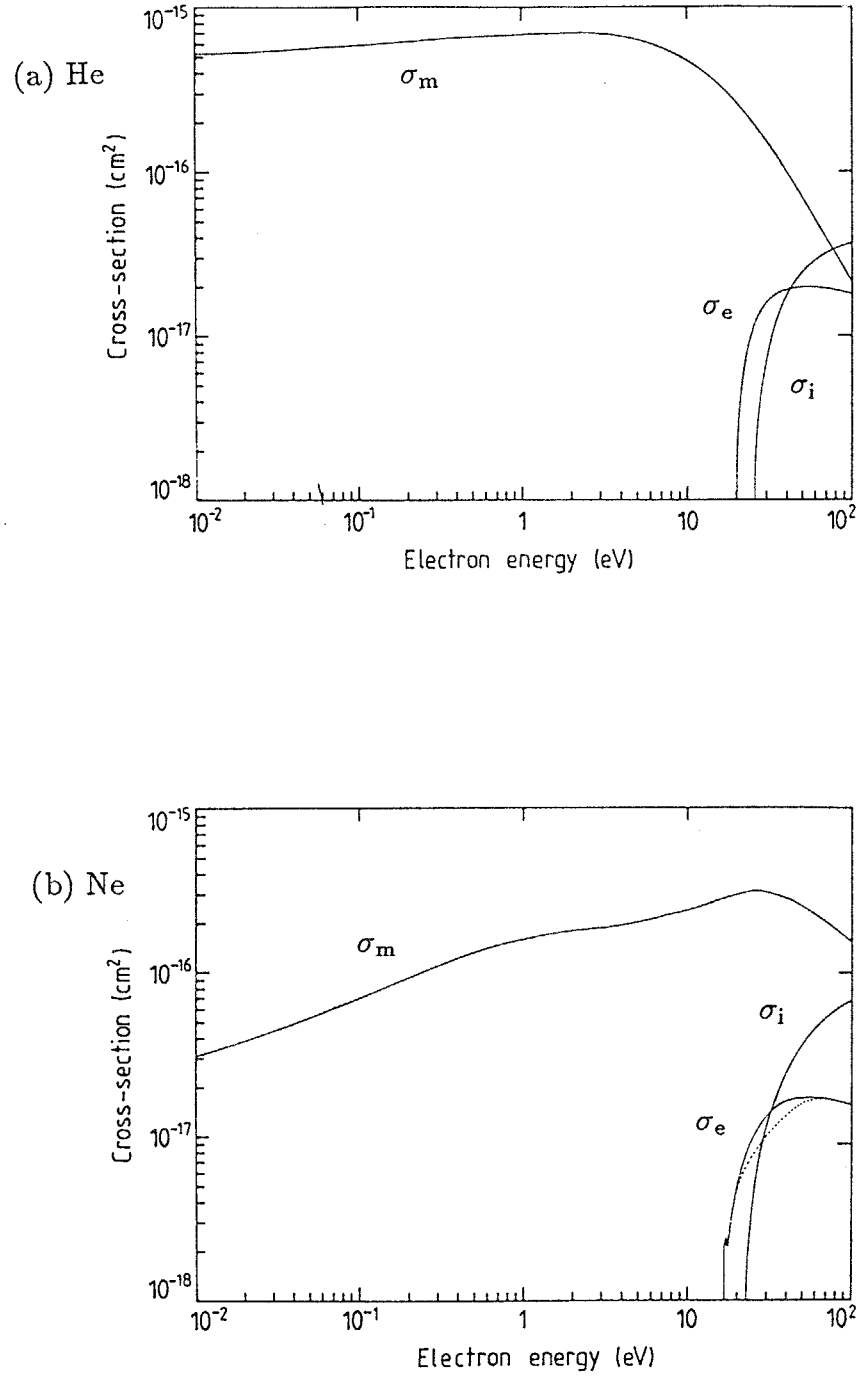

Fig. 6.3. Cross sections of electrons in the noble gases. (a):He, (b):Ne, (c):Ar, (d):Kr, (e):Xe. The quantity σ_m is the elastic momentum transfer cross section, σ_e is the total excitation cross section, and σ_i is the ionization cross section. Broken curves correspond to Hayashi's original total excitation cross section.

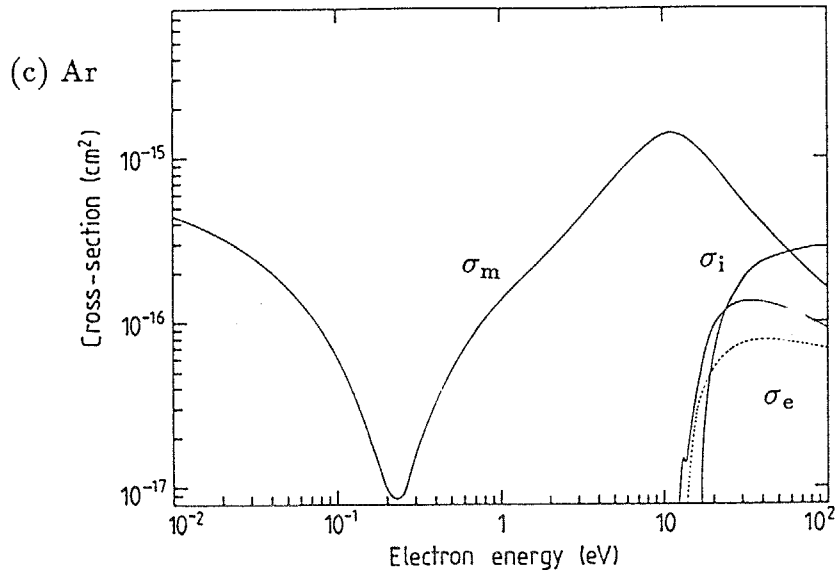
(c) Ar
Cross-section (cm²)
10⁻¹⁵
10⁻¹⁶
10⁻¹⁷
σm
σi
σe
10⁻²
10⁻¹
1
10
10²
Electron energy (eV)

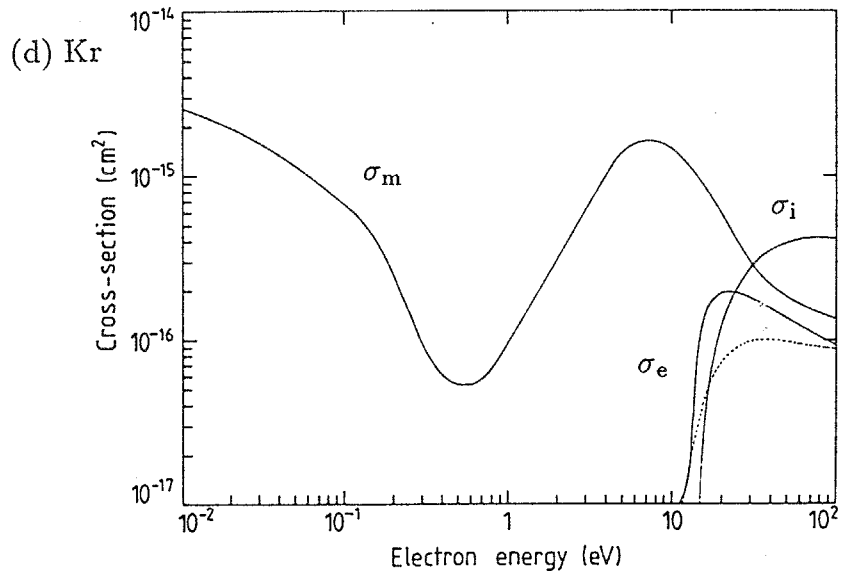
(d) Kr
Cross-section (cm²)
10⁻¹⁴
10⁻¹⁵
10⁻¹⁶
10⁻¹⁷
σm
σi
σe
10⁻²
10⁻¹
1
10
10²
Electron energy (eV)

Fig. 6.3. (Contd.)

(e) Xe

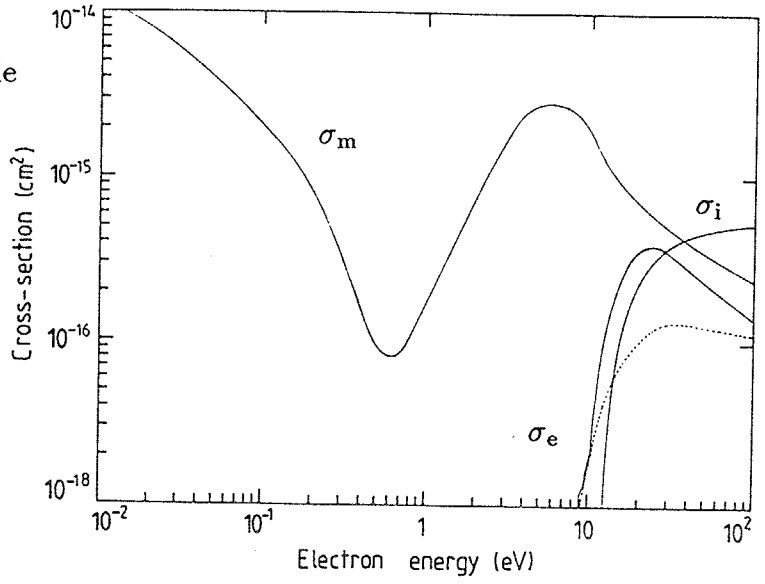

Fig. 6.3. (Contd.)

Chapter 7. Conclusion

7.1 Summary

We have investigated the spectroscopic characteristics of the "Arc-heated magnetically trapped expanding plasma jet". We generated helium, hydrogen, deuterium, and argon plasmas in a recombining phase. The variation of the electron temperature and density is also examined, mainly by the spectroscopic observations. The results and conclusions obtained are summarized in this chapter.

First, we developed a plasma generator, which can continuously generate a cold recombining expanding plasma in a magnetic field. An ordinary arc discharge is used in initial heating before the expansion. We called the generator "an Arc-heated magnetically trapped expanding plasma generator". We generated a helium plasma and examined its electron temperature and density at several positions in a various strength of a magnetic field, by means of a Langmuir probe. We roughly estimated its parameters, and it was confirmed that the electron temperature $T_e \simeq 0.1$ eV and the electron density $n_e \simeq 1 \times 10^{13}$ cm^{-3}. It was expected that the spectroscopic observations could detect the characteristics of the plasma, without being perturbed by the beam-gas interactions. Some other applications were introduced, such as a cluster preparer. These were shown in chapter 2.

Next, we examined the spectroscopic characteristics of the helium plasma. We measured the population densities of some excited levels of He I states. Population inversions were observed between several low-lying level pairs, such as $4^1S - 3^1P$, and $4^3P - 3^3D$, in optically allowed transitions, although it was still insufficient for us to oscillate a cw He I laser. For high-lying levels, the population densities were considered to be described by the Saha-Boltzmann equation [Eq. (3.2)], and the levels were in the states of LTE (local thermodynamic equilibrium). The radial distributions of some excited states were examined by applying the Abel inversion. At the edge of the plasma off axis, the popula-

tion densities of N^1P levels were larger than the other levels. It means that the resonance absorption of the VUV lines of the transitions to the ground state was essential, and the plasma was considered to be optically thick for the transitions. The electron temperature and density were determined by the spectroscopic observations. Then, we discussed the effect of the magnetic field and the pressure of the plasma expansion area on the plasma parameters. Consequently, it was found that the electron temperature was roughly controlled by the pressure of the expanding plasma region, whereas the electron density was roughly controlled by the magnetic field. The cooling of the electron in the plasma under a substantial magnetic field was mainly accomplished by the collisions with residual gas molecules in the expanding region. These were discussed in chapter 3.

In chapter 4, we treated the numerical analysis of excited-level populatins of He I levels based on a collisional radiative model. We modified slightly the conventional collisional radiative model for the recombining plasmas in which the opacity effect for the transitions to the ground state was not negligible. We included the radiation trapping by the background residual helium in the calculation. It was shown that our helium plasma was optically thick for the transitions to the ground state, while it was optically thin for any other transitions. The population densities of the singlet state were drastically affected by the background pressure, whereas those of the triplet state were hardly affected. For the level pairs of the singlet system when the plasma was optically thin, the laser lower levels depopulated mainly through radiative decay. On the other hand, when it became optically thick for the transitions to the ground state, they depopulated mainly through electron collisional-deexcitation, and the total depopulation frequency decreased. The optical thickness was found to be an obstacle for making large population inversions, particularly for the level pairs whose lower level was 2^1P. We discussed the background pressure required for the laser oscillation between some level pairs. The background pressure should be in the range of 10^{-1} Pa. When we made the pressure about this level, the electrons were not cooled effectively. Therefore, if we would like to cool the electron gas without increasing the optical thickness, the plasma should be cooled by contact with

another kind of gases other than the plasma itself. The experimental results described in chapter 3 were well explained by the calculation when the Abel inversion was applied to the data.

In chapter 5, we treated the hydrogen plasma. Strictly speaking, the plasma was a hydrogen-helium mixed plasma. The spectroscopic observations, however, showed that almost all the ions in the plasma were hydrogen ions, and it may be called a hydrogen plasma in that sense. The helium gas in the discharging region took a role of a buffer gas. The populations of excited levels were measured like a helium plasma. It was found that the population inversion was sufficient for the cw lasing between the levels of the principal quantum number $4-3$ and $5-4$. The plasma parameters were also examined. The variations of the electron temperature and density were investigated for a deuterium plasma as well as a hydrogen plasma. They were found to be not much different from each other. It was considered that the collisions between charged particles and neutral species were frequent in the pressure range $1-20$ Pa. The numerical analysis was carried out by the collisional radiative model in which the plasma was optically thin. The experimental results were well explained by the model. The hydrogen plasma was considered to be optically thin, which was quite different from the helium plasma. The residual hydrogen took a form of a diatomic molecule, not a monoatomic molecule, hence the plasma became optically thin. The electron temperature was so low in the plasma that the sufficient attention should be paid to calculating the rate coefficeints of the elementary proceses in the plasma.

Finally, in chapter 6, we examined the argon plasma experimentally. Being different from the plasmas of helium and hydrogen, the inversion of allowed transitions were not observed. The electron temperature was much higher than those of the plasmas of helium and hydrogen. It was already found that the electron was cooled mainly by the collisions in the expanding plasma area. And the total elastic collision cross section of electrons in argon gas had a minimum value at $T_e \simeq 0.2$ eV owing to the Ramsauer effect. It meant that the electron with about this energy hardly collided with the argon molecule.

Therefore the cooling of the electrons in the argon plasma became ineffective. If we would like to cool the electrons in the plasma, we must let another kind of gas mix with the expanding regions, such as hydrogen, which has a large cross section, and collide electrons with them. These results can be applied to the cooling of the plasma in a magnetic field, such as a divertor plasma of a nuclear fusion reactor. It means that the principles of gas target divertor were, in some sense, confirmed in the present study. Even when the adiabatic expansion is not expected because of the strong magnetic field, the gas contact cooling was effectively accomplished.

7.2 Concluding Remarks

7.2.1 Scaling for a short-wavelength laser in terms of atomic processes

It was shown that the recombining hydrogen plasma could be a lasing medium in Chapter 5. Of course, in the present study, it was limited to an infrared wavelength range, since we would use the Paschen series. However, the recombination pumping is expected to be effective for a short-wavelength region, therefore, it is worth while to confirm the scaling law to a hydrogen-like ion of multicharged ions of heavy elements [13].

Now we consider atomic parameters for a hydrogen-like ion with nuclear charge $\tilde{z}$. We suffix the corresponding parameter of neutral hydrogen atom with "H". The present scaling laws are valid for the ions for which relativistic effects are insignificant ($\tilde{z} \leq 20$). The derivation of these scaling laws was shown in Ref. [13] in detail, therefore, we show only the results here. For the following coefficients, we have

$$f_{q,p} = f^{\mathrm{H}}_{q,p}, \tag{7.1}$$

$$A(p,q) = \tilde{z}^4 A^{\mathrm{H}}(p,q), \tag{7.2}$$

$$C(q,p;T_{\mathrm{e}}) = \tilde{z}^{-3} C^{\mathrm{H}}(q,p;T^{\mathrm{H}}_{\mathrm{e}}), \tag{7.3}$$

$$F(p,q;T_{\rm e}) = \tilde{z}^{-3} F^{\rm H}(p,q;T_{\rm e}^{\rm H}), \tag{7.4}$$

$$S(q;T_{\rm e}) = \tilde{z}^{-3} S^{\rm H}(q;T_{\rm e}^{\rm H}), \tag{7.5}$$

$$\alpha(q;T_{\rm e}) = \tilde{z}^{-3} \alpha^{\rm H}(q;T_{\rm e}^{\rm H}), \tag{7.6}$$

$$\beta(q;T_{\rm e}) = \tilde{z} \beta^{\rm H}(q;T_{\rm e}^{\rm H}), \tag{7.7}$$

using the scaled electron temperature $T_{\rm e}^{\rm H}$. For the electron temperature and density, the scaling law is written as follows:

$$T_{\rm e} = \tilde{z}^2 T_{\rm e}^{\rm H}, \tag{7.8}$$

$$n_{\rm e} = \tilde{z}^7 n_{\rm e}^{\rm H}. \tag{7.9}$$

We refer $T_{\rm e}^{\rm H}$ and $n_{\rm e}^{\rm H}$ as the reduced electron temperatrure and the reduced electron density, respectively. With these scaling, the time derivative of the population density of the level p is written as follows:

$$\begin{aligned}
\frac{{\rm d}n(p)}{{\rm d}t} = \; & \tilde{z}^4 \left[\sum_{q<p} C^{\rm H}(q,p) n_{\rm e}^{\rm H} n(q) + \sum_{q>p} \left\{ F^{\rm H}(q,p) n_{\rm e}^{\rm H} + A^{\rm H}(q,p) \right\} n(q) \right] \\
& - \tilde{z}^4 \left[\left\{ \sum_{q<p} F^{\rm H}(p,q) + \sum_{q>p} C^{\rm H}(p,q) + S^{\rm H}(p) \right\} n_{\rm e}^{\rm H} + \sum_{q<p} A^{\rm H}(p,q) \right] n(p) \\
& + \tilde{z}^8 \left\{ \alpha^{\rm H}(p) n_{\rm e}^{\rm H} + \beta^{\rm H}(p) \right\} n_{\rm i} n_{\rm e}^{\rm H}.
\end{aligned} \tag{7.10}$$

If the ion density is scaled as

$$n_{\rm i} = \tilde{z}^{-4} n_{\rm i}^{\rm H}, \tag{7.11}$$

then, the reduced population density of the level p becomes completely the same with the hydrogen plasma whose electron temperature is $T_{\rm e}^{\rm H}$ and whose electron density is $n_{\rm e}^{\rm H}$. On the other hand, the threshold overpopulation density for the laser oscillation is given by Eq. (5.4). When we consider the photon energy scales as $\tilde{z}^2$, it means

$$\lambda \propto \lambda^{\mathrm{H}}/(\tilde{z}^2). \tag{7.12}$$

If we consider Eq. (7.2) and other coefficients are assumed to be constant, we have the scaling law as

$$\Delta[n/g]_{\mathrm{th}} \propto \tilde{z}^2. \tag{7.13}$$

As a matter of fact, it is very difficult to manufacture mirrors with a high reflectivity in a short-wavelength region. Therefore, the laser oscillation is much more difficult than that given by Eq. (7.12).

Fortunately, the upper limit of the ion density is not given by Eq. (7.11). When the ions are fully ionized, the upper limit of the ion density is given by the following:

$$n_{\mathrm{i}}^{\text{Fully Stripped}} = n_{\mathrm{e}}/\tilde{z} = \tilde{z}^6 n_{\mathrm{e}}^{\mathrm{H}}. \tag{7.14}$$

If we substitute $n_{\mathrm{i}}^{\text{Fully Stripped}}$ for n_{i} in Eq. (7.10), the corresponding ion density becomes $\tilde{z}^{10} n_{\mathrm{i}}$. We showed the population densities in a recombining plasma was given by the first term in Eq. (5.20). Namely, in a fully stripped recombining hydrogen-like plasma, the population density becomes $\tilde{z}^{10}$ times of that of the hydrogen plasma with the same reduced electron temperature and density, since the population coefficients are independent of the ion density. Therefore, even if the threshold population density increases much more rapidly than that shown in Eq. (7.13), we can expect the laser oscillation using a multi-charged hydrogen-like ion. Of course, it requires substantial energy, therefore, it is still difficult to oscillate cw short wavelength lasers.

There is another reason that the recombination pumping is not advantageous for a long-pulse laser. It is obvious that the time scale for the recombination becomes shorter as $\tilde{z}$ increases from Eq. (7.10). As for the recombination term, the dependence is $\propto \tilde{z}^8$. On the other hand, other terms have $\tilde{z}^4$ dependence. In other words, with an increase in $\tilde{z}$, the recombination rate coefficient increases much faster than other rate coefficients.

Hence, if we would like to have a short wavelength laser, we should concentrate on an oscillation of a pulse mode. At present, it is very difficult to develop a cw short wavelength laser.

In terms of atomic processes, the investigations on the short wavelength lasers are scaled in the present study. Namely, when the electron temperature and density are given, we can calculate the population densities in the way described so far. Therefore, the next problem is how to make such a plasma with a low electron temperature and a high density. We need fluid dynamical investigations in order to solve this problem, which is beyond this thesis. We already described that the source flow calculation was easy. But if we use sufficiently strong magnetic field, the problem becomes very difficult. In addition, if we try to solve the dynamic equations with reactions in a magnetic field, the equations seem to be stiff. It seems that the problem is too difficult for us to solve now, and it is our future task.

7.2.2 Future R & D Issues in a nuclear fusion engineering

So far, we described the characteristics of our plasma observed experimentally. When we try to use our plasma generator as a simulator of a divertor plasma, it is found that the number density of electrons and ions is sufficient, but that the electron temperature is not as high as that in a divertor. Table 7.1 shows the characteristic values of some of the divertor simulators [54]. If we would like to simulate it, we have to heat the plasma after being spouted from the nozzle like NAGDIS-I.

In TPD-I, the plasma is only coming out from the nozzle, and they use PIG discharge with a LaB_6 cathode. In NAGDIS, they also use a LaB_6 cathode. In the present study, we used a simple arc discharge with a thoriated tungsten cathode. It is obvious that the arc discharge is less advantageous than the PIG discharge with regard to the initial temperature. We should improve our apparatus in two points. (1) we should use a PIG discharge with a LaB_6 cathode and increase the initial temperature of the plasma before

expansion. (2) we should heat the plasma after coming out to the expanding area like NAGDIS-I. For example, we can propose RF heating. It is our future task.

However, the density is satisfactory, and even now, we can propose many experiments with this apparatus in a field of nuclear fusion engineering, particularly material irradiation and heat flux measurements, although they are beyond the scope of this thesis. When we estimate the heat flux from the divertor plasma to a divertor plate, we often use the heat transfer coefficient of a sheath. However, if we use only the sheath theory, we cannot consider the recombination effects of ions and the reflection of ions, which are very dominant processes in the plasma of a low temperature and a high density. When we need a lower temperature plasma in the investigations of surface errosion of various materials for reactor walls, it is naturally concluded that the present appatratus is very useful even at present.

Table 7.1 Comparison of the characteristic parameters of the present divertor simulators and the present plasma generator.

	NAGDIS-I	TPD-I	MAP-2	PISCES-A	Present
Cathode	LaB_6	LaB_6	LaB_6	LaB_6	W-Th
B (T)	0.15	0.5	0.06	0.2	0.16
Working Gas	H_2, D_2, He,Ar	H_2, D_2, He	H_2, He, Ar	H_2, D_2, He,Ar	H_2, D_2, He,Ar
Mode	cw, pulse	cw	cw	cw, pulse	cw
DC Power	200V×150A	200V×150A	100V×70A	250A	20V×120A
Plasma Length (m)	2	2		1.6	0.3
Plasma Diameter (cm)	~ 12	~ 2	~ 5	~ 5	$\sim 5-8$
n_e (10^{13} cm^{-3})	0.5(H_2) 1(Ar)	10(He)	1 (H_2)	0.5 (H_2) 10(Ar)	1 (H_2) 10(Ar)
T_e (eV)	$5 \sim 15$	$5 \sim 10$	$2.5 \sim 14$	$3 \sim 30$	$0.07 \sim 0.5$
T_i (eV)	$1 \sim 3$	$1 \sim 3$	$1 \sim 3$	$1 \sim 3$	$0.07 \sim 0.4$

Acknowledgments

The author thanks Professor M. Suzuki of Research Laboratory for Nuclear Reactors (R.L.N.R.) of Tokyo Institute of Technology (T.I.Tech.) very much, for valuable discussions and continuous encouragements throughout this work. He also thanks Professor R. Shimada, Professor M. Okamoto, Professor H. Yamasaki, and Professor Y. Oguri, of R.L.N.R. of T.I.Tech., Professor H. Kitazawa and Professor Y. Hatano of T.I.Tech., Professor T. Fujimoto of Kyoto University, Professor K. Sato of National Institute for Fusion Science for their kind discussions, and Mr. H. Miyabayashi of R.L.N.R. of T.I.Tech. for his technical support on this program. The author acknowledges his indebtness to Professor J. Heberline of University of Minnesota. The author is also grateful to T. Goto, M. Ohta, Y. Aihara, M. Nishikubo, M. Yamamoto, T. Sone, H. Kinoshita, M. Komatsubara, M. Hirayama, M. Umebayashi, and N. Ohtsuki, who are graduates or students of Suzuki Laboratory of R.L.N.R. of T.I.Tech., for their collaborations. He thanks Dr. H. Tsutsui of R.L.N.R. of T.I.Tech. for his advice on the compilation of this thesis, and Dr. M. Okubo and Mr. F. Nishimura of R.L.N.R. of T.I.Tech. for their help in collecting some of the references in this thesis. The author also thanks Dr. A. Okino of T.I.Tech., who majors in plasma spectroscopy, gave the author valuable advice, and is a genuine colleague of the author.

He thanks Professor Y. Fujii-e, Professor A. Shimizu, Professor Y. Fujii, Professor R. Takagi, Professor H. Sekimoto, Professor H. Tomiyasu, Professor M. Igashira, Professor T. Yano, Professor T. Hattori, Professor M. Saito, Professor H. Ninokata, Dr. T. Kato, Mr. M. Harada, Mr. T. Sawada, Mr. T. Ohsaki, Mr. H. Matsuura and, especially, Mr. T. Obara of R.L.N.R. of T.I.Tech. for their continuous encouragements. He also thanks many other professors, researchers and students of R.L.N.R. of T.I.Tech. for their encouragements. He thanks Mr. T. Hamuro of Canon Inc. for his encouragement on the fundamental researches, and Mr. T. Shinoda, general manager of NEC Corp., for his kind encouragement beyond self-interest. The author thanks Professor M. Tomita of

Kyoto Prefectural University and the late Professor M. Sakisaka of Kyoto University, who taught what the physical experimets and the science should be to the author. Finally, he thanks Dr. S. Kawamura of Caltech., who shows the author how and what the scientists should be and how precious the science is, including cultural and social sciences.

This work was partially supported by the Grant-in-Aid for Scientific Research (No. 04780001) from the Ministry of Education, Science, and Culture, Japan (1992).

References

[1] G. M. W. Kroesen, D. C. Schram, and M. J. F. van de Sande, *Plasma Chem. Plasma Proc.*, **10**, 49 (1990).

[2] T. Sone, H. Akatsuka, and M. Suzuki, *Plasma Sources Sci. Technol.*, **2**, 46 (1993).

[3] G. M. W. Kroesen, C. J. Timmermans, and D. C. Schram, *Pure & Appl. Chem*, **60**, 795 (1988).

[4] M. C. M. van de Sanden, J. M. de Regt, G. M. Janssen, D. C. Schram, J. A. M. van der Mullen, and B. van der Sijde, *Rev. Sci. Instrum.*, **63**, 3369 (1992).

[5] H. R. Griem, *Plasma Spectroscopy*, New York: McGraw Hill, (1964).

[6] J. Cooper, *Rep. Prog. Phys.*, **29**, 35 (1966).

[7] L. I. Gudzenko, L. A. Shelepin, and S. I. Yakovlenko, *Usp. Fiz. Nauk* **114**, 457 (1974) [*Sov. Phys. Usp.*, **17**, 848 (1975)].

[8] M. Suzuki, *Hyojun Kogen (Standard Light Sources)*, [Spectrosc. Soc. Jpn. Sokuteihou (measurements methods) Series, Vol. 9, 2nd Ed., Edited by S. Murayama], Tokyo: Gakkai Shuppan Senta, (1985) (in Japanese).

[9] I. Langmuir and H. M. Mott-Smith, *Phys. Rev.*, **28**, 727 (1926).

[10] S. Teii, *Purazuma Kiso Kogaku (Plasma Fundamental Technology) 2nd Ed.*, Tokyo: Uchida Rokakuho, (1989) (in Japanese).

[11] G. Spiwak and E. Reichrudel, *Zh. Tekh. Fiz.*, **5**, 715 (1938).

[12] J. S. Chang, B. Evans, R. M. Hobson, M. Kamitsuka, S. Teii, and K. Teshima, *Planet. Space Sci.*, **29**, 1345 (1981).

[13] T. Fujimoto, *J. Phys. Soc. Jpn.*, **47**, 265 (1979), **47**, 273 (1979), **49**, 1561 (1980), **49**, 1569 (1980), **54**, 2905 (1985).

[14] L. I. Gudzenko and L. A. Shelepin, *Zh. Eksp. Teor. Fiz.* **45**, 1445 (1963) [*Sov. Phys. JETP*, **18**, 998 (1963)].

[15] P. Hoffmann and W. L. Bohn, *Z. Naturforsch*, **27a**, 878 (1972).

[16] S. W. Bowen and C. Park, *AIAA-Journal* **10**, 522 (1972).

[17] K. Sato, *J. Phys. Soc. Jpn.*, **43**, 1027 (1977).

[18] K. Sato, M. Shiho, M. Hosokawa, H. Sugawara, T. Oda, and T. Sasaki, *Phys. Rev. Lett.*, **51**, 109 (1980).

[19] E. M. Campbell, R. G. Jahn, W. F. von Jaskowsky, and K. E. Clark, *Appl. Phys. Lett.*, **30**, 575 (1977).

[20] W. T. Silfvast, L. H. Szeto, and O. R. Wood II, *Appl. Phys. Lett.*, **31**, 334 (1977).

[21] W. T. Silfvast, L. H. Szeto, and O. R. Wood II, *Appl. Phys. Lett.*, **33**, 936 (1978).

[22] W. T. Silfvast, L. H. Szeto, and O. R. Wood II, *Opt. Lett.*, 4, 271 (1979).

[23] E. M. Campbell, R. G. Jahn, W. F. von Jaskowsky, and K. E. Clark, *J. Appl. Phys.*, **51**, 109 (1980).

[24] T. Hara, K. Kodera, M. Hamagaki, K. Matsunaga, M. Inutake, and T. Dote, *Jpn. J. Appl. Phys.*, 7, L386 (1980).

[25] T. Hara, K. Kodera, M. Hamagaki, K. Matsunaga, M. Inutake, and T. Dote, *Jpn. J. Appl. Phys.*, **10**, L606 (1980).

[26] U. Furukane and T. Oda, *J. Quant. Spectrosc. Radiat. Transfer*, **22**, 239 (1979).

[27] U. Furukane, Y. Tsuji, and T. Oda, *J. Quant. Spectrosc. Radiat. Transfer*, **27**, 557 (1982).

[28] T. Oda and U. Furukane, *J. Quant. Spectrosc. Radiat. Transfer*, **29**, 553 (1983).

[29] U. Furukane and T. Oda, *J. Quant. Spectrosc. Radiat. Transfer*, **33**, 645 (1985).

[30] L. I. Gudzenko and L. A. Shelepin, *Dokl. Akad. Nauk SSSR*, **160**, 1296 (1965) [*Sov. Phys. -Dokl.*, **10**, 147 (1965)].

[31] V. M. Goldfarb, E. V. Ilyina, I. E. Kostygova, G. A. Lukyanov, and V. A. Silantyev, *Opt. Spektrosk.*, **20** 1085 (1966) [*Opt. Spectrosc. (USSR)*, **20**, 602 (1966)].

[32] L. I. Gudzenko, S. S. Filippov, and L. A. Shelepin, *Zh. Eksp. Teor. Fiz.*, **51**, 1115 (1966) [*Sov. Phys. JETP*, **24**, 745 (1967)].

[33] V. M. Goldfarb, E. V. Ilina, I. E. Kostygova, and G. A. Lukyanov, *Opt. Spektrosk.*, **27**, 204 (1969) [*Opt. Spectrosc. (USSR)*, **27**, 108 (1969)].

[34] B. F. Gordiets, L. I. Gudzenko, and L. A. Shelepin, *Zh. Eksp. Teor. Fiz.*, **55**, 942

(1968) [*Sov. Phys. JETP*, **28**, 489 (1969)].

[35] E. L. Latush and M. F. Sém, *Zh. Eksp. Teor. Fiz.*, **64**, 2017 (1973) [*Sov. Phys. JETP*, **37**, 1017 (1973)].

[36] L. I. Gudzenko, M. V. Nezlin, and S. I. Yakovlenko, *Zh. Tekh. Fiz.*, **43**, 1931 (1973) [*Sov. Phys. Tech. Phys.*, **18**, 1218 (1974)].

[37] S. A. Reshetnyak and L. A. Shelepin, *Zh. Tekh. Fiz.*, 44, 1724 (1973) [*Sov. Phys. Tech. Phys.*, **19**, 1076 (1975)].

[38] G. M. Zhinzhikov, G. A. Luk'yanov, V. V. Nazarov, and N. O. Pavlova, *Zh. Tekh. Fiz.*, **48**, 949 (1978) [*Sov. Phys. Tech. Phys.*, **23**, 554 (1978)].

[39] M. F. Veresh, I. P. Zapesochnyi, and V. P. Starodub, *Opt. Spektrosk.*, **62**, 245 (1987) [*Opt. Spectrosc. (USSR)*, **62**, 145 (1987)].

[40] M. F. Veresh, I. P. Zapesochnyi, and V. P. Starodub, *Zh. Tekh. Fiz.*, **57**, 572 (1987) [*Sov. Phys. Tech. Phys.*, **32**, 347 (1987)].

[41] S. Suckewer, C. H. Skinner, H. Milchberg, C. Keane, and D. Voorhees, *Phys. Rev. Lett.*, **55**, 1753 (1985).

[42] T. Hara, K. Ando, N. Kusakabe, H. Yashiro, and Y. Aoyagi, *Jpn. J. Appl. Phys.*, **28**, L1010 (1989).

[43] A. E. Harris and J. F. Young, *J. Opt. Soc. Am.*, **B 4**, 547 (1987).

[44] Y. Kato, *Kakuyugo Kenkyu*, **65**, 338 (1991) (in Japanese).

[45] S. Suckewer and H. Fishman, *J. Appl. Phys.*, **51**, 1922 (1980).

[46] W. T. Silfvast and O. R. Wood II, *J. Opt. Am.*, **B 4**, 609 (1987).

[47] H. Azuma, Y. Kato, K. Yamagawa, T. Tachi, M. Nishio, H. Shiraga, S. Nakai, S. A. Ramsden, G. J. Pert, and S. J. Rose, *Opt. Lett*, **15**, 1011 (1990).

[48] Y. Kato, H. Azuma, K. Murai, K. Yamakawa, H. Shiraga, G. J. Pert, S. A. Ramsden, M. H. Key, and C. P. J. Barty, *Inst. Phys. Conf. Ser.*, **116**, *Int. Colloq. X-ray Lasers, York*, 1 (1991).

[49] Y. Kato, *J. Plasma Fusion Res.*, **70**, 820, (1994) (in Japanese).

[50] T. Hara, *J. Plasma Fusion Res.*, **70**, 826, (1994) (in Japanese).

[51] G. M. W. Kroesen, D. C. Schram, A. T. M. Wilbers, and G. J. Meeusen, *Contrib. Plasma Phys.*, **31**, 27 (1991).

[52] M. C. M. van de Sanden, J. M. de Regt, and D. C. Schram, *Phys. Rev. E*, **47**, 2792 (1993).

[53] H. Nishiyama, T. Sato, and S. Kamiyama, *Mem. Inst. Fliud Sci, Tohoku Univ.*, 4, 1 (1993) (in Japanese).

[54] Y. Uesugi, *J. Plasma Fusion Res.*, **69**, 1163 (1993) (in Japanese).

[55] M. Shimada, *J. Plasma Fusion Res.*, **69**, 1155 (1993) (in Japanese).

[56] N. Ohyabu, *J. Plasma Fusion Res.*, **69**, 1170 (1993) (in Japanese).

[57] T. Shoji, *J. Plasma Fusion Res.*, **69**, 1174 (1993) (in Japanese).

[58] M. Shimada, *J. Plasma Fusion Res.*, **69**, 1184 (1993) (in Japanese).

[59] H. Akatsuka and M. Suzuki, *Rev. Sci. Instrum.*, **64**, 1734 (1993).

[60] M. Suzuki, *Proc. Jpn. Symp. Plasma Chem.*, **2**, 251 (1989).

[61] M. Suzuki, *Kagaku Kogaku Ronbunshu*, **16**, 614 (1990) (in Japanese).

[62] H. Akatsuka and M. Suzuki, *Phys. Rev. E*, **49**, 1534 (1994).

[63] M. Otsuka, R. Ikee, and K. Ishii, *J. Quant. Spectrosc. Radiat. Transfer*, **15**, 995 (1975).

[64] M. Otsuka, R. Ikee, and K. Ishii, *J. Quant. Spectrosc. Radiat. Transfer*, **21**, 41 (1979).

[65] K. Sato, *Rev. Laser Eng.*, **19**, 508 (1991) (in Japanese).

[66] S. Masuzaki, N. Ohno, M. Takagi, and S. Takamura, *T. IEE Japan*, **112-A**, 913 (1992) (in Japanese).

[67] Report of IPFR, UCLA PPG #1380 (1991).

[68] H. Akatsuka and M. Suzuki, *Plasma Sources Sci. Technol.*, 4, 125, (1995).

[69] H. Akatsuka and M. Suzuki, *Contrib. Plasma Phys.*, **34**, 539, (1994).

[70] H. Akatsuka and M. Suzuki, *J. Plasma Fusion Res.*, **70**, 1196 (1994) (in Japanese).

[71] A. Kanzawa, *Purazuma Dennetsu (Plasma Heat Transfer)*, Tokyo: Shinzansha Shuppan, (1992) (in Japanese).

[72] P. C. Kong, M. Suzuki, R. Young, and P. Pfender, *Plasma Chem. Plasma Proc.*, **3**, 115 (1983).

[73] M. Suzuki, K. Etemadi, and E. Pfender, *Kagaku Kogaku Ronbunshu*, **11**, 412 (1985) (in Japanese).

[74] J. B. Hopkins, P. R. R. Langridge-Smith, M. D. Morse, and R. E. Smalley, *J. Chem. Phys.*, **78**, 1627 (1983).

[75] T. Nishimura and T. Sato, *J. Spectrosc. Soc. Jpn.*, **42**, 253 (1993) (in Japanese).

[76] M. Czerny and A. F. Turner, *Z. Phys.*, **61**, 792 (1930).

[77] *Hikari no Keisoku Manyuaru*, (Manuals for optical measurements) Ed. by the Illuminating Engineering Institute of Japan, Chapter 7, Tokyo: Nihon Rikou shuppankai, (1990) (in Japanese).

[78] H. Ashkenas and F. S. Sherman, *Rarefied Gas Dynamics*, **1**, New York: Academic Press Inc., (1965).

[79] R. S. Devote and C. P. Li, *J. Plasma Phys.*, **2**, 17 (1968).

[80] E. Holzhauer, *Phys. Lett.*, **62A**, 495 (1977).

[81] W. Kasparek, K. Hirsch, and E. Holzhauer, *Plasma Phys.*, **22**, 555 (1980).

[82] M. Nagatsu and T. Tsukishima, *Jpn. J. Appl. Phys.*, **20**, 2155 (1981).

[83] I. Kamitsuka and M. Okazaki, *Jpn. J. Appl. Phys.*, **6**, 123 (1967).

[84] M. Sato, *Phys. Fluids*, **17**, 1903 (1974).

[85] M. Hayashi, *J. Phys. (Paris)*, **40-C7**, 45 (1979).

[86] M. Hayashi, *J. Phys. D*, **15**, 1411 (1982).

[87] M. Mitchner and C. H. Kruger Jr., *Partially Ionized Gases*, New York: A Wiley Interscience Publication, (1973).

[88] L. Spitzer Jr., *Physics of Fully Ionized Gases, 2nd Ed.*, New York: Interscience Publishers, (1962).

[89] J. R. Holway, *Rarefied Gas Dynamics*, vol.1, 193, New York: Academic Press Inc., (1965).

[90] Y. S. Chou and L. Talbot, *AIAA-Journal*, **5**, 2166 (1967).

[91] H. Tahara *et.al*, *AIAA Paper*, **AIAA-87**, 1093 (1987).

[92] S. Nishizawa and T. Nagoshi, *J. Spectrosc. Soc.Jpn.*, **42**, 177 (1993) (in Japanese).

[93] T. Sone, H. Akatsuka, and M. Suzuki, *Proc. Jpn. Symp. Plasma Chem.*, **5**, 143 (1992).

[94] M. Sumida and K. Koki, *AIAA Paper*, **AIAA-87**, 1066 (1987).

[95] W. L. Wiese, M. W. Smith, and B. M. Glennon, *Atomic Transition Probabilities, Vol. 1. Hydrogen Through Neon*, Natl. Bur. Stand. Ref. Data Ser., Natl. Bur. Stand. (U.S.) Circ. No. 4 (U.S. GPO, Washington, DC, 1966).

[96] S. Bashkin and J. O. Stoner Jr., *Atomic Energy Levels and Grotorian Diagrams, Vol. 1*, North-Holland Publishing Company and American Elsevier Publishing Company (1975).

[97] M. Otsuka, *BUTSURI*, **35**, 428 (1980) (in Japanese).

[98] K. Bochasten, *J. Opt. Soc. Am.*, **51**, 943 (1961).

[99] R. Paquette and W. L. Wiese, *Appl. Opt.*, **3**, 291 (1964).

[100] P. Elder, T. Jerrick, and J. W. Birkeland, *Appl. Opt.*, 4, 589 (1965).

[101] T. Fujimoto and R. W. P. McWhirter, *Phys. Rev. A*, **42**, 6588 (1990).

[102] J. A. M. van der Mullen, *Phys. Rep.*, **191**, 109 (1990).

[103] U. Furukane, K. Sato, and T. Oda, *J. Phys. D*, **22**, 390 (1989).

[104] U. Furukane, K. Sato, and T. Oda, *Jpn. J. Appl. Phys.*, **29**, 1814 (1990).

[105] T. Fujimoto, *J. Quant. Spectrosc. Radiat. Transfer*, **21**, 439 (1979).

[106] J. Slavík, *Contrib. Plasma Phys.*, **31**, 605 (1991), **31**, 613 (1991).

[107] R. K. Janev, W. D. Langer, K. Evans Jr., and D. E. Post Jr., *Elementary Processes in Hydrogen-Helium Plasmas, Springer Series on Atoms and Plasmas Vol. 4*, Springer Verlag, Germany (1987).

[108] T. Tsuda, *Suuchi Shori Puroguramingu (Numerical Processing in Programming)*, [The Iwanami Software Science Ser. 9], Tokyo: Iwanami Shoten (1988) (in Japanese).

[109] C. G. Broyden, *Comput. J.*, **12**, 94 (1969).

[110] K. L. Bell, H. B. Gilbody, J. G. Hughes, A. E. Kingston, and F. J. Smith, *J. Phys. Chem. Ref. Data*, **12**, 891 (1983).

[111] W. J. Karzas and R. Latter, *Astrophys. J. (Suppl.)*, **6**, 167 (1961).

[112] R. H. Garstang, *Astrophys. J.*, **148**, 579 (1967).

[113] R. S. van Dyck Jr., C. E. Johnson, and H. A. Shugart, *Phys. Rev. Lett.*, **25**, 1403 (1970).

[114] H. W. Moos and J. R. Woodworth, *Phys. Rev. Lett.*, **30**, 775 (1973).

[115] A. V. Phelps, *Phys. Rev.*, **99**, 1307 (1955).

[116] A. W. Johnson and J. B. Geraldo, *Phys. Rev. A*, **7**, 925 (1973).

[117] T. Kato, *Purazuma Shindan no Kiso (Fundamentals of Plasma Diagnostics), Ch5*, Ed. by the Japan Society of Plasma Science and Nuclear Fusion Research, Nagoya: Nagoya Univ. Shuppankai (1990) (in Japanese).

[118] H. R. Griem, *Spectral Line Broadening by Plasmas*, New York: Academic Press, (1974).

[119] E. L. Lewis, M. M. Rebbeck and J. M. Vaughan, *J. Phys. B: Atom. Molec. Phys.*, **4**, 741 (1971).

[120] J. S. Chang, R. M. Hobson, Y. Ichikawa and T. Kaneda, *Denri Kitai no Genshi Bunshi Katei (Atomic and Molecular Processes of Ionized Gases)*, Tokyo: Tokyo Denki Univ. Shuppankyoku (1982) (in Japanese).

[121] J. L. Delcroix, C. M. Ferreira and A. Richard, *"Metastable Atoms and Molecules in Ionized Gas" in "Principle of Laser Plasma"*, Ed. G. Bekefi, New York: John Wiley, (1976).

[122] T. Fujimoto, I. Sugiyama, and K. Fukuda, *Mem. Fac. Eng. Kyoto Univ.*, **34**, 249 (1972).

[123] A. Hirabayashi, Y. Nambu, M. Hasuo, and T. Fujimoto, *Phys. Rev. A*, **37**, 77 (1988).

[124] L. Frommhold and M. A. Biondi, *Phys. Rev.*, **185**, 244 (1969).

[125] P. Manschbach and J. Keck, *Phys. Rev.*, **181**, 275 (1969).

[126] F. Devos, J. Boulmer, and J. -F. Delpech, *J. Phys. (Paris)*, **40**, 215 (1979).

[127] H. W. Drawin, *Association Euratom-CEA*, Report No. **EUR-CEA-FC-383**, (1967) (unpublished).

[128] A. Unsöld, *Physik der Sternatmosphären*, 2nd ed., Berlin: Springer-Verlag, (1955).

[129] S. Kasai, A. Funahashi, S. Konoshima, M. Nagani, T. Sugie, and K. Mori, *Jpn. J. Appl. Phys.*, **17**, 1625 (1978).

[130] W. L. Wiese, M. W. Smith, and B. M. Miles, *Atomic Trasition Probabilities, Vol. 2, Sodium Through Calcium*, Natl. Bur. Stand. Ref. Data Ser., Natl. Bur. Stand. (U.S.) Circ. No. 22 (U.S. GPO, Washington, DC, 1969).

[131] K. Katsonis and H. W. Drawin, *J. Quant. Spectrosc. Radiat. Transfer*, **23**, 1, (1980).

[132] T. Hasegawa, K. Fuwa, and H. Haraguchi, *Chem. Lett.*, **1984**, 2027 (1984).

[133] T. Hasegawa and H. Haraguchi, *Spectrochimica Acta*, **40B**, 1067 (1985).

[134] H. Massey, *Atomic and Molecular Collisions*, London: Taylor and Francis Ltd., (1979).